university of groningen / faculty of science and engineering / kapteyn astronomical institute

Master Thesis

Constraining the Milky Way's gravitational potential with the Helmi Streams' clumps

A complex story involving resonances and chaos

Author:
H.C. Woudenberg
S3238989

Supervisor:
A. Helmi

In any part of the Universe
there is a whole Universe.

ALBARRAN CABRERA

Abstract

Stellar streams are the remnants of dwarf galaxies and globular clusters that have been tidally disrupted while orbiting the Milky Way. They are promising tools to map the gravitational potential of the Milky Way, because they follow close trajectories. In particular, have been used to constrain the shape and mass of its dark matter halo, for which usually narrow distant streams are used. The focus of this thesis are the dynamical properties of the phase-mixed Helmi Streams. These streams originate in a disrupted small dwarf galaxy that was cannibalised by the Milky Way several Gyr ago. The Helmi Streams now orbit the inner Galaxy and depict peculiar dynamical properties. Specifically, they appear to be separated into two clumps in angular momentum space which differ in their degree of phase-mixing. In this thesis, I explore the formation mechanism and the conservation of the gap between the two clumps in time as a way to provide a novel constraint on the Galactic potential.

The two clumps have a distinct v_z and orbital frequency distribution, but are indistinguishable in their stellar populations. The asymmetry in the number of stars in the streams can be linked to the fact that one clump has undergone a slower dynamical evolution than the other. This is appears to be caused by dynamics specific to the potential of the Milky Way. The region of the potential probed by the Helmi Streams hosts multiple resonances. In the correct potential, the less phase-mixed clump is trapped by the $\Omega_\Phi : \Omega_Z$ is $1:1$ resonance while the other clump is located off-resonance. Furthermore, to maintain the gap in time, a potential that transitions to being spherical in the region occupied by the Helmi Streams is required.

The gap between the two clumps could possibly be caused by orbital diffusion due to a chaotic region in the potential. This tightly constrains the Galactic potential as chaotic regions are generally small. The separatrix of the $\Omega_z : \Omega_R$ is $2:3$ resonance, which is located close to the Helmi Streams, is found to cause stochastic behaviour. When an ensemble of stars occupies the region of phase-space surrounding this layer, a gap can be formed on small enough timescales ($\sim$ 6 Gyr). This resonance, however, does not overlap exactly with the region of phase-space occupied by the Helmi Streams in a Milky Way potential. Modifying the analytic potential by varying its characteristic parameters using an MCMC shows that a too high mass enclosed is needed to move the resonance to the required location.

To move away from the restrictions of parametrisation and allow for a more generic description of the dark matter halo's shape, a method is introduced that uses basis function expansions, where the basis functions are spherical harmonics. By performing a low-order expansion of an axisymmetric dark matter halo and by varying the coefficients and their derivatives at the gridpoints using an MCMC, the shape of the halo can be explored in a novel way. Applying this method with the objective to get the Helmi Streams closer to the $\Omega_z : \Omega_R$ is $2:3$ resonance shows again that a too high mass enclosed is needed, indicating that more freedom in the functional form does not resolve this issue. Instead, it seems that a more complex model, for example one that radially varies in shape which transitions from being spherical to triaxial farther out, might be necessary.

Contents

1 Introduction **1**
1.1 Thin and Thick Disk . . . 2
1.2 Central Region . . . 3
1.3 Halo: Satellites and Stellar Streams . . . 3
1.4 Stellar halo: Building Blocks of our Milky Way . . . 5
1.5 Galactic Dynamics . . . 6
1.5.1 Orbits and Orbit Integration . . . 6
1.5.2 Integrals of Motion . . . 6
1.6 The Milky Way's Circular Velocity Curve . . . 7
1.7 Milky Way Dynamical Models . . . 9
1.7.1 Milky Way Mass Models . . . 9
1.7.1.1 The McMillan 2017 Milky Way Mass Model . . . 9
1.7.1.2 Other Milky Way Mass Models . . . 10
1.7.2 Estimates of the Dark Matter Halo's Mass . . . 10
1.7.3 Total Potential Flattening . . . 10
1.7.4 Default Potential . . . 11
1.7.4.1 Values of Characteristic Galactic Constants . . . 12
1.8 Outline of this Thesis . . . 12

2 Characterisation of the Helmi Streams' clumps **14**
2.1 The Helmi Streams in *Gaia* EDR3 . . . 14
2.2 The Helmi Streams in *Gaia* DR3 . . . 16
2.3 Characterising the Helmi Streams: Phase-Space Distribution . . . 17
2.4 Characterising the Helmi Streams: Orbital Properties . . . 19
2.4.1 Orbital Frequencies . . . 19
2.4.2 Orbits . . . 21
2.5 A Kinematically Cold Subclump . . . 24
2.6 Summary . . . 24

3 Proof of concept: Basis Function Expansions **26**
3.1 `AGAMA`'s `Multipole` Expansion . . . 27
3.1.1 Generalities . . . 27
3.1.2 How Many Terms do we Need? . . . 28
3.2 Turning an NFW Profile into a Hernquist Profile . . . 31
3.3 An Application of BFE: Maximising Clump Distance . . . 32
3.3.1 Using the Helmi Streams as a Constraint on the Galactic Potential . . . 32
3.3.2 BFE: Freedom to Maximise the Clump Distance . . . 34
3.4 Summary . . . 37

4 Explaining the Gap: Chaos! **39**
4.1 Chaoticity Explained . . . 39
4.2 Chaos Indicators . . . 40
4.3 The Behaviour of an Ensemble of Stars near the Gap in the Default Potential . . . 42
4.4 Zooming in around the $2:2:3$ Resonance . . . 45

5 Chaos: a constraint on the Galactic potential **48**
5.1 Getting the Streams on the $2:2:3$ Resonance . . . 48
5.2 Mapping the Resonances in the $2:2:3$ Potential . . . 53
5.3 BFE: Freedom to the $2:2:3$ Resonance? . . . 56
5.4 Summary . . . 57

6 Discussion **58**
6.1 Other Applications of Orbital Frequencies . . . 58
6.1.1 The Helmi Streams, Sagittarius and Jhelum . . . 58
6.2 `SuperFreq`: $\Omega_z : \Omega_R$ is $1:2$ versus $2:3$ for the Helmi Streams . . . 59
6.3 Basis Function Expansions . . . 59
6.4 Chaos and Resonances . . . 60

7 Conclusions **62**

A The Helmi Streams in *Gaia* DR3 **64**

B Dependence Orbital Frequencies on Characteristic Parameters **68**
B.1 Varying the Flattening of the Halo 68
B.2 Varying the Scale Radius of the Halo 68
B.3 Varying the Mass of the Stellar Disks 68

C Exploring the MCMC Chains of McMillan 2017 and Cautun et al. 2020 **72**

D Dependency Orbital Structure on the Gravitational Potential **75**

E Actions and Angles **76**

References **89**

1 Introduction

Our home, the **Milky Way**, is a barred spiral galaxy which is made up several components, see Fig. 1. There are more than 100 billion stars in the Milky Way, which add up to a mass of approximately $5 \pm 1 \cdot 10^{10} M_{\odot}$ (Bland-Hawthorn and Gerhard 2016). Most of these stars reside in the stellar disks and bar/bulge component, which are surrounded by the diffuse stellar halo, containing some of the oldest and most metal-poor stars in our Galaxy. The stellar halo contains at most a few percent of the total amount of stars in our Galaxy (Bland-Hawthorn and Gerhard 2016; Deason et al. 2019), but, as we will see later, these have proven to be very important tracers of the history of the Milky Way. The different stellar components of the Milky Way differ in their kinematics, age and chemistry, pointing to different formation histories (Helmi 2020).

The stars in the Milky Way are embedded in a large and massive dark matter (DM) halo, which has an extent of about 200 kpc and a mass of about $1 \cdot 10^{12} M_{\odot}$ (Shen et al. 2021), meaning that $\sim$ 95 % of the mass of our Galaxy is dark. The DM halo therefore has a profound impact on the dynamics of the Milky Way's stars, especially in the outer regions of the Galaxy. There, the DM halo dominates the gravitational potential. Though obviously important, the distribution of mass and the shape of the DM halo are uncertain and debated (e.g. Koposov et al. 2010; Küpper et al. 2015; Posti and Helmi 2019; Vasiliev et al. 2021).

Within the context of the Λ Cold Dark Matter (ΛCDM) cosmological model, structure formation happens hierarchically and dark matter halos grow predominantly via mergers (e.g. White and Rees 1978). This means that galaxies like our Milky Way have grown over time, particularly in mass, by merging with other smaller galaxies. Such mergers can trigger star formation and may have shaped the Galaxy to the structure we see today. As a result of the merger process, the stellar halo is not smooth. Instead, it is made up of many accreted satellite galaxies and stellar clusters at different stages of disruption. Some are entirely mixed in with the Galaxy and are not visible as coherent structures anymore. Others, such as the Large and Small Magellanic Cloud dwarf galaxies, have only just fallen in (Besla et al. 2007) and are largely intact, see Fig. 1. In many cases we can actually see the disruptive power of the Milky Way at work. An important example is the Sagittarius dwarf galaxy (Ibata et al. 1994), whose extended tidal tails wrap itself around the Milky Way[1]

The goal of the field Galactic Archaeology is to reconstruct the assembly history of the Milky Way over time and find out what its different building blocks are. This can be done using the stars themselves, as they retain a memory of their origin in their phase-space position (position and velocity) and their chemistry. Stars thus provide us with a window back in time, and the stellar halo is one of the best places to learn about the Milky Way's history as that is where most of the debris from the accreted satellites will end up. To achieve the goal set out by Galactic archaeologists, we require the 6D phase-space positions of stars in order to fully characterise their kinematics and orbital properties. If we complement this with data on the chemistry and ages of the stars, we can distinguish stars from different progenitors more easily. The bigger our sample of 6D phase-space positions and chemistry is, the better and more conclusive our picture of the Milky Way's history will become. In that sense, the second data release from the *Gaia* mission was a revolution (Gaia Collaboration et al. 2016; Gaia Collaboration et al. 2018). At once astronomers had access to the astrometry and photometry of millions of stars with great precision. With *Gaia* EDR3 (Gaia Collaboration et al. 2021a) this dataset has become even larger and more accurate. With WEAVE (Dalton et al. 2014) and 4MOST (de Jong et al. 2019) getting ready for first light, allowing us to get spectroscopic data for many more stars, and *Gaia* DR3 (Gaia Collaboration et al. 2022) having been released June 13 2022, we live in very exciting times!

At the basis of the understanding of the history of the Milky Way is the study of the system itself. Using the observed motions and distributions of stars of our Galaxy, Galactic dynamicists try to infer, amongst other things, how the mass of the Milky Way is distributed and what the total mass of the system is. This provides important constraints on our understanding of galaxy formation (e.g. Bower et al. 2017; Behroozi et al. 2019) and allows us to identify and simulate realistic Milky Way analogues in cosmological simulations (Wetzel et al. 2016; Grand et al. 2017; Libeskind et al. 2020). Moreover, the Milky Way's mass is an important parameter in determining the kinematics its satellite galaxies (e.g. Fritz et al. 2018) and can even be used to constrain the nature of dark matter. Within the ΛCDM cosmological framework, there are two important problems with the small-scale predictions for dark matter that rely on the mass of our Milky Way's DM halo. Firstly, the "Missing Satellites" problem (Moore et al. 1999; Klypin et al. 1999), which is the prediction that many more satellites should exist than we observe. Within 300 kpc, ΛCDM can predict up to $\sim$ 1000 dark subhalos which could possibly host galaxies, while we observe only 50 dwarf galaxies around our Milky Way (Bullock and Boylan-Kolchin 2017; McConnachie and Venn 2020). Feedback and tidal stripping can keep satellites dark, providing

[1] "It is always Sagittarius" - due to Sagittarius' large extent and the fact that its stars dominate in their contribution to the outer stellar halo ($25 - 50$ kpc, Naidu et al. 2020), Sagittarius is often recovered when looking for substructure in the outer halo.

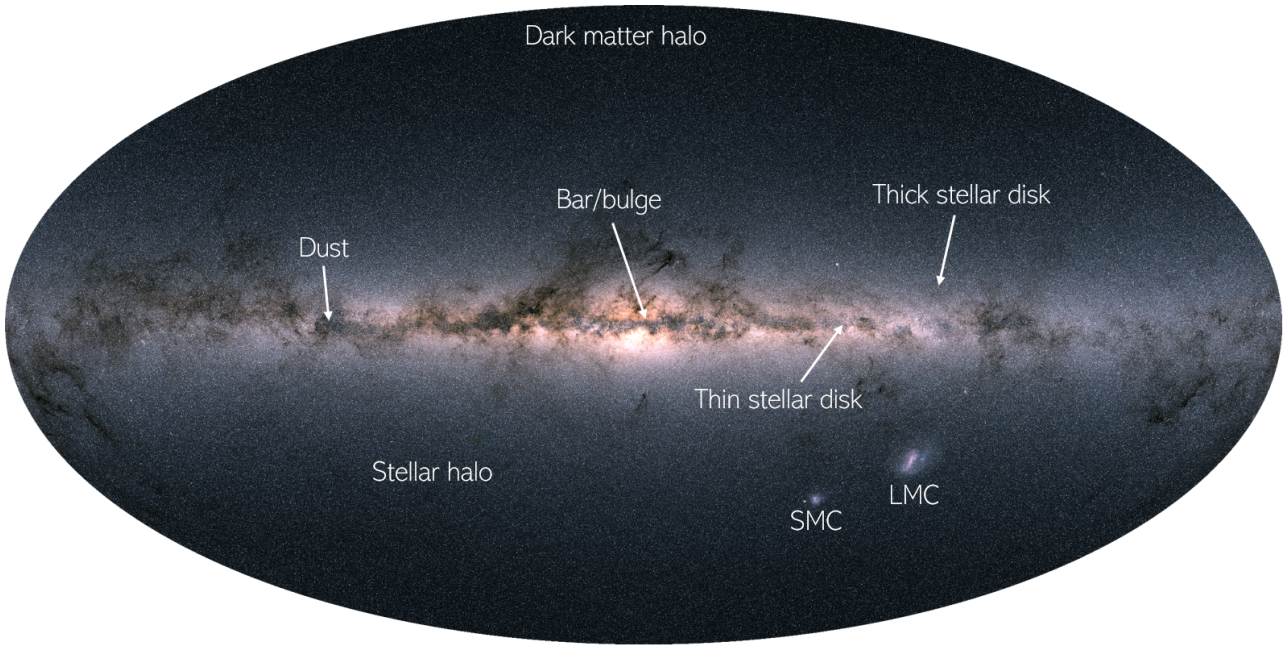

Figure 1: The Milky Way and its components. This map is based on *Gaia* DR2 data. The Small Magellanic Cloud (SMC) and Large Magellanic Cloud (LMC) are two satellite galaxies orbiting the Milky Way. Image adapted from ESA/Gaia/DPAC, CC BY-SA 3.0 IGO.

a possible explanation for the problem. This however does not resolve the second problem, the "Too Big To Fail" problem (Boylan-Kolchin et al. 2011; Boylan-Kolchin et al. 2012), which argues that the predicted number of massive satellites with high central densities is higher than is observed, given the number of observed less massive satellites that did succeed in forming stars (Bullock and Boylan-Kolchin 2017). The problem's name thus refers to the fact that these predicted massive satellites can hardly fail to form stars, but we do not see them. In both cases, the problem can largely be resolved if the mass of the Milky Way is relatively low (e.g. Cautun et al. 2014), as this lowers the predicted number of (massive) satellites. Another way to resolve the problem is by assuming a Warm Dark Matter cosmology, as this lowers the central density of massive satellites (Anderhalden et al. 2013). In conclusion, a well-constrained estimate of the mass and mass profile of our Milky Way allows us to place our own Galaxy and its satellites in a larger cosmological and theoretical context.

This introduction is further split up in several parts and aims to familiarise the reader with the structure and history of our Milky Way. This sets the scene for a Galactic Dynamics view of our Galaxy. Section 1.1 and 1.2 introduce the stellar disks and bulge a bit more in depth, while Section 1.3 focuses on the stellar halo and the satellites and streams it hosts. This brings us to an overview of the recent efforts and results in the field of Galactic Archaeology in Section 1.4. After providing an introduction to some important concepts in Galactic Dynamics in Section 1.5, I give an overview of the observational constraints I use throughout this thesis in Section 1.6. I review our current knowledge on the total mass and mass distribution of our Milky Way in Section 1.7. Finally, Section 1.8 provides an outline of this thesis.

1.1 Thin and Thick Disk

The Milky Way contains a thin and a thick stellar disk. Both disk populations are well described by an exponential profile (e.g. Jurić et al. 2008; Bovy et al. 2016b). It is thought that the thick disk is a result of a merger with the large dwarf galaxy Gaia-Enceladus-Sausage that took place about 10 Gyr ago, which heated up the early gas-rich disk and triggered star formation (Gallart et al. 2019; Helmi 2020). This merger "splashed" the existing disk stars to hotter orbits, and the thin disk formed in a quiescent way afterwards. This sequence of events is supported by the stellar age-metallicity distribution of our Galaxy (Xiang and Rix 2022). Given this formation history, it can be expected that the thin disk is larger in extent than the thick disk. Other properties of the thin disk, such as the number and extent of the spiral arms, are not very well constrained, as there is quite strong dust extinction in the midplane.

The disk scale length quantifies the extent of the disks, which varies under different definitions. Stars belonging

to the thin and thick disk can be identified using α-abundances (e.g. Bensby et al. 2011; Cheng et al. 2012)[2], but different stellar populations can be also used to distinguish the two disks. Cepheids, for example, trace the thin disk as they are a young population of stars (Bobylev and Bajkova 2021). In an analysis of 130 refereed papers, Bland-Hawthorn and Gerhard 2016 found disk scale lengths ranging between $1.8-6.0\,$kpc, and using a weighted average they find a thin disk scale length of $2.6\pm0.5\,$kpc and a thick disk scale length of $R_{thick} = 2.0\pm0.2\,$kpc.

1.2 Central Region

Baade 1946 and Stebbins and Whitford 1947 first identified the Galactic bulge as a distinct component of our Galaxy. Nowadays, we think that the central part of our Galaxy contains a barred bulge. It is hard to study this central region because it is a crowded region that is heavily obscured by dust, see also Fig. 1. The bulge seems to have a boxy-peanut (X) shape which is typical for barred galaxies, and most of the mass, about ~ 90 %, is in the triaxial rotating bar. The stars in the bulge cover a broad range of metallicities, -1.5 $\lesssim$ [Fe/H] $\lesssim$ +0.5, which is dependent on the field location, suggesting that the bulge hosts multiple stellar populations (Barbuy et al. 2018). Indeed, though the bulge is predominantly made up of old stars (older than 10 Gyr), it also hosts a younger population that is more metal-rich (ages below 8 and even 5 Gyr, Ness et al. 2013; Bensby et al. 2017).

1.3 Halo: Satellites and Stellar Streams

The halo hosts a large population of objects, including dwarf galaxies (DG) and globular clusters (GC), some of which were formed inside the Milky Way (in situ), while others have been accreted. In this section I will shortly describe these objects and explain how stellar streams, of which GC and DG are the progenitor, are formed.

Globular clusters are thought to be old objects (age $\sim$ 12 Gyr, VandenBerg et al. 2013) that are devoid of gas, dust, dark matter and young stars. Our Milky Way hosts over 150 GC, of which the most metal-poor GC belong to the oldest objects present in the Galaxy (Harris 2010). About 40% of the Galactic GCs have likely formed in the Milky Way itself, while the rest has been brought in by merger events (Massari et al. 2019; Horta et al. 2020; Callingham et al. 2022). GCs are made up of $10^4 - 10^6$ stars that are packed closely together and are self-gravitating, with typical half-mass radii of 5-10 pc (de Boer et al. 2019) . All stars roughly have the same metallicity and age (typical spreads in [Fe/H] are of the order of $\sim$ 0.03 dex, see e.g. Yong et al. 2013), so it was long thought that they could be described by a single stellar population (Binney and Tremaine 2008). However, there is increasing evidence that there exist star-to-star variations in the abundances of light elements such as C, N, O and Na in old GC (age $\gtrsim$ 2 Gyr). In other words, GCs host multiple stellar populations, which can even be segregated spatially (Cordero et al. 2017; Bastian and Lardo 2018; Milone et al. 2018; Dalessandro et al. 2019). The existence of these multiple stellar populations turns the formation scenario of GC into an open question in the field, and many interesting (and even exotic) formation paths have been proposed (e.g. Denissenkov and Hartwick 2014; Renzini et al. 2022).

Dwarf galaxies contain stars, sometimes gas and are thought to be amongst the most dark matter dominated objects in our Galaxy (and even the Universe, Strigari et al. 2008; Tolstoy et al. 2009; Simon et al. 2011). Dwarf galaxies have masses between $10^3 - 10^8 M_\odot$, which is related to their metallicity via the mass-metallicity relation (Kirby et al. 2013; Hidalgo 2017), and half-light radii ranging from 10's till 1000's of pc (Wolf et al. 2010). Over 50 dwarf galaxies are known to orbit the Milky Way (McConnachie and Venn 2020). This is only a small part of the total number of dwarfs that once orbited our Galaxy, as about 70-80 % is thought to be destroyed (Santistevan et al. 2020; Fattahi et al. 2020). Because dwarf galaxies have extended star formation histories, they show a significant spread in metallicity, over $\sim$ 0.2 dex (Tolstoy et al. 2009; Willman and Strader 2012). This spread, amongst other things, allows Galactic archaeologists to distinguish between GC and DG progenitors.

When satellites like DG or GC orbit the Milky Way, they experience tidal forces which strip away the most weakly bound stars. These stars approximately follow their progenitor's orbit, and over a time a **stellar stream** is formed (Eyre and Binney 2009; Newberg 2016). Stars with a higher binding energy compared to the progenitor will form the leading arm, while stars with a lower binding energy will form the trailing arm, see Fig. 3. About 100 stellar streams have so far been discovered (Mateu 2022). A map showing some stellar streams of the Milky Way is shown in Fig. 2. Stellar streams appear as narrow bands of stars on the sky, but streams with a globular cluster progenitor (e.g. Pal 5 (Odenkirchen et al. 2001), Phoenix (Balbinot et al.

[2] α-elements are elements that are released in core-collapse supernovae (Type II) of short-living massive stars, such as Mg, Si, Ca, Ti and Na. Iron-peak elements, such as Fe, can also be released in supernovae Type Ia, which take place on a longer timescale than supernovae Type II. The trend in [α/Fe] versus [Fe/H] is thus indicative of the star formation history of a system, which differs per system (Helmi 2020).

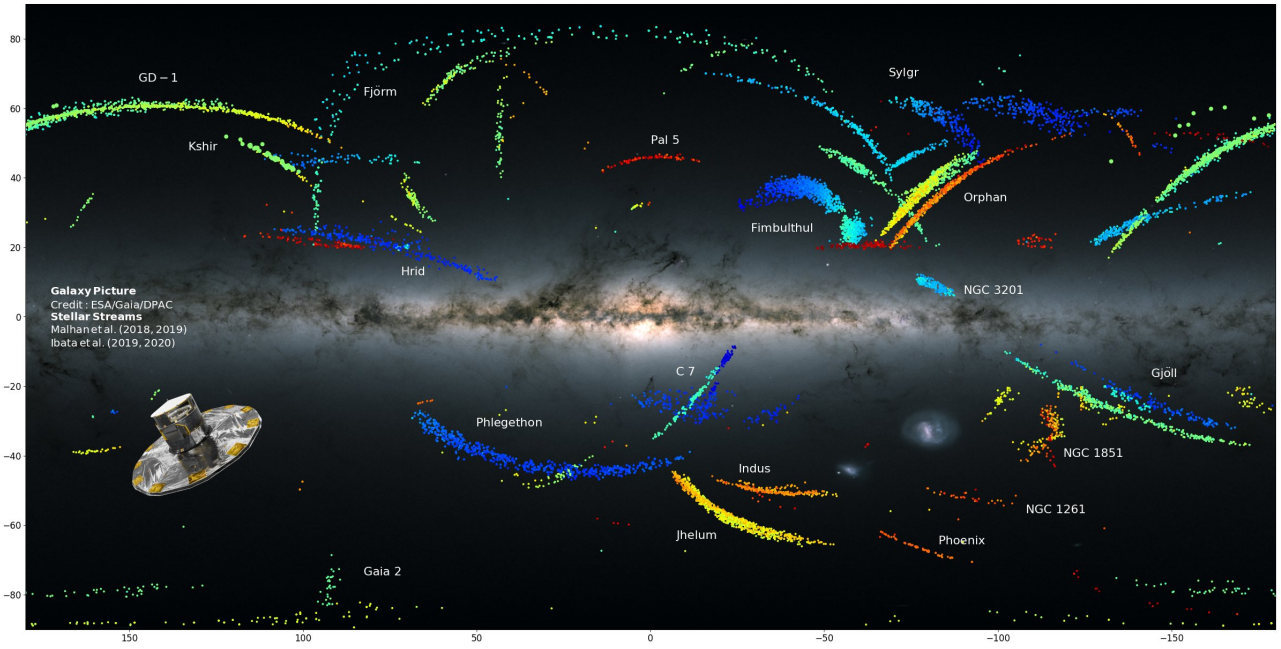

Figure 2: Stellar streams in the Milky Way found with the `STREAMFINDER` algorithm using *Gaia* DR2 and EDR3 data (Malhan and Ibata 2018; Malhan et al. 2018; Ibata et al. 2019). The stellar streams are colour-coded by their heliocentric distance, where red (blue) means farther away (closer). A part of the streams are labelled by their name. Image credits: Khyati Malhan 2021.

2016), or GD-1, found by Grillmair and Dionatos 2006) are physically thinner and dynamically colder than streams with a dwarf galaxy progenitor (e.g. Orphan, Grillmair 2006; Belokurov et al. 2007). There is however increasing evidence that stellar streams are not just simple bands of stars, but that they can have complex stream morphologies. Substructures such as gaps, overdensities and off-stream features are expected to be produced by interactions with DM subhalos, which are predicted to orbit the halos of galaxies (Yoon et al. 2011; Erkal et al. 2016; Koppelman and Helmi 2021). For example, upon closer inspection of the stellar stream GD-1, interesting features such as the "spur" and "gap" become apparent (Price-Whelan and Bonaca 2018; de Boer et al. 2020). Stellar streams thus seems to be a promising tool to study the DM subhalo population of the Milky Way, but first other possible causes for substructure should to be excluded (e.g. Amorisco et al. 2016; Pearson et al. 2017; Banik and Bovy 2019; Woudenberg et al. 2022).

Because stellar streams approximately trace out the progenitor's orbit, they can be used to probe the underlying Galactic gravitational potential (e.g. Johnston et al. 1999). This fact has been exploited to constrain the mass enclosed and shape of the DM halo (e.g. Koposov et al. 2010; Bovy et al. 2016a; Malhan and Ibata 2019). However, it has become clear that this should be done with caution, as our Galaxy is being perturbed by the infall of the massive LMC (e.g. Garavito-Camargo et al. 2019; Garavito-Camargo et al. 2021). This influences the kinematics of stellar streams (Vera-Ciro and Helmi 2013; Erkal et al. 2019; Vasiliev et al. 2021), as it induces torques and reflex motion, depending on the stream's orbit with respect to the LMC (Gómez et al. 2015; Petersen and Peñarrubia 2020; Shipp et al. 2021). A more extensive overview of the efforts to constrain the mass enclosed and shape of the DM Halo will be given in Section 1.7.3.

The more metal-poor an object is, the earlier in time it should have formed. The discovery of the exceptionally metal-poor stellar stream C-19 with a metallicity of [Fe/H] = -3.4 dex therefore provides us with a window far back in time (Martin et al. 2022a; Martin et al. 2022b). Because it has a low metallicity dispersion and shows signs of the presence of multiple stellar populations, it is thought that its progenitor should be a GC. However, the stream is dynamically hot and quite broad, pointing to a DG progenitor. Moreover, it is on an orbit with a short orbital period, so its formation scenario is an open question (Yuan et al. 2022). It is very well possible that (destroyed) systems formed in the early Universe differed from the stellar systems that we can still see today, and alternative formation scenarios are needed to explain the existence of C-19 (Errani et al. 2022).

Phase-mixed streams are stellar streams that have been orbiting the Milky Way for a sufficiently long time such that they are completely mixed in with the Galaxy. With time, the stars of a stellar stream spread along the orbit of the progenitor, meaning that at a specific moment in time stars are at an increasingly different orbital phase. This happens faster for stellar streams with short orbital periods, such as streams that orbit the

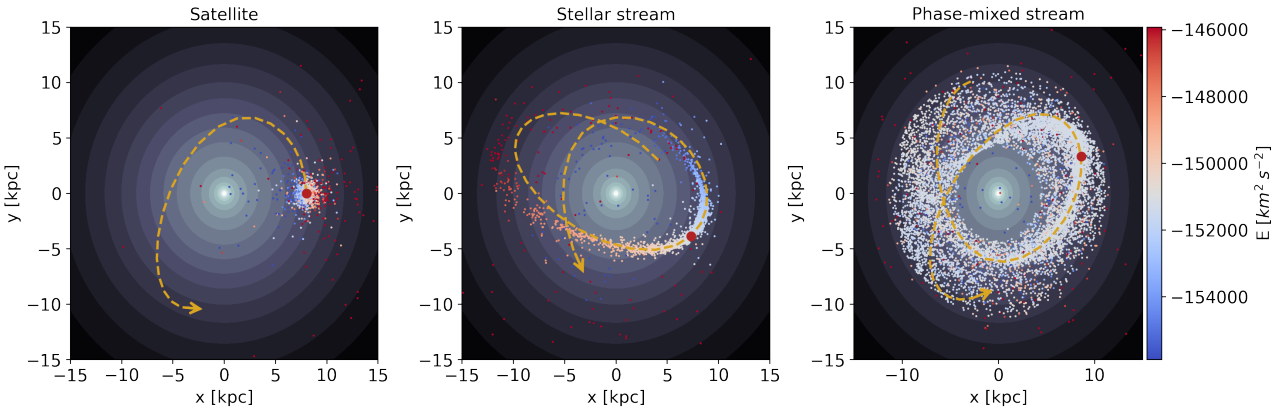

Figure 3: Illustration of a satellite at different stages of disruption. The left panel shows the intact satellite, the middle panel shows the stellar stream and the right panel shows the stream in a much more advanced stage of phase-mixing. The red dot shows the position of the progenitor. The yellow dotted line shows the orbit of the progenitor 0.2 Gyr forward and backward in time (for the intact satellite, only 0.2 Gyr forward is shown), the arrow shows the direction of the orbit. The 10^4 particles are plotted with a colourmap showing their energy. The contour map shows the density of the McMillan 2017 potential.

inner Galaxy. This mixing continues indefinitely, meaning that as time passes the stream becomes completely mixed in with the Galaxy and it is no longer apparent as a distinct spatially coherent structure, see Fig. 3[3]. This thesis focuses on (the use of) the phase-mixed **Helmi streams** (Helmi et al. 1999), which is the debris of a dwarf galaxy with a mass of $10^8 M_\odot$ that was accreted by the Milky Way 5 to 8 Gyr ago (Kepley et al. 2007; Koppelman et al. 2019b).

1.4 Stellar halo: Building Blocks of our Milky Way

The stellar halo is thought to be largely made up of the debris of disrupted stellar systems (e.g. Di Matteo et al. 2019; Naidu et al. 2020). Once satellites have fallen into the Milky Way, over time their stars get mixed in with the Galaxy. Though we can no longer recognise these building blocks from their coherent spatial distribution, they can still be distinguished from each other in Integrals of Motion (IoM) space (Helmi and de Zeeuw 2000; Helmi and de Zeeuw 2002; Gómez et al. 2010).

Integrals of Motion are quantities that describe an orbit and stay conserved over time, such as E, L_z and $L_\perp$ for a spherical potential (see also Section 1.5.2). Individual satellites each have their own distinct IoM distribution, as they come in on different orbits and each have their intrinsic IoM spread, depending on for example the mass of the system (Koppelman et al. 2019a). As IoM stay conserved with time, we can recognise different systems as "clumps" in IoM space even today, aided by additional information on the chemistry and ages of stars. This principle has been used to identify the building blocks of our Galaxy, pioneered with the discovery of the Helmi Streams (Helmi et al. 1999). With the release of *Gaia* DR2, this method led to the discovery that the local stellar halo is dominated by the debris of a large, single merger event: Gaia-Enceladus-Sausage (GES, Helmi et al. 2018; Belokurov et al. 2018). GES is thought to be the remnants of a dwarf galaxy with a mass of about $\sim 10^9$ $M_\odot$ that was accreted about 10 Gyr ago, and in merging with the MW heated stars of the existing disk onto halo-like orbits, creating the hot thick disk (Di Matteo et al. 2019). Since this discovery, more major building blocks have been identified, such as Sequoia, Thamnos and Kraken/Heracles (Myeong et al. 2019; Koppelman et al. 2019a; Kruijssen et al. 2019; Horta et al. 2021)[4]. Other, smaller building blocks have also been discovered, such as Arjuna (Naidu et al. 2020), LMS-1/Wukong (Yuan et al. 2020; Naidu et al. 2020) and Pontus (Malhan 2022), but their relation to the previously discovered mergers and sometimes their existence is still debated.

While the field started out by doing empirical selections in IoM space (e.g. Koppelman et al. 2019a, Naidu et al. 2020), recently more sophisticated methods such as clustering algorithms have been employed to actually detect substructure in IoM space or related spaces. Using for example a single-linkage clustering algorithms in IoM space (Lövdal et al. 2022; Ruiz-Lara et al. 2022b), a density-based hierarchical group finding algorithm in energy

[3] As a stream spatially mixes, the velocity dispersion of the stream will decrease due to the conservation of phase-space density (Helmi and White 1999)

[4] Kraken and Heracles have been found independently by Kruijssen et al. 2019 and Horta et al. 2021, respectively. Forbes 2020 seems to have identified the same structure, but named it Koala instead. This illustrates an outstanding issue in the field: using various methods and tracers, the same building blocks are recovered but named differently until their equivalence or association is confirmed.

and action space (Malhan et al. 2022) or a friends-of-friends algorithm on stellar orbital parameters (Wang et al. 2022), different groups have been trying to recover our Galaxy's building blocks in a more robust way. Still, the interpretation of these results is not always straightforward, and comparisons to cosmological simulations could provide more insight in the properties and relations between the different identified substructures (Helmi 2020, see e.g. Callingham et al. 2022, Amarante et al. 2022).

Of course, satellites that merged with our Milky Way did not only bring in single stars, but also their own globular clusters and possibly satellite galaxies, which can similarly be used to probe our Milky Way's past (e.g. Malhan et al. 2022). While disentangling the GC that formed in-situ from the accreted GC, we can learn about the merger events that brought the accreted GC in (Massari et al. 2019; Kruijssen et al. 2019; Horta et al. 2020; Callingham et al. 2022). GC and DG may over time disrupt into stellar streams, of which part has been confirmed to be of accreted origin (Carlberg 2018; Bonaca et al. 2021; Malhan et al. 2022). In conclusion, it seems that slowly a coherent picture of the history of our Galaxy is emerging, and with the release of *Gaia* DR3 and an ever increasing amount of spectroscopic data from ground-based surveys we can hope to unveil even more of the remnants buried in our halo. This ongoing as we speak (Dodd et al. 2022; Myeong et al. 2022; Tenachi et al. 2022).

1.5 Galactic Dynamics

How is the Milky Way built up, and what is the best way to describe it? How is its matter distributed, and how does that compare to what we have seen in simulations? Our Milky Way is the closest laboratory that we have to address such questions, and it is the field of Galactic Dynamics that tries to answer them.

This Section will provide the reader with a short introduction to a few important concepts in Galactic Dynamics.

1.5.1 Orbits and Orbit Integration

An **orbit** is the trajectory that a body, given its initial conditions, has in time due to the influence of gravity in a gravitational field. An orbit in any system can be described by its 6D phase-space coordinates $\vec{x}(t) = [x(t), y(t), z(t)]$ and $\vec{v}(t) = \mathrm{d}\vec{x}/\mathrm{d}t = [v_x(t), v_y(t), v_z(t)]$, i.e. its position and velocity at each point in time. This holds for bodies that can be considered test particles, which are bodies with a mass that is negligible in comparison to the mass distribution that governs the gravitational field. An orbit of a test particle is fully determined by its initial phase-space coordinates, $(\vec{x}_0, \vec{v}_0)$, and the gravitational field it is embedded in.

The gravitational potential $\Phi(\vec{x})$ and the density $\rho(\vec{x})$ of self-consistent systems are related via the Poisson equation,

$$\nabla^2\Phi(\vec{x}) = 4\pi G\rho(\vec{x}) \tag{1}$$

The gravitational field, $\vec{g}(\vec{x})$, is related to the gravitational potential via the potential's gradient, $\vec{g}(\vec{x}) = -\nabla\Phi(\vec{x})$. The motion of a test particle in a gravitational field is determined by its equations of motion, $d^2\vec{x}/dt^2 = \vec{g}(\vec{x})$, which is a second-order differential equation. To **integrate an orbit** means to numerically solve the equations of motion as a function of time given the initial conditions and the description of the gravitational potential, such that we obtain the orbit $(\vec{x}(t), \vec{v}(t))$.

1.5.2 Integrals of Motion[5]

An **integral of motion** I is a quantity that depends only on a body's phase-space coordinates and is constant along an orbit,

$$I\left[\vec{x}(t_1), \vec{v}(t_1)\right] = I\left[\vec{x}(t_2), \vec{v}(t_2)\right] \tag{2}$$

An orbit can have zero to five integrals of motion (IoM). IoM can follow from symmetries of the Galactic potential, and if they can be expressed analytically, these are called **classical** IoM. For example, in a time independent potential, the total energy E is a classical IoM, which is equal to the sum of a star's kinetic and potential energy, namely

$$E = E_k + E_{pot} = \frac{1}{2}\left(v_x^2 + v_y^2 + v_z^2\right) + \Phi(x, y, z) \tag{3}$$

[5]A part of this Section is adapted from Section 3.1.1 of Binney and Tremaine 2008

In a spherical potential, the three components of the angular momentum vector $\vec{L}$ are classical IoM. The angular momentum of a star is the cross product of its position and momentum, namely

$$\vec{L} = \vec{r} \times \vec{p} = \begin{pmatrix} L_x \\ L_y \\ L_z \end{pmatrix} = \begin{pmatrix} yv_z - zv_y \\ zv_x - xv_z \\ xv_y - yv_x \end{pmatrix} \tag{4}$$

Note that throughout this work, we take L_z such that it is positive for the Sun, so we flip its sign, $L_z = yv_x - xv_y$. As L_x and L_y are IoM in a spherical potential, this means that the perpendicular component of the angular momentum, $L_\perp$, also is a classical IoM, where $L_\perp$ is defined as

$$L_\perp = \sqrt{L_x^2 + L_y^2} = \sqrt{z^2 v_R^2 + z^2 v_\phi^2 + R^2 v_z^2 - 2 z v_z R v_R} \tag{5}$$

However, the Milky Way is not spherical, as it has stellar disks, which are flattened in shape. An often made and generally well-justified approximation is to assume that the Milky Way is axisymmetric in shape. In an axisymmetric potential, of all of the three components of the angular momentum vector, only L_z is an integral of motion. In Galactocentric cylindrical coordinates, $L_z = -Rv_\phi$. Though $L_\perp$ is not a true integral of motion in an axisymmetric potential, it is often used to characterise the orbits of stars. Depending on the orbit and on the assumed potential, $L_\perp$ varies with the phase of the orbit.

Integrals of motion are important quantities in Galactic Dynamics and Galactic Archaeology, see Section 1.4. Often, a time-independent axisymmetric Galactic potential is assumed, meaning that E and L_z are IoM, and $L_\perp$ is a roughly conserved quantity. Another set of IoM that are often used to describe the orbits of stars are the three actions $\vec{J} = (J_R, J_\phi, J_z)$, which are discussed in more detail in Appendix E.

1.6 The Milky Way's Circular Velocity Curve

The circular velocity curve of the Milky Way, $v_c(R)$ constrains the distribution of (dark) matter within radius R. The circular velocity at different Galactocentric radii can be measured via various tracers, such as star kinematics or masers. Given the moments of the velocity distribution, $\langle v_R^2 \rangle$, $\langle v_\phi^2 \rangle$ and $\langle v_R v_z \rangle$, and the density distribution ν of the tracer, one can assume an axisymmetric gravitational potential and derive the circular velocity from the cylindrical form of the Jeans equations (see also Binney and Tremaine 2008):

$$v_c^2(R) = \langle v_\phi^2 \rangle - \langle v_R^2 \rangle \left(1 + \frac{\partial \ln \nu}{\partial \ln R} + \frac{\partial \ln \langle v_R^2 \rangle}{\partial \ln R} + \frac{R}{\langle v_R^2 \rangle} \frac{\partial \ln \langle v_R v_z \rangle}{\partial z} \right) \tag{6}$$

Once a circular velocity curve is derived, it can be compared to Milky Way mass models (see Section 1.7), as the circular velocity in the plane of an axisymmetric potential is given by

$$v_c^2(R) = R \frac{\partial \Phi}{\partial R}\bigg|_{z=0} \tag{7}$$

where z is the height above the Galactic plane. In this way, the circular velocity curve provides a powerful constraint on any Milky Way mass model. Therefore, I use a circular velocity curve as a constraint throughout this thesis, and to that end combine the circular velocity curve obtained by Eilers et al. 2019 with circular velocity data based on Cepheids (Mróz et al. 2019)[6].

Eilers et al. 2019 measured the circular velocity curve between $5 \leq R \leq 25$ using a sample of more than 23.000 luminous red giants located in the disk with 6D phase-space information. The distances of the red giants are derived from spectrophotometric parallax estimates (Hogg et al. 2019). Assuming an axisymmetric gravitational potential and an exponential radial density function for the red giants, the authors solve the cylindrical form of the Jeans equations (see Eq. 6) to derive the circular velocity in bins of $\Delta R = 0.5$ kpc or a minimum number of three stars per bin. The formal uncertainties are determined via bootstrapping (see their Fig. 1 and

[6]Note that there are several more rotation curve datasets or compilations reaching out to even hundreds of kpc (e.g. Huang et al. 2016, Sofue 2020), but these datasets assume different values for $R_\odot$, $v_\odot$ and $(U, V, W)_\odot$ and are thus not compatible with Eilers et al. 2019's rotation curve data. In other cases the measurements have relatively large uncertainties, so they are not very constraining (Iocco et al. 2015; Pato and Iocco 2017; Karukes et al. 2019).

Table 1), while various systematic uncertainties are estimated independently as well as summed together (see their Fig. 4).

An important assumption of Jeans modelling is that the system that is being modelled is in steady state. However, there is substructure in the disk, such as the phase spiral (Antoja et al. 2018; Hunt et al. 2022), and there exist non-negligible asymmetries in velocity (dispersion) above and below the plane (Gaia Collaboration et al. 2021b). This suggests that the Milky Way's disk is not in equilibrium, which could lead to biased results when applying Jeans modelling (Haines et al. 2019). Moreover, when deriving the circular velocity, Eilers et al. 2019 neglect the cross-term $\partial\langle \ln v_R v_Z\rangle/\partial z$ (see Eq. 6), which introduces a systematic uncertainty that varies with radius. Eilers et al. 2019 used an old tracer population, which is subject to asymmetric drift, meaning that in Jeans modelling the radially varying cross-term $\partial\langle \ln v_R v_Z\rangle/\partial z$ could be important. This term is neglected but accounted for via a systematic uncertainty, but as the correlation between the uncertainties in distance and velocity is not taken into account as a systematic error by Eilers et al. 2019, this effect could possibly be underestimated, especially at larger radii.

Beyond $R = 20$ kpc, the different systematic and measured uncertainties in Eilers et al. 2019 rotation curve rise steeply because there are only few red giants with 6D phase-space information at those distances. Interestingly, there is a quite steep decline in the rotation curve for $18 \lesssim R$, which is not seen in other rotation curve datasets (e.g. Huang et al. 2016). A dynamical model of the Milky Way disk based on *Gaia* EDR3 and APOGEE data is not able to match this dip either (Nitschai et al. 2021). Taking also the limitations mentioned in the previous paragraph into account, we decide to exclude the rotation curve data from Eilers et al. 2019 beyond $R > 16$ kpc from our analysis. As an estimate for the total uncertainty per datapoint, following de Salas et al. 2019, we quadratically add the summed systematic uncertainty to the measured uncertainty, such that $\sigma^2_{v_c,tot} = \sigma^2_{meas} + \sigma^2_{syst}$. Because the measured uncertainties are asymmetric, we first take their mean. We extract the summed systematic uncertainties from Fig. 4 of Eilers et al. 2019 (black curve), assuming a systematic uncertainty of 12% for the five bins largest in R.

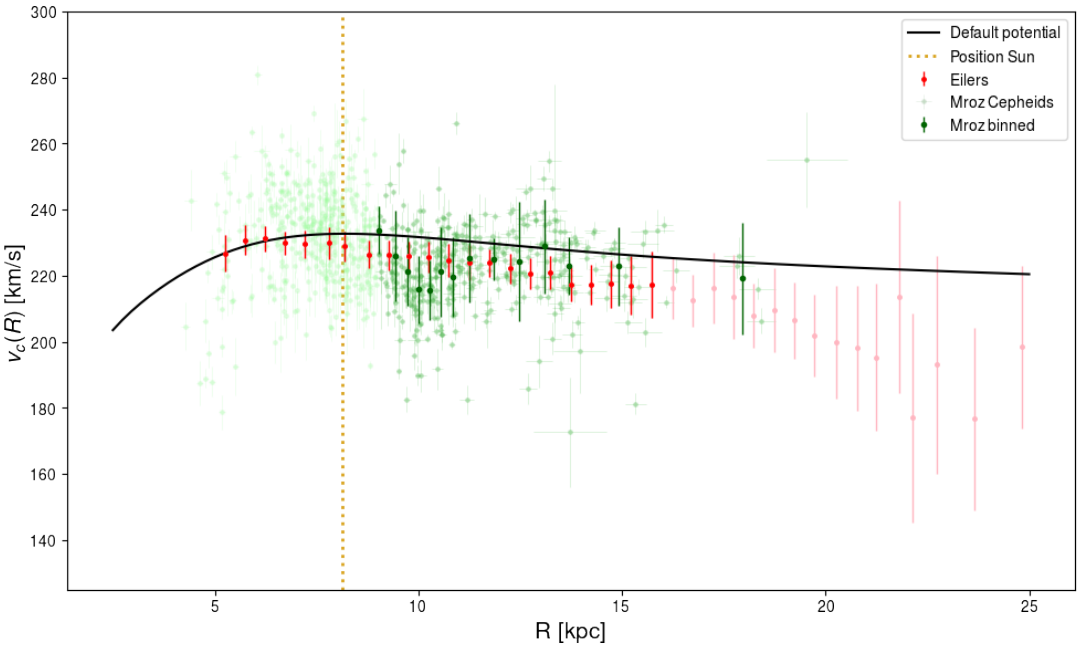

Figure 4: Rotation curve data from Eilers et al. 2019 (red for $R < 16$ kpc and light red for $R > 16$ kpc) and the Cepheids for $R < 9$ kpc (light green) and $R > 9$ kpc (dark green) from Mróz et al. 2019. The binned Cepheids dataset is shown in dark green. Overplotted is the rotation curve corresponding to the Default Potential (see Section 1.7.4).

We supplement Eilers et al. 2019's rotation curve with data from 773 Classical Cepheids, whose distances have been determined based on mid-infrared period-luminosity relations (Wang et al. 2018; Skowron et al. 2019; Mróz et al. 2019). Classical Cepheids trace a young stellar population (< 400 million years), contrary to the old red giants used in Eilers et al. 2019, and they are bright enough to be detected even out to extragalactic distances. The distances are combined with proper motions, radial velocities and positions on the sky from *Gaia* DR2 (Gaia Collaboration et al. 2018). The data and code to reconstruct the rotational velocity of each

Cepheid is publicly available[7]. The code allows user-specified values of the characteristic Galactic constants $R_\odot$, $v_\odot$ and $(U, V, W)_\odot$, so we choose those to agree with the values used in Eilers et al. 2019 (see Section 1.7.4). We exclude Cepheid data for $R < 9$ kpc because of asymmetries above and below the plane and a non-smooth rotation curve, which could possibly be due to the spiral arms.

The rotation curve data and their total uncertainties are shown in Fig. 4. To show the overall trend, the Cepheids data has been binned in bins with approximately equal size, about 30 datapoints per bin, requiring a binsize of $\Delta R \geq 0.2$ kpc. The mean and uncertainty of each bin is calculated using the weighted mean and weighted standard deviation. The Cepheids data and Eilers et al. 2019's rotation curve agree within the 1σ uncertainty range, though the rotation curve of Eilers et al. 2019 declines steeper at higher radii.

1.7 Milky Way Dynamical Models

Given a star's present-day phase-space position, we can determine a star's orbit if the gravitational potential in which it moves is known (see Section 1.5.1). The mass profile of our Milky Way is thus paramount for determining the dynamics and history of objects like satellite galaxies (e.g. Kallivayalil et al. 2013; Garavito-Camargo et al. 2019) and stellar streams (e.g. Fardal et al. 2019), but also to determine the dynamics of members of the Local Group (e.g. van der Marel et al. 2012). Many efforts have been done to synthesise our current theoretical understanding and various observational constraints into a realistic mass model of the Milky Way. This is a pursuit that has been ongoing for decades (e.g. Schmidt 1956), and as our knowledge increased and our numerical methods advanced these models have become increasingly accurate.

This Section aims to introduce the reader to the characteristics of Milky Way mass models. Section 1.7.1 will discuss four Milky Way mass models that are used often in the literature today and Section 1.7.2 will give an overview of recent DM halo mass estimates. Section 1.7.3 compares the potential flattening of the four Milky Way mass models and Section 1.7.4 introduces our Default Potential and assumed characteristic Galactic constants.

1.7.1 Milky Way Mass Models

1.7.1.1 The McMillan 2017 Milky Way Mass Model

An observationally well-motivated and popular Milky Way mass model is the McMillan 2017 model, which consists of a bulge, a stellar thin disk, a stellar thick disk, a HI gas disk, a molecular gas disk and a DM halo. The gas disks are described by an exponential profile with a hole in the centre. The HI gas disk has a mass of $1.1 \cdot 10^{10}$ $M_\odot$, and the molecular gas disk has a mass of $1.2 \cdot 10^9$ $M_\odot$. The bulge is described by a power-law with an exponential cut-off and has a mass of $8.9 \cdot 10^9$ $M_\odot$. The halo follows a spherical NFW profile (Navarro et al. 1996), which is given by

$$\rho_{halo}(\tilde{r}) = \frac{\rho_0}{\frac{\tilde{r}}{r_s}\left(1 + \frac{\tilde{r}}{r_s}\right)^2} \tag{8}$$

where $\rho_0 = 8.5 \cdot 10^6$ $M_\odot$ kpc^{-3} and the scale radius is $r_s = 19.57$ kpc. Moreover,

$$\tilde{r} = \sqrt{R^2 + \frac{z^2}{q^2}} \tag{9}$$

with R and z Galactocentric cylindrical coordinates and $q = c/a$ the flattening in the density, which is equal to 1 in the case of a spherical potential. If $c > a = b$, the model is called prolate, and if $c < a = b$, the model is called oblate.

The stellar disks are described by an exponential profile

$$\rho_{disk}(R, z) = \frac{\Sigma_0}{2z_d} \exp\left(-\frac{|z|}{z_d} - \frac{R}{R_d}\right) \tag{10}$$

[7] See ftp://ftp.astrouw.edu.pl/ogle/ogle4/ROTATION CURVE/

The total mass of such a disk is $M_d = 2\pi\Sigma_0 R_d^2$. The thin disk has characteristic parameters $z_{d,thin} = 0.3$ kpc, $R_{d,thin} = 2.5$ kpc, $M_{d,thin} = 3.5 \cdot 10^{10}$ $M_\odot$, while the thick disk has characteristic parameters $z_{d,thick} = 0.9$ kpc, $R_{d,thick} = 3.0$ kpc, $M_{d,thick} = 1 \cdot 10^{10}$ $M_\odot$.

1.7.1.2 Other Milky Way Mass Models

A widely used Galactic potential model is the `MWPotential2014` model implemented in `galpy` by Bovy 2015. It consists of a bulge, modelled as a power-law density profile with an exponential cut-off, a Miyamoto Nagai disk (Miyamoto and Nagai 1975) and a spherical NFW DM halo with a scale radius $r_s = 16$ kpc. The `MWPotential` or Price-Whelan 2017 potential, implemented in `gala` (Price-Whelan 2017; Price-Whelan et al. 2020), follows a similar approach but adds a Hernquist nucleus (Hernquist 1990) to this description. Its other components are a Hernquist bulge (Hernquist 1990), a Miyamoto Nagai disk (the same as the one used in `MWPotential2014`) and a spherical NFW DM halo with a scale radius $r_s = 15.62$ kpc. Finally, the recent model by Cautun et al. 2020 is tailored to match the rotation curve by Eilers et al. 2019. It borrows the gas disks and bulge from McMillan 2017 but has lighter and more extended thin and thick stellar disks. It has a (debated) circumgalactic medium component and a contracted NFW DM halo, which takes into account the gravitational effect of the baryonic components on the DM halo. None of these models include a description of the bar, which makes the inner region of the Galaxy strongly non-axisymmetric.

1.7.2 Estimates of the Dark Matter Halo's Mass

The majority of the mass of our Milky Way resides in its DM halo, which we cannot observe directly. This means we need to resort to luminous tracers to infer its properties, such as its total mass and mass distribution as a function of radius. An overview of different attempts to estimate the mass of the Milky Way is shown in Fig. 5 (Shen et al. 2021, but see also Fig. 1 in Wang et al. 2020). Over the past decades, the mass of the Milky Way has been constrained using various methods, for example using the timing argument (Zaritsky et al. 2020), high-velocity stars (Piffl et al. 2014; Monari et al. 2018; Grand et al. 2019), (distribution function analysis of) satellite dynamics (Barber et al. 2014; Posti and Helmi 2019; Callingham et al. 2019; Correa Magnus and Vasiliev 2022; Rodriguez Wimberly et al. 2022), modelling of stellar streams (e.g. Küpper et al. 2015) and rotation curve analysis (Karukes et al. 2020; Cautun et al. 2020). Though there seems to be a broad consensus on the mass of the Milky Way, roughly $M_{200} = 1 \cdot 10^{12} M_\odot$, the Milky Way's total mass is still uncertain within a factor slightly smaller than two (Wang et al. 2020).

1.7.3 Total Potential Flattening

The flattening of the total potential as a function of radius of the four mass models discussed in Section 1.7.1 are shown as dashed lines in Fig. 6. The flattening of the four models differs mostly in the inner region ($R \lesssim 8$ kpc) of the Galaxy, due to the different assumptions for the (gas/stellar) disk(s) and the presence/absence of a nucleus. Farther out the models are rather similar as all assume a spherical NFW DM halo, which dominates in the outer parts of our Galaxy.

Various methods have been employed to constrain the shape of the Galactic potential, and here I will provide a non-exhaustive overview. As stellar streams roughly trace out the progenitor's orbit, they can be used to constrain, for example, the flattening q (see Eq. 9) of the DM halo. In the correct gravitational potential, the integrated orbit or modelled stellar stream should reproduce the observed stream track. Using this principle, Koposov et al. 2010 performed single orbit fits to the stellar stream GD-1[8], finding an overall potential flattening of $q_\phi = 0.87^{+0.07}_{-0.04}$. A similar effort by Malhan and Ibata 2019 confirmed this result. Different streams contain different information about the gravitational potential of the Milky Way depending on their orbit (Bonaca and Hogg 2018). For example, while stellar streams orbiting the inner part of the Galaxy will more tightly constrain the properties of the stellar disks, stellar streams orbiting farther out will more strongly constrain the shape and mass of the DM halo. Therefore, Bovy et al. 2016a combined the constraining power of Palomar 5 and GD-1 and modelled the streams in action-angle space to find an overall potential flattening of $q_\phi = 0.94 \pm 0.05$ in the density.

Next to stream modelling/fitting, other methods have also been used in constraining the Galactic potential. For example, using distribution function analysis of the proper motions of 75 GC and 20 distant clusters, Posti and Helmi 2019 showed that the Milky Way's DM halo is best described as an NFW halo with an exponential cut-off at the virial radius with a flattening in the density of $q = 1.30 \pm 0.25$. Moreover, recently, Dodd et al.

[8] Although single orbits are not expected to exactly match the observed stream track (Sanders and Binney 2013), this is not a bad approximation for a dynamically cold stream like GD-1 (Bowden et al. 2015; Bonaca et al. 2019).

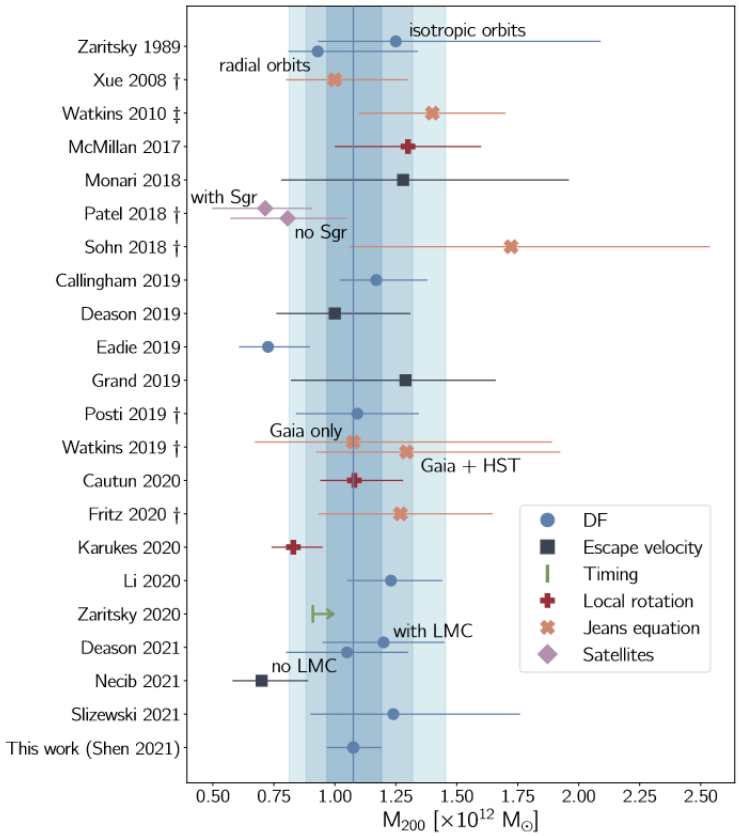

Figure 5: Compilation of estimates of M_{200} for the Milky Way's dark matter halo using various methods. Figure adapted from Shen et al. 2021.

2021 showed that the distribution in angular momentum space of the Helmi Streams can be used to constrain the flattening in the density of the NFW DM halo, $q = 1.2$, while further assuming the McMillan 2017 potential.

The total potential flattening of each of these papers is shown in Fig. 6 as a solid line. These clearly differ from each other and from the total potential flattening of the four Milky Way mass models. This is partly a result of the fact that stellar streams measure local properties of the Galactic potential based on their orbit (Bonaca and Hogg 2018), explaining for example the difference between the results of Koposov et al. 2010 and Posti and Helmi 2019, of which the latter is probing a region farther away from the Galactic center. This seems to indicate that our DM halo cannot simply be described by a flattened or spherical NFW profile, but that it instead radially varies in shape (see also Vera-Ciro and Helmi 2013; Vasiliev et al. 2021). A method to explore the shape of the halo more freely will be discussed in Section 3.

1.7.4 Default Potential

Throughout this thesis, I adopt a slightly modified version of the McMillan 2017 potential as default Galactic potential model. Following Dodd et al. 2021, we modify the flattening in the density of the halo such that $q = 1.2$. Because this increases the density of the potential at a given point (see Eq. 8), we reduce ρ_0 to $\rho_0 = 7.7 \cdot 10^6\ \mathrm{M}_\odot\ \mathrm{kpc}^{-3}$. In that way the constraints to which the McMillan 2017 potential was tailored are still satisfied. By construction, in this potential part of the Helmi Streams' stars fall on the $\Omega_\phi : \Omega_z$ is $1:1$ resonance (see Section 2.4.1). As the default potential is an axisymmetric potential, both E and L_z are integrals of motion. $L_\perp$ is not a true integral of motion and will thus vary along the orbit.

Fig. 7 and 8 show the contributions of the different components of the default potential to the mass enclosed within radius r. This illustrates what component of the potential dominates at what radius. While at small radii the bulge dominates, the farther out, the more the halo starts to dominate. The contribution of the stellar disks is most prominent between $3 < r < 10$ kpc.

The rotation curve of the Default Potential is shown in Fig. 4, and while it largely agrees within 1σ with the Cepheids data, it lies consistently above the Eilers et al. 2019 rotation curve. This is not surprising, as Eilers et al. 2019 estimate a much lower virial mass, $0.7 \cdot 10^{12}\ \mathrm{M}_\odot$ than McMillan 2017, $1.3 \cdot 10^{12}\ \mathrm{M}_\odot$, and the circular

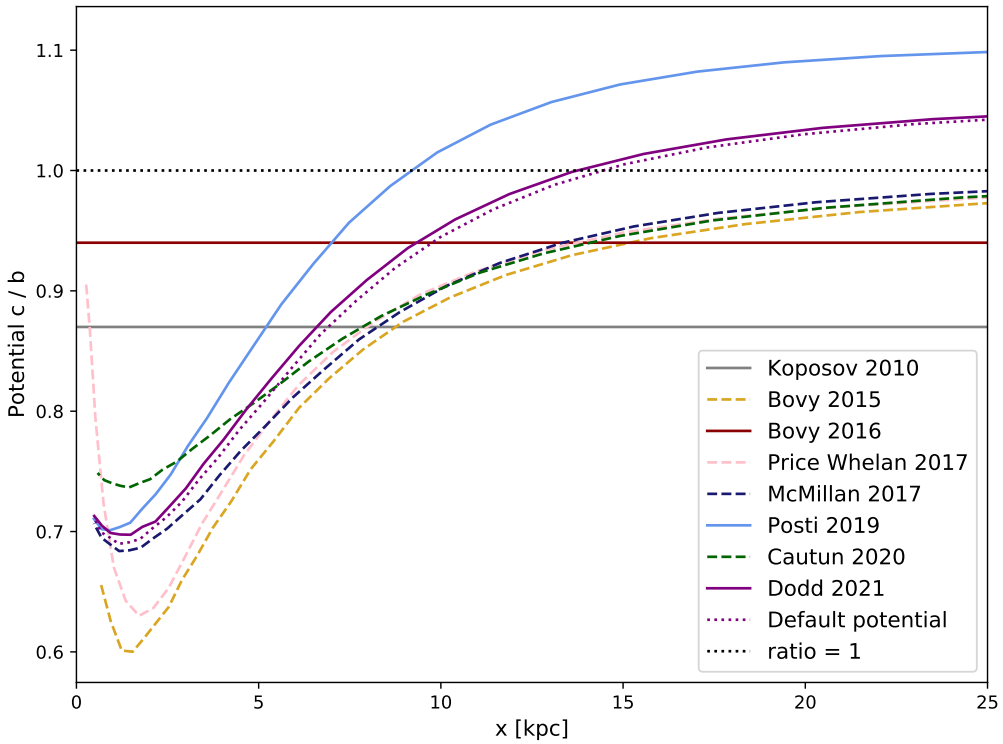

Figure 6: Overview of the flattening c/b in the potential of different analytical Milky Way mass models (dashed lines) and Milky Way mass models constrained by stellar streams (e.g. Bovy et al. 2016a), satellite dynamics (Posti and Helmi 2019) and phase-mixed streams (Dodd et al. 2021).

velocity $v_{circ}(R)$ is a measure of $M(R)$, the mass enclosed within radius R. As the estimates of M_{200} that are discussed in Section 1.7 are also consistently higher, this might indicate that Eilers et al. 2019's rotation curve declines too steeply.

1.7.4.1 Values of Characteristic Galactic Constants

We follow Eilers et al. 2019 and assume a distance from the Sun to the Galactic centre of $R_\odot = 8.122 \pm 0.031$ kpc (Gravity Collaboration et al. 2018). We assume the Galactocentric velocity of the Sun to be $v_{\odot,x} = -11.1\ \mathrm{km\,s^{-1}}$, $v_{\odot,y} = 245.8\ \mathrm{km\,s^{-1}}$, $v_{\odot,z} = 7.8\ \mathrm{km\,s^{-1}}$ and the circular velocity at the position of the Sun to be $v_c(R_\odot) = 229\ \mathrm{km\,s^{-1}}$. Lastly, we set the height above the Galactic mid-plane to $z_\odot = 20.8$ pc (Bennett and Bovy 2019).

The circular velocity at the position of the Sun, $v_c(R_\odot)$ is a measure of the mass within radius $R_\odot$. There is a relatively good consensus on $v_c(R_\odot)$, providing a stringent constraint on any Galactic potential. Therefore, in this thesis, we restrict ourselves to potentials that give rise to a correct velocity at the position of the Sun within 5% assuming $V_{\mathrm{circ}}(R_\odot) = 233\ \mathrm{km\,s^{-1}}$ (Reid et al. 2014; McMillan 2017; Hayes et al. 2018; Eilers et al. 2019; Mróz et al. 2019). Note that the Default Potential has $V_{\mathrm{circ}}(R_\odot) = 232.7\ \mathrm{km\,s^{-1}}$ and thus lies well within this range.

1.8 Outline of this Thesis

The goal of this thesis is to investigate the peculiar dynamical properties of the phase-mixed Helmi Streams and to use these to provide a novel constraint on the Galactic potential. First, Section 2 discusses the phase-space distribution and orbital properties of the Helmi Streams in detail. Then, Section 3 introduces a new method to relatively freely vary the potential of the DM halo based on Basis Function Expansions, and applies it to the Helmi Streams. Section 4 tries to find an explanation for the observed peculiar dynamical properties of the Helmi Streams, and advocates that resonances and chaos might play an important role. Using this, Section 5 tries to provide a constraint on the Galactic potential, but finds that probably a model with more freedom is needed. Section 6 provides a discussion and outlook on future work, and Section 7 concludes the thesis.

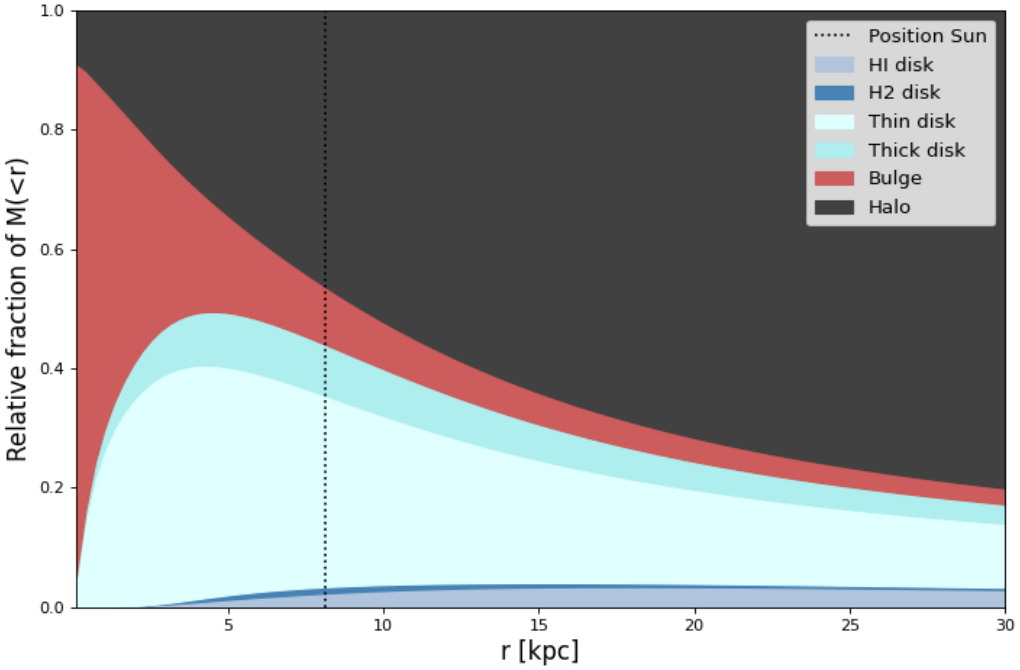

Figure 7: Fraction of the total mass enclosed within a sphere of radius r for the different components of the Default Potential.

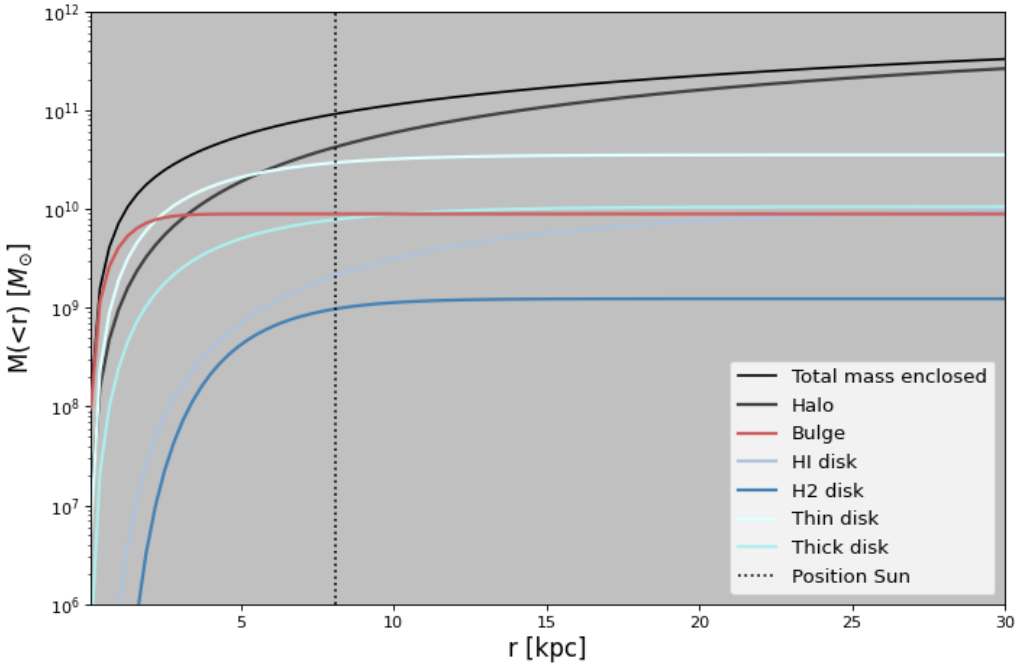

Figure 8: Mass enclosed within radius r for the different components of Default Potential.

2 Characterisation of the Helmi Streams' clumps

The Helmi Streams were discovered in Integrals of Motion space by Helmi et al. 1999 and are thought to be the remnants of a dwarf galaxy with a mass of $\sim 10^8 M_\odot$ that was accreted 5 to 8 Gyr ago (Chiba and Beers 2000; Kepley et al. 2007; Koppelman et al. 2019a; Koppelman et al. 2019b). The stars of the Helmi Streams are chemically distinct from the bulk of stars in the Milky Way's stellar halo (Matsuno et al. 2022), as is its progenitors' star formation history (Ruiz-Lara et al. 2022a). About 10 to 15 GC are thought to be associated to the Helmi Streams (Koppelman et al. 2019b; Massari et al. 2019; Callingham et al. 2022). As noted by Helmi 2020, it is interesting that the Helmi Streams, which seem to have a relatively light progenitor, are found to orbit the inner halo but appear to have been accreted relatively recently, as inferred from their degree of phase mixing. This could have a dynamical origin, as the Helmi Streams seem to lie close to orbital resonances, which could slow down the phase-mixing of the streams and thereby decrease the inferred timescale of accretion (Koppelman et al. 2021; Dodd et al. 2021). Another possibility is that the progenitor of the Helmi Streams fell in with a group of other satellites (see also Section 6.1.1), allowing it to quickly sink towards the inner halo.

This is not the only interesting dynamical feature of the Helmi Streams. Recently, Dodd et al. 2021 found that the Helmi Streams exhibit peculiar behaviour in angular momentum space. Instead of being a coherent structure, the stars are split into two clumps, one having a higher $L_\perp$ than the other. The two clumps were also recovered as two independent structures using a single-linkage algorithm to find clusters of stars in IoM space (Lövdal et al. 2022; Ruiz-Lara et al. 2022b; Dodd et al. 2022). Though separated in angular momentum space, the two clumps seem to stem from the same stellar population, as shown in the next Section. A convincing explanation for the existence of the two clumps has not been found yet, though it seems that orbital resonances could play an important role (Dodd et al. 2021). This thesis aims to investigate the peculiar dynamical properties of the Helmi Streams in more detail, and finally use the existence of the gap to provide a constraint on the Galactic potential.

On 13 June 2022, *Gaia* DR3 was released. While for the majority of the time I worked with the *Gaia* EDR3 sample, the final month of my thesis I was able to look at the Helmi Streams in a new light. I use the *Gaia* DR3 sample to confirm the trends and characteristics of the Helmi Streams seen in *Gaia* EDR3 with more confidence (the majority of this analysis can be found in Appendix A). The main body of this thesis will however be based on the *Gaia* EDR3 sample.

2.1 The Helmi Streams in *Gaia* EDR3

In this thesis, I use a sample of local Helmi Streams' stars (heliocentric distance < 2.5 kpc) selected by Dodd et al. 2021[9]. This sample has accurate 6D phase-space information, allowing the accurate determination of the stars' L_z, $L_\perp$ and energy E. In this sample, positions and proper motions are from *Gaia* EDR3 (Gaia Collaboration et al. 2021a) and distances are found by inverting *Gaia*'s parallaxes (correcting for the -0.017 mas parallax zero-point offset, see Lindegren et al. 2021). Stars are required to have `parallax_over_error` > 5 and `RUWE` <1.4. The best-quality 6D sample has radial velocities from *Gaia*'s Radial-Velocity Spectrometer (RVS) and contains 84 stars. The sample with radial velocities is extended by cross-matching it with the spectroscopic surveys GALAH DR3 (Buder et al. 2021), APOGEE DR16 (Ahumada et al. 2020), RAVE DR6 (Steinmetz et al. 2020) and LAMOST DR6 (Cui et al. 2012). This extended 6D sample contains 284 stars.

The RVS and extended sample have undergone a selection in angular momentum space, which separates the Helmi Streams into two clumps, and a cut in energy as described in Dodd et al. 2021. The two clumps can roughly be described by two ellipsoids that are rotated by 30 degrees in $(L_z, L_\perp)$ space[10]. The clump with higher perpendicular angular momentum will be called the hiL clump and will be shown in red in all forthcoming plots, while the clump with lower perpendicular angular momentum will be called the loL clump and will be shown in blue. The RVS sample contains 41 stars in the hiL clump and 43 stars in the loL clump, while the extended sample contains 154 stars in the hiL clump and 130 in the loL clump. The angular momentum distribution of the hiL and loL clump stars in both samples is shown in Fig. 9. The two clumps seem to stem from the same stellar population, as their colour absolute-magnitude diagram (CaMD) and metallicity distribution (see also Matsuno et al. 2022) appear to be consistent with each other, see Fig. 10. A Kolmogorov-Smirnov test also

[9]Note that for this selection and also the selection in DR3, (U,V,W) = $(11.1, 12.24, 7.25)\,\mathrm{km\,s^{-1}}$ (Schönrich et al. 2010), $v_{LSR} = 232.8\,\mathrm{km\,s^{-1}}$, $R_\odot = 8.2$ kpc (McMillan 2017) and $z_\odot = 0.014$ kpc (Binney et al. 1997) are used. This differs slightly from the values I use throughout the rest of the thesis, but the impact of these changes is negligible.

[10]The hiL clump is described by an ellipse centred on $(L_z, L_\perp) = (1225, 2255)\,\mathrm{kpc\,km\,s^{-1}}$ with major and minor axis lengths of 855 and 570 $\mathrm{kpc\,km\,s^{-1}}$, respectively. The loL clump is described by an ellipse centred on $(L_z, L_\perp) = (1420, 1780)\,\mathrm{kpc\,km\,s^{-1}}$ with major and minor axis lengths of 860 and 430 $\mathrm{kpc\,km\,s^{-1}}$, respectively.

confirmed that the metallicity distribution functions of the two clumps are similar (Ruiz-Lara et al. 2022b).

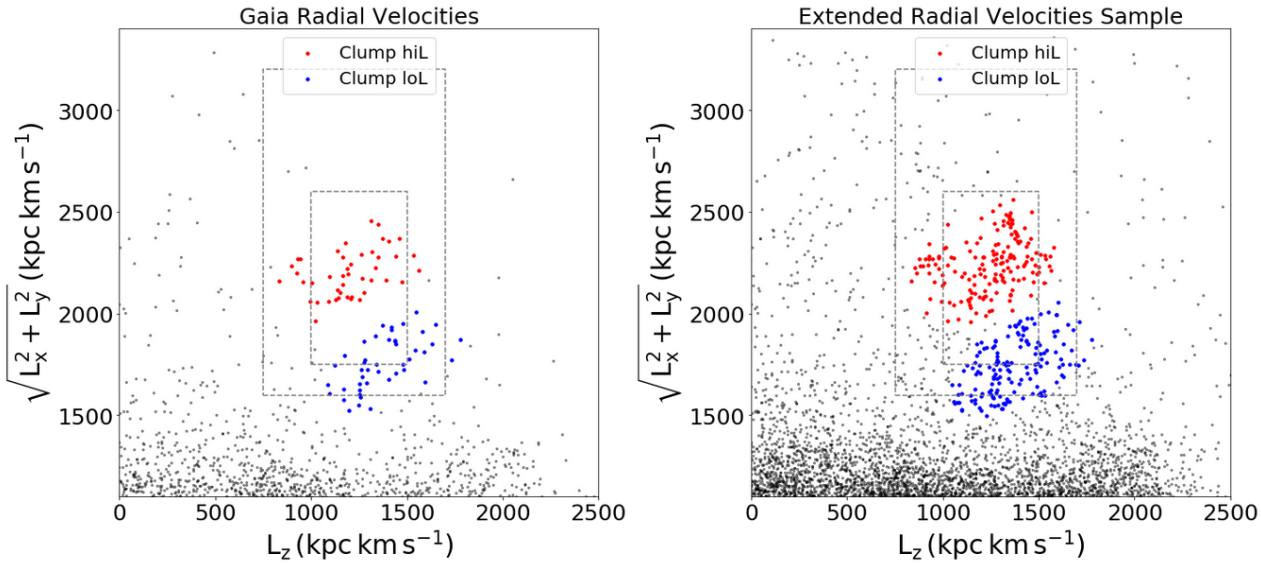

Figure 9: *Left panel*: Angular momentum distribution of hiL clump stars (red) and loL clump stars (blue) in the RVS sample within a heliocentric distance of 2.5 kpc, selected following Dodd et al. 2021. The black dots show remaining stars of the halo sample within a volume of 2.5 kpc, the dashed lines show the selections of the Helmi Streams previously used by Koppelman et al. 2019b. *Right panel:* Similar as the left panel but for the extended sample. Figure adapted from Dodd et al. 2021.

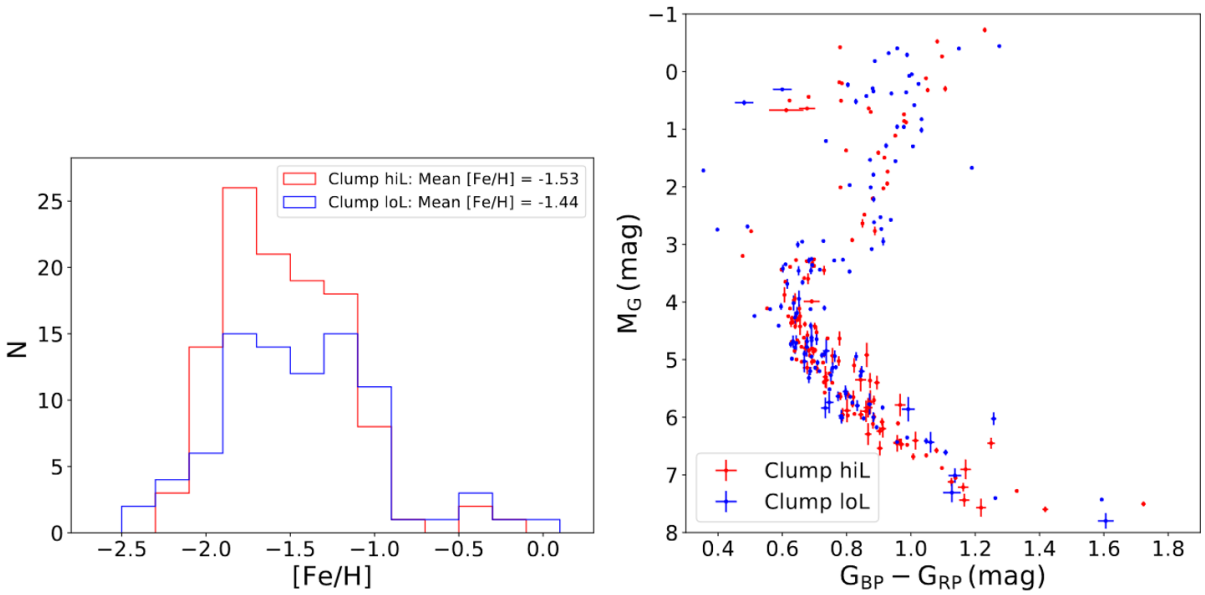

Figure 10: *Left panel*: Metallicity distributions from LAMOST Low Resolution Spectra of hiL clump stars (red) and loL clump stars (blue) of the extended sample. Both distributions peak around [Fe/H] ~ -1.5. *Right panel:* CaMD of the extended sample. The CaMD and metallicity distribution of the hiL and loL clump are similar, supporting a common origin. Figure adapted from Dodd et al. 2021.

2.2 The Helmi Streams in *Gaia* DR3

The release of *Gaia* DR3 (Gaia Collaboration et al. 2022) on 13 June 2022 brought a more than six-fold increase in the number of stars with *Gaia* RVS radial velocities, with a total of 33812183 stars (Katz et al. 2022). *Gaia* DR3's RVS sample allows me to confirm the trends and characteristics of the Helmi Streams seen in *Gaia* EDR3 with more confidence. The selection of a sample of halo stars with reliable 6D phase-space positions is described in more detail in Appendix A. The distribution in angular momentum space of the stars in this sample within different volumes is shown in Fig. 11, which shows the region of angular momentum space occupied by the Helmi Streams. In comparison to Fig. 9 there is a very clear increase in the number of stars with *Gaia* radial velocities. Moreover, not only do the Helmi Streams stand out more clearly from the background, the hiL and loL clump remain separated out to large distances. More information and details on the DR3 properties of the streams are discussed in Appendix A. The analysis serves to confirm what we see in *Gaia* EDR3.

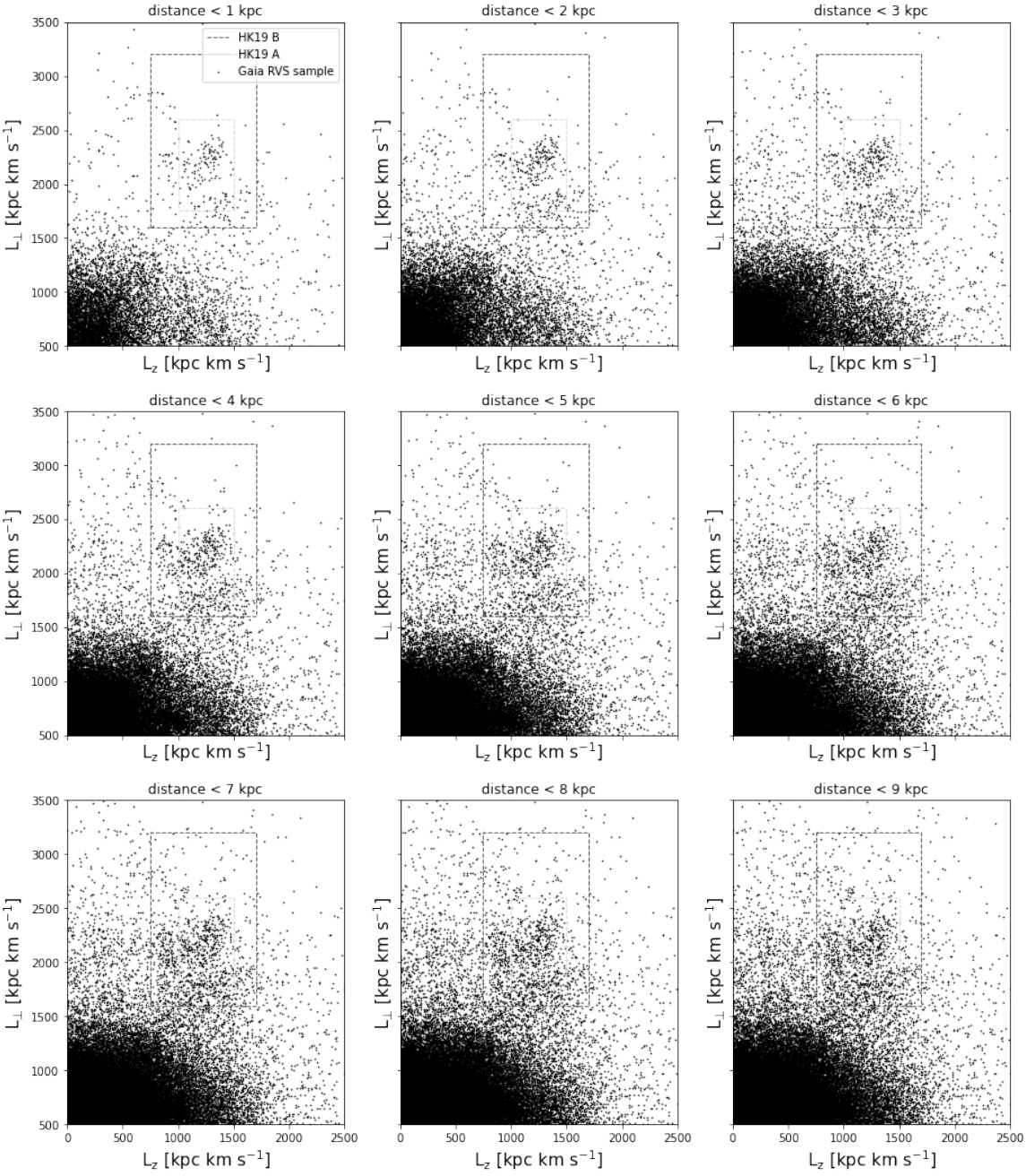

Figure 11: Distribution in angular momentum space of the *Gaia* DR3 RVS halo sample with `parallax_over_error` > 5, `RUWE` <1.4 and $|V - V_{LSR}| > 210\,\mathrm{km\,s^{-1}}$ in different volumes. The dashed lines show the selections of the Helmi Streams previously used by Koppelman et al. 2019b. The Helmi Streams consistently stand out as an overdensity.

2.3 Characterising the Helmi Streams: Phase-Space Distribution

The 6D phase-space, energy and angular momentum distribution of the Helmi Streams' stars are shown in Fig. 12. The hiL and loL clump stars have similar distributions in configuration space, with the only major difference that the distribution of the hiL clump stars is more peaked around $x = -8$ kpc. However, the two clumps clearly differ from each other in their kinematics, with the hiL clump spanning a smaller range in v_y and having larger $|v_z|$. As we can approximate $L_\perp \sim R|v_z|$ at the location of the Sun, the larger $|v_z|$ reflects the fact that the hiL clump has a higher $L_\perp$. Also the total energy E of the hiL clump stars is on average higher as their kinetic energy is generally larger. The loL clump stars span a wider range of energies with the result that part of the loL clump stars are on more bound orbits.

Fig. 12 shows that the Helmi Streams occupy both a positive and negative v_z group, meaning that part of the stars is moving away from the Galactic plane and others are moving towards it. This bimodality in the v_z distribution, which is roughly $1:3$ for $(v_z > 0) : (v_z < 0)$ in the RVS sample, has been used to obtain a rough estimate for the time of accretion (Kepley et al. 2007; Koppelman et al. 2019b), which can be done as it is the result of multiple wraps of tidal debris crossing the Solar neighbourhood. When tidal debris is fully phase mixed, half of the stars will cross the Galactic plane in each direction and the ratio will thus be $1:1$ (Kepley et al. 2007). The bimodality in the v_z distribution is thus indicative of a structure's degree of phase-mixing. What is peculiar is that the loL clump is distributed more equally over the two v_z groups, $(v_z > 0) : (v_z < 0) \sim 2:3$, while the hiL clump mostly populates the negative v_z group, $(v_z > 0) : (v_z < 0) \sim 1:6$. The difference in this ratio is even larger in *Gaia* DR3. While the loL clump stars are distributed as $(v_z > 0) : (v_z < 0) \sim 2:3$, the hiL clump stars are distributed as $(v_z > 0) : (v_z < 0) \sim 1:9$, see Fig. 53 in Appendix A. Another difference, which is seen even more clearly in DR3, is that the hiL clump stars seem to form a more coherent structure in velocity space, while the distribution of loL clump stars appears to be more diffuse. In other words, the hiL clump seems to be less phase mixed. Interestingly, following the argument before, this would lead to a different accretion time estimate for the hiL and loL clump, with the loL clump being accreted earlier in time. However, this cannot be the case, as the two clumps belong to the same structure (see Section 2.1).

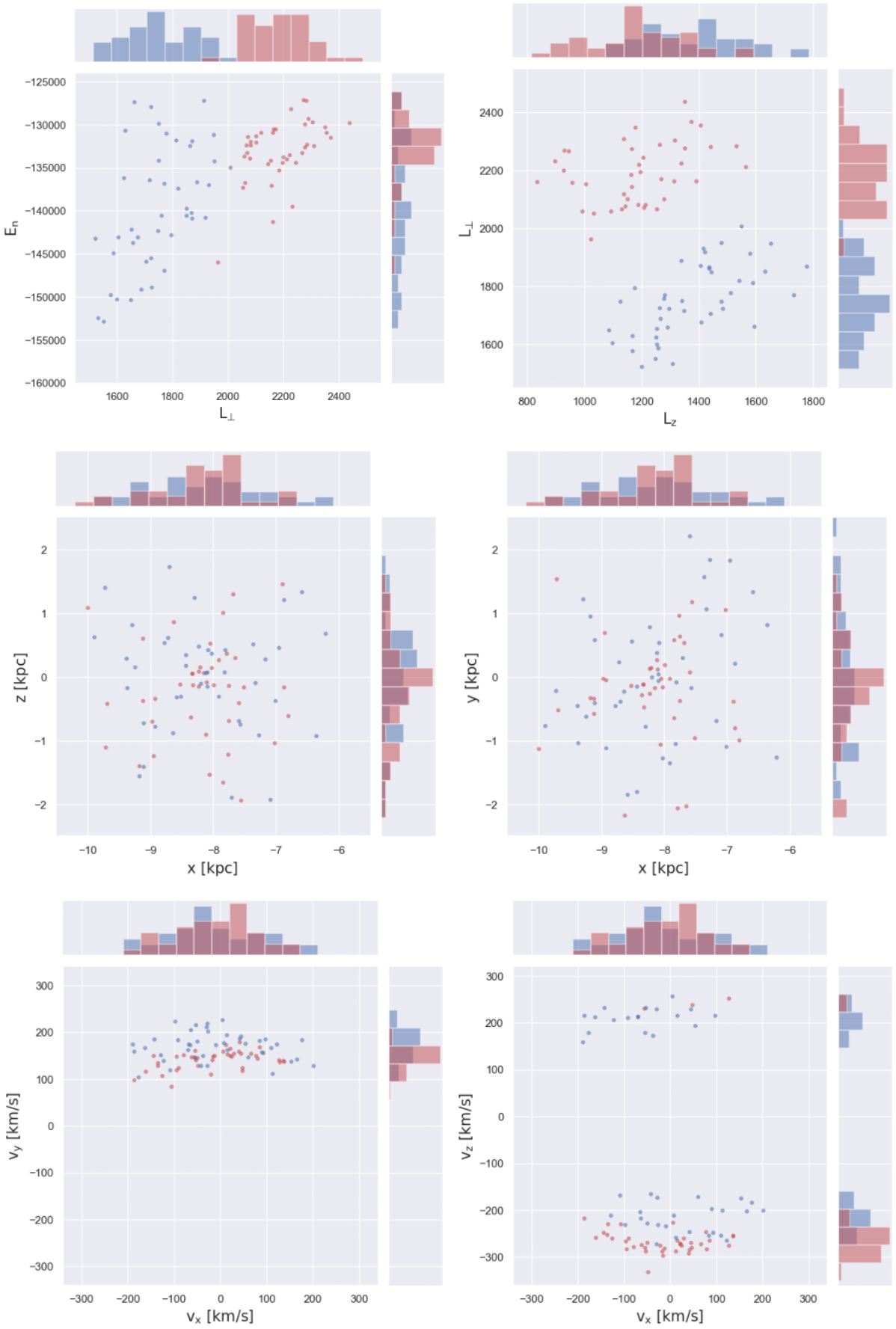

Figure 12: Phase-space, energy and angular momentum distribution of the hiL clump (red, 41 stars in total) and loL clump (blue, 43 stars in total) in the *Gaia* EDR3 RVS sample in the Default Potential (see Section 1.7.4). Histograms on the top and right of each plot show the distributions in one dimension.

2.4 Characterising the Helmi Streams: Orbital Properties

How does the difference in phase mixing and the existence of the clumps translate itself into the orbital properties of the Helmi Streams' stars? To investigate this, I compare the orbital frequencies of the two clumps and I inspect their orbits.

2.4.1 Orbital Frequencies

As discussed in Section 1.5.2, integrals of motion can be used to characterise an orbit. In a similar way, an orbit can be described by its three fundamental frequencies (see also Appendix E), which describe oscillations in different directions in a given coordinate system. In cylindrical coordinates, the three fundamental frequencies are

- Ω_R, measuring the oscillation in the radial direction
- Ω_ϕ, measuring the oscillation around the Galactic center
- Ω_z, measuring the oscillation in the vertical direction

To determine the fundamental orbital frequencies we use `SuperFreq` (Price-Whelan 2015), which is an implementation of the Numerical Approximation of Fundamental Frequencies (NAFF) method introduced in Laskar 1993[11]. After integrating the orbits of the stars for a period of 100 Gyr with a time-step of 10 Myr in the Default Potential (see Section 1.7.4), we transform to Poincaré's symplectic polar variables and pass the phase-space positions to `SuperFreq` as three complex time series, for example $z(t) + iv_z(t)$ (Koppelman et al. 2021)[12]. `SuperFreq` then performs a Fourier transform of each time series and selects the frequency with the highest amplitude as the fundamental frequency. The uncertainties in the orbital frequencies were determined by Monte Carlo sampling. For each star, we generate 500 mock stars with 6D phase-space positions sampled from the Gaussian distributions of the observables of each star (α, δ, ϖ, μ^*_α, μ_δ, v_{rad})[13]. The orbit of each mock star is integrated and the orbital frequencies are computed using `SuperFreq`. This results in a distribution of 500 sampled frequencies for each of the three fundamental frequency of each star. We take the standard deviation of the resulting distributions as an estimate for the uncertainty in the frequencies.

The resulting fundamental frequencies with their associated uncertainties are shown in Fig. 13. In general, the hiL clump spans a smaller range of orbital frequencies, which reflects the fact that the hiL clump stars span a smaller range in energy. Moreover, the mean fundamental frequencies of the hiL clump are lower, which reflects the fact that the hiL clump stars are on less bound orbits which have longer orbital periods and thus lower orbital frequencies. The loL clump has a more diffuse frequency distribution in all three fundamental frequencies due to its more phase-mixed nature. The features seen in the RVS sample persist in the larger extended sample.

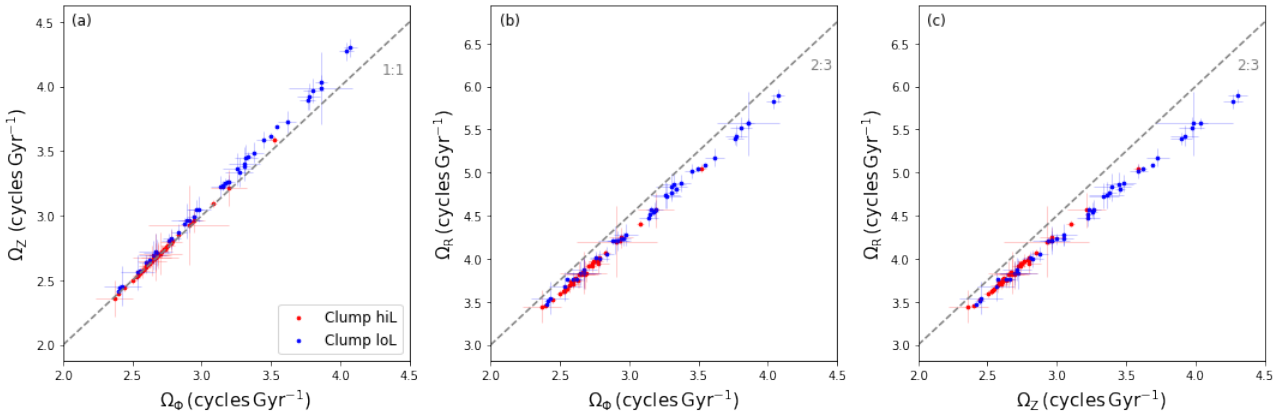

Figure 13: Orbital frequencies of the hiL clump stars (red) and loL clump stars (blue) in the *Gaia* EDR3 RVS sample in the Default Potential (see Section 1.7.4). The uncertainties were determined by Monte Carlo sampling with $N = 500$. Some resonances are indicated as grey dashed lines.

[11] For more information on `SuperFreq`, see also Appendix B of Price-Whelan et al. 2016b.

[12] Note that, because the orbits are integrated in a Galactic potential, the orbital frequencies depend on the assumed Galactic potential.

[13] α is the right ascension, δ is the declination, ϖ is the parallax, $\mu^*_\alpha = \mu_\alpha \cos(\delta)$ is the azimuthal proper motion in right ascension, μ_δ is the proper motion in declination, and v_{rad} is the radial velocity.

Panel (a) of Fig. 13 shows that the hiL clump lies on the $1:1$ resonance in $\Omega_\phi : \Omega_z$, while the loL clump seems to be shifted towards a lower ratio[14]. This is seen more clearly in Fig. 14, which shows the histograms of the orbital frequency ratios. The frequency ratio $\Omega_\phi : \Omega_z$ is related to the total flattening of the potential[15], which, as shown in Fig. 56 in Section 1.7.3, varies with radius and is in part spherical in the region occupied by the Helmi Streams. In a spherical potential, the variation in $L_\perp$ is minimal, as this is then an integral of motion. Hence, the fact that we see the two angular momentum clumps today shows that the total potential flattening has to transition to being spherical within the region probed by the Helmi streams, as this will ensure that the clumps remain separated in angular momentum space in time. This explains why the Helmi Streams' clumps are sensitive to the total flattening of the potential, and why the existence of the gap in angular momentum space can be used as a constraint on the shape of the Galactic potential (see Dodd et al. 2021). We should however realise that the Helmi Streams are sensitive to the overall flattening of the Galactic potential, not just the flattening of the DM halo. In a Galactic potential with a bulge, disk and halo, there will therefore be a degeneracy between the shape of the halo and the mass of the disk, as the disk is a flattened structure. If the halo is made spherical but the disk heavier, this will lead to the same overall potential flattening as when the halo is made more oblate and the disk lighter. It is also important to note that a perfectly spherical potential (without disk or bulge) can not explain the existence of the two clumps, as in a spherical potential there are no resonances or causes for substructure.

In panel (b) and (c) of Fig. 14 we see that the Helmi Streams' orbital frequency ratios are roughly $\Omega_{\phi,z} : \Omega_R \sim 0.7$, a bit above the $2:3$ resonance. While in $\Omega_\phi : \Omega_R$ the distribution of the hiL and loL clump mostly overlap, in $\Omega_z : \Omega_R$ the distribution of the loL clump spans a range that is about twice as large and reaches a higher frequency ratio. This is a reflection of the splitting that is also observed in $\Omega_\phi : \Omega_z$.

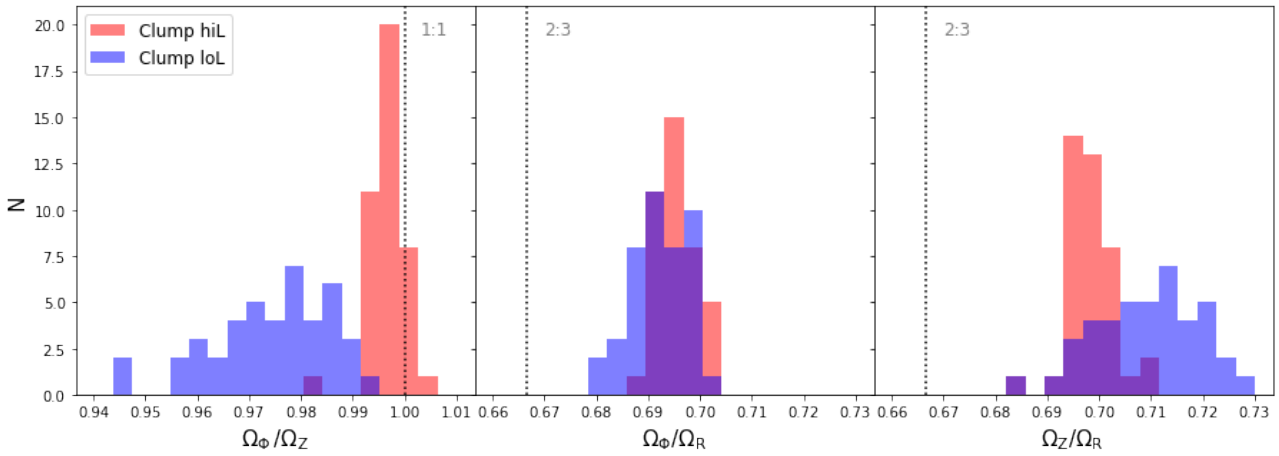

Figure 14: Orbital frequency ratio distribution of hiL clump stars (red) and loL clump stars (blue) in the *Gaia* EDR3 RVS sample in the Default Potential (see Section 1.7.4). Some resonances are indicated as grey dashed lines.

[14]Note that the Default Potential (see Section 1.7.4) is constructed such that the hiL clump lies on the $\Omega_\phi : \Omega_z$ is $1:1$ resonance, see also (Dodd et al. 2021).

[15]In spherical coordinates (r, θ, ϕ), the three fundamental frequencies are Ω_r, Ω_θ and Ω_ϕ. If a star is on the $\Omega_\theta : \Omega_\phi$ is $1:1$ resonance, this indicates that the region of the potential occupied by the star's orbit is (at least in part) spherical, as the orbital periods in the θ and ϕ direction are equal. In cylindrical coordinates, the relation between the $\Omega_\phi : \Omega_z$ is $1:1$ resonance and the sphericity of the potential is not one to one.

2.4.2 Orbits

This Section explores the orbits of the Helmi Streams' stars. In particular, the focus is on how the differences in the clumps' phase-space structure and frequencies result in different kinds of orbital families.

To visualise where the Helmi Streams' stars spend most of their time while orbiting the Milky Way, we integrate the orbits of the stars for 10 Gyr with a time-step of 10 Myr in the Default Potential and discard the first 1 Gyr of integration time. We then consider each time-step to be a "star", and plot all "stars" in a density map. This is shown in Fig. 15, which clearly show that the orbits of the hiL clump stars (left panels) and loL clump stars (right panels) differ. More specifically, though all stars seem to be on tube orbits, the hiL clump stars seem to be on orbits that are flattened in the y-direction, see panel (c). This is the result of the stars being on the $\Omega_\phi : \Omega_z$ is $1 : 1$ resonance, which reduces the dimensionality of the orbits to 2 degrees of freedom. The loL clump stars, which are off-resonance, are on tube orbits which seem to have a more boxy shape in (x, z) and (y, z) (see panel (b) and (c)) and clearly occupy a three-dimensional space. Because a resonant orbit has a lower dimensionality, it phase-mixes slower, explaining the difference in the observed degree of phase-mixing of the hiL and loL clump. While a non-resonant orbit phase-mixes at a rate $\propto t^{-3}$, where t is time, a resonant orbit phase-mixes at a rate $\propto t^{-2}$. When an orbit is on two resonances, for example a circular orbit, it phase-mixes at an even slower rate, $\propto t^{-1}$, as its dimensionality is reduced even further (Helmi and White 1999; Vogelsberger et al. 2008).

Fig. 16 shows the density map in Galactocentric cylindrical coordinates, which reveals that the hiL clump stars seem to occupy a region the probes farther out in the potential, more specifically higher above and below the Galactic plane. Another difference is that the hiL stars seem to have more similar apo- and pericenters, producing pile-ups of "stars" in the density map. To clarify this, Fig. 17 shows the mean peri- and apocenters over an integration period of 10 Gyr of all stars in the RVS sample. The loL clump indeed covers a wider range of apo and pericenters. This can be explained by the fact that the loL clump stars cover a wider range of energies, and therefore have more diverse orbits. In contrast, the hiL clump stars have more similar orbits with on average higher apo- and pericenters than the loL clump. This means that the hiL clump stars experience a different overall potential flattening than the loL clump stars, as the flattening varies with distance from the Galactic center (see Fig. 6).

The fact that the hiL clump stars follow more similar orbits can also be appreciated from Fig. 18, which shows the Surfaces of Section (or in short, SoS) of the hiL clump stars (left panel) and loL clump stars (right panel). SoS are a useful tool to inspect orbits. In cylindrical coordinates (R, z, ϕ) in an axisymmetric potential, the coordinate ϕ does not contain much information due to axisymmetry. To describe an orbit, therefore, only four coordinates are needed, namely R, v_R, z, v_z. As any orbit will pass through the Galactic plane, we take a slice of the orbit through $z = 0$ and plot (R, v_R) whenever the star passes the plane with a positive v_z (hence, we only plot the star when it moves upwards through the plane). These individual points in the SoS are called consequents. For a regular orbit, the consequents appear to lie on a smooth curve, called the invariant curve of the orbit, which can for example be a loop, as is the case for the Helmi Streams' stars in Fig. 18. The fact that some orbits show a dotted or dashed invariant curve shows that they are trapped by a higher order resonance, for example $\Omega_z : \Omega_R$ is $7 : 10$. The surfaces of section in the left panel look comparable in shape and size. In contrast, the surfaces of section in the right panel look more scattered and of different size and shape. This is a consequence of the fact that the loL clump stars are on more diverse orbits.

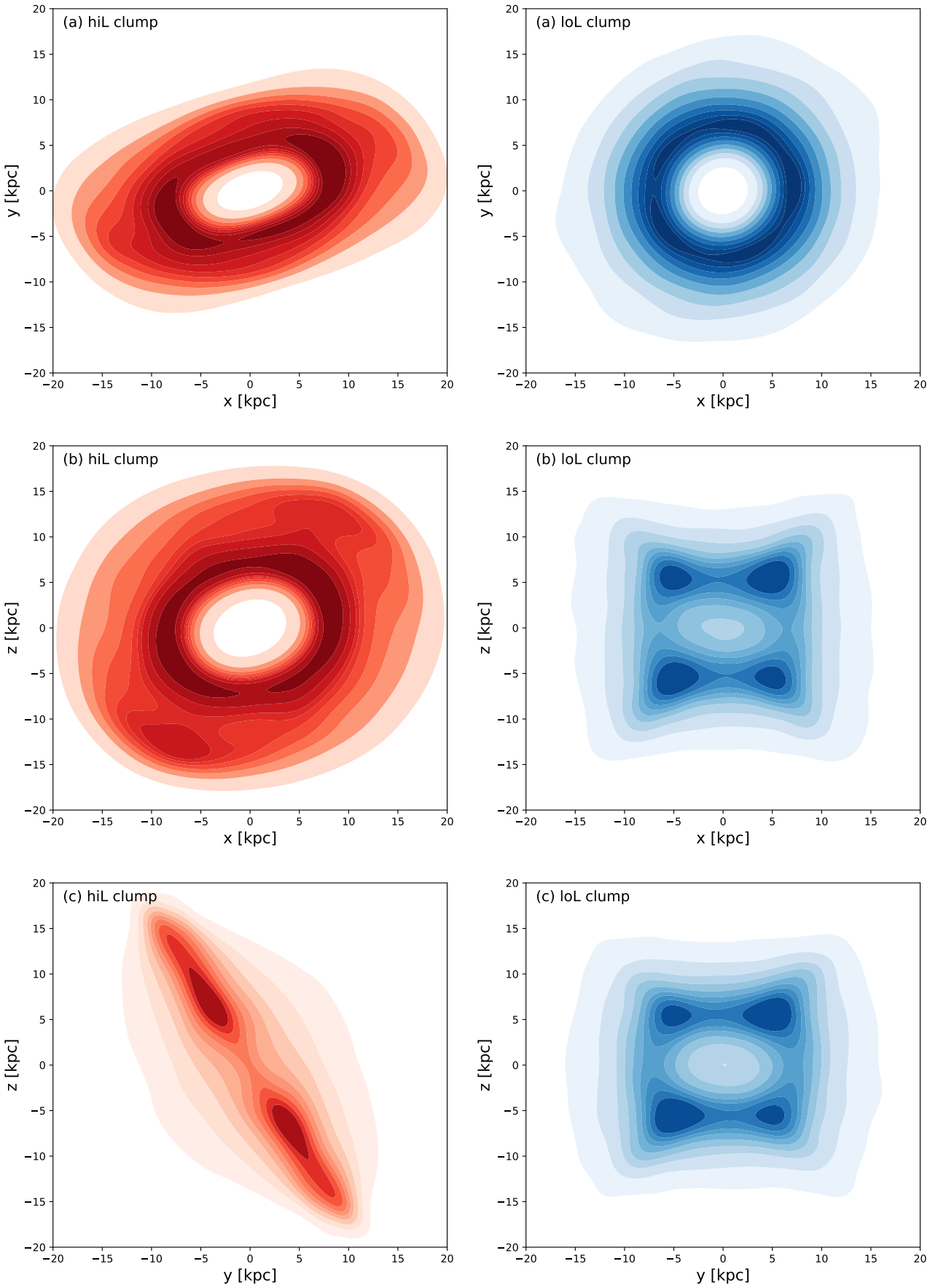

Figure 15: *Left panels:* Smoothed density map in Galactocentric coordinates showing where the hiL clump stars in the *Gaia* EDR3 RVS sample spend most of their time while orbiting the Milky Way. The darker the red, the higher the density of stars is. Each "star" corresponds to a time-step of an orbit integration of 10 Gyr, where we discarded the first 1 Gyr of integration. *Right panels:* Similar as the left panel but for the loL clump stars in the *Gaia* EDR3 RVS sample. The darker the blue, the higher the density of stars is.

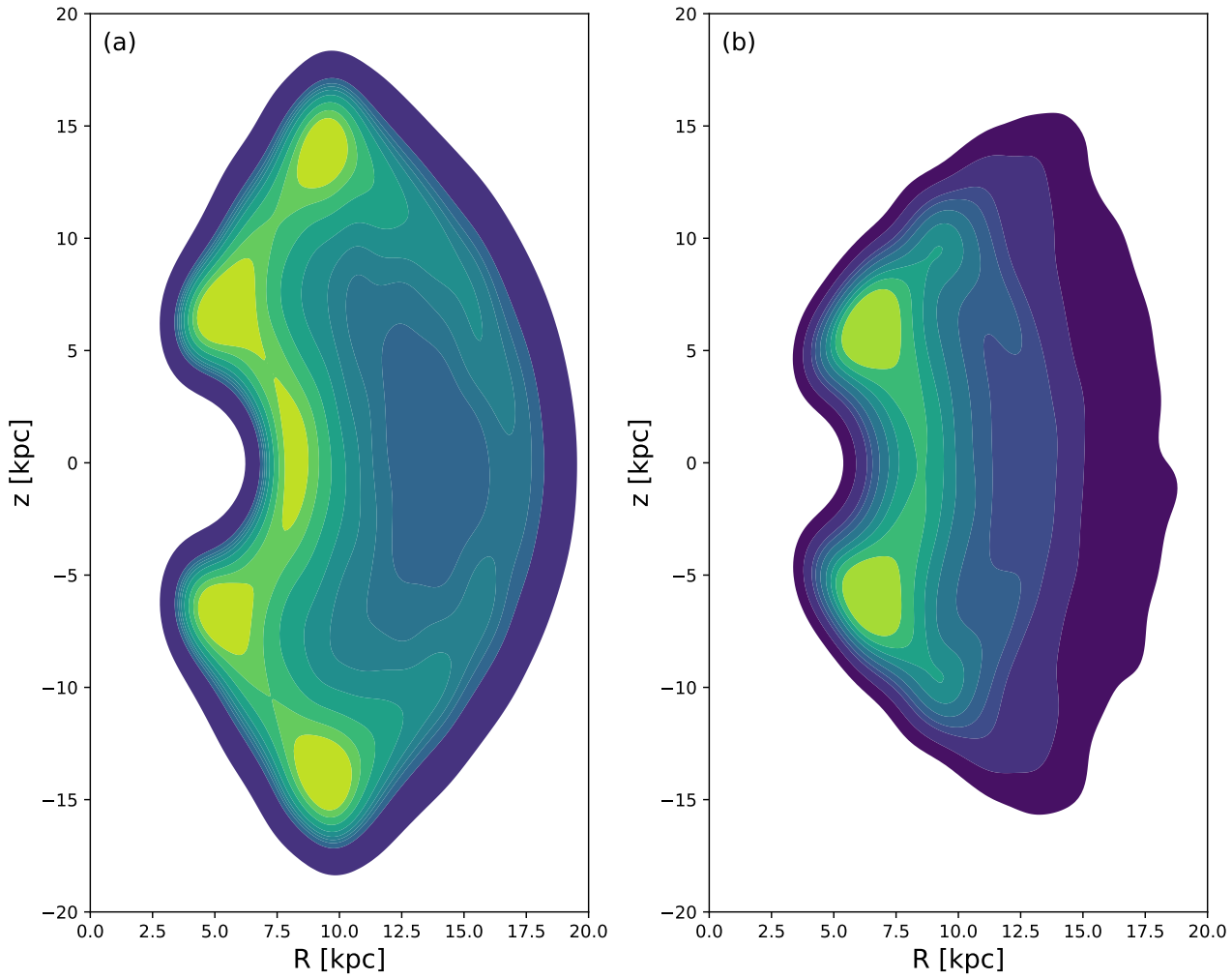

Figure 16: *Left panel:* Smoothed density map in Galactocentric cylindrical coordinates showing where the hiL clump stars in the *Gaia* EDR3 RVS sample spend most of their time while orbiting the Milky Way in the Default Potential (see Section 1.7.4). The more towards the yellow, the higher the density of stars is. Each "star" corresponds to a time-step of an orbit integration of 10 Gyr, where we discarded the first 1 Gyr of integration. *Right panel:* Similar as the left panel but for the loL clump stars in the *Gaia* EDR3 RVS sample.

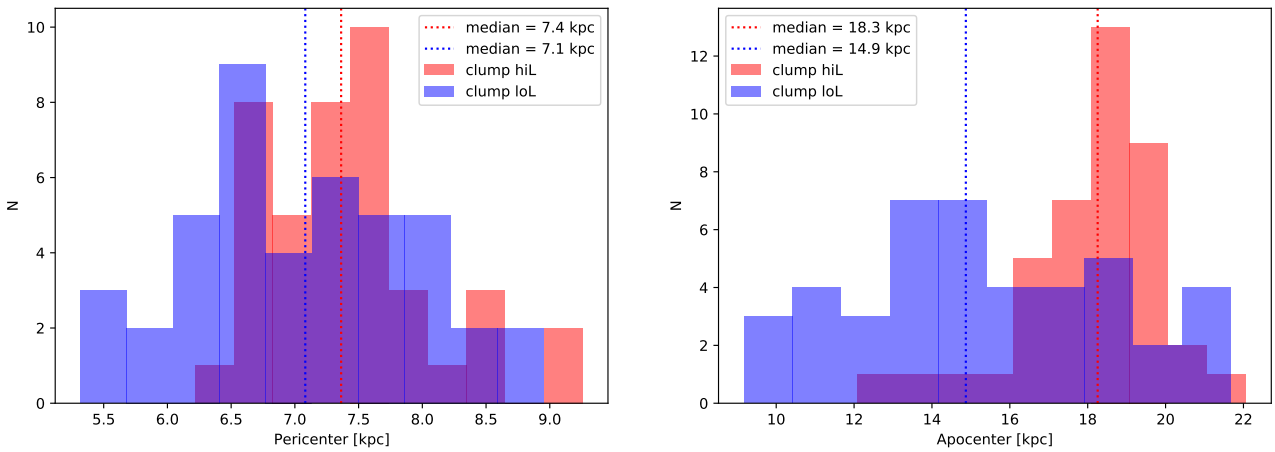

Figure 17: *Left panel*: Mean apocenters over an integration period of 10 Gyr of the hiL clump stars (red) and loL clump stars (blue) in the *Gaia* EDR3 RVS sample in the Default Potential (see Section 1.7.4). The hiL clump stars have a smaller spread in and on average higher apo- and pericenters. *Right panel*: Similar as the left panel but showing the mean pericenters.

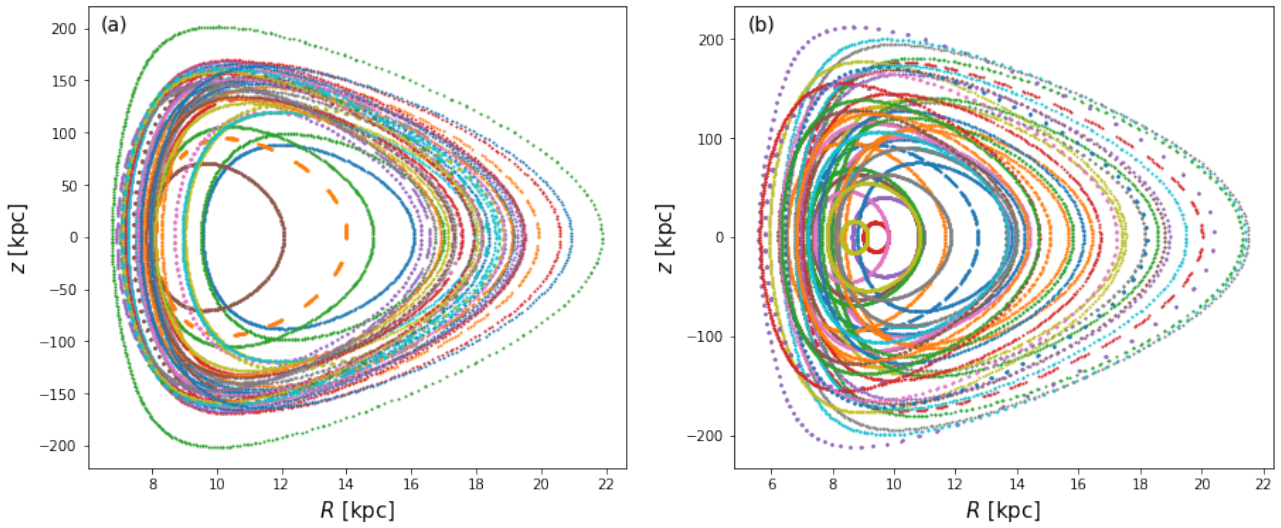

Figure 18: *Left panel*: Surfaces of section in the plane $z = 0$ for $v_z > 0$ km s^{-1} of the hiL clump stars in the *Gaia* EDR3 RVS sample for an integration time of 300 Gyr with a time-step of 0.1 Myr. *Right panel*: Similar as the left panel but for the loL clump stars in the *Gaia* EDR3 RVS sample.

2.5 A Kinematically Cold Subclump

When carefully examining the phase-space and energy and angular momentum distribution of the Helmi streams stars (extended sample, see Fig. 19), an overdensity in hiL clump stars around $v_x \sim 0\,\mathrm{km\,s^{-1}}$ stands out. This overdensity has been identified as the S2 stream by Myeong et al. 2018. A subset of these stars forms a very tight sequence in all subspaces. When selecting these stars empirically in angular momentum space ($1320 < L_z < 1410\,\mathrm{km^2 s^{-1}}$, $2330 < L_\perp < 2500\,\mathrm{km^2\,s^{-1}}$, $v_z < 0\,\mathrm{km\,s^{-1}}$), we see that they trace out a stream in configuration space and form a coherent clump in velocity space, see Fig. 19. Also in frequency space they form a very tight sequence. This subset of stars is chemically similar to the rest of the Helmi Streams stars.

It thus seems that this specific subset of stars has somehow undergone an even slower evolution than the rest of the hiL stars, as they are less phase mixed. We thus see an interesting scenario unfold: while the hiL stars have undergone a slower evolution than the loL stars, the subclump has undergone an even slower evolution. It could be that the subclump is stabilised by a different resonance, while the loL clump is too far away from the(se) resonance(s) and thus undergone evolution at a "normal" rate.

2.6 Summary

The Helmi Streams can be separated into two clumps in angular momentum space which are clearly distinct in velocity space, especially in v_z. Moreover, the loL clump appears to be more phase mixed than the hiL clump. The Helmi Streams' orbits probe a dynamically interesting region of the gravitational potential of the Galaxy that hosts multiple resonances and seem to be located close to the $2:2:3$ for $\Omega_\phi : \Omega_Z : \Omega_R$ resonance. While the hiL clump falls on the $\Omega_\phi : \Omega_Z$ is $1:1$ resonance in the Default Potential, the loL clump is shifted to a lower ratio. Moreover, the loL clump has a more diffuse frequency distribution, reflecting its more phase-mixed nature. These features are robust under uncertainties and sample size. We identify a kinematically cold subclump within the hiL clump that seems to be even less phase-mixed.

As the hiL clump stars are on resonant orbits in the Default Potential, these orbits have a lower dimensionality, which is particularly apparent in configuration space. On the other hand, as the loL clump stars are not on resonant orbits, their orbits are three-dimensional structures in configuration space. A resonant orbit is expected to phase-mix slower, $\propto t^{-2}$, than a non-resonant orbit, $\propto t^{-3}$, explaining the observed difference in the degree of phase-mixing between the two clumps. The loL clump stars span a larger range of apo- and pericenters as they have a larger spread in energy, while the hiL clump stars are on more similar orbits. Moreover, the hiL stars seem to occupy a region that probes farther out in the potential and farther above the Galactic plane, meaning that they experience a different overall flattening of the potential than the loL clump stars. This is reflected in the difference in $\Omega_\phi : \Omega_z$ frequency ratio.

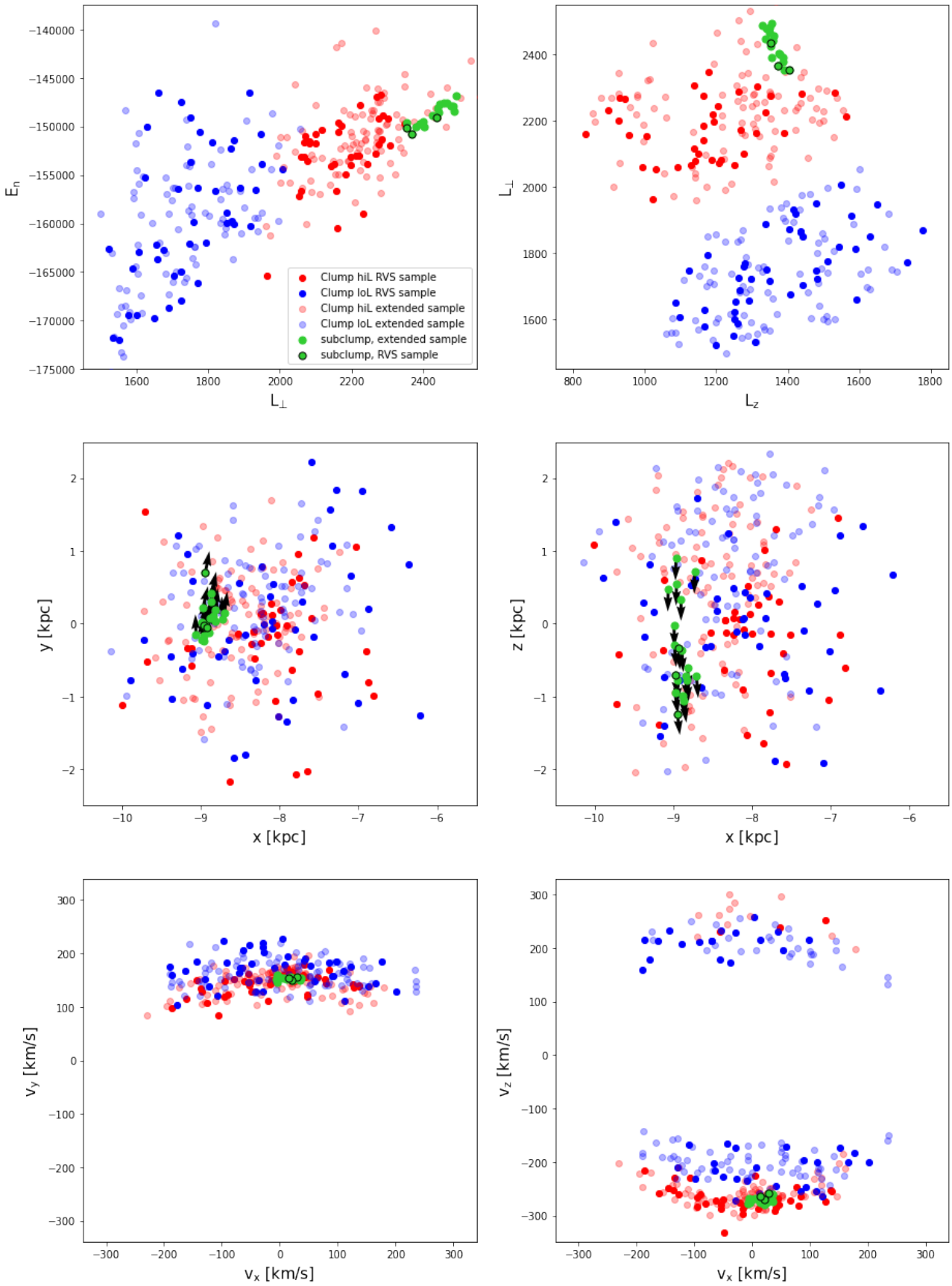

Figure 19: Phase-space, energy and angular momentum distribution of the hiL clump (red, 41 stars in total) and loL clump (blue, 43 stars in total) in the *Gaia* EDR3 RVS sample in the Default Potential (see Section 1.7.4). The distribution of the subclump is overplotted in green, and the subset of stars that are part of the RVS sample are shown with a black edgecolour. The subclump has been selected empirically as $1320 < L_z < 1410\,\mathrm{km^2 s^{-1}}$, $2330 < L_\perp < 2500\,\mathrm{km^2\,s^{-1}}$, $v_z < 0$. In configuration space, the stars clearly trace out a stream. Black arrows indicate the direction in which the stars are moving.

3 Proof of concept: Basis Function Expansions

All models of the Galactic potential presented in earlier Sections are parametrised models, meaning that they are descriptions using specific functional forms characterised by a set of parameters. These models are usually made up of several components to describe the distinct components of our Milky Way, such as the disk(s), the bulge and the halo. In the case of the McMillan 2017 potential, the DM halo is described by an NFW profile using two parameters (see Eq. 8), while the stellar disks are described by an exponential profile with each three parameters (see Eq. 10). The bulge is described by five parameters, and the gas disks are each described by four parameters. This means that our entire Galaxy, a body that has lived through many mergers and consists of billions of stars, is reduced to a description of 20 parameters. This description, of course, relies on assumptions and simplifications.

Many of the gravitational potential models assume a spherical NFW halo (see Section 1.7.3). Only two parameters, namely the density ρ_0 and the scale radius r_s (see Eq. 8), describe how the density profile of the halo varies with radius[16]. While the NFW profile is motivated by the shapes of DM halos in N-body simulations (Navarro et al. 1996), it is only a zeroth-order, idealised description. In fact, simulations have shown that DM halos are often triaxial in shape (Frenk et al. 1988). Moreover, observations seem to advocate for a DM halo that varies in shape with radius. It has been found that individual stellar streams, probing different regions of the underlying Galactic potential based on their orbit (Bonaca and Hogg 2018), can each prefer a different description of the DM halo's shape (Woudenberg 2019, see also Section 1.7.3). A dark matter halo that radially varies in shape seems in fact to be required to fit the Sagittarius dwarf galaxy stream (Vera-Ciro and Helmi 2013; Vasiliev et al. 2021). N-body simulations of Milky Way analogues also support a radially varying shape of the halo (Zavala and Frenk 2019; Shao et al. 2021). This shows that we need more than a simple, (axi)symmetric description of the DM halo to match our observations.

This is where parametrised models become restrictive. By choosing a certain model, one is restricted by that model. A pure NFW profile specified by its two characteristic parameters will not be able to describe a halo that radially varies in shape. If the actual shape of our DM halo is different from what is seen in cosmological simulations, fitting the NFW's parameters to find a description of the halo will be offset from the truth, and will not be able to get closer to the truth because the parametrised model does not allow that. Of course, parametrised descriptions of components of the Galactic potential are often easy to work with. For example, the Miyamoto Nagai disk (Miyamoto and Nagai 1975) allows analytic computations of the potential, forces, and density, simplifying orbit integrations. We are thus looking for something that allows for a greater freedom in the description of potential profiles, but is also computationally inexpensive. Such a toolset are Basis Function Expansions (BFE).

Basis function expansions can be used to describe the potential and density as the sum of orthogonal basis functions[17]. Each function adds a degree of freedom, and each functions' coefficient describes its contribution to the system. In principle, any profile can be described using a basis function expansion, as long as the number of terms is large enough. This means that descriptions in basis function expansions can be very flexible, and we are no longer limited by restrictive parametrisations. Once such a description is obtained, the value of the potential and forces at any arbitrary point are easily computed. While computing forces for N particles in a full N-body simulation scales as $O(N^2)$, in a BFE this is only $O(N)$, though of course this depends on the number of terms (Sanders et al. 2020). This is why basis function expansions have been used in the past as a computationally inexpensive way to solve the Poisson equation (e.g. Hernquist and Ostriker 1992).

There are many advantages to BFE. For example, BFE can be used to describe the time evolution of DM halos of complex shapes if the coefficients become a function of time. Snapshots of (high resolution) simulations can be expanded into basis functions, and by interpolating the coefficients, a time-dependent description can be obtained (e.g. Lowing et al. 2011; Sanders et al. 2020). Furthermore, since stellar systems like our Milky Way can be assumed to be collisionless (meaning that individual encounters between stars do not govern the motion of a star), stars move due to a smooth, mean gravitational field generated by all mass present in the system (Binney and Tremaine 2008). A BFE can therefore be used as a smooth description of a "grainy" N-body simulation. While it is computationally expensive to, for example, do orbit integration in a full N-body simulation, BFEs

[16] An NFW profile can similarly be described by its mass and concentration. Effectively, the NFW profile is described by only one parameter, because there is a correlation between these two parameters, though with a large scatter (Zavala and Frenk 2019).

[17] Recall that two vectors $\vec{a}$ and $\vec{b}$ are orthogonal if their inner product (or dot product) satisfies $\langle \vec{a}, \vec{b} \rangle = 0$. Cartesian coordinates are an example of an orthogonal basis. Similarly, the inner product of two orthogonal basis functions is equal to zero (see also Section A.2.1 in Vasiliev 2018). For example, $\langle \sin(nx), \sin(mx) \rangle \equiv \int_{-\pi}^{\pi} \sin(nx) \sin(mx) dx = \delta_{n,m}$. As the inner product of this basis function with itself is equal to $\delta_{n,n} = 1$, this forms an orthonormal basis.

can give a realistic description that is computationally inexpensive to evaluate (e.g. Ngan et al. 2015).

An interesting application of BFE is to describe perturbations, such as the impact of the Large Magellanic Cloud onto the Milky Way, which is currently at first infall (Besla et al. 2007). The infall of the LMC is inducing large-scale asymmetric perturbations to the Milky Way's DM halo, meaning that it cannot simply be described by an axisymmetric or triaxial halo model (Garavito-Camargo et al. 2019). The infall of the LMC induces reflex motion, meaning that the Milky Way disk is moving with respect to stars farther out in the stellar halo (Petersen and Peñarrubia 2020). This happens because the LMC's mass is $\sim 1.4 \cdot 10^{11}\,\mathrm{M}_\odot$, about 10-20% of the Milky Way's present-day mass (Erkal et al. 2019; Shipp et al. 2021). A BFE with a large number of terms can be used to describe the effect of the LMC onto the Milky Way's DM halo based on N-body simulations (Garavito-Camargo et al. 2021). This allows the study of, for example, the evolution of stellar streams in a time-dependent Galactic potential (Lilleengen et al. 2022). An analytic potential would not be able to capture the deformations in the Galactic potential induced by the LMC, again proving the great value of a non-parametrised description.

This section aims to present the reader with a proof of concept. Here I show that it is possible to find a description of the Galactic DM halo that satisfies our imposed constraints using a low-order BFE. First, the used set of basis functions is explained in more detail. Then, I describe how a Monte Carlo Markov Chain (MCMC) can be used to vary relatively freely the shape of the DM halo with a BFE as a basis, and prove that using this, an NFW profile can be turned into a Hernquist profile. Using the right constraints, a BFE could be a promising tool to explore the shape of the DM halo without the restrictions of a parametrised halo model. To illustrate this, I will try to find a description for the halo that maximises the distance between the two Helmi Streams' clumps. Throughout this Section, I will assume an axisymmetric potential.

3.1 AGAMA's Multipole Expansion[18]

3.1.1 Generalities

In AGAMA's Multipole expansion potential, the potential is represented by a sum of individual spherical-harmonic terms with coefficients $\Phi_{l,m}(r)$ that are arbitrary functions of radius:

$$\Phi(r,\theta,\phi) = \sum_{l=0}^{l_{max}} \sum_{m=-m_0(l)}^{m_0(l)} \Phi_{l,m}(r) Y_l^m(\theta,\phi) \tag{11}$$

where $m_0(l) = \min(l, m_{max})$ and $m_{max} \leq l_{max}$. m_{max} and l_{max} can be chosen by the user. $Y_l^m(\theta,\phi)$ are the real-valued spherical harmonics

$$Y_l^m(\theta,\phi) = \sqrt{4\pi}\tilde{P}_l^m \mathrm{trig}(m\phi) \tag{12}$$

$$\mathrm{trig}(m\phi) \equiv \begin{cases} 1 & \text{if} \quad m = 0 \\ \sqrt{2}\cos(m\phi) & \text{if} \quad m > 0 \\ \sqrt{2}\sin(|m|\phi) & \text{if} \quad m < 0 \end{cases} \tag{13}$$

where $\tilde{P}_l^m(\cos\theta)$ are normalised associated Legendre polynomials. $Y_l^m(\theta,\phi)$ describes the angular dependence of the distribution, while $\Phi_{l,m}(r)$ describes the radial dependence. An illustration of $Y_l^m(\theta,\phi)$ for different l and m is shown in Fig. 20.

While l governs the order of the expansion in the meridional angle θ, m governs the order of the expansion in the azimuthal angle ϕ. Thus, if a potential is spherically symmetric, this means that there is symmetry with both the angle ϕ and θ, and so both l and m will be equal to zero. The expansion is then solely governed by the coefficients $\Phi_{l=0,m=0}(r)$, as $l = 0$, $m = 0$ simply corresponds to a monopole, see Fig. 20. If a potential is axisymmetric, this means that there is symmetry with the angle ϕ, and therefore we can set $m = 0$. Moreover, for an axisymmetric potential the odd l terms will be equal to zero because they correspond to spherical harmonics that are not symmetric under reflection[19]. For example, $l = 1$, $m = 0$, corresponds to a dipole, see Fig. 20. An axisymmetric potential can thus be described using only the even l terms and the radial coefficients $\Phi_{l,m}(r)$.

[18] A large part of this section is adapted from Section 2.2.2 and A.4.1 of Vasiliev 2018

[19] i.e. symmetric under the transformation $\{x, y, z\} \to \{-x, -y, -z\}$.

The higher order l terms become more important once the potential diverges more from spherical symmetry. For potentials close to spherical symmetry, l_{max} as small as 2-8 can be used (Vasiliev 2019).

A Multipole expansion can be constructed in two ways. If a potential is given, the spherical-harmonic transform is computed at the nodes of a one-dimensional radial grid to obtain $\Phi_{l,m}(r_{grid})$ and its derivative $\mathrm{d}\Phi_{l,m}(r_{grid})/\mathrm{d}r$. An interpolated quintic spline gives the radial dependence in between these nodes, $\Phi_{l,m}(r)$ and $\mathrm{d}\Phi_{l,m}(r)/\mathrm{d}r$. The coefficients are normalised such that $\Phi_{l=0,m=0}(r) = \Phi(r)$ for a spherically symmetric potential (recall that $l = 0$, $m = 0$ represents a monopole).

If instead a density profile is given, the coefficients $\rho_{l,m}(r)$ are first determined via a spherical-harmonic transform

$$\rho_{l,m}(r) \equiv \frac{1}{\sqrt{4\pi}} \int_1^1 d\cos(\theta) \tilde{P}_l^m(\cos\theta) \int_0^{2\pi} d\phi \, \mathrm{trig}(m\phi)\rho(r,\theta,\phi) \tag{14}$$

where $\mathrm{trig}(m\phi)$ is given by Eq. 13. Then, since the potential and thus the coefficients of the potential, $\Phi_{l,m}(r)$, and density, $\rho_{l,m}(r)$ are related via the Poisson equation (see Eq. 1) $\Phi_{l,m}(r)$ can be found using

$$\Phi_{l,m}(r) = \frac{4\pi G}{2l+1}\left[r^{-l-1}\int_o^r \rho_{l,m}(r')r'^{(l+1)} + r^l \int_r^\infty \rho_{l,m}(r')r'^{(1-l)}dr'\right] \tag{15}$$

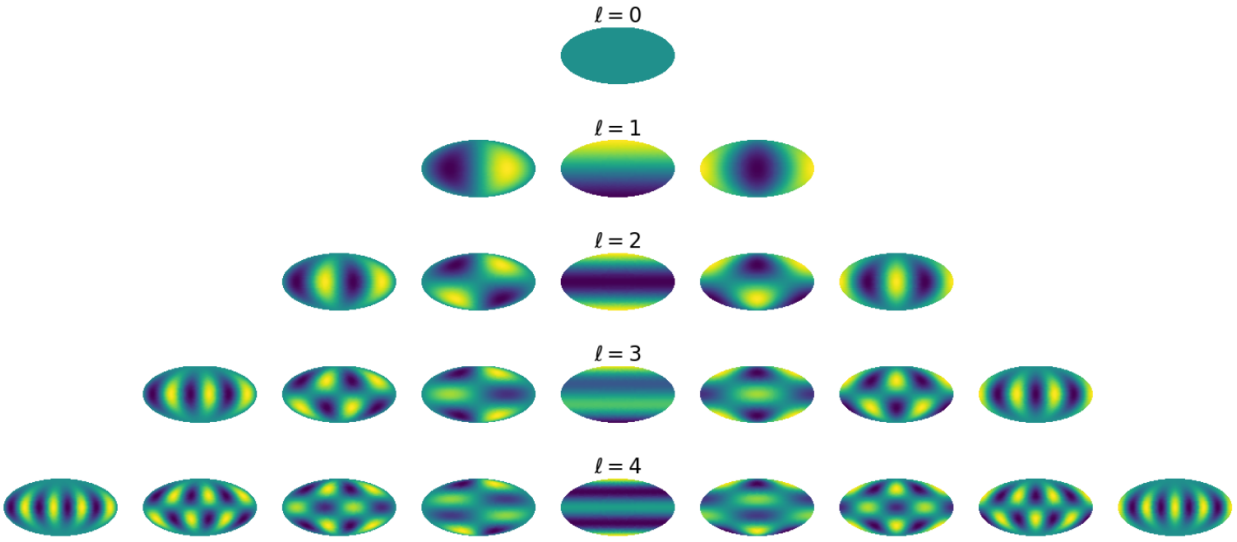

Figure 20: Spherical harmonics, plotted in Mollweide projection, evaluated from $l = 0$ (top row) to $l = 4$ (bottom row), for each $-l \leq m \leq l$. The central column thus shows the spherical harmonics for which $m = 0$, which are axisymmetric. $l = 0$, $m = 0$ corresponds to a monopole, $l = 1$, $m = 0$ corresponds to a dipole, $l = 2$, $m = 0$ corresponds to a quadrupole, and so on. The spherical harmonics with non-zero m clearly break axisymmetry. Figure adapted from Cunningham et al. 2020.

3.1.2 How Many Terms do we Need?

It is instructive to understand how many terms and gridpoints are needed for an accurate BFE of the potential. Since we are only considering axisymmetric potentials, $m = 0$ and l is even. The number of terms needed, l_{max}, depends on the required accuracy and the shape of the potential. If the shape is close to spherically symmetric, l_{max} as small as 2-8 can be used (Vasiliev 2019). Also the number of gridpoints of a Multipole potential influences the accuracy of the description. To illustrate the dependence on these two quantities, I show the density residuals, $\Delta\rho_{norm}(R,z) = [\rho(R,z)_{BFE} - \rho(R,z)_{analytic}]/\rho(R,z)_{analytic}$, for different l_{max} and different numbers of gridpoints of a Multipole BFE of the default halo (which is an NFW halo with a flattening of $q = 1.2$ in the density). As I will apply the developed BFE method to the Helmi Streams in Section 3.3, we are interested in the region probed by the Helmi Streams, which ranges from about $5 - 20$ kpc. Therefore, we set the minimum gridpoint at $r_{min} = 3$ kpc and the maximum gridpoint at $r_{max} = 40$ kpc to avoid boundary condition issues.

Fig. 21 shows the density residuals for different l_{max} (red, blue and green curves). The number of gridpoints is left as a free parameter and is optimised by AGAMA, and the nodes are equally spaced in $\log(r)$. One can already

see the effect of the edge of the grid for $r \gtrsim 23$ kpc, but in the region probed by the Helmi Streams the density is matched at the percentage level even for $l_{max} = 2$. Increasing l_{max} gives order(s) of magnitude improvement in the accuracy of the description. Fig. 22 shows the resulting orbits in the analytic Default Potential with a basis function expansion halo for different values of l_{max} (so the `Multipole` halo potentials have been added to the McMillan 2017 stellar disks, gas disks and nucleus to create a Milky Way potential). These are compared to orbits in the analytic Default Potential. The initial conditions that have been integrated for 2.5 Gyr correspond to a randomly sampled Helmi Streams' star. In this case, even $l_{max} = 2$ seems to suffice, as the deviations from the orbit in the analytic potential are only minor, especially on short timescales. During the first Gyr, the deviation from the orbit in the analytic potential is on average on the sub-percentage level for $l_{max} = 2$, though this increases to percentage level for longer timescales, most notably in the z direction, where the potential is flattened. For higher l_{max} the deviations stay below the percentage level over the entire considered range in time. Clearly, an expansion with a higher l_{max} is better at capturing the flattened shape of the halo.

Fig. 21 also shows the density residuals for $l_{max} = 2$ and a range of $2 - 4$ gridpoints (orange, cyan and purple curves). A gridsize of 2 is outperformed by a gridsize of 3 and 4 (which give similar results), though the density is still matched up to percentage level. For $l_{max} = 2$, one can see clearly the effect of the spline interpolation between the gridpoints. Fig. 22 shows a comparison of the orbits in the analytic Default Potential and the orbits in the analytic Default Potential with a basis function expansion halo with different numbers of gridpoints. The orbit in the `Multipole` potential with a gridsize of 2 deviates most notably from the orbit in the analytic potential, while the orbits in the `Multipole` potentials with a gridsize of 3 and 4 deviate less and at a similar level. Again, the effect of deviation from the analytic potential is strongest in z direction where potential is flattened. This difference rises to the order of 10's of percent (gridsize = 2) and 10 percent (gridsize = 3, 4) after 2 Gyr, meaning that more gridpoints are needed to obtain an accurate description on longer timescales. Still, over short orbital timescales, ~ 1 Gyr, all orbits agree within percentage (gridsize = 2) and sub-percentage (gridsize =3, 4) level.

To get an accurate basis function expansion description of more complex shapes, a higher number of terms is needed. To illustrate this, Fig. 23 shows a comparison of the Default Potential and expansions for different l_{max}. $l_{max} = 1000$ is needed to capture accurately the flat disks in the Galactic plane. In this case, a different set of basis functions, more suitable for flattened distributions, would have been more efficient (i.e. a lower number of terms would suffice), as the spherical harmonics start from a spherical distribution, so strong higher order correction terms are needed to capture the flattened shape of a disk.

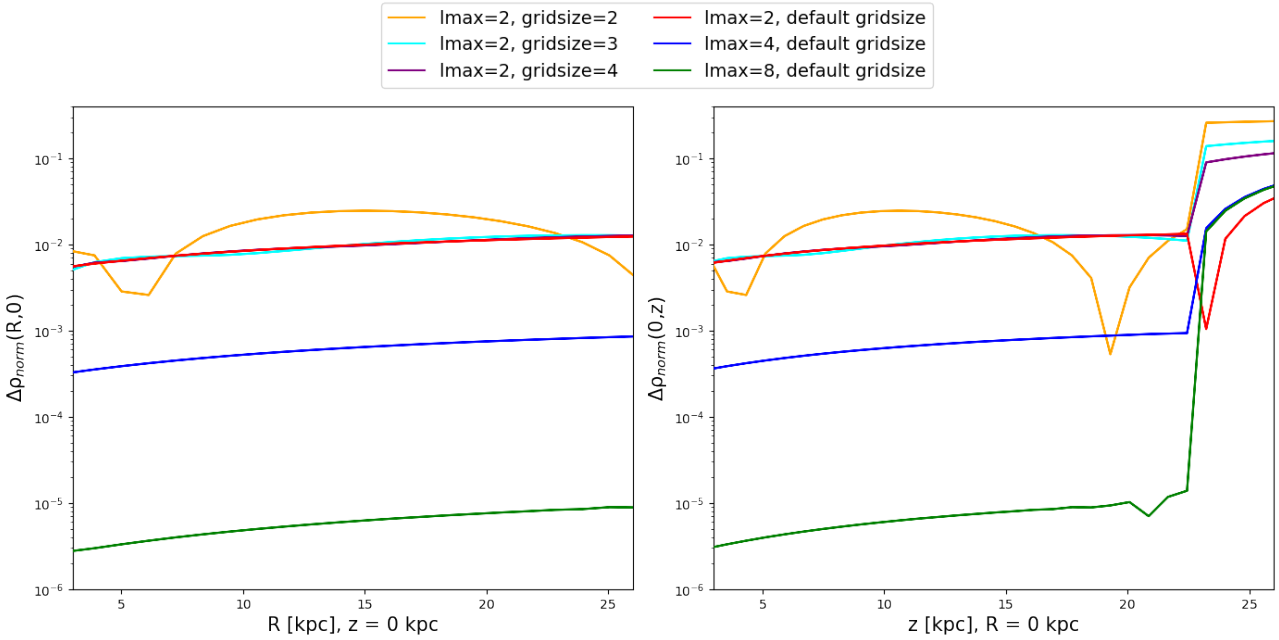

Figure 21: Density residuals $\Delta\rho_{norm}(R,z) = \left[\rho(R,z)_{BFE} - \rho(R,z)_{analytic}\right] / \rho(R,z)_{analytic}$ of a comparison between the analytic default NFW (see Section 1.7.4) and the derived `Multipole` potential for different values of l_{max} and different numbers of gridpoints. Boundary conditions become an issue at larger radii.

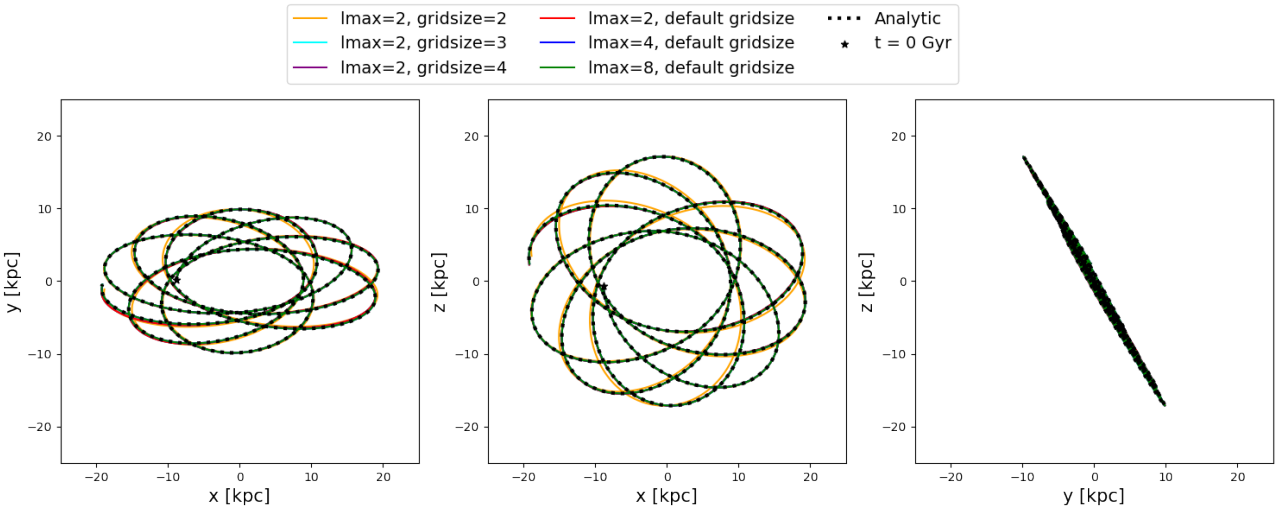

Figure 22: Comparison of orbits in the analytic Default Potential (black dashed lines, see Section 1.7.4) and the analytic Default Potential with a basis function expansion halo for different values of l_{max} and different numbers of gridpoints. The orbits have been integrated for 2.5 Gyr, the initial conditions correspond to a randomly chosen Helmi Streams' star with (x, y, z, v_x, v_y, v_z) = (-8.85 kpc, -0.11 kpc, -0.73 kpc, 24.9 km s^{-1}, 143.5 km s^{-1}, -275.8 km s^{-1}).

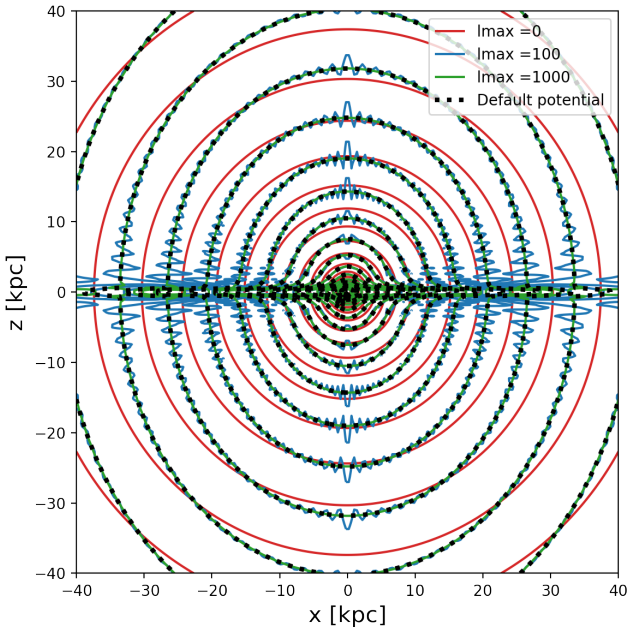

Figure 23: Isopotential contours of the Multipole expansion of the Default Potential (see Section 1.7.4) for different l_{max} (red, blue, green), compared to the isopotential contours of the Default Potential (dotted black). $l_{max} = 0$ shows, as expected, spherical isopotential contours. Only $l_{max} = 1000$ is able to capture the flattened nature of the disks well.

3.2 Turning an NFW Profile into a Hernquist Profile

As a proof of concept, let us investigate if, by varying the BFE's coefficients and their derivatives in a Monte Carlo Markov Chain (MCMC), an NFW profile can be reshaped into a Hernquist profile. We start with an expansion of the default NFW (which is an NFW halo with a flattening of $q = 1.2$ in the density) and then vary the corresponding coefficients and their derivatives in such a way that they in the end describe a flattened Hernquist profile. For the purpose of this proof of concept, we only care about relatively short orbital timescales, say 1 Gyr. Hence, $l_{max} = 2$ and 2 gridpoints can be used to obtain an accurate enough (percentage level accuracy) BFE description of the potential. The potential is then described by 8 parameters in total: $\Phi_{l=0,m=0}$, $\mathrm{d}\Phi_{l=0,m=0}/\mathrm{d}r$, $\Phi_{l=2,m=0}$ and $\mathrm{d}\Phi_{l=2,m=0}/\mathrm{d}r$ at the two gridpoints, which are chosen to be $r_{min} = 1$ kpc, $r_{max} = 50$ kpc. The flattened Hernquist profile is given by

$$\rho(R,z) = \frac{\rho_0}{\frac{\tilde{r}}{a}\left(1+\frac{\tilde{r}}{a}\right)^3} \tag{16}$$

where $\tilde{r}$ is defined as before in Eq. 9, $a = 20$ kpc, $\rho_0 = 10^7\ \mathrm{M_\odot kpc^{-3}}$ and I choose $q = 1.3$.

To vary the coefficients and their derivatives, I use `emcee`, an affine-invariant ensemble sampler for MCMC by Foreman-Mackey et al. 2013. While a Monte Carlo means a random sampling, the Markov Chain ensures that each next step depends on the previous step. An affine-invariant sampler follows many walkers at the same time, such that the next step depends on the relative location of the other walkers. It is therefore easy to sample non-linear structures, as the group of walkers shrinks and stretches through the parameter space. A drawback is that this group might get stuck on a local maxima. Another drawback is that in high dimensions, MCMC's are not efficient in exploring the parameters space[20] However, with only 8 free parameters the MCMC should perform fine. To make the MCMC run faster, I use a `Pool` object from the `multiprocessing` module to let `emcee` run on multiple CPUs, which can be done because of the parallel nature of the ensemble method.

To go from an NFW to a Hernquist profile, the likelihood consists of a χ^2 which compares the analytic Hernquist forces and potential to the `Multipole` forces and potential[21]:

$$\chi^2_{tot} = \sum_i \sum_j \frac{(F^{BFE}_{i,j} - F^{Hernquist}_{i,j})^2}{F^{Hernquist}_{i,j}} + \sum_i \frac{(\Phi^{BFE}_i - \Phi^{Hernquist}_i)^2}{\Phi^{Hernquist}_i} \tag{17}$$

where j is x, y, z and i are the radii at which the potential and forces of the BFE are compared to the analytic Hernquist model. F_j refers to the different components of the force, Φ refers to the potential. By minimising the χ^2, the BFE will move closer to the analytic Hernquist profile. I let the MCMC run with 40 walkers for 4000 steps, after which it has converged[22]. Fig. 24 shows the initial orbit in the default NFW potential, the orbit in the resulting best-fit BFE potential and the orbit in the analytic Hernquist potential for comparison. Though slightly offset due to the low l_{max} and low number of gridpoints, the BFE orbit and analytic Hernquist orbit agree well. This result holds independently of the choice of initial conditions, and it turns out to hold for all Helmi Streams' stars. Fig. 25 shows the initial NFW, best-fit BFE and analytic Herqnuist density and potential profile, which agree on percentage (density) and sub-percentage (potential) level. This shows that varying the coefficients and their parameters in an MCMC, given the right constraints, allows us to reshape an initial BFE potential, providing opportunities to explore the shape of the DM halo.

[20] There is exponentially more parameter volume when the number of free parameters is increased, so when a new random step in the parameter space is proposed, the chances are very high that that step is in a direction of lower likelihood, which will likely be rejected. The acceptance fraction, the fraction of proposed steps that gets accepted, will thus be very low. Therefore, for a large parameter space, the walkers only take tiny steps and hence the parameter space is not explored well and in an inefficient way. This shows that random guesses do not work in high dimensions.

[21] In principle, if we are only interested in the orbits and density profile of the potential, a likelihood can be used that solely does a χ^2 on the different force components. The resulting potential profile will then be offset from the true Hernquist potential by an arbitrary integration factor as the choice of zero-point for the potential is arbitrary, but the forces and density profile will match. A χ^2 solely on the density or potential however does not constrain the forces well enough to obtain matching orbits due to the integrations/derivations involved.

[22] The amount of steps the MCMC needs to run is usually determined by looking at the auto-correlation time of the chain, which is the time (number of steps) it takes before the chain forgets where it started. Following Foreman-Mackey et al. 2013, about 50 times the auto-correlation time should be the time the MCMC needs to run before it converges.

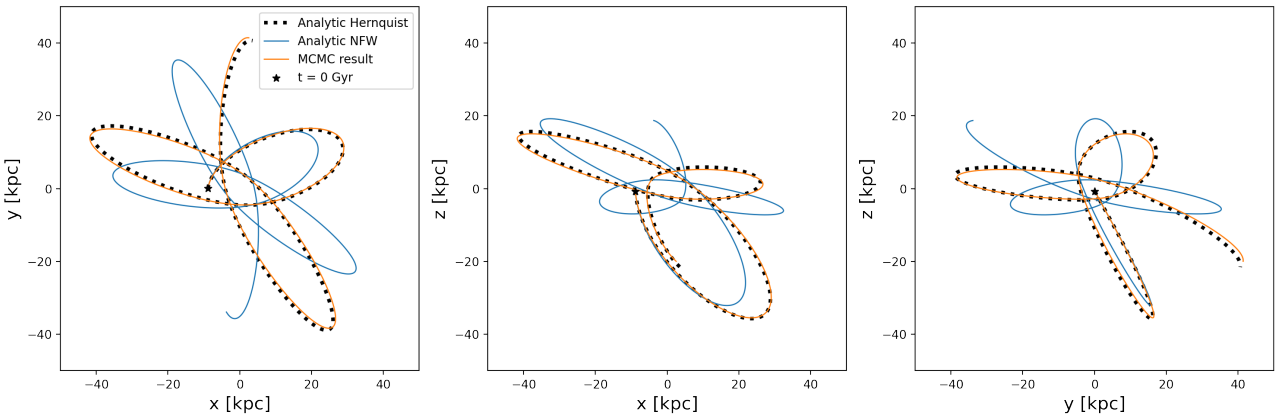

Figure 24: Initial orbit in the NFW potential (blue) and the orbit in the best-fit BFE potential (orange) compared to the orbit in the analytic Hernquist potential (dotted black). The orbits have been integrated for 2.5 Gyr, the initial conditions correspond to a randomly chosen Helmi Streams' star with (x, y, z, v_x, v_y, v_z) = (-8.85 kpc, -0.11 kpc, -0.73 kpc, 24.9 km s^{-1}, 143.5 km s^{-1}, -275.8 km s^{-1}).

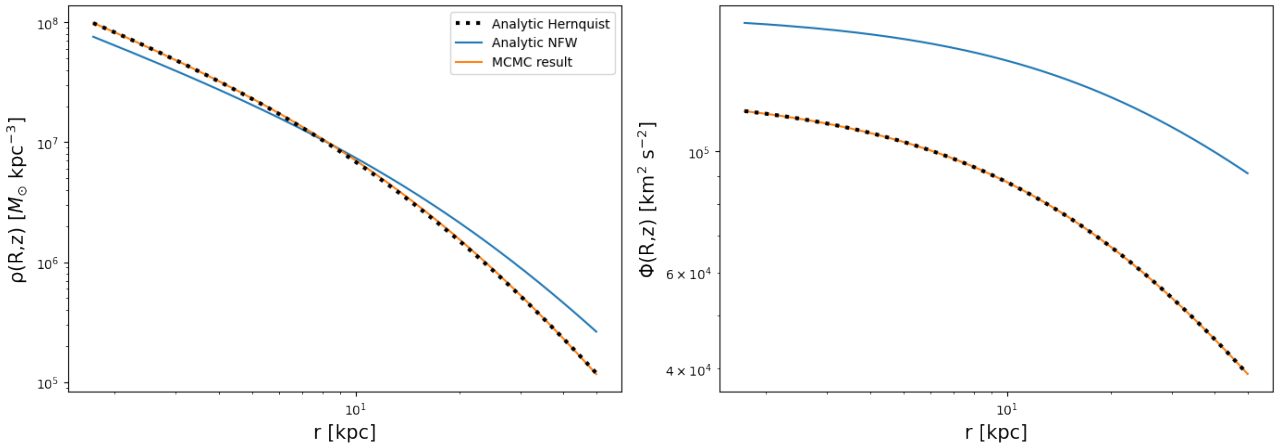

Figure 25: *Left panel:* Density and *right panel:* potential profile of the initial default NFW profile (blue), analytic Hernquist profile (dotted black) and best-fit BFE result (orange). The analytic Hernquist profile agrees with the best-fit BFE result on percentage (density) and sub-percentage (potential) level.

3.3 An Application of BFE: Maximising Clump Distance

The two Helmi Streams' clumps are sensitive to the overall flattening of the potential (see Section 2.4.1), as also explored by Dodd et al. 2021. The existence of the two clumps can therefore serve as a constraint on the shape of the Galactic potential, because the correct Galactic potential should preserve the gap between the two clumps that we see today (note that L_z and $L_\perp$ as measured today only depend on observables, while their evolution in time depends on the Galactic potential). Section 3.3.1 explores how the distance between the two clumps can be used to measure how well the Galactic potential conserves the gap. Section 3.3.2 takes this a step further and tries to reshape a BFE potential to maximise the clump distance.

3.3.1 Using the Helmi Streams as a Constraint on the Galactic Potential

The distance between the two clumps can be used as a measure of how well the Galactic potential conserves the gap. If the clumps reside in a region of the potential that is spherical, they will remain coherent as $L_\perp$ is conserved. Then the distance between the two clumps will remain constant. To quantify the distance between the clumps, we first rotate the clumps in angular momentum space by $\theta = 30$ degrees, such that *rotated* $L_z = \cos(\theta)L_z + \sin(\theta)L_\perp$ and *rotated* $L_\perp = -\sin(\theta)L_z + \cos(\theta)L_\perp$, see Fig. 26. We then take the mean of the four stars with the lowest *rotated* $L_\perp$ value in the hiL clump, and the mean of the four stars with the highest *rotated* $L_\perp$ value in the loL clump, and define the distance, dist_{clumps}, as the difference between these two means. This is illustrated in the left panel of Fig. 26. We take this mean to account for outliers, and we checked that there is no significant difference in the sensitivity to the potential flattening if we take fewer or more stars into account in determining this mean. A positive distance signifies that the two clumps

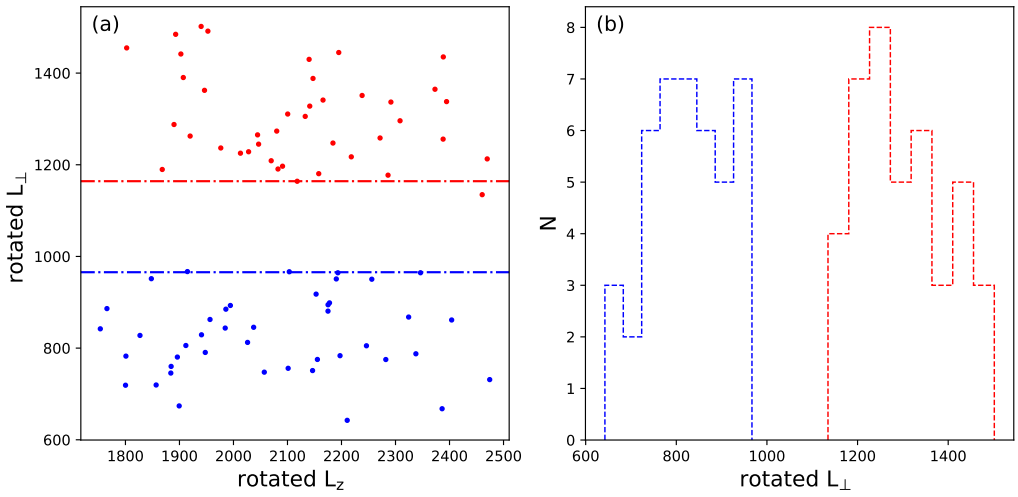

Figure 26: *Left panel:* Angular momentum distribution of the hiL clump stars (red) and loL clump stars (blue) (see Fig. 12) rotated by $\theta = 30$ degrees. Here, *rotated* $L_z = \cos(\theta)L_z + \sin(\theta)L_\perp$ and *rotated* $L_\perp = -\sin(\theta)L_z + \cos(\theta)L_\perp$. The red dash-dotted line represents the mean of the four stars with the lowest *rotated* $L_\perp$ in the hiL clump, while the blue dash-dotted line represents the mean of the four stars with the highest *rotated* $L_\perp$ in the loL clump. The distance between the clumps is defined to be the difference between these two means. *Right panel:* Histogram in *rotated* $L_\perp$ space, illustrating the clear separation between the two clumps in this space.

are separated in angular momentum space, while a negative distance signifies that the two clumps overlap and start to mix (see Fig. 8 in Dodd et al. 2021 for an illustration). The most realistic potential will give rise to a mean distance that is close to the distance between the clumps we observe today.

We take the McMillan 2017 potential and let q, the flattening in the density of the NFW halo (see Eq. 8 and 9), vary[23]. The behaviour of the distance as a function of time and the mean distance over ~ 10 Gyr for different values of q are shown in Fig. 27. The distance varies around a mean value as a function of time, as $L_\perp$ is not an integral of motion in a non-spherical potential, so it varies with the phase of the orbit (see Section 1.5.2). For an oblate halo ($q = 0.85$, yellow line), the amplitude with which the distance varies is larger, and the mean distance is negative, which should be interpreted as that the clumps overlap and mix. Such an oblate potential does thus not conserve the gap. For a prolate halo ($q = 1.15$, grey line), the amplitude with which the distance varies is smaller and the mean distance comes closest to the present-day distance, meaning that for this experiment, $q = 1.15$ seems to be preferred.

We find that an integration period of 600 Myr with a time-step of 1 Myr is enough to give a robust estimate on the mean distance. We visualise the dependence on q by calculating the mean distance for a large range of values of q, which is shown in Fig. 28. The distribution, which has a smooth behaviour with q, peaks at $q = 1.13$. This dependence shows that the Helmi Streams' gap can be used as a constraint on the shape of the Galactic potential[24]. Still, the mean distance for $q = 1.13$ is $\sim 150\,\mathrm{km}^2\,\mathrm{s}^{-2}$, which is below the present-day value, $\sim 200\,\mathrm{km}^2\,\mathrm{s}^{-2}$. Therefore, to see if more freedom in the description of the halo can give rise to a distance that matches the present-day value, I turn to a BFE description in the next Section.

[23]Note that in this exercise we keep all other parameters of the potential fixed. This means that for a higher flattening, the density at a fixed point will increase.

[24]The Helmi Streams' clumps are sensitive to the overall flattening of the Galactic potential, not just q. In a Galactic potential with a bulge, disk and halo, there will therefore be a degeneracy between the shape of the halo and the mass of the disk, as the disk is a flattened structure. If the halo is made spherical but the disk heavier, this will lead to the same overall potential flattening as when the halo is made more oblate and the disk lighter.

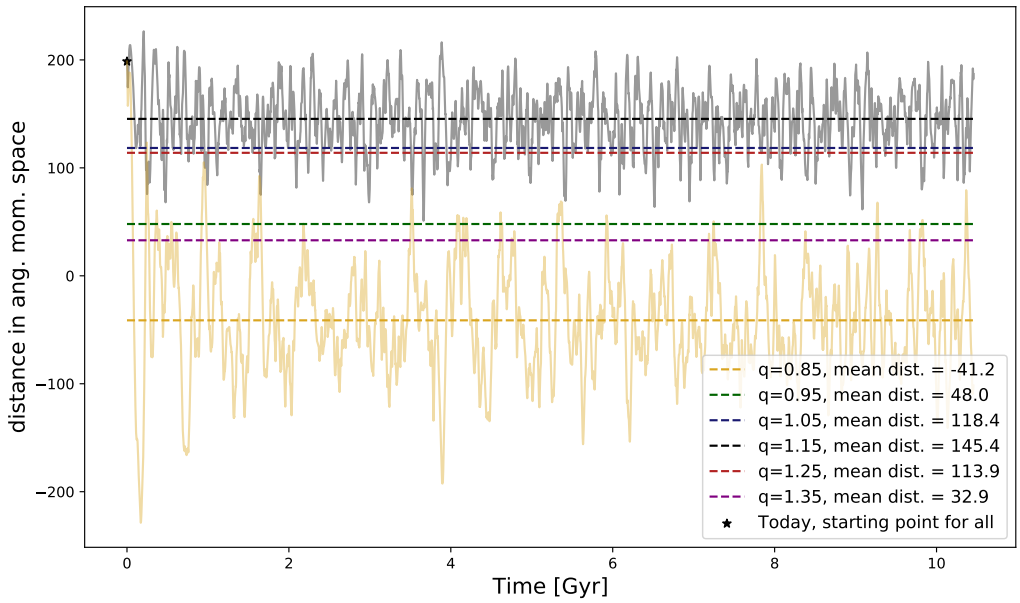

Figure 27: Distance between the two clumps in rotated angular momentum space as a function of integration time for $q = 1.15$ (grey) and $q = 0.85$ (yellow). The dashed lines show the mean distance for different values of q over an integration time of ~ 10 Gyr, which vary with different values of q. The black star indicates the distance between the clumps that we observe today, which depends on observables and is thus independent of the Galactic potential and q.

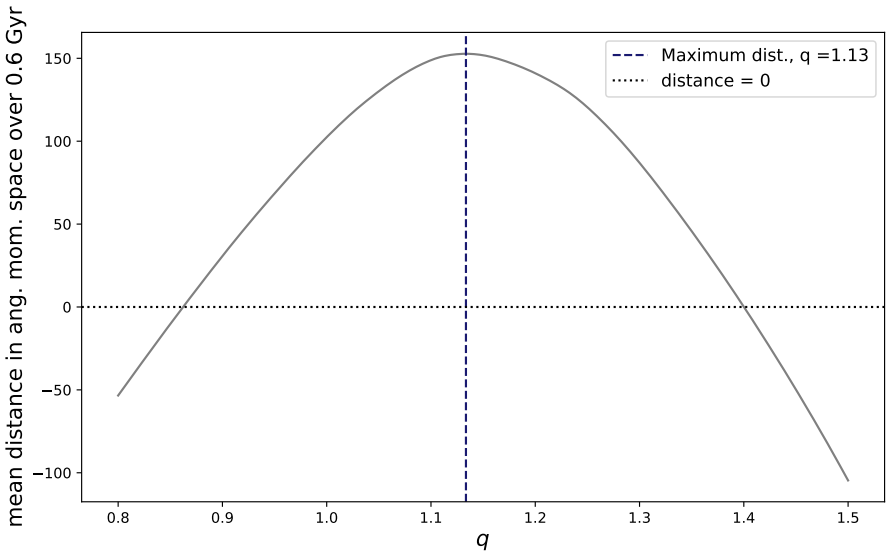

Figure 28: Mean distance between the two clumps in rotated angular momentum space over 0.6 Gyr as a function of halo density flattening q. The behaviour with q is smooth. If the distance is negative, this means that the clumps start to overlap and mix.

3.3.2 BFE: Freedom to Maximise the Clump Distance

Using a set of realistic constraints, we try to shape the halo (keeping the stellar disks, gas disks and bulge fixed) in such a way that the distance between the two Helmi Streams' clumps is maximised over time. To maximise the distance between the clumps effectively means to minimise the variation in $L_\perp$, and hence to move towards a potential that is spherical in the region occupied by the Helmi Streams. This therefore puts a constraint on the shape of the potential. Another constraint on the mass distribution and forces is given by the rotation curve and the required velocity at the position of the Sun (see Section 1.6). To make sure the mass distribution is constrained well enough, I use the full extent of Eilers et al. 2019 rotation curve, covering $5 < R < 25$ kpc (see Section 1.6). The distance between the clumps, dist_{clumps} is parametrised as described in Section 3.3.1. The likelihood is then given by

$$\ln \mathcal{L} = -\frac{1}{2} \sum_{i}^{N} \frac{\left(v_{c,i}^{d} - v_{c,i}^{m}\right)^2}{\sigma_{v_c}^2} + K \, \mathrm{dist}_{clumps} \tag{18}$$

where the superscripts d and m denote the data and the model, respectively, and K is a normalising factor which is set equal to one. The logarithmic likelihood of the rotation curve can be added to the distance between the clumps in this way because they are both a measure of "distance". The log likelihood of the rotation curve measures the distances between the BFE potential's rotation curve and the rotation curve data, while dist_{clumps} measures the average distance over an integration time of 0.6 Gyr in angular momentum space between the two clumps.

As we only care about relatively short orbital timescales, I use $l_{max} = 2$ and gridsize = 2 (as was done in Section 3.2), giving me 8 free parameters[25]. I set $r_{min} = 3$ kpc and $r_{max} = 40$ kpc, as the region probed by the Helmi Streams is roughly $5 - 20$ kpc. I set the following prior

$$P(\vec{\theta}) = \begin{cases} 1 & \text{if} \begin{cases} 0.1 < l_0(r_{min})/l_{0,i}(r_{min}) < 10 \\ 0.1 < l_2(r_{min})/l_{2,i}(r_{min}) < 10 \\ -0.1 < l_2(r_{min})/l_0(r_{min}) < 0.1 \\ -0.1 < l_2(r_{max})/l_0(r_{max}) < 0.1 \end{cases} \\ 0 & \text{otherwise.} \end{cases} \tag{19}$$

which is motivated by the fact that the l_2 terms are a first-order correction to the spherical monopole $\Phi_{l=0,m=0}(r)$. Given that we do not expect the halo to be extremely flattened, the l_2 terms should contribute at most up to about 10 % to the total description of the system (this was tested for several flattened NFW profiles, and holds even up to a high flattening of q=0.3). Moreover, because we only directly constrain the forces and shape of the potential, $l_0(r_{min})$ and $l_0(r_{max})$ can be increased or decreased by an arbitrary integration constant. Hence, we restrict the $l_0(r_{min})$ term to be within a range of 0.1 to 10 times the initial value $l_{0,i}(r_{min})$. This indirectly also constrains $l_0(r_{max})$. For a similar reason, we constrain $l_2(r_{min})$ to be within a range of 0.1 to 10 times the initial value $l_{2,i}(r_{min})$. As an initial guess, I use the expansion of the default NFW halo (see Section 1.7.4) and add an offset which is a Gaussian distribution centred around zero with a width of 0.01 times the expansion parameters.

I let the MCMC run with 40 walkers for 2000 steps, after which it converged. The posterior distribution is shown in a corner plot in Fig. 32. As expected, the $l = 0$ terms are not strongly constrained but are strongly correlated. The derivatives, determining the shape of the potential but also directly the forces, are well constrained. Fig. 30 shows the distance between the two clumps as a function of integration time. For the best-fit BFE potential, the distance between the clumps over the past 0.6 Gyr is about equal to today's value ($\sim 185\,\mathrm{kpc\,km\,s^{-1}}$ versus $\sim 200\,\mathrm{kpc\,km\,s^{-1}}$). Hence, this outperforms the Default Potential, which has a lower average clump distance ($\sim 130\,\mathrm{kpc\,km\,s^{-1}}$). Clearly, the variation in the distance, and thus $L_\perp$, spans a much smaller range in the BFE potential ($\sim 50\,\mathrm{kpc\,km\,s^{-1}}$) than in the Default Potential ($\sim 150\,\mathrm{kpc\,km\,s^{-1}}$). This is a result of the fact that the resulting total potential's shape is roughly spherical in the region occupied by the Helmi Streams, as is illustrated in Fig. 29, which shows the total flattening of the best-fit BFE potential in comparison to the Default Potential. The best-fit BFE halo has a radially varying flattening. It compensates the more flattened inner part of the potential, where the disks dominate, by being more prolate there, which makes the total potential more spherical. The grey shaded area in Fig. 29, corresponding to the axis ratios of BFE halo's that have been randomly sampled from the MCMC chains, indicates that the Helmi Streams most strongly constrain the potential between $12 \lesssim R \lesssim 20$ kpc, as the range spanned in axis ratio is smallest.

The right panel of Fig. 29 shows the density profile of the best-fit BFE halo, which cannot be well fitted by an NFW potential due to the steep cut-off at higher radii. This is possibly a result of the steeply declining Eilers et al. 2019 rotation curve, which is fitted well, as is shown in Fig. 31. Moreover, the rotation curve becomes less constraining at larger radii, giving the BFE more freedom. Of course, beyond 25 kpc there are no longer any constraints from the rotation curve. Beyond that radius, the density actually goes to zero and then becomes negative, which is possible as the basis function expansion is in the potential, and we did not require a non-negative. The mass of the BFE halo within 20 kpc is $M_h(r < 20\,\mathrm{kpc}) = 0.1 \cdot 10^{12}\ M_\odot$, which corresponds to a total mass within 20 kpc, $M_{tot}(r < 20\,\mathrm{kpc}) = 0.2 \cdot 10^{12}\ M_\odot$, which is within the range of current estimates (Küpper et al. 2015; Malhan and Ibata 2019; Watkins et al. 2019; Posti and Helmi 2019). However, as the

[25]The choice of a low l_{max} and a low number of gridpoints is also justified by the fact that we are not using the BFE to represent, for example, an NFW halo. In that case, the accuracy of the BFE representation would be too low. Instead, however, the BFE halo is used to explore the shape of the halo, making it a potential object with a shape its own.

density goes to zero and becomes negative beyond 30 kpc, it is not possible to extrapolate the halo profile to radii farther out, calling for constraints at larger distances.

Overall, we can conclude that we succeeded in our objective to maximise the distance between the clumps using a BFE MCMC. The resulting potential is however not realistic, showing that one needs to be careful when imposing local constraints and defining a likelihood.

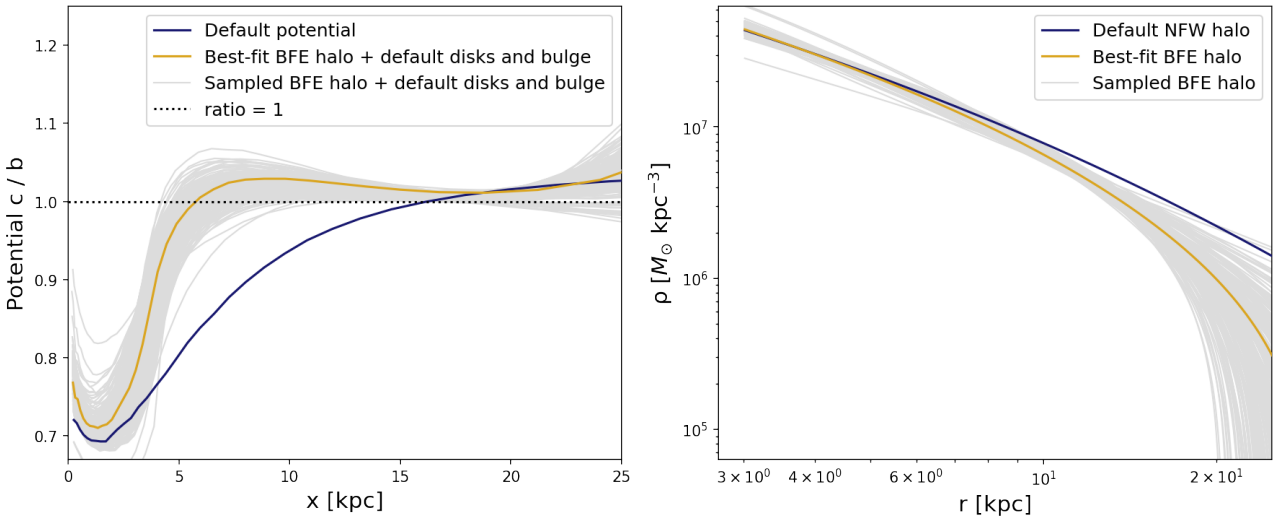

Figure 29: *Left panel:* Axis ratio of the Default Potential (dark blue, see Section 1.7.4) versus the total best-fit BFE potential (yellow), a sum of the default stellar disks, gas disks, bulge and the best-fit BFE halo, which shows that the total best-fit BFE potential is roughly spherical in the region occupied by the Helmi Streams. The light grey lines show the axis ratio of 200 potentials randomly sampled from the MCMC chains. *Right panel:* Density profile of the best-fit BFE halo versus the default halo. The best-fit BFE halo shows a steep cut-off in density at larger radii.

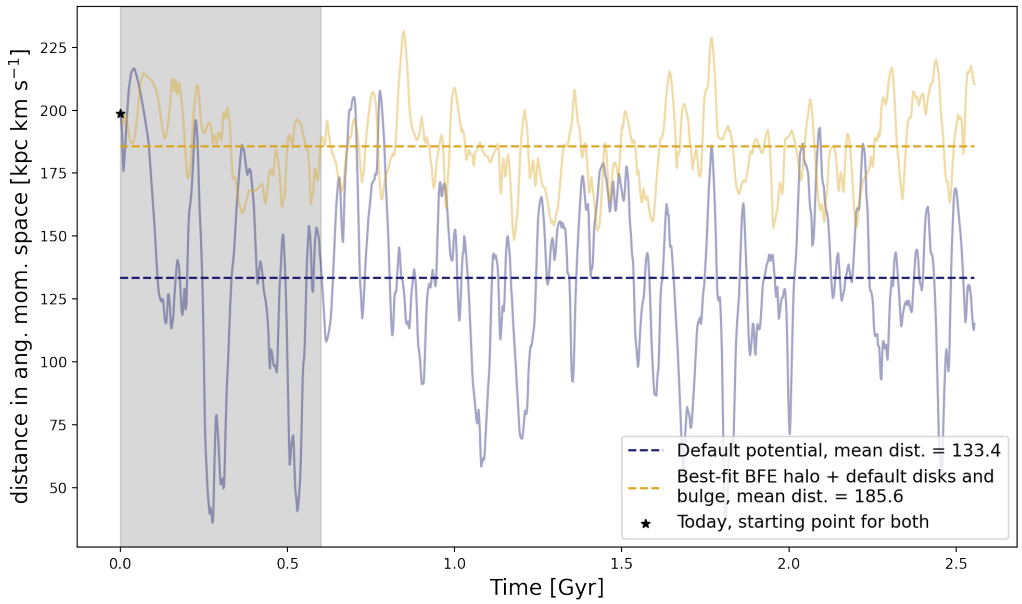

Figure 30: Distance between the two clumps in rotated angular momentum space as a function of integration time in the Default Potential (dark blue, see Section 1.7.4) and in the total best-fit BFE potential (yellow), a sum of the default stellar disks, gas disks, bulge and the best-fit BFE halo. The dashed lines show the mean distance in both potentials over an integration time of ~ 2.5 Gyr. The black star indicates the distance between the clumps that we observe today. The grey shaded area covers a range of 0.6 Gyr and corresponds to the integration time over which the mean distance between the two clumps was computed in the MCMC run.

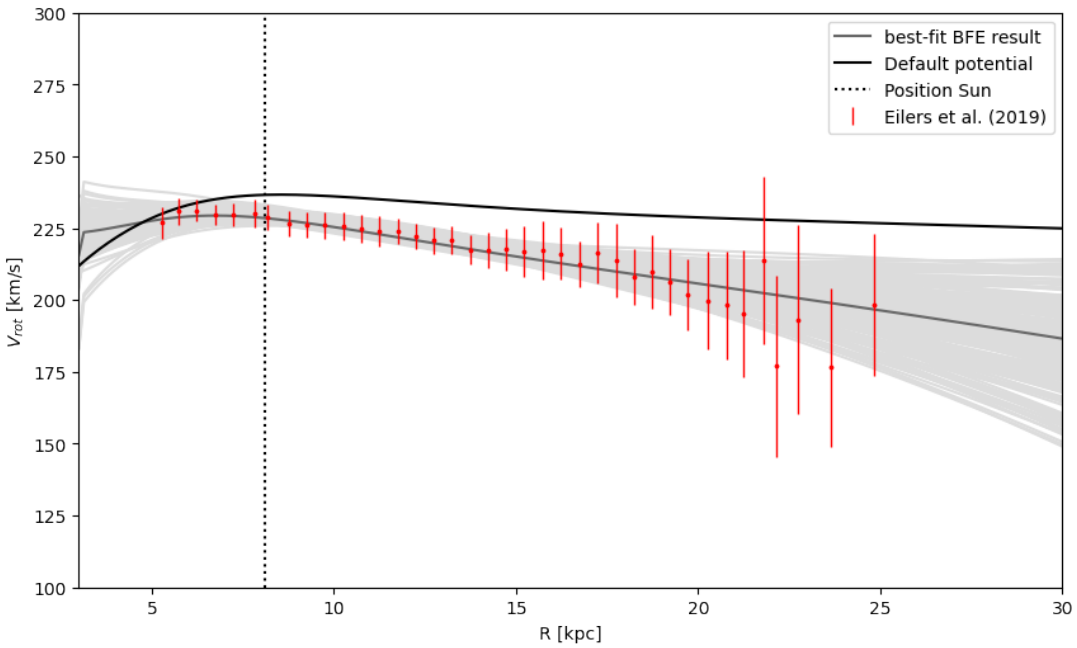

Figure 31: Rotation curve data from Eilers et al. 2019 (red) in its full extent, covering $5 < R < 25$ kpc (see Section 1.6). Overplotted in black is the rotation curve corresponding to the Default Potential (see Section 1.7.4). The rotation curve of the best-fit BFE potential, a sum of the default disks and bulge and best-fit BFE halo, is plotted in dark grey. The rotation curves corresponding to 200 potentials with characteristic parameters randomly sampled from the MCMC chains are shown in light grey.

3.4 Summary

Basis Function Expansions (BFE) are a promising way to explore the shape of the DM halo without the restrictions of a parametrised model. Due to the large amount of freedom, it is important to use good constraints.

We need only a relatively low number of terms and gridpoints to obtain a BFE that is accurate enough. For example, $l_{max} = 2$ and a gridsize of 2 give an accuracy on the percentage level for Gyr timescales. As a test, I have shown that an NFW profile can be turned into a Hernquist profile by varying the coefficients and their derivatives at the gridpoints using an MCMC. As an application, I show that I can obtain a potential that maximises the distance between the Helmi Streams' clumps using a set of realistic constraints on the mass distribution (in the form of rotation curve data) and the shape of the potential (in the form of the distance between the two clumps). The total flattening of this potential is close to spherical within the region occupied by the Helmi Streams and the potential has a total mass $M_{tot}(r < 20\,\mathrm{kpc}) = 0.2 \cdot 10^{12} M_{\odot}$, which agrees with current estimates. However, the potential's density profile goes to zero and becomes negative at radii beyond the observational constraints, showing that constraints at larger distances are needed. From these experiments, we can thus conclude that by varying the coefficients of a `Multipole` potential we obtain the freedom to reshape that potential, given the right constraints.

Within this chapter, I only explored low-order axisymmetric BFE that are relatively close to spherical symmetry. For a good description of more complex axisymmetric shapes, a higher number of l_{max} and a larger number of gridpoints is needed. It would be interesting to use this method in the case of a triaxial or asymmetric halo, though this will increase the number of free parameters.

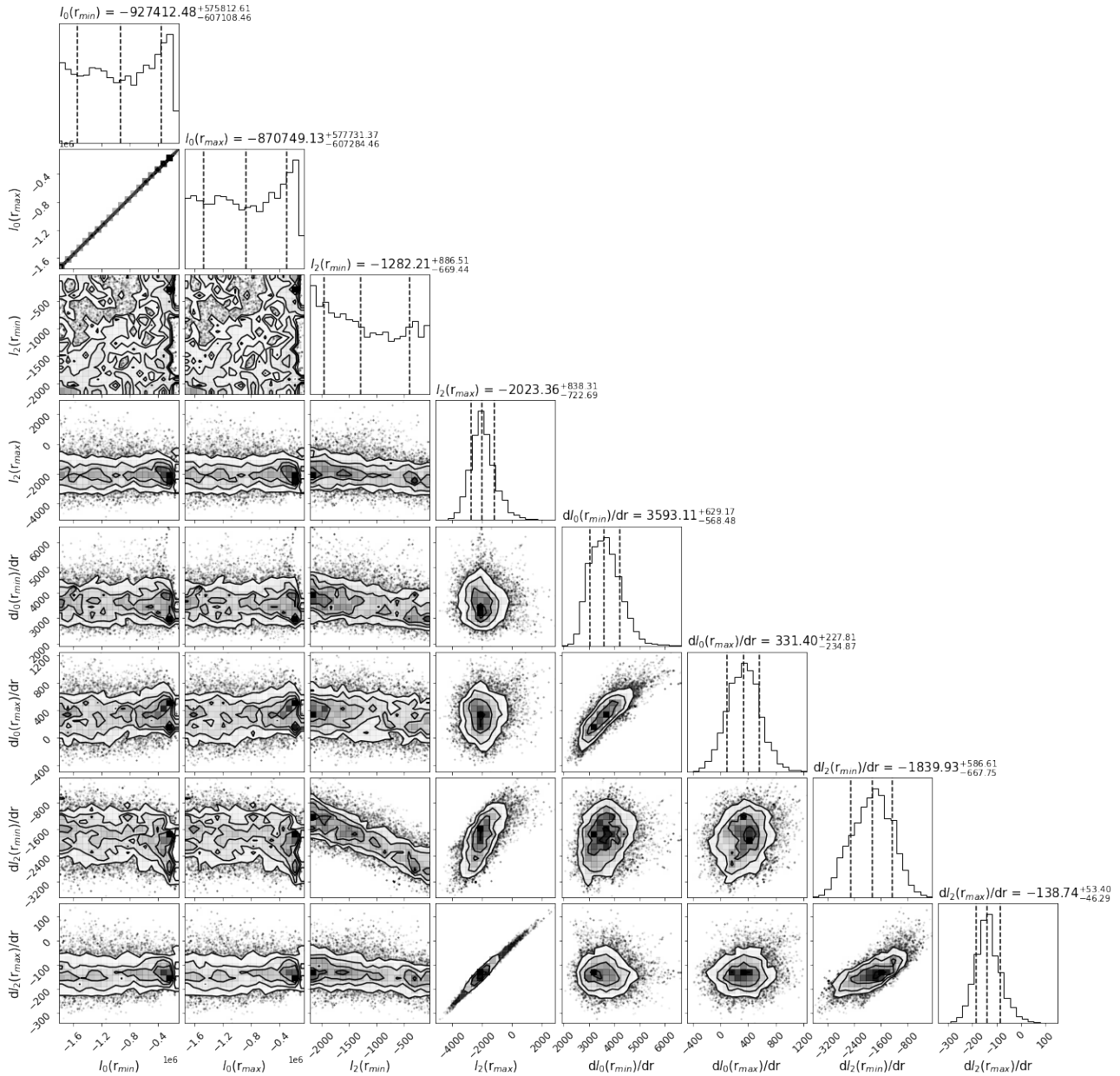

Figure 32: Posterior distribution of the coefficients and their derivatives at the two gridpoints $r_{min} = 3$ kpc and $r_{max} = 40$ kpc. As expected, $l_0(r_{min})$ and $l_0(r_{max})$ are strongly degenerate. The set of constraints only directly constrains the forces/mass distribution and the shape of the potential, i.e. the derivatives of the coefficients. Therefore, $l_0(r_{min})$ and $l_0(r_{max})$ can be increased or decreased by an arbitrary integration constant, explaining why both occupy such a large parameter space.

4 Explaining the Gap: Chaos!

The gap between the Helmi Streams' clumps can be maintained in a potential that is roughly spherical, but the question remains how a gap can be created. As the gap is an empty region in $L_\perp$, which is not a fully conserved quantity in a non-spherical potential, a mechanism that makes stars diffuse out of the gap region is required. This could possibly happen in a potential that hosts a stochastic region in between the two clumps. A stochastic region is a region that hosts chaotic orbits, which are orbits that do not have a third integral of motion, leading to orbital diffusion. This section aims to show that the variation in $L_\perp$ induced by stochasticity could possibly explain the gap. First, Section 4.1 gives an introduction to chaotic orbits and the regions of the potential in which they are hosted. Next, Section 4.2 discusses several chaos indicators. By generating stars in the gap, I show in Section 4.3 that a region in phase-space close to the Helmi Streams hosts a resonance which is surrounded by a stochastic layer. In Section 4.4 I show that a gap can be formed over time for an ensemble of stars that occupies the phase-space surrounding this layer.

4.1 Chaoticity Explained

A regular orbit in three dimensions is determined by three degrees of freedom: its apocenter, pericenter and height z_{max} above the midplane, or its fundamental frequencies Ω_ϕ, Ω_R and Ω_z or its L_z, $L_\perp$ and E. These three sets of parameters can all be used to describe an orbit and are related to each other in a non-linear way. Broadly speaking, orbits can be separated into three categories:

1. Regular orbits, including resonant orbits
2. Sticky or sticky-chaotic orbits
3. Chaotic/irregular orbits

A regular orbit has three isolating integrals of motion, which restrict the orbit to a subspace of phase-space (Binney and Tremaine 2008), while a (sticky-)chaotic orbit only has two, leading to orbital diffusion. In the case of an axisymmetric time-independent potential, L_z and E are classical, isolating integrals of motion. The third integral of motion is a non-classical integral of motion which is likely related to $L_\perp$. In the case of a resonant orbit, which is a regular orbit, two or three fundamental frequencies are commensurate, meaning that one is a multiple of the other. This will reduce the dimensionality of the orbit, as the number of degrees of freedom is reduced. If a star is on a chaotic orbit, it does not have a third integral of motion. It can then be recognised as being chaotic by looking at the parameters that describe the orbit: large variations in $L_\perp$, a change in orbital frequency, or a changing z_{max}, apo- or pericenter.

Sticky orbits are orbits that exhibit chaotic behaviour over long timescales: a star can be trapped around a regular orbit for a long time (10's or 100's of Gyr) before it escapes to become trapped around another regular orbit. Sticky orbits can thus appear to be regular orbits for long periods of time (Contopoulos and Harsoula 2010; Maffione et al. 2015; Price-Whelan et al. 2016b), while they are actually chaotic. In this work, we will consider stars that take more than 10 Gyr to show chaotic behaviour to be sticky.

Stochastic regions can be found in near- or non-integrable potentials, and most potentials are of this type[26]. Even simple models like the Miyamoto Nagai potential host stochastic regions (Pascale et al. 2022). In more realistic Galactic models, the bar, which makes the inner Galactic potential triaxial and time-dependent, has been found to give rise to chaotic orbits (e.g. Manos and Athanassoula 2011). This stochasticity has been invoked as explanation for the peculiar morphology and kinematics of the Ophiuchus stream orbiting the inner Galaxy (Price-Whelan et al. 2016a). However, since the Helmi Streams probe a region of the potential beyond 5 kpc, it is unlikely that the bar has a large effect.

Other regions where chaotic orbits can be found are at the edge of a family of resonantly trapped orbits[27] (Binney and Tremaine 2008, p. 257). Such a region is called a separatrix, and is the boundary between orbit families. As shown by Yavetz et al. 2021, stellar streams on orbits near separatrices tend to diffuse more quickly in configuration space (stream fanning) and frequency space than streams on a single orbital family (see also their Fig. 2). Also regions of resonance overlap can give rise to chaotic behaviour, as two or more resonances are trying to trap the orbit at the same time (Binney and Tremaine 2008). The amount of chaotic orbits present in a Galactic potential depends on the potential's characteristic parameters, for example the flattening of the DM halo (see e.g. Caranicolas and Zotos 2010; Zotos 2014).

[26] An integrable potential admits the transformation to action-angle variables, see Appendix E. In an integrable potential, all orbits are regular. The Default Potential is a non-integrable potential and thus hosts stochastic regions.

[27] See Fig. 1 in Price-Whelan et al. 2016b for an illustration.

In the context of the Helmi Streams, we observe that the Helmi Streams can be separated into two clumps in angular momentum space, of which one is more phase mixed than the other. This is clear especially in velocity and frequency space. We observe a splitting in the orbital frequency ratio between the hiL and loL clump, with the hiL clump lying closer to the $\Omega_\phi : \Omega_z$ resonance than the loL clump. While separatrices next to resonances can lead to chaotic behaviour, resonances themselves can stabilise and resonantly trap orbits. A resonant orbit is a two-dimensional structure, but a resonantly trapped orbit has a finite libration amplitude around the resonant orbit, making it a three-dimensional structure (Binney and Tremaine 2008, p. 265). A possible explanation for the observed behaviour of the hiL and loL clump could thus be that the hiL clump is resonantly trapped by the $\Omega_\phi : \Omega_z$ is $1:1$ resonance, stabilising their orbits, while the loL clump is located slightly off-resonance, perhaps on a separatrix, explaining its more diffuse frequency distribution and more strongly phase mixed features. This would tie in with the observations by Yavetz et al. 2021 but also Mestre et al. 2020, who find that chaos enhances the diffusion of streams in configuration space and velocity. However, it could also be that a second resonance is involved.

4.2 Chaos Indicators

How can we recognise a chaotic orbit in an efficient way? I will illustrate this using a sticky orbit that I found near the region in phase-space occupied by the Helmi Streams. It is a star with a high kinetic energy located at the left edge of the gap. The orbit mapped in cylindrical coordinates is shown in Fig. 33. In the first 100 Gyr, the star seems to follow a regular pattern. However, somewhere around 100 Gyr, the star jumps to another close-by stable orbit and thus between $100 - 200$ Gyr its orbital pattern differs from the first 100 Gyr.

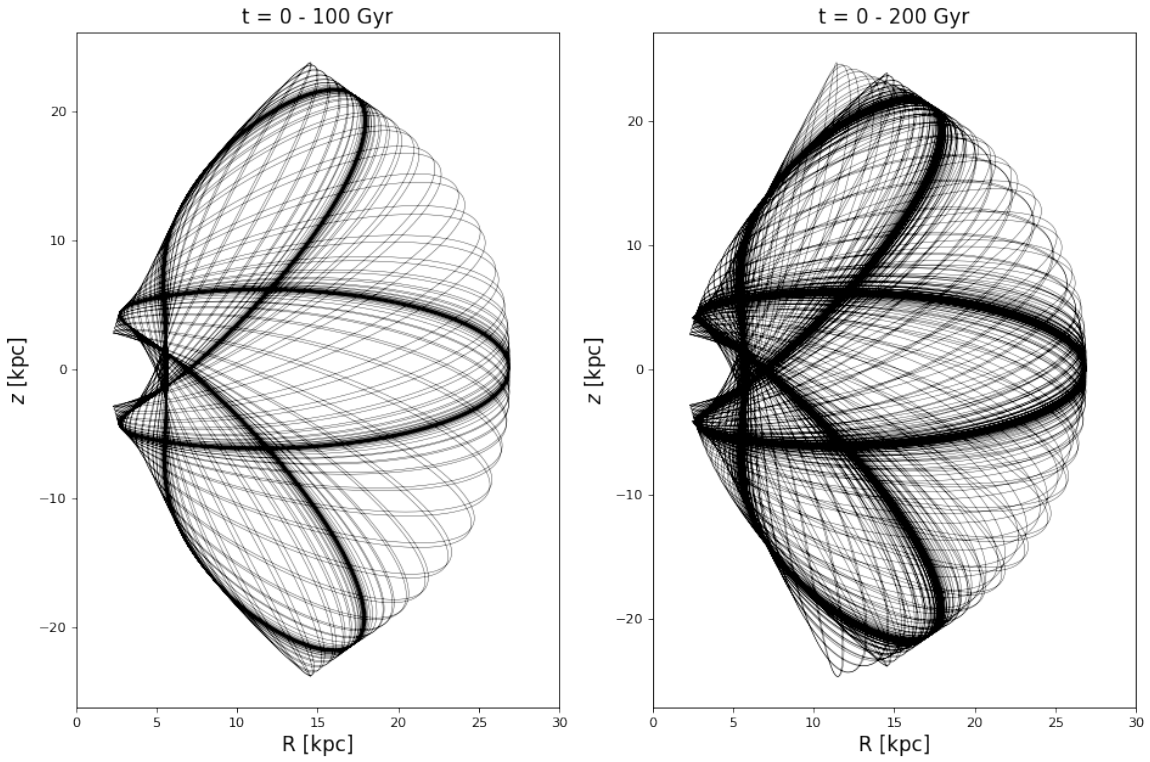

Figure 33: *Left panel*: Sticky orbit over an integration time of 100 Gyr and in the Default Potential (see Section 1.7.4). *Right panel*: Similar as the left panel but over an integration time of 200 Gyr. In the first 100 Gyr, the star seems to follow a regular pattern. However, somewhere around 100 Gyr, the star jumps to another close-by stable orbit and thus between $100 - 200$ Gyr its orbital pattern differs from the first 100 Gyr.

Another visual way to explore whether an orbit is chaotic is by plotting its surface of section (SoS in short, see Section 2.4.2). The individual points in a SoS are called consequents. For a regular orbit, the consequents appear to lie on a smooth curve, called the invariant curve of the orbit, which can for example be a loop (see e.g. Fig. 18). The consequents of a chaotic orbit will instead fill the plane. The SoS of the sticky orbit is shown in Fig. 34. Though the plane is not filled, we do see locations where the consequents seem to pile up. Comparing the left and right panel, those are exactly the locations where the transition to the other stable orbit takes place. The transition to the other stable orbit is also apparent in a change in $L_\perp$ and frequency space, see Fig. 35. The star jumps from having $\Omega_z : \Omega_R$ slightly below the $2:3$ resonance to slightly above it. Layers

around resonances are known to be stochastic, as is illustrated by this example. The change in orbital frequency shows that the frequency diffusion rate, which is the difference in orbital frequency between consecutive parts of an orbit, can also be used as an indicator of chaos, as it is large for a chaotic orbit but zero for a regular orbit (Price-Whelan et al. 2016b).

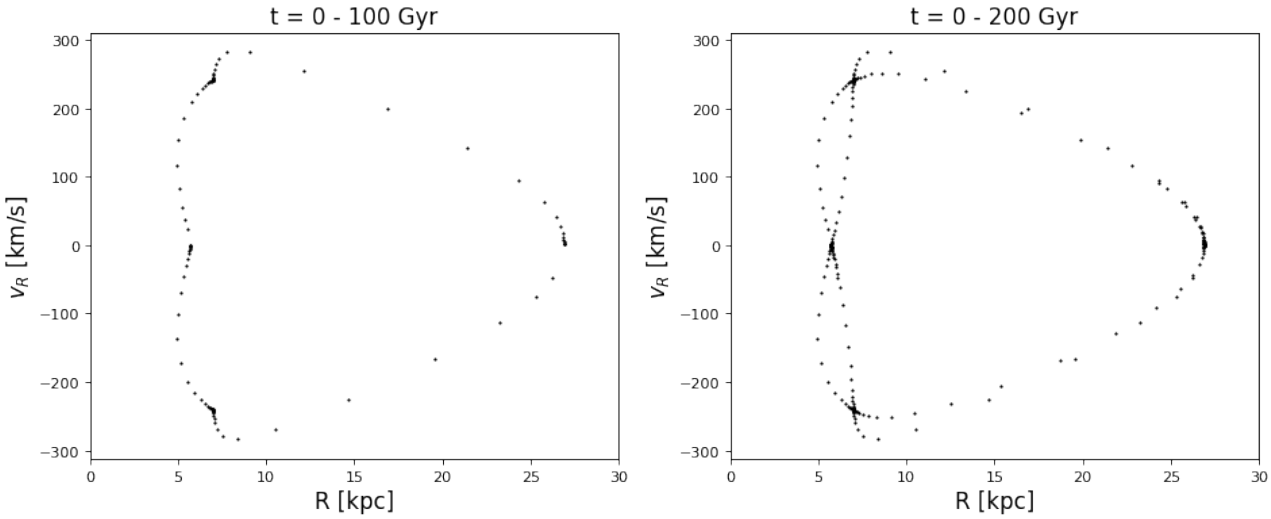

Figure 34: Surface of section of a sticky orbit over an integration time of 100 Gyr (*left panel*) and 200 Gyr (*right panel*). Around $t \sim 105$ Gyr, the star jumps to another close-by semi-stable orbit so its surface of section changes.

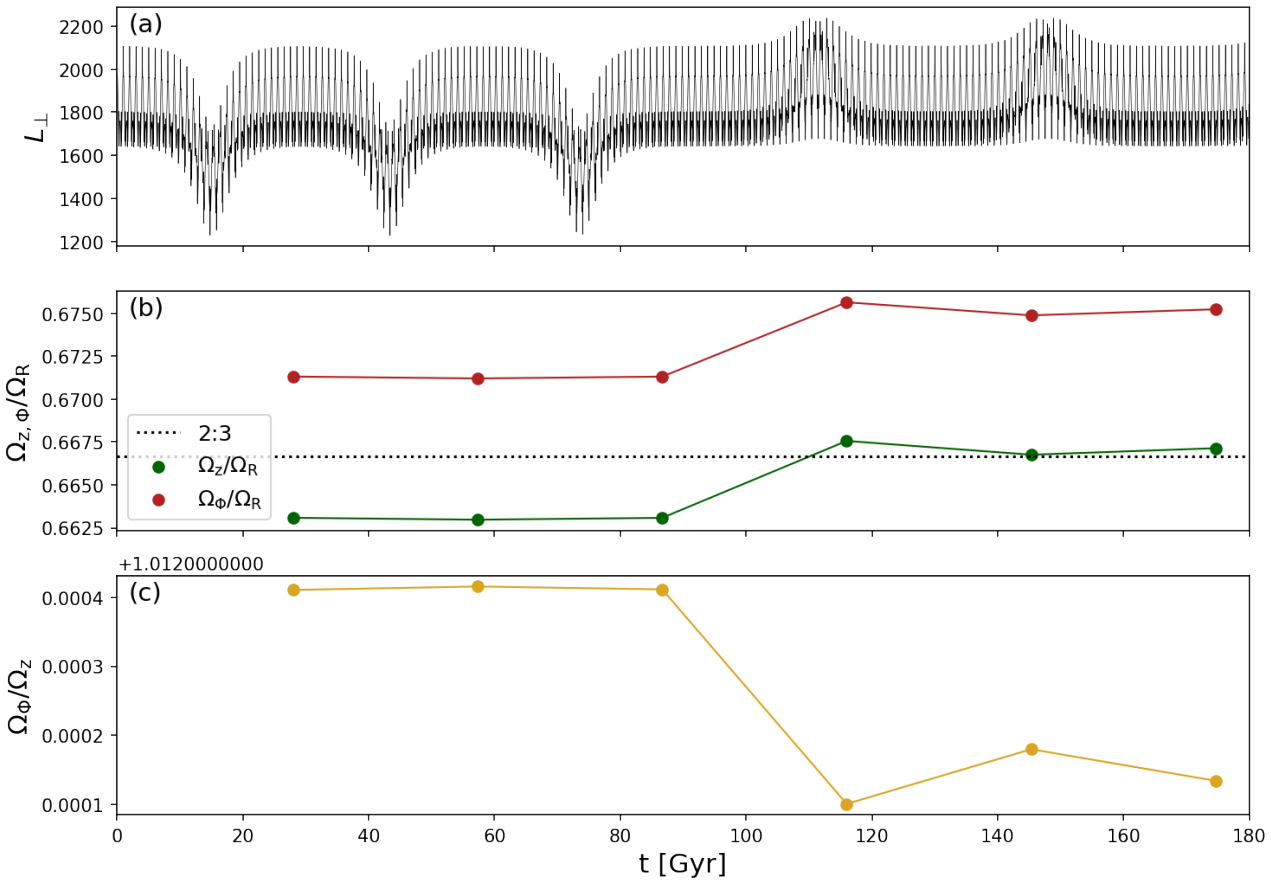

Figure 35: *Panel (a): $L_\perp$* and *panel (b), (c):* the fundamental frequency ratios as a function of time. The frequency ratios are computed for time intervals of 30 Gyr (i.e. $0-30$, ..., $150-180$ Gyr). Around 100 Gyr, the star jumps to another orbit, which can be seen as a transition in $L_\perp$ and the frequency ratios.

The methods to detect chaotic behaviour introduced so far either require visual inspection (SoS or mapping the orbit), are not unambiguous indicators of chaos (variation in $L_\perp$) or are computationally expensive (frequency diffusion rate). A chaos indicator that is in that sense superior is the Lyapunov exponent Λ, or largest Lyapunov exponent. Take an orbit $\vec{x}(t)$ and an orbit infinitely close to it, $\vec{x} + \vec{w}(t)$, where $\vec{w}(t)$ is the so-called deviation vector. Λ then measures the variation of $\vec{w}(t)$ over time,

$$\Lambda \equiv \lim_{t\to\infty} \frac{\ln |\vec{w}|}{t} \tag{20}$$

For a regular orbit, $\vec{w}(t)$ grows linearly with time, while for a chaotic orbit, $\vec{w}(t)$ grows exponentially (Vasiliev 2013; Binney and Tremaine 2008, p. 262). In practice, however, we cannot integrate the orbit for an infinitely long time, and therefore one usually resorts to the finite-time estimate of the Lyapunov exponent. For a time interval when the orbit is regular (this can also be an orbit that is chaotic on long timescales, such as sticky orbits), $\ln |\vec{w}|/t$ will fluctuate around a constant value. When, for a chaotic orbit, the exponential growth of $\vec{w}$ starts, Λ is estimated as the average value $\ln |\vec{w}|/t$ over the period of exponential growth. If no exponential growth occurs, Λ is set to zero. This finite-time estimate of the Lyapunov exponent has been shown to perform similarly to the frequency diffusion rate (Vasiliev 2013), which are both good indicators of chaos. However, their predicted timescales do not capture the importance of chaos for the density evolution of stellar streams, as stellar streams on chaotic orbits tend to diffuse faster than predicted (Price-Whelan et al. 2016b). Yavetz et al. 2021 showed that this could possibly be due to separatrix divergence.

4.3 The Behaviour of an Ensemble of Stars near the Gap in the Default Potential

An important question is to answer how the gap formed, as it possibly holds further clues about the Galactic potential. To investigate this, I take the following approach. I densely sample initial conditions in the gap (L_z, $L_\perp$) in such a way that the positions (x, y, z) and energies E of the generated stars follow the distribution of the Helmi stream stars in the extended sample. For the positions x and y and energy E, I sample randomly assuming that the distributions follow Gaussians. I sample z uniformly over the range of observations, and I sample L_z and $L_\perp$ uniformly in the gap. The velocities follow from $v_\phi = -L_z/R$ and v_R and v_z follow from the definition of energy and $L_\perp$ (see Eq. 3 and 5). Given R, ϕ, z, v_ϕ, E and $L_\perp$, we can solve for v_R and v_z using `scipy.optimize.fsolve`. I populate the clumps with negative and positive v_z following a 2 : 1 ratio (Koppelman et al. 2019b). The resulting phase-space, energy, and angular momentum distribution are shown in Fig. 36. I generated almost 10.000 initial conditions (IC).

A chaotic orbit will exhibit a large variation in $L_\perp$, so in order to identify possibly chaotic IC I integrate them for 100 Gyr and check their variation of $L_\perp$ over time. If this variation is larger than a certain threshold (estimated empirically), I inspect this IC more closely by plotting their SoS. Out of the almost 10.000 IC, there are about 980 IC that satisfy the threshold. A subset of those correspond to IC that are resonantly trapped by the $\Omega_z : \Omega_R$ is 2 : 3 resonance. These IC trace out islands in their SoS and are plotted in a cyan and lime edgecolour in Fig. 36. I find one IC that can be classified as a sticky orbit, which is the IC discussed in Section 4.2. This IC is shown with a magenta edgecolour in Fig. 36. The IC that are resonantly trapped by the $\Omega_z : \Omega_R$ is 2 : 3 resonance are predominantly found at the high energy and relatively low L_z and $L_\perp$.

To illustrate what it means for an orbit to be resonantly trapped, I select two IC that are resonantly trapped by the $\Omega_z : \Omega_R$ is 2 : 3 resonance and show their behaviour in configuration space in Fig. 37 and their SoS in Fig. 38. Both orbits are three-dimensional structures because they have a finite libration amplitude around the resonant orbit (Binney and Tremaine 2008), but they are clearly restricted to a subspace of configuration space (see the (x, z) and (y, z) plane) and velocity space (see the SoS), even after 100 Gyr of integration time. This libration amplitude is in fact larger for the orange orbit than the blue orbit, as the blue orbit is closer to the 2 : 3 resonance (10^{-6} instead of 10^{-2} removed from it). This can also be appreciated from Fig. 37, which shows that the blue orbit fills a smaller volume (this is particularly apparent in the (x, y) projection). If an orbit is truly a resonant orbit, it will be restricted to a 2D surface as it is then determined by only two degrees of freedom. Thus, if the libration amplitude would go to zero, the two orbits would reduce to a 2D structure in configuration space.

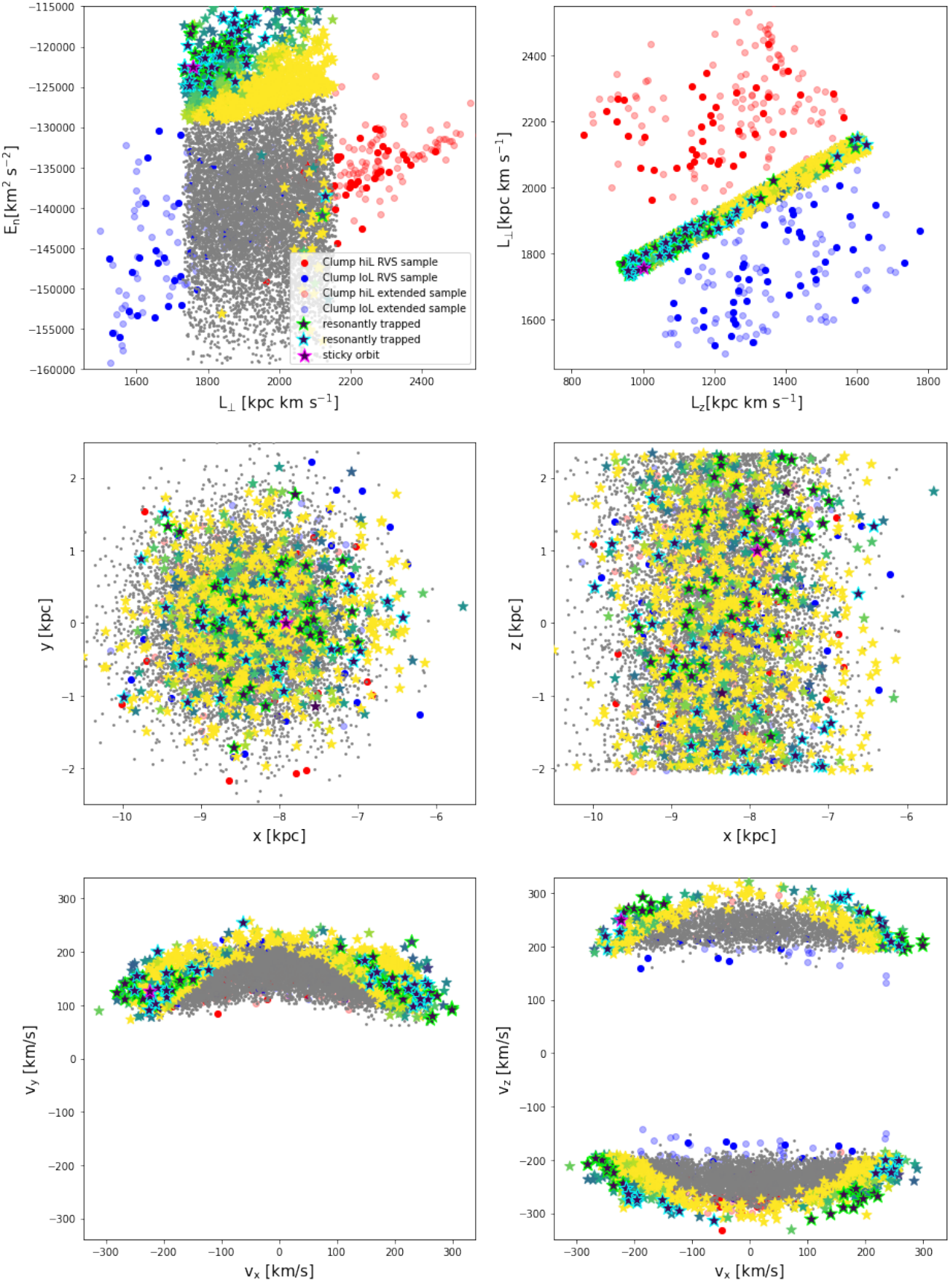

Figure 36: Phase-space, energy, and angular momentum distribution of almost 10.000 generated initial conditions overlaid on the hiL clump stars and loL clump stars in the *Gaia* EDR3 RVS sample and extended sample. The IC with a large variation in $L_\perp$ have been plotted in a colourmap showing how far away from the 2 : 3 resonance the stars are, the darker the closer. The darkest colour indicates that the distance from 2 : 3 is less than 0.0001, and the lightest colour indicates that the distance from 2 : 3 is more than 0.01 in frequency space. Stars that are resonantly trapped are plotted with a lime or cyan edgecolour, which differentiates between the orientation of the orbit. The sticky orbit is plotted with a magenta edgecolour.

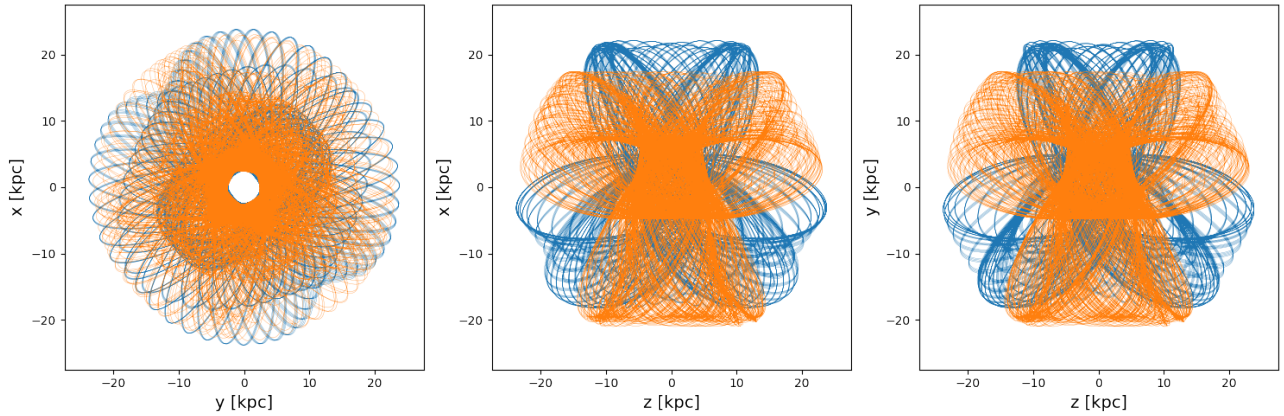

Figure 37: Map of two resonantly trapped orbit in configuration space over an integration time of 200 Gyr in the Default Potential (see Section 1.7.4). The $\Omega_z : \Omega_R$ is $2:3$ resonance is restricting the orbits to a subspace of phase-space.

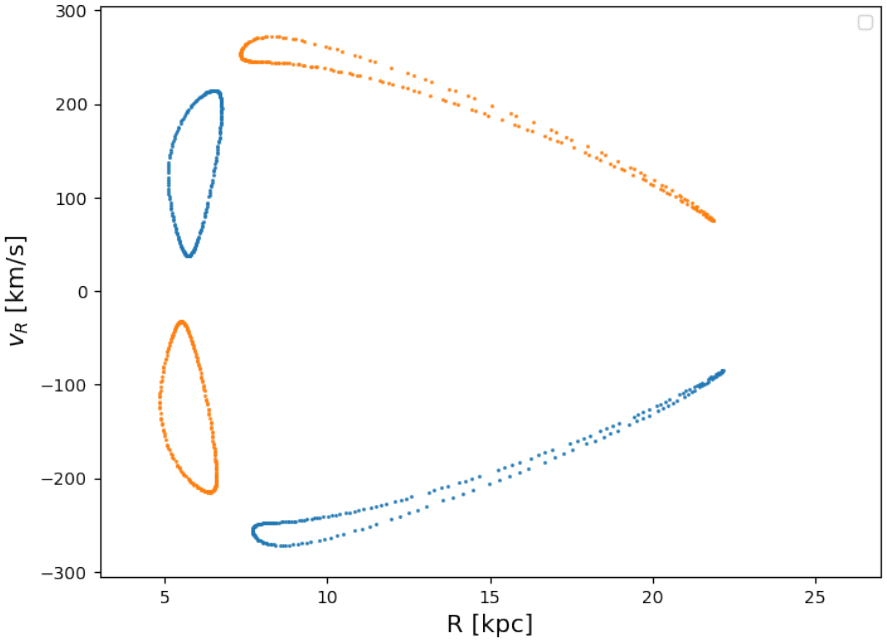

Figure 38: SoS of two resonantly trapped orbit over an integration time of 200 Gyr in the Default Potential (see Section 1.7.4). The resonance is restricting the orbits to a subspace in phase-space. If the stars were exactly on the $\Omega_z : \Omega_R$ is $2:3$ resonance, they would trace out a dot in the SoS. We now see that they are resonantly trapped with a finite libration amplitude.

4.4 Zooming in around the 2 : 2 : 3 Resonance

Having found a star close to the 2 : 2 : 3 resonance that exhibits a large variation in $L_\perp$, I generate an ensemble of 9 stars with similar initial conditions. These stars have E = -122500 km^2 s^{-2}, L_z = 1000km^2 s^{-1}, 7.5 $\leq R \leq$ 8.3 kpc, z = 1 kpc, $\phi = \pi$, v_z = 250km s^{-1}. v_ϕ and v_R follow from the definition of energy (see Eq. 3) and $L_z = -Rv_\phi$. Their positions in phase-space, energy and angular momentum are shown in Fig. 40. The 9 stars have $\Omega_\phi : \Omega_z \sim 1.012$ and span a range of $0.661 \leq \Omega_z : \Omega_R \leq 0.672$. Fig. 39 shows their surfaces of section, which shows that the stars closest to the $\Omega_z : \Omega_R$ is 2 : 3 resonance have an invariant curve that traces out four islands that touch at $R \sim 7.4$ kpc, $v_R \pm 230$ km s^{-1}.

Fig. 41 shows the evolution of the ensemble over time in (L_z, $L_\perp$). Because the stars closer to the 2 : 3 resonance exhibit a larger variation in $L_\perp$ relative to the stars farther away from the 2 : 3 resonance, over time a gap is formed. This gap is formed on small enough timescales ($\sim$ 6 Gyr) for it to be able to explain the gap observed in the Helmi streams. This therefore forms a possibly stringent constraint on the Galactic potential: it should to host a chaotic region at the position of the gap observed in the Helmi streams. Furthermore, the location of this ensemble of stars is not far from that of the gap for the Default Potential. This suggests that small modifications of it could potentially result in a Milky Way mass model that reproduces the observations.

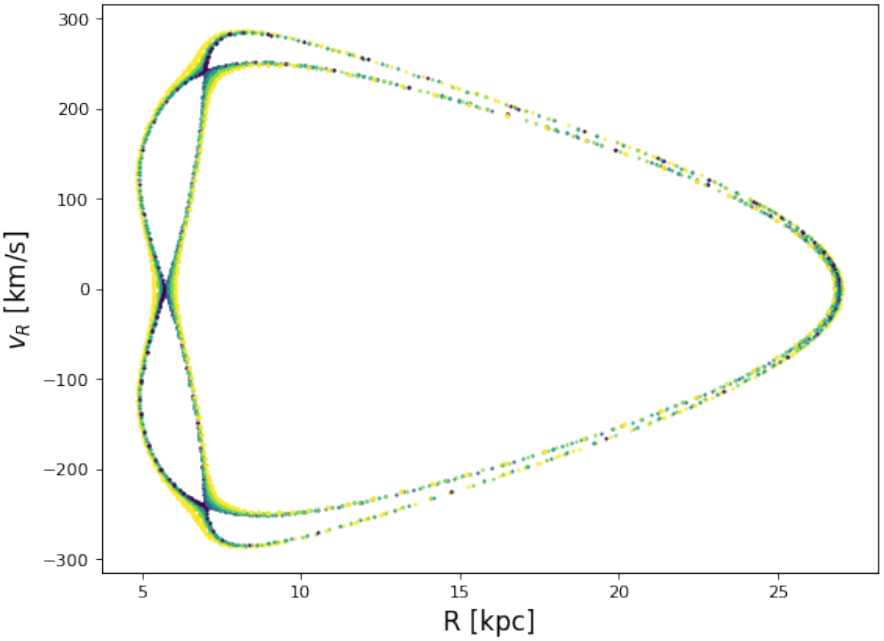

Figure 39: Surface of section for an integration time of 200 Gyr for stars with E = -122500 km^2 s^{-2}, L_z = 1000km^2 s^{-1}, 7.5 $\leq R \leq$ 8.3 kpc, z = 1 kpc, $\phi = \pi$, v_z = 250km s^{-1}. v_ϕ and v_R follow from the definition of energy and L_z. The colours indicate how far away from the $\Omega_z : \Omega_R$ is 2 : 3 resonance the stars are, the darker the closer, where the darkest colour indicates that the distance from the 2 : 3 resonance is less than 0.002, and where the lightest colour indicates that the distance from the 2 : 3 resonance is more than 0.005 in frequency space.

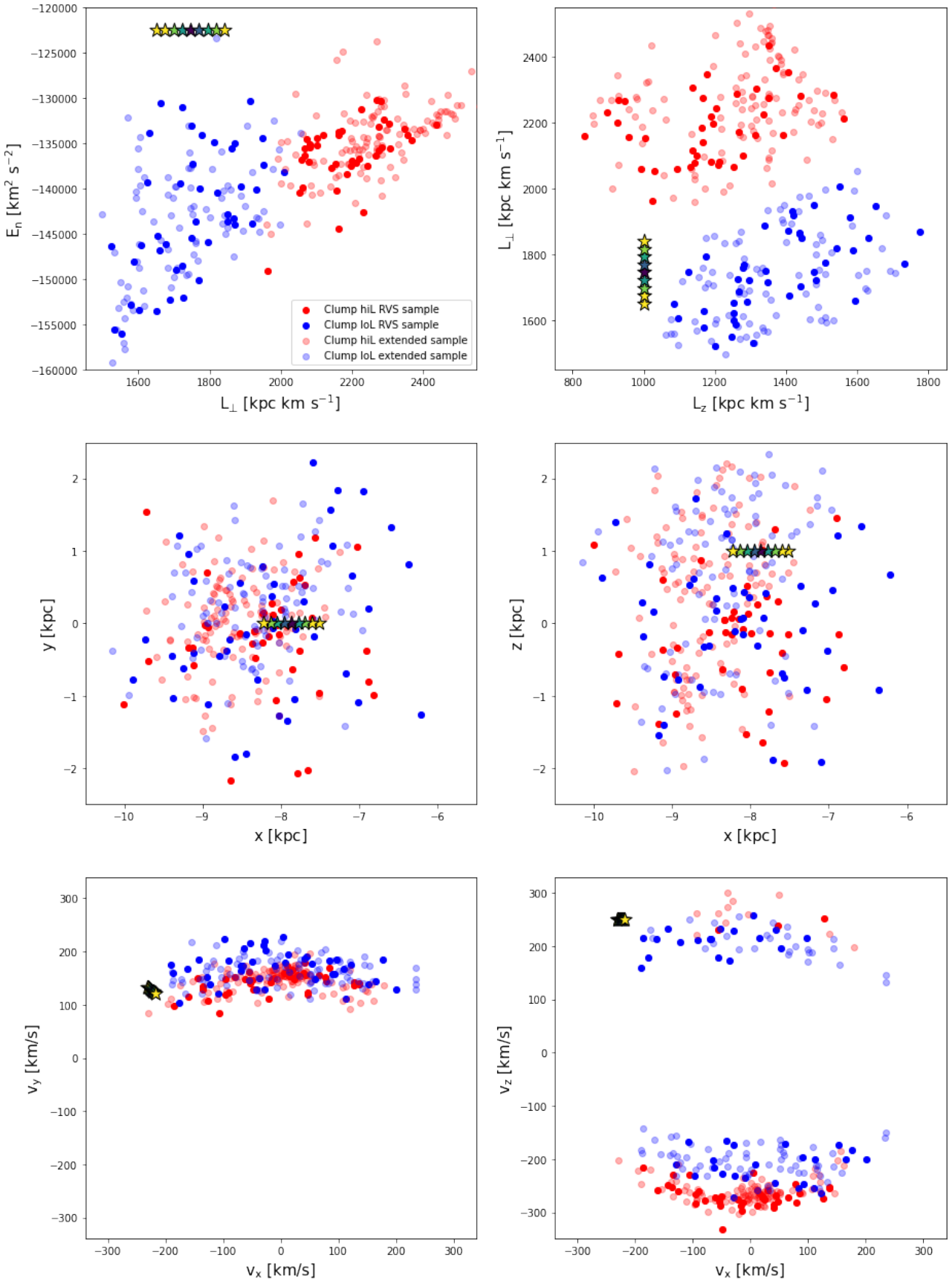

Figure 40: Phase-space, energy, and angular momentum distribution of an ensemble of 9 stars close to the 2 : 2 : 3 resonance with respect to the hiL clump stars (red) and loL clump stars (blue) in the Default Potential (see Section 1.7.4). The stars have E = -122500 km^2 s^{-2}, $L_z = 1000$km^2 s^{-1}, $7.5 \leq R \leq 8.3$ kpc, $z = 1$ kpc, $\phi = \pi$, $v_z = 250$km s^{-1}. v_ϕ and v_R follow from the definition of energy and L_z. The colours indicate how far away from the $\Omega_z : \Omega_R$ is 2 : 3 resonance the stars are, the darker the closer, where the darkest colour indicates that the distance from the 2 : 3 resonance is less than 0.002, and where the lightest colour indicates that the distance from the 2 : 3 resonance is more than 0.005 in frequency space.

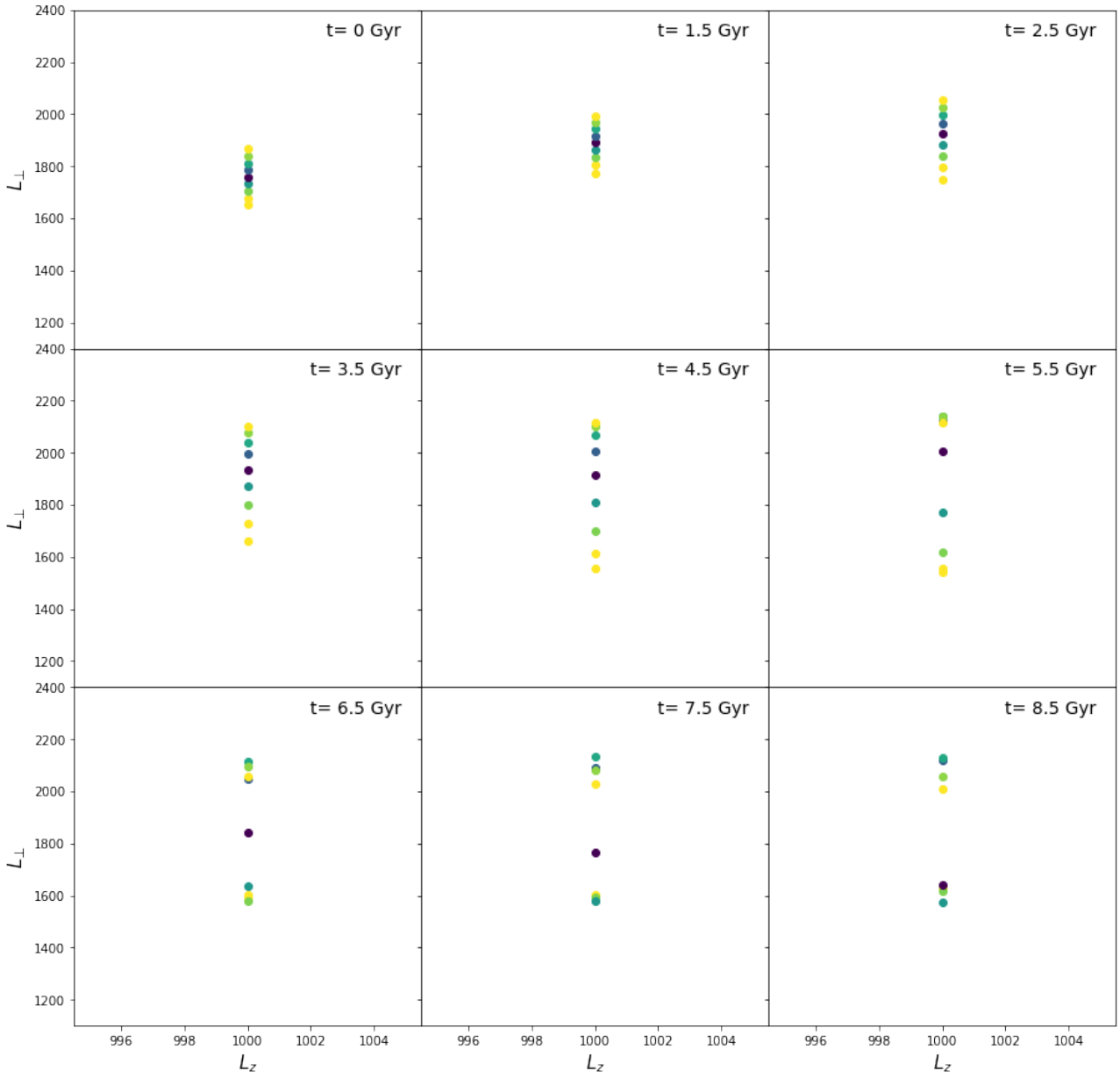

Figure 41: The position of the ensemble of 9 stars in L_z, $L_\perp$ space over time. The colours indicate how far away from the $\Omega_z : \Omega_R$ is 2 : 3 resonance the stars are, the darker the closer, where the darkest colour indicates that the distance from the 2 : 3 resonance is less than 0.002, and where the lightest colour indicates that the distance from the 2 : 3 resonance is more than 0.005 in frequency space. Because the stars closer to the 2 : 3 resonance exhibit a larger variation in $L_\perp$ relative to the stars farther away from the 2 : 3 resonance, over time a gap is formed.

5 Chaos: a constraint on the Galactic potential

An empty region in angular momentum space can possibly be the result of a stochastic region in the potential. Therefore, to explain the gap between the Helmi Streams' clumps, we can try to find a potential which hosts a stochastic region at the right location, that is in between the clumps. In Section 4 I found that the $\Omega_z : \Omega_R$ is $2:3$ resonance resides in the proximity of the region of phase-space occupied by Helmi Streams but at higher energy. The $2:3$ resonance's separatrix seems to give rise to chaotic behaviour, while the gap can be maintained over time if the $\Omega_\phi : \Omega_Z$ is $1:1$ resonance overlaps with the hiL clump. Thus, we require a potential in which the $2:2:3$ resonance overlaps with the hiL clump. An even stricter constraint could be to let the $2:2:3$ resonance overlap with the kinematically cold subclump (see Section 2.5). Resonances can trap orbits and slow down their dynamical evolution (see Section 2.4.2). Hence, the $2:2:3$ resonance could also explain why the subclump seems so dynamically cold, even in comparison to the hiL clump.

Given that the orbital frequencies depend on the underlying gravitational potential, we can try to modify the characteristic parameters of the potential in such a way that the $2:2:3$ resonance overlaps with the kinematically cold subclump. The Default Potential is our starting point, which means that $\Omega_\phi : \Omega_z$ should be kept fixed on the $1:1$ resonance, while $\Omega_z : \Omega_R$ should be decreased, as it is around ~ 0.7 in the Default Potential[28]. It is instructive to first develop an intuition of what properties of the potential each of the fundamental frequencies is sensitive to (this is explored in more detail in Appendix B and C). For example, of the three fundamental frequencies, Ω_z is most sensitive to a change in disk mass. By making the disk heavier, the vertical force will increase, which decreases the orbital period and therefore increases the orbital frequency Ω_z. The ratio $\Omega_z : \Omega_R$ will then increase, while $\Omega_\phi : \Omega_z$ decreases. Similarly, Ω_z is sensitive to the flattening of the potential, as it affects the distribution of mass in the vertical direction. On the other hand, Ω_R is mainly sensitive to the mass enclosed within the orbit, which is measured by the rotation curve. If the mass enclosed increases, the radial force increases, which decreases the orbital period and therefore increases the orbital frequency Ω_R. The ratio $\Omega_z : \Omega_R$ will then decrease. In summary, $\Omega_\phi : \Omega_z$ is most sensitive to a variation in the flattening of the potential (and thus q or the disk mass), via Ω_z, while $\Omega_z : \Omega_R$ is more sensitive to the mass enclosed, via Ω_R, and to the mass of the disk, via Ω_z.

Milky Way potential models from the literature do not get the subclump on the $2:2:3$ resonance (see also Appendix C), and therefore I resort to varying the parameters of the Galactic potential using an MCMC in Section 5.1. I map the resonances in the Default Potential and the " $2:2:3$ potential" in Section 5.2. Finally, in Section 5.3, I use the BFE method (developed in Section 3) to investigate how well a more freely varying axisymmetric description is able to satisfy the observationally desired constraints.

5.1 Getting the Streams on the $2:2:3$ Resonance

To investigate whether we can modify the Galactic potential in such a way that the $2:2:3$ resonance coincides with the hiL clump, or even better, the kinematically cold subclump, we vary five parameters of the McMillan 2017 potential model in a MCMC, $\vec{\theta} = \{q, R_{d,thin}, R_{d,thick}, r_s, \rho_{0,halo}\}$. The mass of the stellar disks is kept fixed. We parametrise $\rho_{0,halo}$ in a more intuitive way as

$$M_{spherical}(r < 20\text{kpc}) = 4\pi\rho_{0,halo} r_s^3 \left[\ln\left(1 + \frac{20}{r_s}\right) - \frac{\frac{20}{r_s}}{1 + \frac{20}{r_s}} \right] \tag{21}$$

where $M_{spherical}(r < 20\text{kpc})$ is the mass enclosed within 20 kpc for a spherical NFW profile of density $\rho_{0,halo}$ and scale radius r_s. Of course, given that we vary q, the flattening of the halo, this will not correspond to the true mass enclosed of the halo within 20 kpc, but it gives a first-order estimate.

In the MCMC run, the mass distribution of the Galaxy is constrained by the rotation curve and the required velocity at the position of the Sun (see Section 1.6). The likelihood is set up in such a way that it modifies the potential to get the subclump stars on the $2:2:3$ resonance. Therefore, in each step of the MCMC, the frequencies of the subclumps stars are computed using an integration time of 30 Gyr with a time-step of 10 Myr. The likelihood then compares the average frequency ratios of these stars to the $\Omega_\phi : \Omega_z$ is $1:1$ resonance and $\Omega_z : \Omega_R$ is $2:3$ resonance. We thus define a log-likelihood with three components

[28] The $\Omega_z : \Omega_R$ is $7:10$ resonance is a higher order resonance that does not seem to give rise to stochastic behaviour.

$$\ln \mathcal{L} = K_1 W_1 \ln \mathcal{L}_{RC} + K_2 W_2 \ln \mathcal{L}_{\Omega_\phi/\Omega_z} + K_3 W_3 \ln \mathcal{L}_{\Omega_z/\Omega_R} \tag{22}$$

where K_1, K_2 and K_3 are normalising factors and W_1, W_2 and W_3 are the weights of the individual components such that $W_1 + W_2 + W_3 = 1$. I set $W_1 = W_2 = \frac{1}{5}$ and $W_3 = \frac{3}{5}$. Furthermore,

$$\ln \mathcal{L}_{RC} = C + \frac{1}{N} \sum_i^N \frac{(d_i - m_i)^2}{\sigma_i^2} \tag{23}$$

where C is a constant depending on the uncertainties in the RC data, which can be neglected. d_i and m_i denote the data and model RC values respectively, and σ_i is the uncertainty associated to datapoint d_i. The likelihood term associated to the frequency ratio $\Omega_\phi : \Omega_Z$ is defined as

$$\ln \mathcal{L}_{\Omega_\phi/\Omega_z} = -\ln\left(\sqrt{2\pi}\sigma_{\Omega_\phi/\Omega_z}\right) + \frac{1}{2}\frac{\left(\mu_{\Omega_\phi/\Omega_z} - 1\right)^2}{\sigma^2_{\Omega_\phi/\Omega_z}} \tag{24}$$

Here, $\sigma_{\Omega_\phi/\Omega_z}$ and $\mu_{\Omega_\phi/\Omega_z}$ are the dispersion and mean in Ω_ϕ/Ω_z of the subclump stars for a given potential. We fix $\sigma_{\Omega_\phi/\Omega_z} = 0.002$. Because we want the subclump stars to be on the $1:1$ resonance, we compare the value of the mean to 1. Similarly,

$$\ln \mathcal{L}_{\Omega_z/\Omega_R} = -\ln\left(\sqrt{2\pi}\sigma_{\Omega_z/\Omega_R}\right) + \frac{1}{2}\frac{\left(\mu_{\Omega_z/\Omega_R} - 2/3\right)^2}{\sigma^2_{\Omega_z/\Omega_R}} \tag{25}$$

Here, $\sigma_{\Omega_z/\Omega_R}$ and μ_{Ω_z/Ω_R} are the dispersion and mean in Ω_z/Ω_R of the subclump stars for a given potential. We fix $\sigma_{\Omega_z/\Omega_R} = 0.002$. Because we want the subclump stars to be on the $2:3$ resonance, we compare the value of the mean to $\frac{2}{3}$.

To restrict the exploration of the parameter space to regions that give rise to a (reasonably) realistic potential, I set a flat prior

$$P(\vec{\theta}) = \begin{cases} 1 & \text{if} \begin{cases} 0.8 < q < 1.5 \\ 5 < r_s < 50\,\text{kpc} \\ 1.5 < R_{d,thin} < 4\,\text{kpc} \\ 1.5 < R_{d,thick} < 4\,\text{kpc} \\ R_{d,thick} < R_{d,thin} \end{cases} \\ 0 & \text{otherwise.} \end{cases} \tag{26}$$

which is motivated by literature (see Section 1.1 and 1.7). If the flat prior is satisfied, it is convoluted with a Gaussian prior

$$P(r_s) = -\frac{(r_s - 20)^2}{2 \cdot 10^2} \tag{27}$$

$$P(R_{d,thin}) = -\frac{(R_{d,thin} - 2.6)^2}{2 \cdot 0.5^2} \tag{28}$$

$$P(R_{d,thick}) = -\frac{(R_{d,thick} - 2.2)^2}{2 \cdot 0.5^2} \tag{29}$$

The posterior distribution is the product of the priors and the likelihood. As an initial guess, I take the parameters of the Default Potential and add an offset which is a Gaussian distribution centred around zero with a width of 0.01 times the parameters of the Default Potential. I run the MCMC with 40 walkers for 2000 steps, and delete the first 300 steps as burn-in. The values of the frequencies and likelihood components are saved at each step. The resulting posterior distribution is shown in Fig. 42. The degeneracy between $M(r < 20\text{kpc})$ and q is a result of the rotation curve constraint. A higher q means a higher local density, and hence a lower $\rho_{0,halo}$ or $M(r < 20\text{kpc})$ is needed to keep the same amplitude of the rotation curve (see Section 1.7.1, where

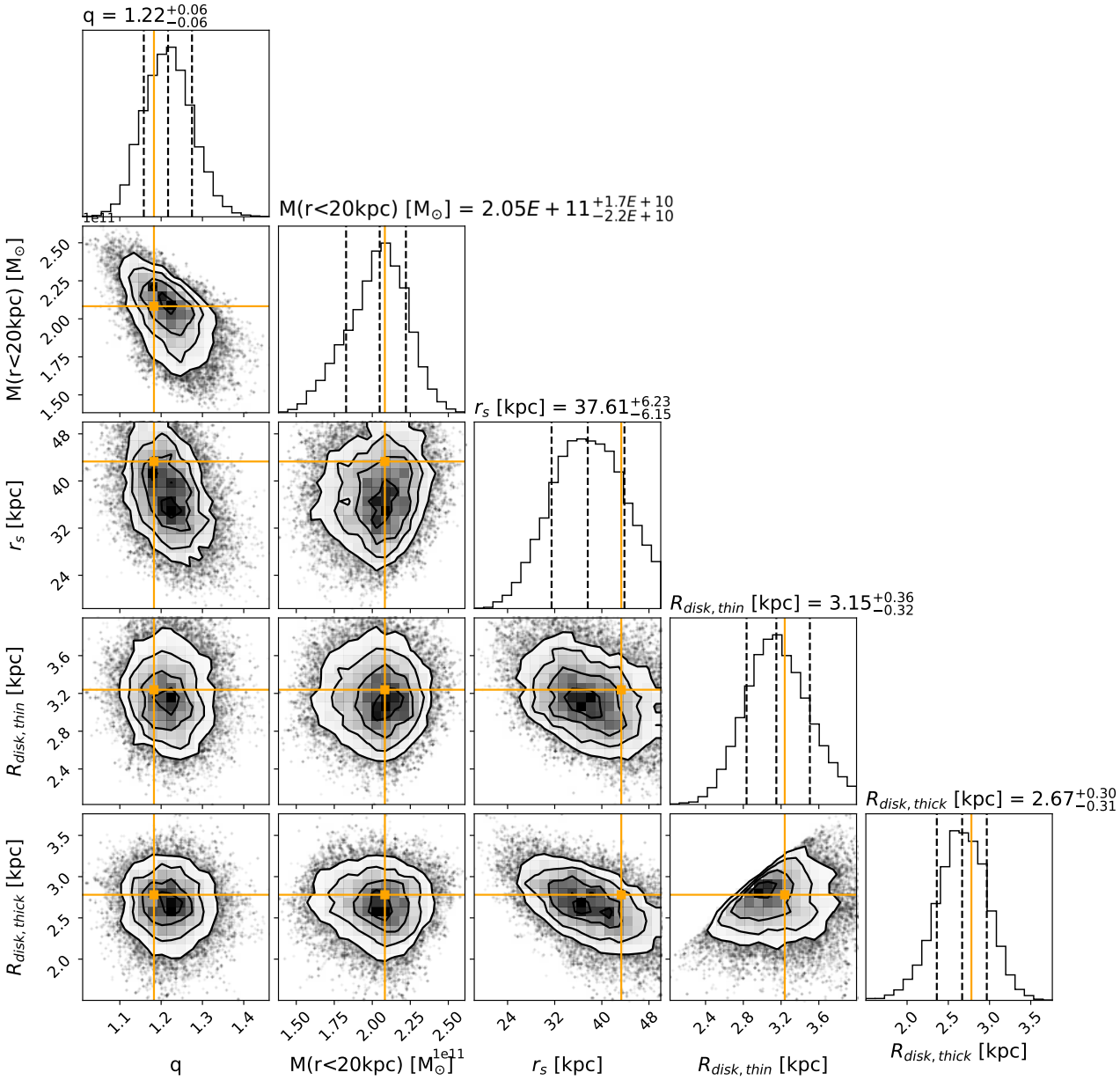

Figure 42: Posterior distribution of the Galactic potential parameters. The set of parameters indicated in yellow corresponds to the 2 : 2 : 3 potential which brings the subclump on the $\Omega_\phi : \Omega_z : \Omega_R$ is 2 : 2 : 3 resonance.

we lower the density of the Default Potential in comparison to the McMillan 2017 model for the same reason). The sharp cut-off seen in the $R_{d,thin}$ and $R_{d,thick}$ panel is a result of the flat prior that $R_{d,thick} < R_{d,thin}$.

To decrease the $\Omega_z : \Omega_R$ ratio to 2 : 3, Fig. 42 shows that the MCMC does two things. Firstly, it increases the disk scale lengths with respect to the Default Potential. The more extended disks will have a smaller surface density as the total mass of the disk is kept fixed, leading to a smaller vertical force at a fixed point and therefore a smaller Ω_z. Secondly, it increases the mass of the halo inside radius R, such that the radial force increases and consequently Ω_R increases. To increase the mass of the halo but also satisfy the strong $v_{circ}(R_\odot)$ constraint, the scale radius is increased (see also Appendix B.2). To get the subclump also on the $\Omega_\phi : \Omega_z$ is 1 : 1 resonance, the MCMC adjusts q given how much the halo contributes to the total flattening of the potential (which changes according to the mass of the halo).

Fig. 43 shows the compatibility of the different contributions to the likelihood (see Eq. 22). We can satisfy simultaneously a good fit to the rotation curve and get the stars on the $\Omega_\phi : \Omega_z$ is 1 : 1 resonance, and we can also simultaneously get the stars both on the $\Omega_\phi : \Omega_z$ is 1 : 1 and $\Omega_z : \Omega_R$ is 2 : 3 resonance. This can be derived from Fig. 43 by noticing that the maximum likelihood can be reached simultaneously for the different likelihood

components. However, from the same Figure we can also conclude that we cannot simultaneously get the stars both on the 2 : 3 resonance and fit the rotation curve well. Fig. 45 shows the rotation curve corresponding to the best-fit model and a set of rotation curves corresponding to potentials randomly sampled from the MCMC chains. The slope of the rotation curve is positive and too large, an indication of a (too) massive halo in the outer regions.

Since this trade-off between fitting the rotation curve and having the subclump on the 2 : 3 resonance exists, and $\ln \mathcal{L}_{\Omega_z:\Omega_R}$ has received the highest weight in the fit, the best-fit potential neither satisfies the rotation curve well nor does it get the subclump exactly on the 2 : 2 : 3 resonance. We choose to investigate a potential that actually gets the subclump on the 2 : 2 : 3 resonance (which we dub the " 2 : 2 : 3 potential") by selecting a set of parameters from the MCMC chain that corresponds to an almost maximal $\ln(\mathcal{L}_{\Omega_z/\Omega_R})$) and $\ln(\mathcal{L}_{\Omega_\phi/\Omega_z})$. The parameters of this potential with respect to the MCMC chains and best-fit are shown in yellow in Fig. 42 and its rotation curve is shown in yellow in Fig. 45. This potential has the following characteristic parameters: $q = 1.18$, $M(r < 20\text{kpc}) = 2.1 \cdot 10^{11} M_\odot$, $r_s = 43$ kpc, $R_{d,thin} = 3.2$ kpc, $R_{d,thick} = 2.8$ kpc. As can already be deduced from this potential's rising rotation curve[29], the halo is very massive. Indeed, the halo has a mass of $M_h(r < 20\,\text{kpc}) = 0.22 \cdot 10^{12} M_\odot$, which gives a total mass $M_{tot}(r < 20\,\text{kpc}) = 0.29 \cdot 10^{12} M_\odot$, which is about 1.5 times as large as the current estimate (Küpper et al. 2015; Malhan and Ibata 2019; Watkins et al. 2019; Posti and Helmi 2019). The halo's mass can be extrapolated to $M(r < 200\text{kpc}) = 3.5 \cdot 10^{12} M_\odot$, which is similarly far above the current estimate, $M_{200} \sim 1 \cdot 10^{12} M_\odot$[30] (see also Section 1.7.3). In the 2 : 2 : 3 potential, the frequencies of the subclump and hiL clump indeed overlap with the 2 : 2 : 3 resonance, see Fig. 44. By inspecting their SoS, I conclude that six stars of the hiL clump and three stars of the loL clump in the *Gaia* EDR3 RVS sample are resonantly trapped around the $\Omega_z : \Omega_R$ is 2 : 3 resonance. Out of the nineteen subclump stars in the extended sample, two are resonantly trapped.

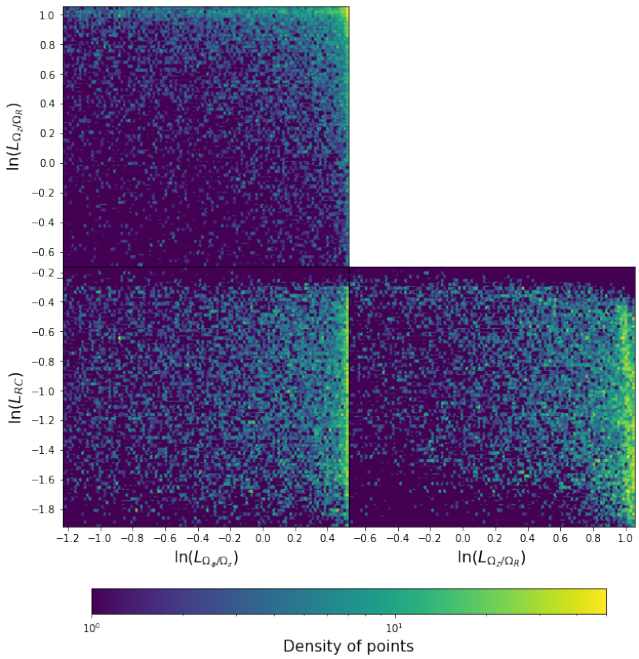

Figure 43: Density map of the different contributions to the likelihood (see Eq. 22). Though we can simultaneously reach the maximum likelihood of both $\ln \mathcal{L}_{\Omega_\phi/\Omega_z}$ and $\ln \mathcal{L}_{\Omega_z/\Omega_R}$ and both $\ln \mathcal{L}_{\Omega_\phi/\Omega_z}$ and $\ln \mathcal{L}_{RC}$, this is not the case for $\ln \mathcal{L}_{\Omega_z/\Omega_R}$ and $\ln \mathcal{L}_{RC}$. This means we either get closer to a solution maximising $\mathcal{L}_{RC}$ or a solution maximising $\ln \mathcal{L}_{\Omega_z/\Omega_R}$, but this cannot happen at the same time.

[29] Such a rising rotation curve has also been suggested by Ibata et al. 2013 to model the Sagittarius dwarf galaxy stream, but given today's observational constraints this seems unrealistic.

[30] Note that M_{200} is not necessarily equal to $M(r < 200\text{kpc})$, as M_{200} is the mass equal to the mass within r_{200}, which is the radius of a sphere that has an average density equal to 200 times the critical density of the Universe, ρ_{crit}.

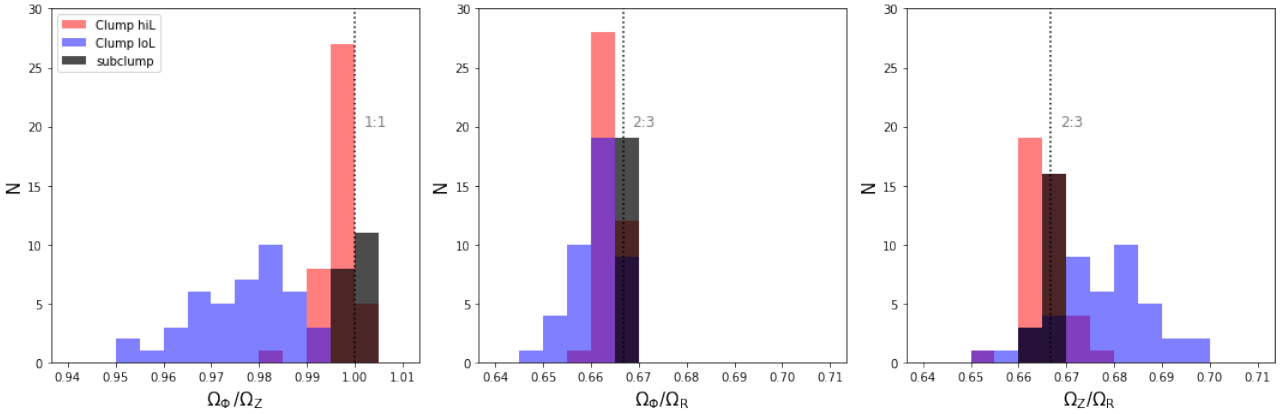

Figure 44: Orbital frequency ratio distribution of hiL clump stars (red) and loL clump stars (blue) in the *Gaia* EDR3 RVS sample and the subclump (black, see Section 2.5) in the 2 : 2 : 3 potential. Some resonances are indicated as grey dashed lines.

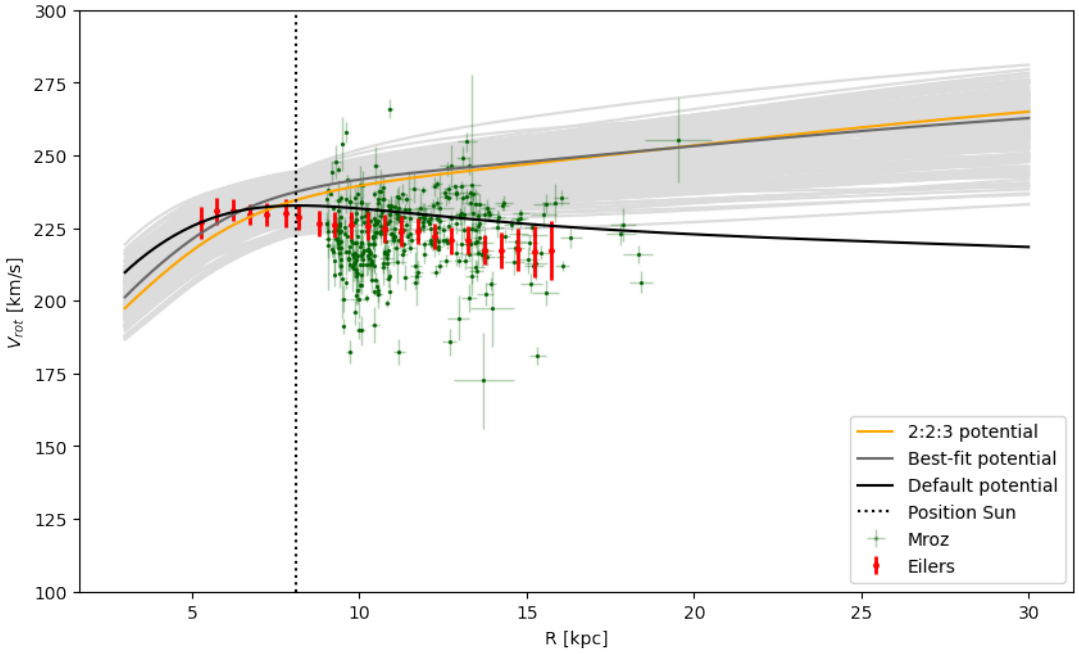

Figure 45: Rotation curve data from Eilers et al. 2019 (red) and the Cepheids (dark green) from Mróz et al. 2019. Overplotted in black is the rotation curve corresponding to the default gravitational potential, best-fit potential (dark grey) and the 2 : 2 : 3 potential (yellow). The rotation curves corresponding to 200 potentials with characteristic parameters randomly sampled from the MCMC chains are shown in light grey.

5.2 Mapping the Resonances in the 2 : 2 : 3 Potential

A resonance is surrounded by a finite region in frequency space (and thus phase-space) in which resonance trapping takes place. To get a feeling for the extent of resonance trapping, I inspect the SoS of stars generated in the 2 : 2 : 3 potential. The initial conditions of these stars are generated such that they overlap with the phase-space distribution of the Helmi Streams' stars (following the procedure described in Section 4.3). I then select stars around the $\Omega_z : \Omega_R$ is 2 : 3 resonance and plot their SoS. Stars that are resonantly trapped will trace out islands in the SoS. I find that the size of the 2 : 3 resonance in frequency is about $\pm(0.0005 - 0.0010)$, and the farther away from the resonance the smaller the fraction of trapped orbits is.

Having developed a feeling for the size of the resonance allows me to map out the resonances present in the Default Potential and 2 : 2 : 3 potential. Using $\Omega_z : \Omega_R = \frac{2}{3} \pm 0.0005$ as a strict definition for the resonance size (within this range, all stars are resonantly trapped), Fig. 46 and 47 show the distribution of the selected resonantly trapped stars in different subspaces. I select stars that are resonantly trapped by the $\Omega_\phi : \Omega_z$ is 1 : 1 resonance in a similar way. It is interesting to see that both the 1 : 1 and 2 : 3 resonance seem to occupy a "band" in $(E, L_\perp)$, which overlap at a certain location. That is where stars that are trapped by the 2 : 2 : 3 resonance are found. While the 1 : 1 and 2 : 3 resonance individually span almost the entire region occupied by the Helmi Streams in L_z and $L_\perp$, the 2 : 2 : 3 resonance only occupies a narrow band. This band is similar to the size of the gap and the size of the subclump. While the 1 : 1 and 2 : 3 resonances both occupy their own subspace in velocity space in the Default Potential, they overlap in the 2 : 2 : 3 potential. The resonances do not seem to be sensitive to the positions of the stars.

It is interesting to see that the potential can be modified in such a way that the resonance is "moved" to the right location in energy and angular momentum space, as we see by comparing Fig. 46 and 47. This opens possibilities to explore and modify the orbital structure of a given potential.

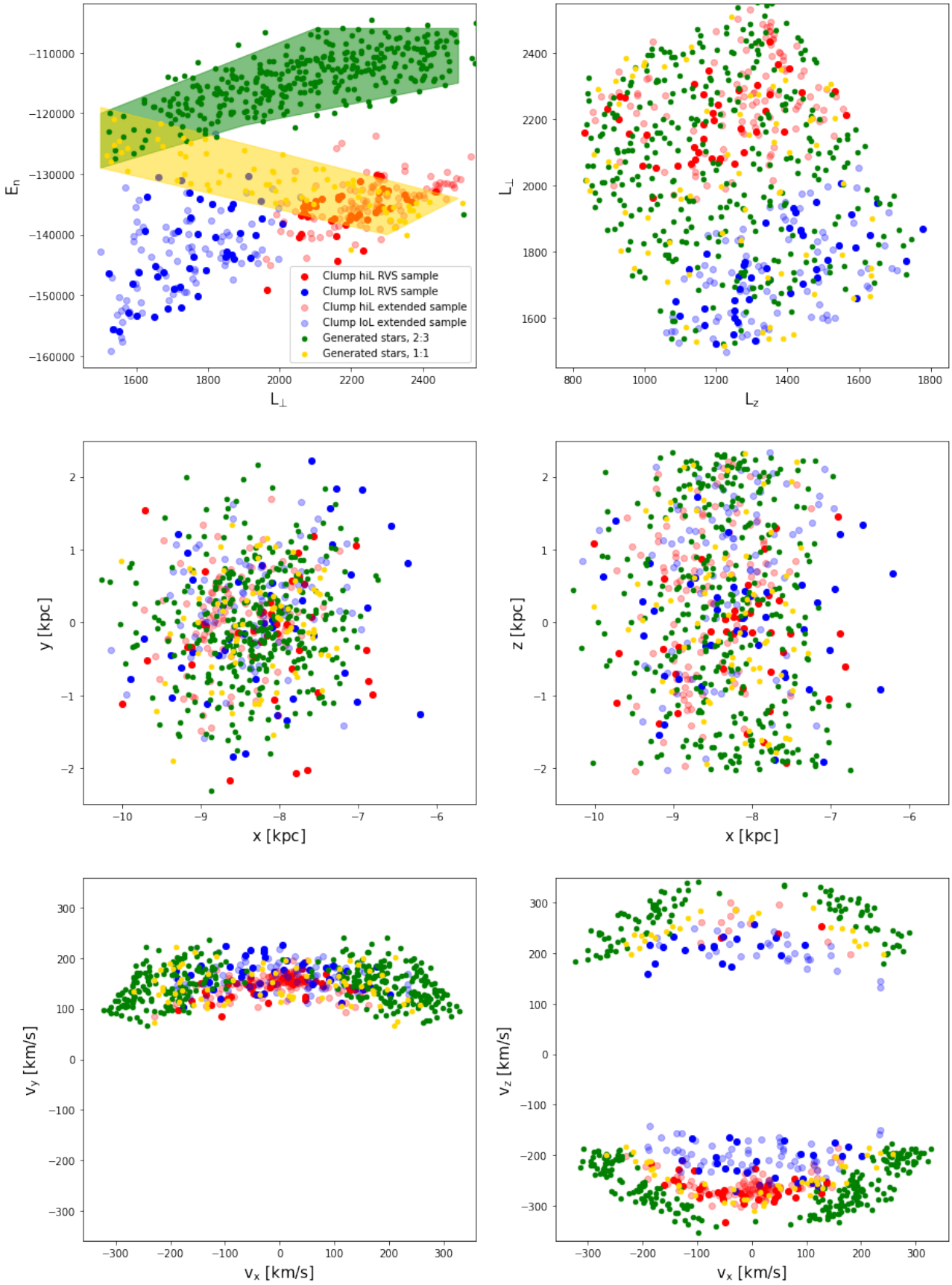

Figure 46: Phase-space, energy and angular momentum distribution of thehiL clump stars (red) and loL clump stars (blue) in the *Gaia* EDR3 RVS sample and generated stars (generated following the procedure described in Section 4.3) within ±0.0005 of the 2 : 3 resonance (green) and 1 : 1 resonance (yellow). This has been analysed in the Default Potential (see Section 1.7.4).

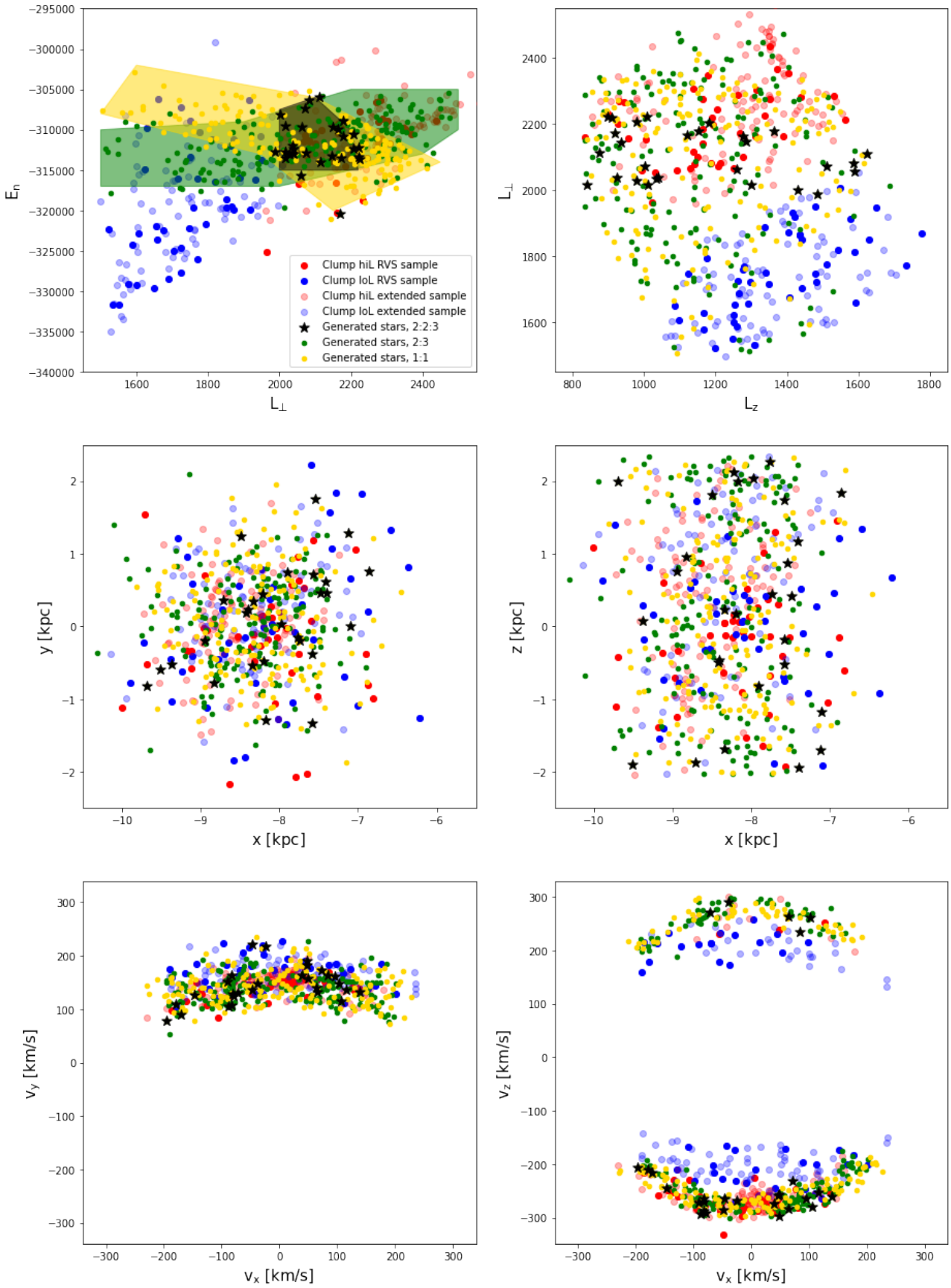

Figure 47: Phase-space, energy and angular momentum distribution of thehiL clump stars (red) and loL clump stars (blue) in the *Gaia* EDR3 RVS sample and generated stars (generated following the procedure described in Section 4.3) within ±0.0005 of the 2 : 3 resonance (green) and 1 : 1 resonance (yellow). This has been analysed in the 2 : 2 : 3 potential, in which the subclump is on the 2 : 2 : 3 resonance.

5.3 BFE: Freedom to the 2 : 2 : 3 Resonance?

I now investigate if a more generic description of the halo allows us to find a realistic potential in which the subclump falls on the 2 : 2 : 3 resonance while also satisfying the rotation curve constraints. To this end, I rerun the MCMC with the same likelihood (see Eq. 22) and constraints as in Section 5.1, but instead of allowing the characteristic parameters of the Galactic potential to vary, I use the BFE method outlined in Section 3.3 to explore the shape of the halo. I keep the bulge, stellar disks and gas disks fixed as in the Default Potential and vary the coefficients and their derivatives of a BFE halo. As before, the rotation curve provides a constraint on the mass distribution, but now the likelihood terms associated to the frequencies also constrain both the mass distribution and shape of the potential. As in Section 3.3, I stick to an axisymmetric BFE with $l_{max} = 2$ and 2 gridpoints, $r_{min} = 3$ kpc and $r_{max} = 40$ kpc, as this seemed to give sufficient freedom to explore the region of the potential probed by the Helmi Streams. I set a flat prior (see Eq. 19), and as an initial guess I use the expansion of the default NFW halo (see Section 1.7.4) and add an offset which is a Gaussian distribution centred around zero with a width of 0.01 times the expansion parameters.

I run the MCMC for 2000 steps with 40 walkers. The mean acceptance fraction is low, 0.17, and it is clear that there is still too much freedom given the constraints. The subclump is put onto the 2 : 2 : 3 resonance, see Fig. 48, and ten out of the nineteen subclump stars in the extended sample are resonantly trapped according to their SoS, outperforming the best-fit MCMC model (see Section 5.1). Again, six stars of the hiL clump and three stars of the loL clump in the *Gaia* EDR3 RVS sample are resonantly trapped. The rotation curve shows a similar result as in Section 5.1, see Fig. 49, namely a rising rotation curve, particularly beyond 10 kpc, which is needed to get the subclump onto the $\Omega_z : \Omega_R$ is 2 : 3 resonance. This means that more freedom in the functional form of the axisymmetric halo does not solve that problem.

In Fig. 49 one can clearly see the effect of the constraints in the resulting rotation curves. All potentials satisfy the $v_{circ}(R_\odot) = 233 \pm 5\%$, and the Eilers et al. 2019 and Mróz et al. 2019 rotation curve data is followed reasonably within $9 - 15$ kpc, where we have the strongest constraint. However, outside of that region, the rotation curve diverges in an unrealistic way. In the inner region the rotation curve rises, which is not expected from observational data (e.g. Karukes et al. 2019; Sofue 2020) nor from Milky Way mass models from literature such as the McMillan 2017 or Cautun et al. 2020 model. Similarly, beyond 15 kpc the rotation curve rises too steeply, indicative of a (too) massive halo as also discussed in Section 5.1. This shows that we might need more than an axisymmetric halo model to explain the Helmi Streams' clumps, as it does not seem to be possible to get a stochastic region at the right location in a realistic axisymmetric potential.

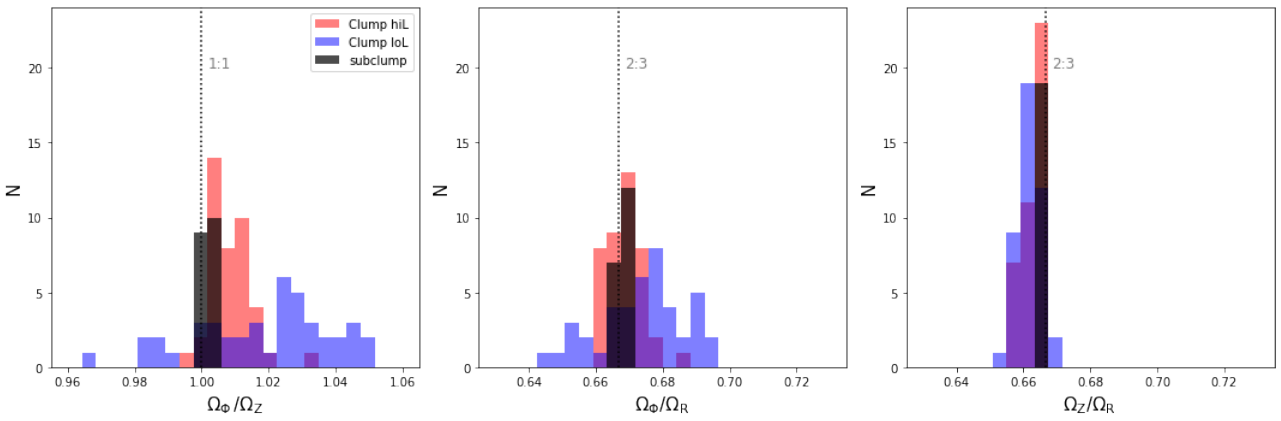

Figure 48: Orbital frequency ratio distribution of hiL clump stars (red) and loL clump stars (blue) in the *Gaia* EDR3 RVS sample and the subclump (black, see Section 2.5) in the best-fit BFE 2 : 2 : 3 potential. Some resonances are indicated as grey dashed lines.

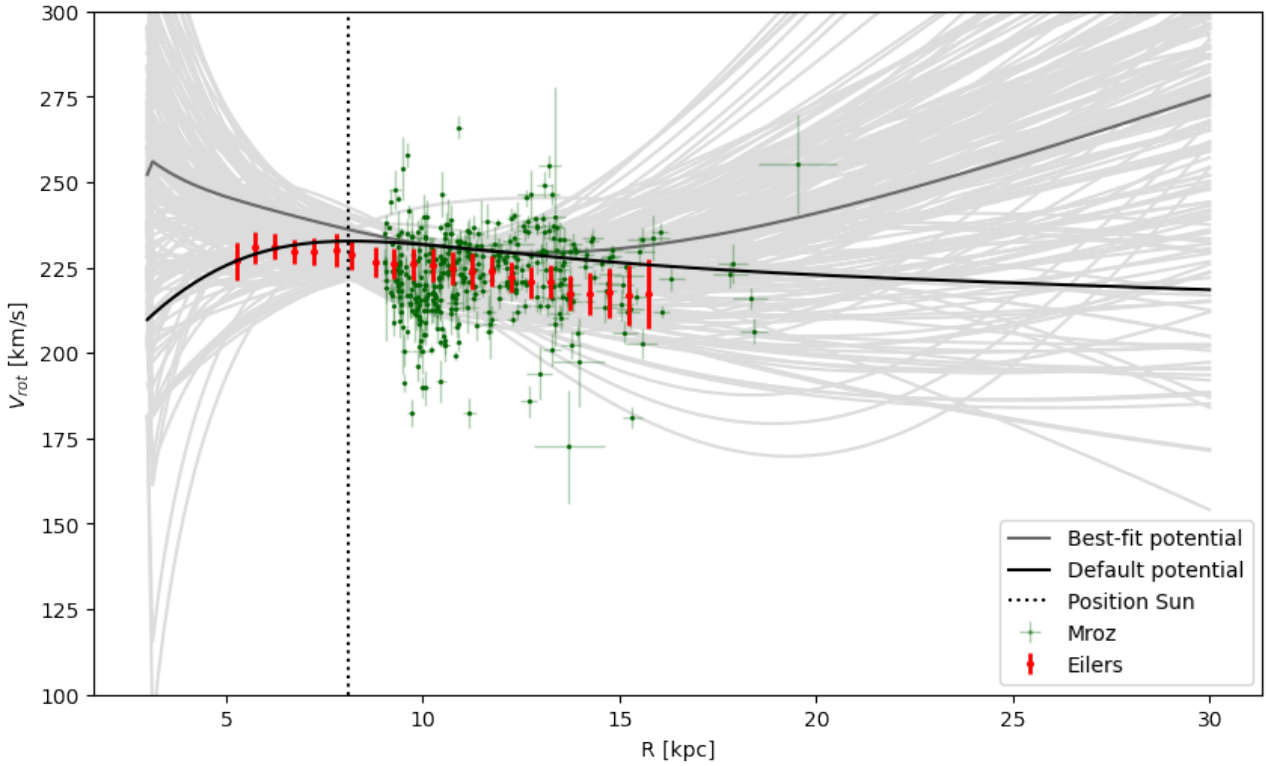

Figure 49: Rotation curve data from Eilers et al. 2019 (red) and the Cepheids (dark green) from Mróz et al. 2019. Overplotted in black is the rotation curve corresponding to the default gravitational potential and the best-fit BFE 2 : 2 : 3 potential (dark grey). The rotation curves corresponding to 200 potentials with characteristic parameters randomly sampled from the MCMC chains are shown in light grey.

5.4 Summary

Orbital frequencies depend on the characteristic parameters of the Galactic potential, so by varying the stellar disk scale radii, the flattening in the halo's density q, the halo scale radius and the density of the halo in an MCMC, we have attempted to modify the potential in such a way that the $\Omega_\phi : \Omega_z : \Omega_R$ is 2 : 2 : 3 resonance overlaps with the kinematically cold subclump. The separatrix of the $\Omega_z : \Omega_R$ is 2 : 3 could possibly give rise to the chaotic behaviour needed to explain the gap, while the $\Omega_\phi : \Omega_z$ is 1 : 1 resonance could slow down the dynamical evolution of the hiL clump. The subclump's evolution could possibly be slowed down further by the second resonance. Resonances seem to occupy a finite region in $(E, L_\perp)$, and the 2 : 2 : 3 resonance also occupies a finite region in angular momentum space. Therefore, knowing which resonance's separatrix causes the gap could provide a strong constraint on the Galactic potential. Though I am able to get the subclump on the $\Omega_\phi : \Omega_z : \Omega_R$ is 2 : 2 : 3 resonance, the required mass of the DM halo is too high, with $M_{tot}(r < 20\,\mathrm{kpc}) = 0.37 \cdot 10^{12} M_\odot$ and the extrapolated halo mass $M_h(r < 200\,\mathrm{kpc}) = 3.5 \cdot 10^{12} M_\odot$ being about twice and thrice as large as the current estimate. This gives rise to a rotation curve that rises steeply beyond the position of the Sun. A similar result is found when I apply the BFE method outlined in Section 3, showing that more freedom in the functional form of the axisymmetric DM halo does not solve the issue. Therefore, it seems like we might need to introduce a potential that radially varies in shape, from spherical at some location in the region probed by the Helmi Streams (to maintain the gap) but triaxial or asymmetric farther out (to explain the gap). Further investigation is into other, non-axisymmetric models is therefore needed.

6 Discussion

We have seen how orbital frequencies can be used in a novel way to constrain the Galactic potential. Orbital frequencies provide us insights that are not easily gathered by looking at a substructure's phase-space or integrals of motion distribution. There are many further possibilities to be explored with orbital frequency analysis. As argued by Valluri et al. 2012, using a frequency map of stellar halo stars, globally important orbital families and resonances in the potential can be identified, which depend on and therefore constrain the Milky Way's distribution function, the shape of the halo and the relative orientation of the disk and halo. Moreover, in the correct potential the fraction of chaotic orbits should be lowest[31], possibly providing a way to distinguish between different Galactic potential models. Lastly, as quiescently growing disk seems to cause resonant trapping, the identification of resonances in the stellar halo could even provide insight into the formation history of the Milky Way (Valluri et al. 2010; Valluri et al. 2012). This also emphasises that the orbital frequency distribution that we see today could be different from what it was in the past, as they can be altered by perturbations and a time-varying potential.

6.1 Other Applications of Orbital Frequencies

Orbital frequency analysis can be used to analyse halo substructures. As our view on the Galaxy is limited to a local volume, we only see stars whose orbits pass through that local volume. In frequency space, individual streams of stars belonging to a single substructure are resolved, and the number of streams increases as the structure becomes more phase mixed (see e.g. Fig. 1 in McMillan and Binney 2008; Gómez and Helmi 2010). Their separation in frequency space thus preserves an imprint of the time of accretion, which remains even if the system in which it is embedded evolved strongly with time. For at least part of the substructures it should be possible to recover the time of accretion even given the observational uncertainties (Gómez et al. 2010). With the release of *Gaia* DR3 complemented by an increasing amount of spectroscopic data from ground-based observations we can therefore hope to gather a large enough sample of accurate 6D phase-space positions of known substructures, such as Gaia-Enceladus-Sausage or Seqoia, and use this principle to infer their time of accretion and possibly properties of the underlying Galactic potential. However, for streams that are on chaotic or resonant orbits, such as the Helmi Streams, this inference is less straightforward due to the captured rate of the orbits.

Orbital frequencies can possibly also be a useful additional tool in studying group infall. As a group of satellites that fell in together is expected to be on roughly similar orbits (e.g. Li and Helmi 2009), an investigation of their orbital frequencies could provide more insight in whether structures are related. The next Section illustrates this with an example.

6.1.1 The Helmi Streams, Sagittarius and Jhelum

As discussed in Section 2, it is unusual that the Helmi Streams, which have a relatively light progenitor, are found to orbit the inner halo but appear to have been accreted relatively recently. One proposed scenario is that the progenitor of the Helmi Streams fell in with a group of other satellites (Helmi 2020). Substructures that fall in together as a group are expected to have similar orbital properties (e.g. Li and Helmi 2009). As noted by Koppelman et al. 2021, the orbital frequencies of Sagittarius seem to be similar to those of the Helmi Streams. Moreover, Sagittarius is believed to have been accreted about 7 Gyr ago (Dierickx and Loeb 2017; Kruijssen et al. 2020), which overlaps with the estimated accretion time of the Helmi Streams (Koppelman et al. 2019b). Having studied the orbital frequencies of the Helmi Streams in detail, it is therefore interesting to see how these compare to those of Sagittarius.

To study this, I use a sample of Sagittarius stars by Vasiliev and Belokurov 2020, requiring positive v_{hel} errors and a distance error smaller than 1 %. The frequencies were determined as before by `SuperFreq` over an integration time of 100 Gyr in the Default Potential (see Section 1.7.4). Next, the stellar stream Jhelum shares an orbital plane with Sagittarius (Woudenberg et al. 2022) and likely has an accreted origin (Bonaca et al. 2021). Bonaca et al. 2021 proposed a possible association of Jhelum with the Helmi Streams or Sagittarius, making it interesting to compare Jhelum's orbital frequencies to theirs. Jhelum's orbital frequencies are determined from randomly sampled initial conditions from the best-fit orbit found in Woudenberg et al. 2022. Fig. 50 shows the orbital frequencies of the three substructures. The fact that the Helmi Streams, Sagittarius and Jhelum have

[31] If a distribution function is not in self-consistent equilibrium with the potential, orbits will diffuse in phase space (i.e. the orbits change, they are chaotic). This diffusion alters the distribution function until an equilibrium with the potential is found (Merritt and Valluri 1996). Hence, a low degree of orbital diffusion indicates self-consistency between the distribution function and potential.

roughly the same orbital frequency ratio, namely close to $\Omega_\phi : \Omega_z : \Omega_R$ is 2 : 2 : 3, indicates that their orbits are similar, possibly suggesting that they fell in together as a group. The fact that Sagittarius has low orbital frequencies is because it orbits far out in the Galaxy, where orbital periods are longer. Jhelum orbits between 8 - 24 kpc (Woudenberg et al. 2022) and therefore falls in between Sagittarius and the Helmi Streams, which occupy the inner Galaxy (5 - 20 kpc). This example shows how orbital frequencies could help in determining associations between substructures and finally reconstructing the dynamical history of the Milky Way.

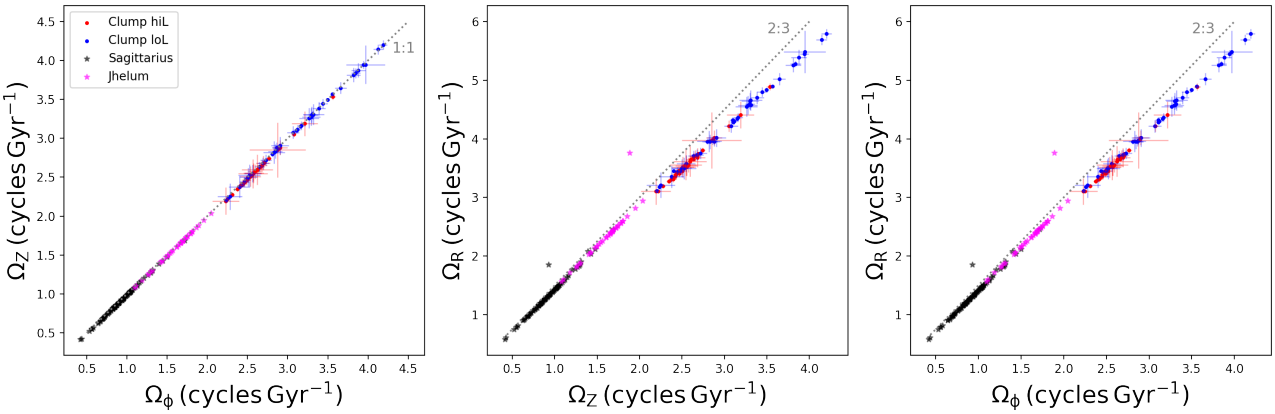

Figure 50: Orbital frequencies of Sagittarius stars (black), the Helmi Streams' hiL clump stars (red) and loL clump stars (blue) in the *Gaia* EDR3 RVS sample, and randomly sampled initial conditions from the best-fit orbit of Jhelum (magenta) from Woudenberg et al. 2022 in the Default Potential (see Section 1.7.4). Some resonances are indicated as grey dashed lines. The uncertainties in the frequencies of the Helmi Streams' stars were determined by Monte Carlo sampling with $N = 500$. Some Jhelum and Sagittarius stars were put on the $\Omega_z : \Omega_R$ is 1:2 branch and are not shown here, as that is likely to be an artefact of `SuperFreq` not working properly (see the Appendix of Dodd et al. 2021 and the discussion in Section 6.2).

6.2 `SuperFreq`: $\Omega_z : \Omega_R$ is 1 : 2 versus 2 : 3 for the Helmi Streams

While working with `SuperFreq`, the determination of the Ω_R frequency was not always consistent for some stars. While the majority of the Helmi Streams' stars was assigned frequencies close to the $\Omega_Z : \Omega_R$ is 2 : 3 resonance, part of the stars were put on the tight $\Omega_Z : \Omega_R$ is 1 : 2 branch. This was noticed before by Koppelman et al. 2021, who also used `SuperFreq` to determine the orbital frequencies. However, Dodd et al. 2021 showed that the 1 : 2 branch seems to be a result of an unreliable fundamental frequency determination, as it does not occur when determining the orbital frequencies in action-angle space using the Stäckel fudge method (see Appendix E). The splitting occurs only in Ω_R, and the difference in value of Ω_R is too large to be a realistic feature of the Helmi Streams (for example, to put a star on the 2 : 3 branch onto the 1 : 2 branch, its Ω_R value needs to increase by a factor $\frac{4}{3}$). Moreover, such a strong resonance (the 1 : 2 branch is very tight) would result in a lower dimensionality of the orbits of these Helmi Streams' stars, which we should be able to see in for example their surfaces of section, but we do not observe such a feature (see Fig. 18). This seems to show that `SuperFreq`'s determination of the fundamental frequencies is not fully reliable. This behaviour needs careful investigation before we can apply `SuperFreq` to a larger sample of stars, or one could resort to a different implementation of an algorithm that determines the fundamental frequencies, such as `NAFF` (Valluri and Merritt 1998) or the Stäckel fudge method (Binney 2012).

Within this thesis I resolved this issue following Dodd et al. 2021. `SuperFreq` performs a Fourier transform of each inputted complex time series, e.g. $R(t) + iv_R(t)$, and selects the frequency with the highest amplitude as the fundamental frequency (see Section 2.4.1). As `SuperFreq` outputs a table containing the frequency spectrum and their corresponding amplitudes, we take the Ω_R frequency with the second highest amplitude as fundamental frequency, which places the Helmi Streams stars onto a single branch, close to the $\Omega_Z : \Omega_R$ is 2 : 3 resonance.

6.3 Basis Function Expansions

We have shown that Basis Function Expansions (BFE) could be a promising way to explore the shape of the DM halo without the restrictions of a parametrised model. Whilst this approach is far more flexible, this demands good constraints and a well-formulated likelihood, which constrain both the shape and the mass distribution of the Galactic potential. In this work, we have only considered the rotation curve as a constraint on the mass distribution. Additional constraints could be helpful in restricting the BFE fit to realistic models, such as

- A more extended circular velocity curve, covering a large range in radius. These exist (e.g. Huang et al. 2016, Sofue 2020) but should first be homogenised to be compatible with, for example, the rotation curve by Eilers et al. 2019.
- A constraint on the virial mass of the halo (see Section 5), as this would require the density profile of the halo to be realistic out to large radii
- A requirement that the density is positive out to large radii. As seen in Section 3.3.2, not setting such a constraint allows for negative densities as the basis function expansion is in the potential.
- A constraint on the vertical force as a function of z (e.g. Kuijken and Gilmore 1991; Bienaymé et al. 2014), or any other force.

In this work, we have focused on a low-order axisymmetric BFE of the DM halo. To be able to explore more complex or more resolved axisymmetric shapes, a higher l_{max} and higher number of gridpoints is needed. It is also possible to explore triaxial and asymmetric shapes using the $m \neq 0$ terms, though this greatly increases the number of free parameters. Of course, a BFE can also be used to represent and model other components of the Milky Way. Depending on the component under consideration, the choice of basis functions might need to be reconsidered. For example, in the case that BFE are used to explore the shape of the disk, spherical harmonics are no longer an optimal choice, as they start from a spherical distribution, while disks are flattened structures. Instead, the `CylSpline` expansion implemented in `AGAMA` could be used, which uses azimuthal Fourier harmonics (Vasiliev 2019). There is a broad range of different sets of basis functions available, including the Hernquist and Ostriker 1992 expansion, which uses a Hernquist model as its zeroth order term and is therefore quite suitable as expansion for a DM halo. The Hernquist and Ostriker 1992 expansion is also included in the family of biorthonormal double-power-law potential-density expansions described in Lilley et al. 2018, which allows more freedom as it uses a more general power-law density model as zeroth order.

6.4 Chaos and Resonances

We have shown that when an ensemble of stars is located around a stochastic region, a gap may form in $L_\perp$ over time because of the different rates of variation in $L_\perp$. The stochastic region that was identified close to the $\Omega_z : \Omega_R$ is $2:3$ resonance is only a small region in phase-space, meaning that only a small subset of the stars with Helmi Streams' like phase-space coordinates falls on the separatrix in the $2:2:3$ potential. As the $2:2:3$ potential moreover is not a realistic potential (if extrapolated it would imply a too large virial for the halo) it is not unlikely that actually another resonance or separatrix is causing the gap between the clumps. Future research including a large range of Galactic potential models is needed to explore this further.

The fact that the Galactic potential has such a strong effect on the phase-space distribution of the Helmi Streams calls for caution in our modelling efforts. If we analyse streams that have morphologies or substructure caused by a stochastic region, or on the other hand, a stabilising resonance, and model them as if they are on a regular orbit, this could lead to biased results. For example, recall that the difference in phase-mixing between the two clumps caused by the resonance could lead to a different estimate of the accretion timescale when analysing them separately. It would be instructive to see how a Helmi Streams analogue behaves in an N-body simulation in a potential that does not host any resonances, such as the McMillan 2017 potential, and in a potential in which the hiL clump is on the $\Omega_\phi : \Omega_Z$ is $1:1$ resonance, so the Default Potential. This comparison would allow us to quantify the dynamical effect of a single resonance on the Helmi Streams. Once a realistic potential is found that hosts a stochastic region at the right location, in between the two clumps, an N-body simulation would similarly be paramount to investigate the effect of such a region on the Helmi Streams' phase-space distribution.

The orbital structure of the Galactic potential, describing the location of resonances, chaotic regions and the type of orbital families that populate it, depends on the characteristic parameters of its components (Caranicolas and Zotos 2010; Zotos 2014) and is linked to its distribution function (Valluri et al. 2012). Hence, if we are able to map out the orbital structure of the Milky Way and identify regions that host resonances or chaotic orbits, we can strongly constrain the Galactic potential. We have seen that the phase-mixed Helmi Streams provide such a constraint, but other stellar streams can possibly help us to map out the Galactic potential even further. As noted by Price-Whelan et al. 2016b, the existence of long, thin stellar streams indicates that the region probed by these streams should host regular orbits. As resonances slow down the evolution of a stellar system (Helmi and White 1999; Vogelsberger et al. 2008), the identification of streams that seemed to have evolved more slowly than should be expected could probe resonant regions of the potential. On the other hand, stellar streams on chaotic orbits diffuse faster (Mestre et al. 2020) and streams near a separatrix can have distinct

stream morphologies (Yavetz et al. 2021). Therefore, identifying such streams[32] or regions devoid of streams and using frequency analysis to provide insight into whether or what resonances might be at play could similarly provide us with a probe of the orbital structure of the Milky Way.

[32]Disentangling different mechanisms causing such a distinct stream morphology is difficult.

7 Conclusions

In this thesis, I have studied the peculiar dynamical properties of the phase-mixed Helmi Streams. The stars are the remnants of an accreted dwarf galaxy orbiting the inner Galaxy, that can be separated into two clumps in angular momentum space. The clump with lower perpendicular angular momentum (the loL clump) is more phase-mixed than the other clump (the hiL clump). This difference in the degree of phase-mixing can be inferred from the difference in the v_z distribution of the two clumps and the fact that the loL clump has a more diffuse orbital frequency distribution. These features are confirmed in the recently released *Gaia* DR3 data (Gaia Collaboration et al. 2022). Within the hiL clump I have found a kinematically cold subclump that seems to be even less phase-mixed. As I have shown here, the Helmi Streams' orbits probe a dynamically interesting region of the gravitational potential of the Galaxy that hosts multiple resonances. While the hiL clump falls on the $\Omega_\phi : \Omega_Z$ is $1:1$ resonance in the Default Potential (see Section 1.7.4), the loL clump is shifted to a lower ratio. As a resonant orbit is expected to phase-mix slower, $\propto t^{-2}$, than a non-resonant orbit, $\propto t^{-3}$, this explains the observed difference in the degree of phase-mixing between the two clumps (Helmi and White 1999; Vogelsberger et al. 2008). Substructure as seen within the Helmi Streams has not been observed before. This is unlikely to be caused by accretion as the two clumps have distinct dynamical properties but share a common origin, and it should therefore be caused by dynamics specific to the Galactic potential. The existence of the two clumps therefore provides a constraint on the potential, as it should be able to reproduce our observations.

I have introduced a method to explore the shape of the DM halo without the restrictions of a parametrised model using Basis Function Expansions (BFE), where the basis functions are spherical harmonics. I have performed a low-order expansion and showed that by varying the coefficients and their derivatives at the gridpoints using an MCMC, I have obtained the freedom to reshape the potential, given the right constraints. This can be used to turn an NFW profile into a Hernquist profile. Moreover, I have shown that it is possible to find a potential that maximises the distance between the two Helmi Streams clumps in time. As the clumps are separated by an empty region in $L_\perp$, and $L_\perp$ is an integral of motion in a spherical potential, this effectively constrains the total potential to be spherical. This concept could be extended to allow the exploration of more complex axisymmetric, triaxial or asymmetric shapes. However, due to the large amount of freedom, it is important to use good constraints on both the mass distribution and the shape of the potential.

While the presence of the clumps and their long-time existence can be explained by the potential found, this does not provide an answer as to how a gap between the clumps is formed. I have explored the possibility that the gap between the two clumps is caused by a chaotic region in the potential, leading to orbital diffusion. As chaotic regions are generally small, this tightly constrains the potential of the Milky Way. Chaotic orbits can be found near separatrices, the boundaries between orbit families, such as stars close to a resonance. By exploring the region of phase-space occupied by the Helmi Streams, I have found that the Default Potential hosts the $\Omega_z : \Omega_R$ is $2:3$ resonance near the Helmi Streams, meaning that the Streams are located close to the $\Omega_\phi : \Omega_Z : \Omega_R$ is $2:2:3$ resonance. The separatrix of the $\Omega_z : \Omega_R$ is $2:3$ resonance can cause chaotic behaviour, and I have shown that a gap can be formed on sufficiently small timescales (~ 6 Gyr) when an ensemble of stars occupies the region of phase-space surrounding the separatrix. Thus, a potential that hosts a chaotic region in between the clumps could possibly explain the existence of the clumps.

Realistic Galactic mass models such as the Default Potential do not seem to host a stochastic region at the right location, in between the clumps. Given that the orbital frequencies depend on the underlying gravitational potential, I have tried to modify the characteristic parameters of the potential in such a way that the $2:2:3$ resonance overlaps with the kinematically cold subclump. This is because its dynamical evolution could possibly be slowed down by the two resonances, while the $2:3$ resonance's separatrix could introduce the sought after stochastic region in between the clumps. Using an MCMC, I have varied the stellar disk scale radii, the flattening in the halo's density q, the halo scale radius and the density of the halo, given constraints on the mass distribution via a circular velocity curve. To get the resonance to the required location, I have found that a too high mass enclosed is needed, resulting in a steeply increasing circular velocity curve. Applying the BFE method using a low-order axisymmetric description to vary the shape of the halo gives a similar result, indicating that more freedom in the functional form does not resolve this issue. This suggests that more than a time-independent axisymmetric model is needed to explain the existence of the Helmi Streams clumps, for example a potential that radially varies in shape. While the region of the potential occupied by the Helmi Streams should be roughly spherical to maintain the gap in time, farther out the shape is unconstrained, allowing asymmetric or triaxial shapes. Further investigation, exploring such triaxial or asymmetric models which possibly include the infall of the LMC or the presence of the bar, is therefore needed.

Acknowledgments

I am very grateful for the past year. I've felt part of and welcome in not only Amina's but also Else's group, which provided me with a very supportive and positive environment to learn about science. Some of the people in these two groups have become my close friends, and I now couldn't imagine my life without them. I feel lucky having had Amina as my supervisor. My weekly meetings with Amina always proved helpful and were able to shed a positive light on my work if I felt it was not going that well. Her sharp and insightful comments but also kind words have taught me a lot about the field and doing research. It is therefore a great joy for me to be able to stay with Amina and thus within the group as I pursue my PhD. There are four exciting and beautiful years ahead of me!

I'd like to give special thanks to a few people. I'd like to thank Glenn for his love, for always being there for me and for giving feedback on this work. I'd like to thank Emma for teaching me all she knew about the clumps (and much more!). I'd like to thank Tom and Akshara for helpful discussions and comments on this work. Finally, I'd like to thank all the people who have supported me throughout this year and made this year worthwhile. It's been a great journey :)

I would like to thank Paul McMillan for sharing his MCMC chains of the McMillan 2017 model, and I'd like to similarly thank Marius Cautun for sharing his MCMC chains of the Cautun et al. 2020 model. This work has made use of data from the European Space Agency (ESA) mission *Gaia* (`https://www.cosmos.esa.int/gaia`), processed by the *Gaia* Data Processing and Analysis Consortium (DPAC, `https://www.cosmos.esa.int/web/gaia/dpac/consortium`). Funding for the DPAC has been provided by national institutions, in particular the institutions participating in the *Gaia* Multilateral Agreement.

Throughout this work, we've made use of the following packages: `astropy` (Astropy Collaboration et al. 2013), `AGAMA` (Vasiliev 2019), `galpy` (Bovy 2015) `emcee` (Foreman-Mackey et al. 2013), `corner` (Foreman-Mackey 2016), `vaex` (Breddels and Veljanoski 2018), `SciPy` (Virtanen et al. 2020), `matplotlib` (Hunter 2007), `gala` (Price-Whelan 2017; Price-Whelan et al. 2020), `SuperFreq` (Price-Whelan 2015) `NumPy` (van der Walt et al. 2011), `seaborn` (Waskom 2021), and Jupyter Notebooks (Kluyver et al. 2016).

A The Helmi Streams in *Gaia* DR3

To construct a sample of stars in *Gaia* DR3 with reliable 6D phase space positions, especially distances, I follow Dodd et al. 2022. Dodd et al. 2022 correct the parallax (ϖ) of each star by their individual zero-points (Δ_ϖ) following Lindegren et al. 2021, and select stars that have

$$\frac{\varpi - \Delta_\varpi}{\sqrt{\sigma_\varpi^2 + \sigma_{sys}^2}} \leq 5 \tag{30}$$

where σ_ϖ is `parallax_over_error` and σ_{sys} is the systematic uncertainty on the zero-point, which is taken to be 0.015 mas (Lindegren et al. 2021). Moreover, the stars are required to have `RUWE` < 1.4 and $\sigma(v_{los}) < 20\,\mathrm{kms}^{-1}$. The uncertainties in the radial velocities are corrected following Babusiaux et al. 2022. To select stars that kinematically belong to the stellar halo, I require $|V - V_{LSR}| > 210\,\mathrm{km\,s}^{-1}$.

I select the hiL and loL clump within a volume of 3 kpc, see also Fig. 51, as

- **hiL clump**: ellipse centred on $(L_z, L_\perp) = (1150, 2220)\,\mathrm{kpc\,km\,s}^{-1}$ with major and minor axis lengths of 800 and 480 $\mathrm{kpc\,km\,s}^{-1}$, respectively. The ellipse is rotated counter-clockwise by 20 degrees. I require $E < -125000\,\mathrm{km}^2\,\mathrm{s}^{-2}$ in the Default Potential.
- **loL clump:** ellipse centred on $(L_z, L_\perp) = (1320, 1750)\,\mathrm{kpc\,km\,s}^{-1}$ with major and minor axis lengths of 840 and 440 $\mathrm{kpc\,km\,s}^{-1}$, respectively. The ellipse is rotated counter-clockwise by 10 degrees. I require $E < -125000\,\mathrm{km}^2\,\mathrm{s}^{-2}$ in the Default Potential.

I find 439 stars in total, of which 223 stars are in the hiL clump and 217 stars are in the loL clump. If I increase the volume, I find up to 697 (5 kpc) and even 1009 (10 kpc) stars, but these samples likely contain more contamination, especially the loL clump which is located close to the thick disk. Moreover, the more distant a star is, the less reliable the distances derived from the parallax become, as the uncertainties increase and the parallax offset becomes of more importance. I therefore use a 3 kpc volume.

To investigate the Helmi Stream's stellar population, I inspect their metallicity distribution using LAMOST DR7[33] (Zhao et al. 2012), and I inspect their Colour absolute-Magnitude Diagram (CaMD) using *Gaia* photometry. I find 64 stars in the *Gaia* DR3 RVS sample with metallicities from LAMOST Low Resolution Spectra, see the left panel of Fig. 52. The mean metallicity of the hiL clump (35 stars) is [Fe/H] = -1.5 ±0.4 dex, and the mean metallicity of the loL clump (29 stars) is [Fe/H] = -1.4 ±0.6 dex. A Kolmogorov-Smirnov test, performed using `scipy.stats.kstest`, shows that the two distributions are statistically compatible, with a p-value of 0.31. The right panel of Fig. 52 shows the CaMD of the hiL and loL clump, which also seem to be consistent with each other. To convert from apparent to absolute magnitude, I first corrected the G-band photometry of the stars following Gaia Collaboration et al. 2021a[34]. Stars are corrected for extinction using the 2D Schlegel et al. 1998 dust maps and applying the *Gaia* passband extinction coefficients[35]. In comparison to the *Gaia* EDR3 CaMD (see Fig. 10), especially the Main Sequence Turn-Off (MSTO) and Red Giant Branch are more densely populated in the *Gaia* DR3 sample. This makes sense, as the *Gaia* DR3 RVS sample goes deeper ($\sim$ 14 mag) than the *Gaia* EDR3 RVS sample ($\sim$ 12 mag). From the comparison of the CaMD and metallicity distributions of the two clumps, we can confirm that the two clumps have a common origin.

The phase-space, energy and angular momentum distribution of the hiL clump stars and loL clump stars is shown in Fig. 53, which confirms what we see in *Gaia* EDR3. The hiL clump stars form a more coherent structure in velocity space. While the loL clump stars are distributed as $(v_z > 0) : (v_z < 0) \sim 2 : 3$, the hiL clump stars are distributed as $(v_z > 0) : (v_z < 0) \sim 1 : 9$. The frequency distribution of the hiL clump stars and loL clump stars is shown in Fig. 54, the orbital frequency ratio distribution is shown in Fig. 55. As in *Gaia* EDR3, the loL clump has a more diffuse frequency distribution than the hiL clump.

[33] http://dr7.lamost.org

[34] This is required for stars with a 6 parameter astrometric solution, see also https://github.com/agabrown/gaiaedr3-6p-gband-correction/blob/main/GCorrectionCode.ipynb

[35] See also http://stev.oapd.inaf.it/cgi-bin/cmd_3.6 and Cardelli et al. 1989 and O'Donnell 1994

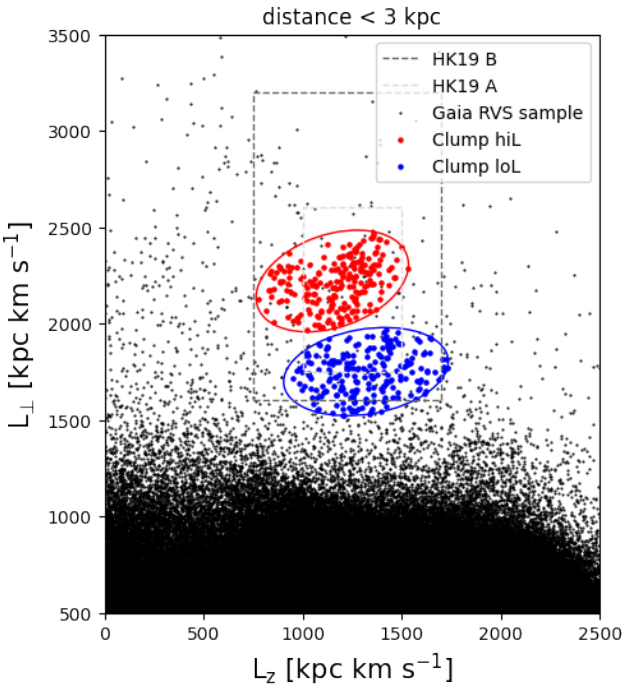

Figure 51: Selection of the hiL clump (red) and loL clump (blue) in angular momentum space in the *Gaia* DR3 RVS sample. The dashed lines show the selections of the Helmi Streams previously used by Koppelman et al. 2019b.

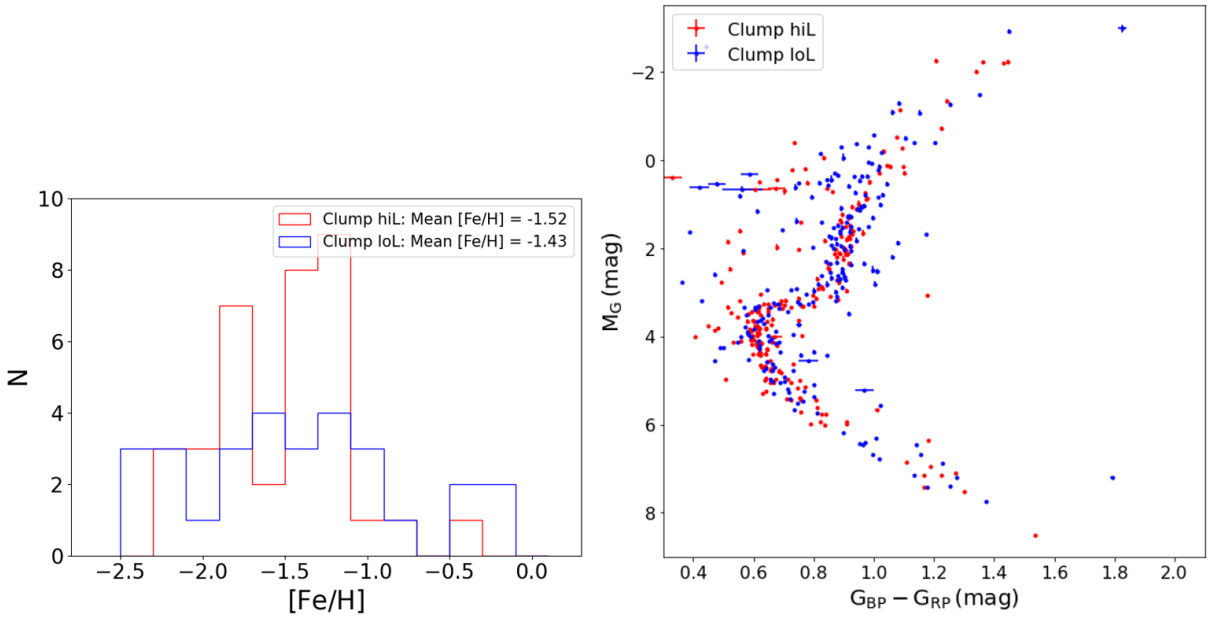

Figure 52: *Left panel*: Metallicity distributions from LAMOST Low Resolution Spectra of hiL clump stars (red) and loL clump stars (blue) in *Gaia* DR3. Both distributions peak around [Fe/H] ~ -1.5. *Right panel:* CaMD of the extended sample. The CaMD and metallicity distribution of the hiL and loL clump are similar, supporting a common origin.

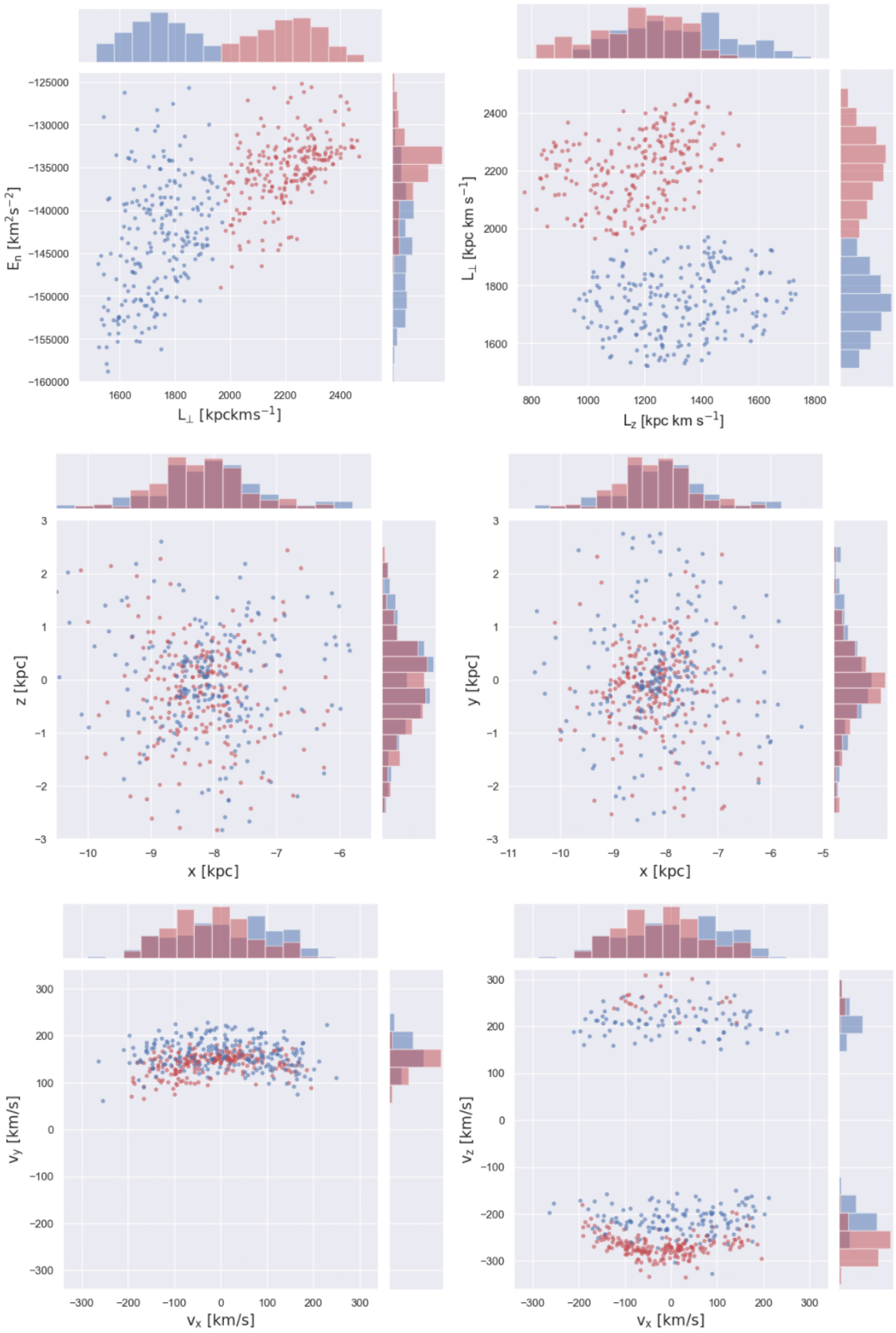

Figure 53: Phase space, energy and angular momentum distribution of the hiL clump stars (red) and loL clump stars (blue) in the *Gaia* DR3 RVS sample in the Default Potential (see Section 1.7.4). Histograms on the top and right of each plot show the distributions in one dimension.

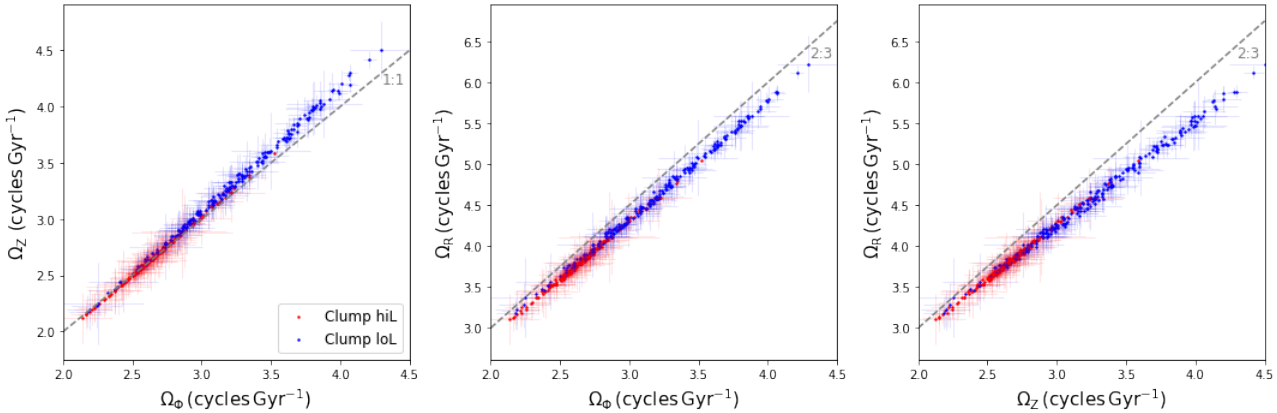

Figure 54: Orbital frequencies of the hiL clump stars (red) and loL clump stars (blue) in the *Gaia* DR3 RVS sample in the Default Potential (see Section 1.7.4). Some resonances are indicated as grey dashed lines. The uncertainties were determined by Monte Carlo sampling with $N = 500$. Some resonances are indicated as grey dashed lines.

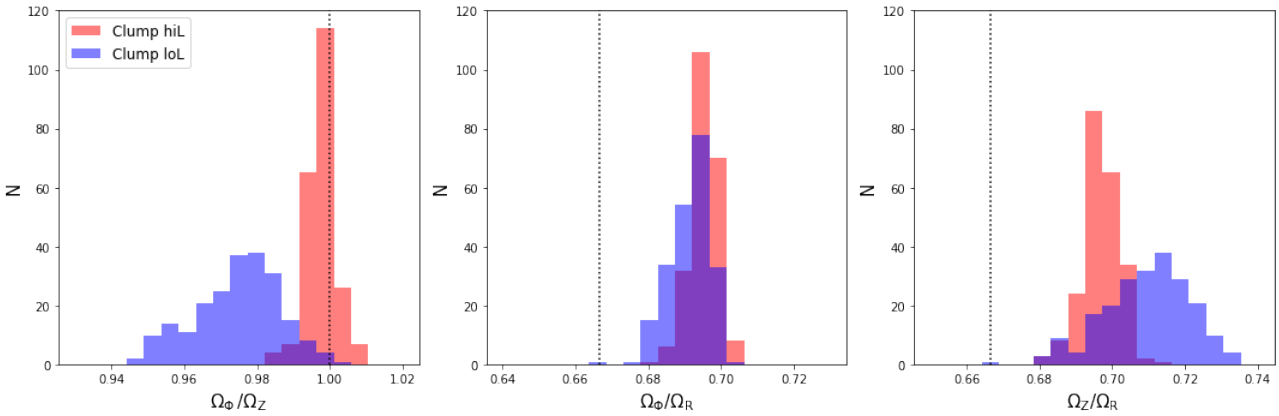

Figure 55: Orbital frequency ratio distribution of hiL clump stars (red) and loL clump stars (blue) in the *Gaia* DR3 RVS sample in the Default Potential (see Section 1.7.4). Some resonances are indicated as grey dashed lines.

B Dependence Orbital Frequencies on Characteristic Parameters

The orbital frequencies of the Helmi Streams' stars depend on the gravitational potential in which the orbits are integrated. To illustrate this dependence, I will vary one parameter of the gravitational potential at the time and show what happens to the ratio of the fundamental frequencies.

I will show that $\Omega_\phi : \Omega_z$ is most sensitive to a variation in the flattening of the potential (and thus q or the disk mass), via Ω_z, while $\Omega_z : \Omega_R$ is more sensitive to the mass enclosed, via Ω_R, and to the mass of the disk, via Ω_z.

B.1 Varying the Flattening of the Halo

Fig. 56 shows the dependence of the frequency ratios on the flattening in the density of the halo. The flattening in the density affects the distribution of mass in the vertical direction. The density is adjusted such that the rotation curves stay consistent with the rotation curve of the Default Potential. $\Omega_\phi : \Omega_z$ seems to be most sensitive to a variation in the flattening and increases as the flattening increases. This is a consequence of the fact that less mass is located near the plane, so Ω_z decreases. This is also reflected in the fact that $\Omega_z : \Omega_R$ decreases. The closer to $\Omega_\phi : \Omega_z$ is $1 : 1$ resonance the hiL clump stars are, the narrower the frequency distribution becomes.

B.2 Varying the Scale Radius of the Halo

Fig. 57 shows the dependence of the frequency ratios on the scale radius r_s of the halo. While $\Omega_\phi : \Omega_z$ does not strongly depend on r_s, $\Omega_\phi : \Omega_R$ and $\Omega_z : \Omega_R$ do. Since I only change the scale radius and not the density of the halo, a larger scale radius corresponds to a more massive halo. While for the Default Potential, $M(r < 20\,\mathrm{kpc}) = 1.6 \cdot 10^{11} M_\odot$, for a potential with $r_s = 25.4$ kpc, $M(r < 20\,\mathrm{kpc}) = 2.5 \cdot 10^{11} M_\odot$. Ω_R is mainly sensitive to the mass enclosed within the orbit. If the mass enclosed increases, the radial force increases, which decreases the orbital period and therefore increases the orbital frequency Ω_R. We see that the potential with the largest scale radius comes closest to the $\Omega_{\phi/z} : \Omega_R$ is $2 : 3$ resonance. $\Omega_z : \Omega_\phi$ remains centred around the $1 : 1$ resonance, showing that it is not strongly sensitive to the mass enclosed.

B.3 Varying the Mass of the Stellar Disks

Fig. 58 shows the dependence of the frequency ratios on the mass of the two stellar disks. A lighter or heavier disk changes the vertical force, which changes the orbital period and hence the orbital frequency Ω_z. The ratio $\Omega_z : \Omega_R$ increases when the disk is made heavier, while $\Omega_\phi : \Omega_z$ decreases. We see that the potential with the smallest disk mass comes closest to the $\Omega_z : \Omega_R$ is $2 : 3$ resonance. As the disks are very flattened distributions of stars, a heavier disk (or, in other words, a larger contribution of the disk to the gravitational potential) will make the overall gravitational potential flatter. For a heavier disk, and thus a more flattened potential, the ratio $\Omega_\phi : \Omega_z$ goes down, while for a lighter disk, and thus a more prolate potential, the ratio goes up. The change in $\Omega_\phi : \Omega_z$ is not as large as when I varied the flattening of the halo, as the contribution of the halo is larger than that of the disks in the region probed by the Helmi Streams, see Fig. 8.

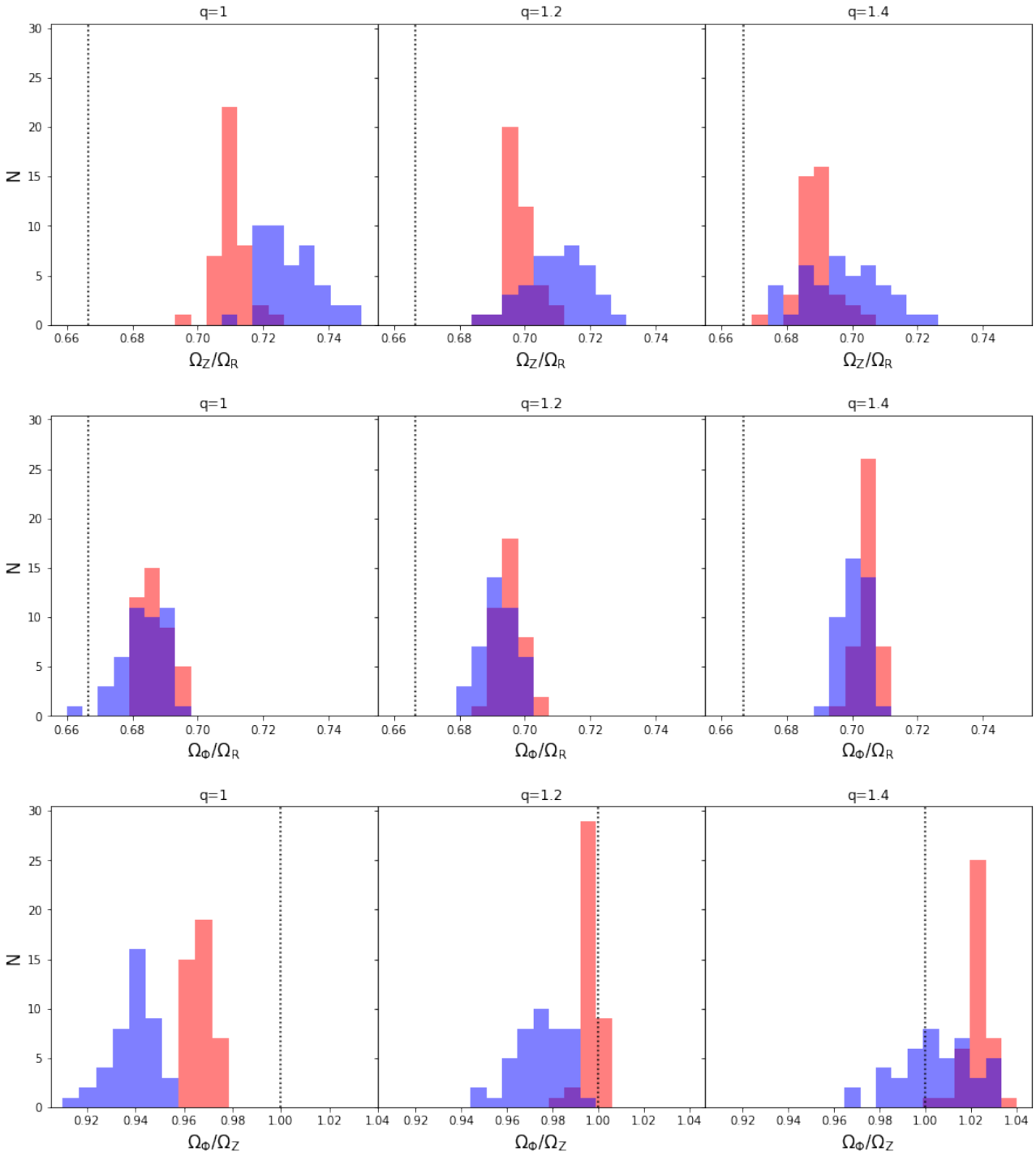

Figure 56: Orbital frequency ratio distribution of hiL clump stars (red) and loL clump stars (blue) in the *Gaia* EDR3 RVS sample in different potentials. *Middle panel:* Default Potential (see Section 1.7.4). *Left and right panel:* Default Potential with a varying flattening in the density of the halo. The density is adjusted such that the rotation curves are consistent. Some resonances are indicated as grey dashed lines.

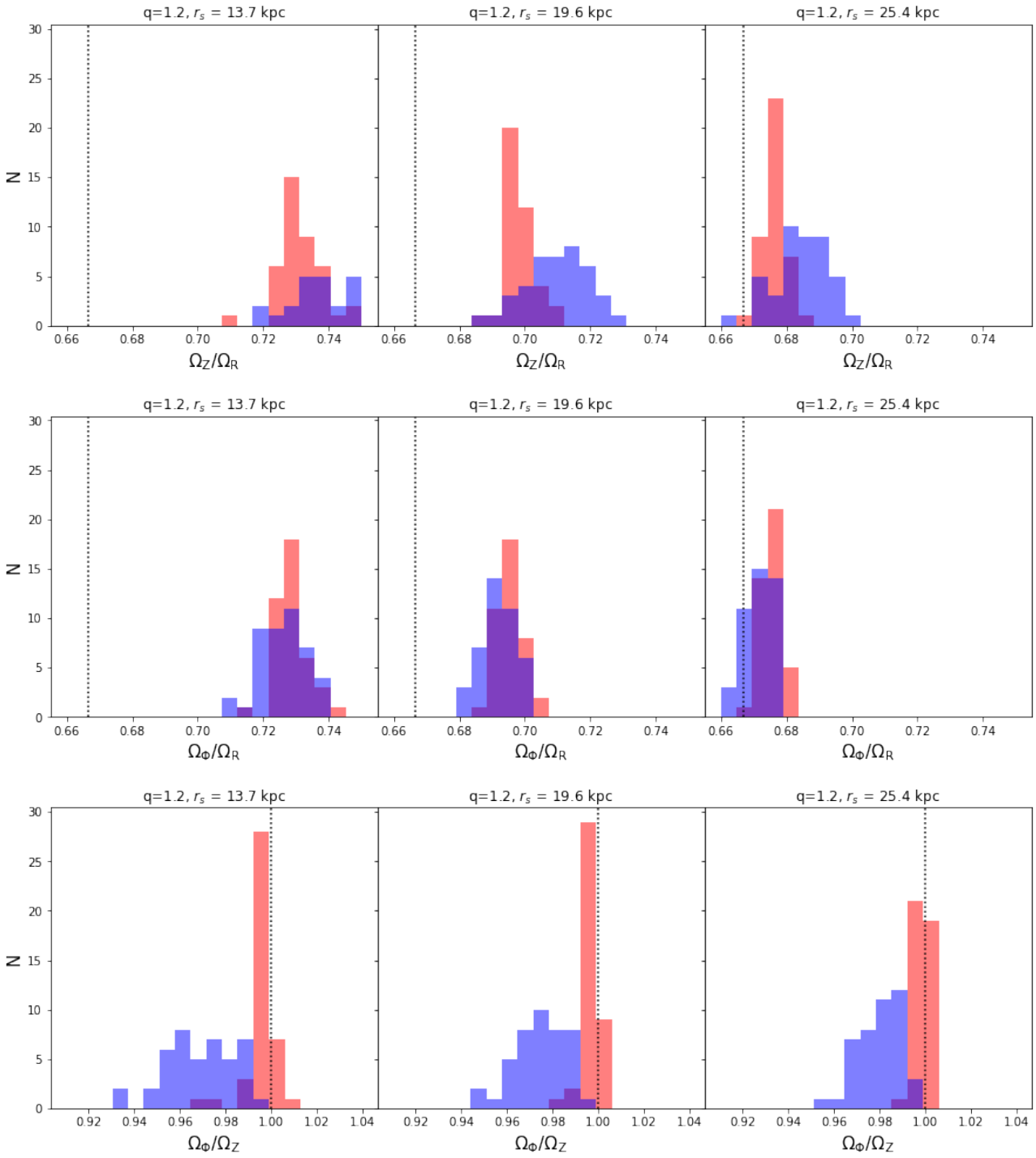

Figure 57: Orbital frequency ratio distribution of hiL clump stars (red) and loL clump stars (blue) in the *Gaia* EDR3 RVS sample in different potentials. *Middle panel:* Default Potential (see Section 1.7.4). *Left and right panel:* Default Potential with a varying halo scale radius r_s. As the density of the halo is kept fixed, a larger scale radius corresponds to a more massive halo. Some resonances are indicated as grey dashed lines.

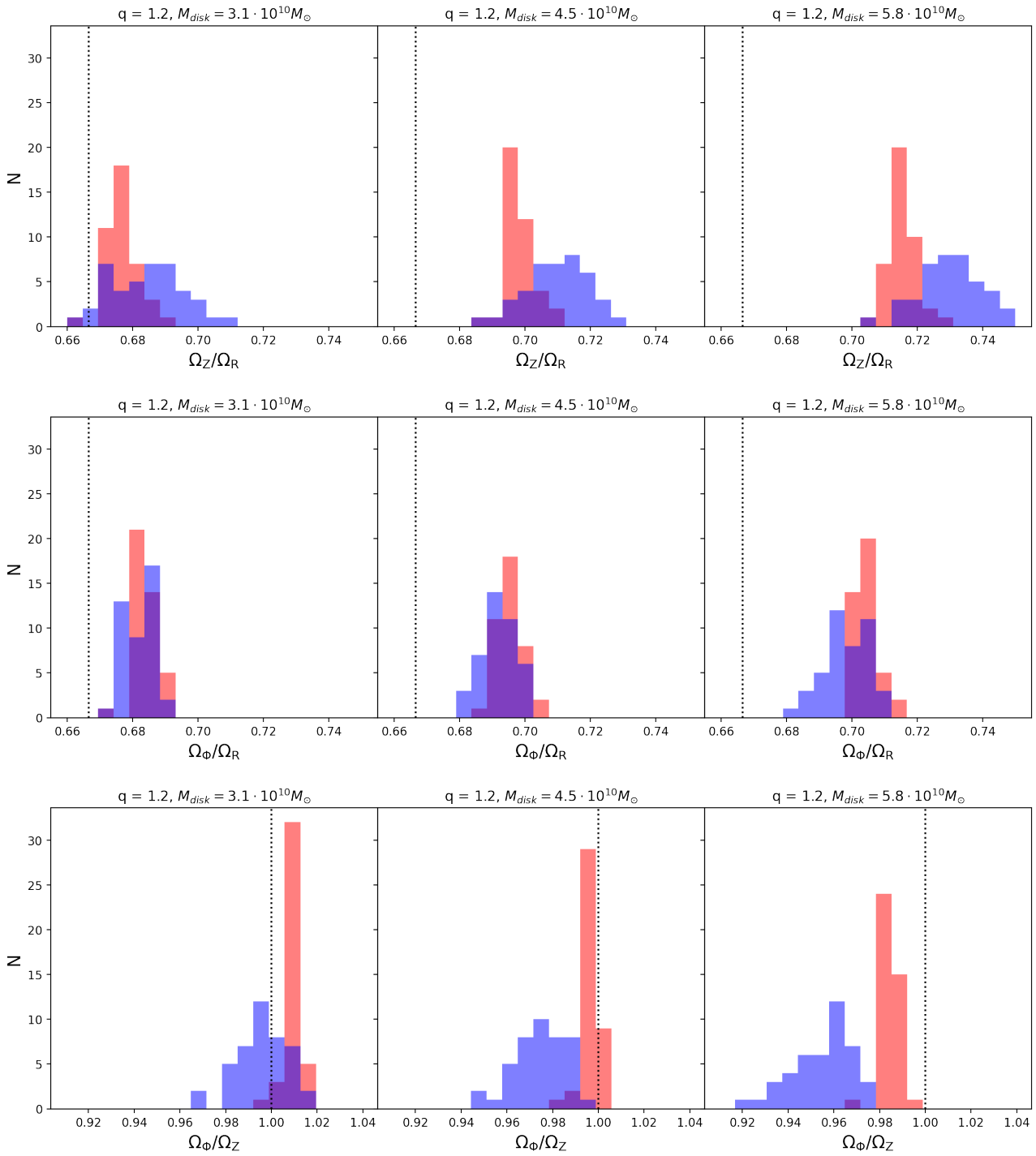

Figure 58: Orbital frequency ratio distribution of hiL clump stars (red) and loL clump stars (blue) in the *Gaia* EDR3 RVS sample in different potentials. *Middle panel:* Default Potential (see Section 1.7.4). *Left and right panel:* Default Potential with varying total stellar disk masses, the ratio of the thin and thick stellar disk mass is kept fixed. Some resonances are indicated as grey dashed lines.

C Exploring the MCMC Chains of McMillan 2017 and Cautun et al. 2020

The McMillan 2017 potential model was determined by doing an MCMC given a likelihood and a set of observational constraints. Therefore, their best fitting model is based on thousands of slightly different potentials, all satisfying those constraints. While the gas disks were kept fixed, parameters of the bulge, stellar disks and DM halo were allowed to vary. It is informative to investigate how the $\Omega_z : \Omega_R$ ratio depends on these parameters.

Paul McMillan was so kind to share the MCMC chains of his Milky Way potential model fit from McMillan 2017. Fig. 59 shows a sample of 210 sets of parameters randomly drawn from the chains. The colourmap indicates how close to the 2 : 3 resonance the hiL clump stars are. It is clear that there is no dependence on the bulge mass. In general, to get the hiL clump closer to the $\Omega_z : \Omega_R$ is 2 : 3 resonance, lower disk scale radii, but also lower disk scale radii in combination with lower disk surface densities are preferred. This implies a preference for a lower disk mass. Moreover, a higher density of the halo in combination with a higher scale radius is preferred, implying a preference for a more massive halo. To confirm this, Fig. 60 shows the same set of parameters but transformed to the respective masses of the stellar disks and mass enclosed within 20 kpc for the halo. We now see clearly that, in order to get the Helmi Streams onto the 2 : 3 resonance, a halo with a high mass within 20 kpc (this increases Ω_R) is needed in combination with low stellar disk masses (this decreases Ω_z). However, within the freedom of the parameters in the MCMC chains, it is not possible to get the stars **on** the 2 : 3 resonance. The hiL stars are on average off by $|\Omega_z/\Omega_R - 2/3| > 0.03$.

I performed a similar exercise with the chains of the Cautun et al. 2020 potential model, as Marius Cautun was so kind to share those. This confirmed what is seen in the McMillan 2017 chains. The Cautun et al. 2020 model has a contracted DM halo and is made to fit Eilers et al. 2019 circular velocity curve, see Fig. 61. The biggest difference with the McMillan 2017 model is therefore that the ratio of $\Omega_z : \Omega_R$ is higher, as the virial mass, and therefore the mass enclosed within, say, 20 kpc is lower.

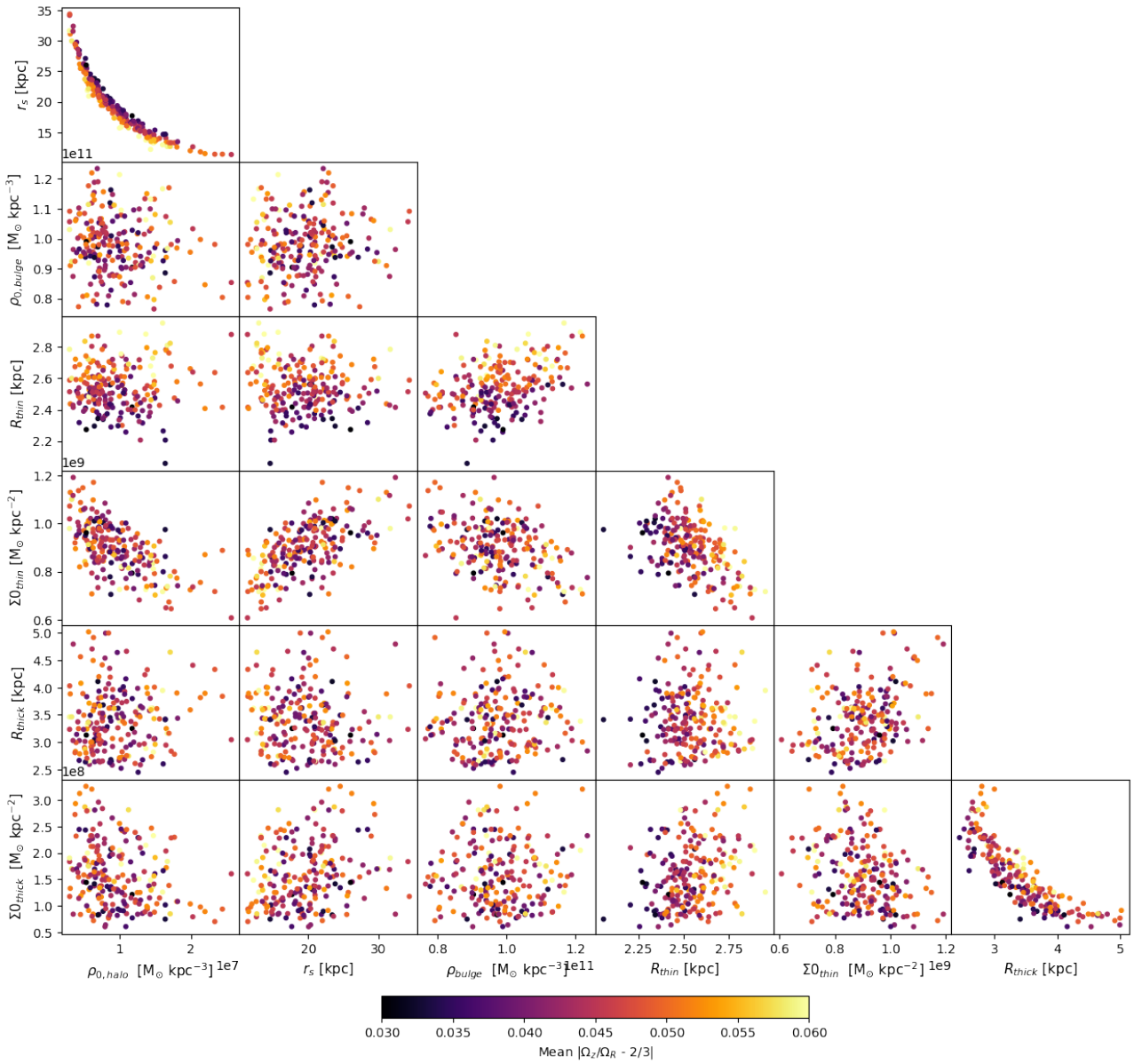

Figure 59: 210 sets of potential parameters randomly sampled from the McMillan 2017 MCMC chains. The parameters of each potential are coloured by the average distance of the hiL clump stars from the $\Omega_z : \Omega_R$ is 2 : 3 resonance.

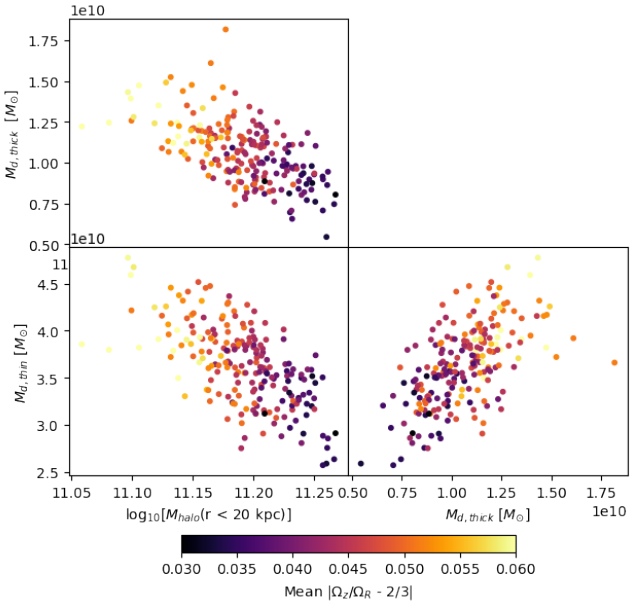

Figure 60: 210 sets of potential parameters randomly sampled from the McMillan 2017 MCMC chains, transformed to the respective masses of the stellar disks and mass enclosed within 20 kpc for the halo. The parameters of each potential are coloured by the average distance of the hiL clump stars from the $\Omega_z : \Omega_R$ is 2 : 3 resonance.

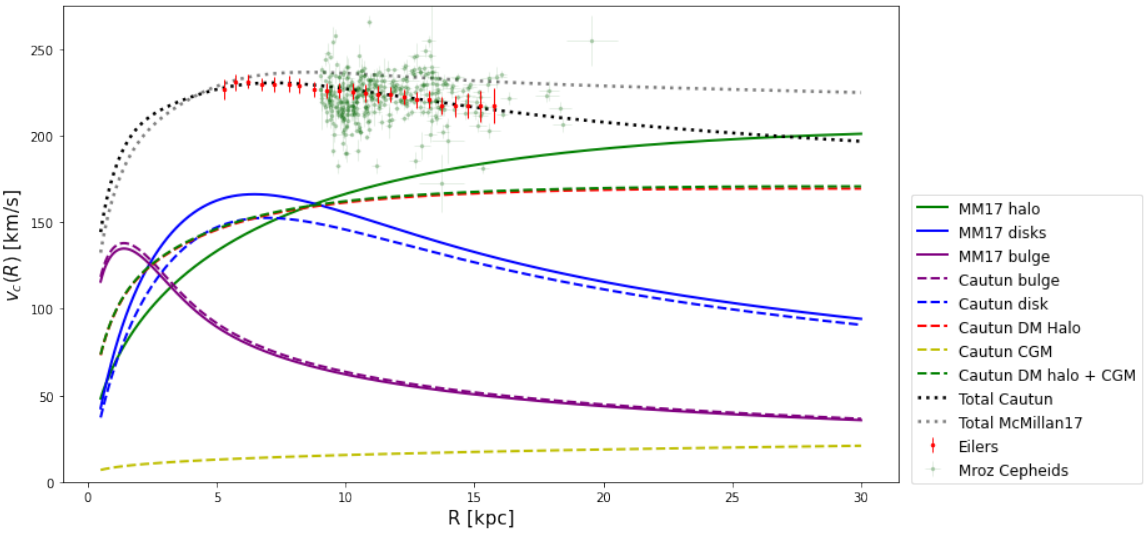

Figure 61: Rotation curves of the different components of the McMillan 2017 (dashed) and Cautun et al. 2020 (solid) potential models. Rotation curve data from Eilers et al. 2019 (red) and the Cepheids from Mróz et al. 2019 are overplotted. The Cautun et al. 2020 disks are lighter and the Cautun et al. 2020 halo is more massive in the centre as it is contracted, but it is lighter farther out. The total Cautun et al. 2020 potential matches the Eilers et al. 2019 rotation curve well.

D Dependency Orbital Structure on the Gravitational Potential

The location in phase space where a resonance can be found is dependent on the potential. To illustrate this, Fig. 62 shows how the location of the resonance changes with a different flattening in the potential. The SoS correspond to a set of 12 stars that are close in phase-space and have $L_z = 1000\text{kpc km s}^{-1}$, $E = -14000\text{km}^2\text{ s}^{-2}$, $z = 1$ kpc, $v_z = 250\text{km s}^{-1}$, $\phi = \pi$, and R ranges from 7 till 9.5 kpc. $v_\phi = L_z/R$ and v_R follows from conservation of energy.

For $q = 1.2$, we see that the there are stars whose consequents trace out islands, which are stars that are resonantly trapped around the $\Omega_z : \Omega_R$ is $2 : 3$ resonance. Stars exactly on the resonance would trace out a dot falling in the middle of the islands, as the resonance reduces the dimensionality of the orbit. Invariant curves of stars with slightly different initial conditions hug around the islands. For $q = 1$, the islands disappear entirely as the stars are no longer close to the resonance, and we thus see that the sphericity of the halo has significantly changed the orbital structure of the potential. For $q = 1.4$, we see something interesting happen. Stars are still resonantly trapped around the $\Omega_z : \Omega_R$ is $2 : 3$ resonance, but at a different location than for $q = 1.2$. The star that comes the closest to the Galactic Center (coloured in yellow because it is far away from the $2 : 3$ resonance) does not trace out an invariant curve, but instead fills a large part of the (R, v_R) plane. This orbit is a chaotic orbit.

Fig. 62 seems to suggest that by simply changing the flattening and density of the potential, the orbital structure of the potential can be changed. Resonances "move" around depending on characteristic parameters of the potential. This has been explored in detail by Zotos 2014 and Caranicolas and Zotos 2010, who for example find that an increasingly prolate (higher value of q) potential gives rise to more chaotic orbits.

E Actions and Angles[36]

Usually we express the phase-space coordinates of an object or star as $(\vec{x}, \vec{v}) = (x, y, z, v_x, v_y, v_z)$. It can however be very useful to use a set of canonical coordinates called action-angle variables, $(\vec{\theta}, \vec{J})$, where $\vec{\theta}$ are the angles and $\vec{J}$ are the actions. As action-angle variables are canonical, the phase-space volume occupied by $d^3\vec{x} \cdot d^3\vec{v} = d^3\vec{\theta} \cdot d^3\vec{J}$. What makes these coordinates special is that the actions are integrals of motion, meaning they are constants (conserved over time), and therefore

$$\dot{J}_i = -\frac{\partial H}{\partial \theta_i} = 0 \tag{31}$$

so the Hamiltonian is independent of $\vec{\theta}$, and hence $H = H(\vec{J})$. This means the angles will simply increase linearly with time

$$\dot{\theta}_i = -\frac{\partial H}{\partial J_i} \equiv \Omega_i(\vec{J}) = \text{const.} \Rightarrow \theta_i(t) = \theta_i(0) + \Omega_i t \tag{32}$$

where $\vec{\Omega}$ are the fundamental frequencies. In a spherical potential, $\Omega_i = \frac{2\pi}{T_i}$, where T_i is the period. An orbit in action-angle variables is thus described by $\vec{J} = \textit{constant}$ and $\vec{\theta} = \vec{\Omega}t + \textit{constant}$, and so the transformation to action-angle variables reduces the description of an orbit in 6D phase-space to a description by three angle coordinates, as the actions are constant. A potential that admits the transformation to action-angle variables is said to be integrable, and unfortunately these are rare. One class of potentials that does admit this is the class of Stäckel potentials. These potentials have three isolating integrals which we can calculate analytically and their Hamilton-Jacobi equation is separable in confocal ellipsoidal coordinates (see e.g. de Zeeuw 1985). Since the motion is separable, the sum of three motions (one in each coordinate) describes the orbit.

Another useful property of actions is that they are adiabatic invariants. When the potential evolves slowly, such that the variations in the potential are slow compared to a typical orbital frequency, it is said to evolve adiabatically. During such adiabatic changes of the potential the actions of stars are constant, making them adiabatic invariants[37]. This makes actions very attractive to study the merger history of the Milky Way, as the actions of substructure are conserved even under adiabatic changes of the gravitational potential. Therefore, stars of substructure are expected to be clustered in action space even today (Wu et al. 2022; Malhan et al. 2022; Callingham et al. 2022), and even when the substructure is fully phase-mixed.

In a spherical or axisymmetric potential, it is useful to express actions in cylindrical coordinates, (J_R, J_z, J_ϕ). J_R, the radial action, describes the extent of oscillations in spherical radius, while J_z, the vertical action, describes the extent of oscillation in the vertical dimension. J_ϕ, the azimuthal action, is equal to the z-component of the angular momentum L_z, which is conserved in spherical and axisymmetric potentials. In a spherical potential, $J_z + |J_\phi| = L$, where L is the total angular momentum (conserved in a spherical potential). Note that for any spherical potential the Hamilton-Jacobi equation is separable, but often the radial action J_R cannot be computed analytically.

We have established that action-angle variables are useful quantities to study the motions of stars, but in order to make use of them we have to be able to compute them from normal phase-space coordinates. However, none of the realistic gravitational potential models popular today (e.g. McMillan 2017) is of Stäckel form, so we cannot compute actions and angles in these potentials analytically. Luckily, we can numerically approximate action-angle variables in potentials that are not Stäckel potentials (see Sanders and Binney 2016 for an extensive overview), which can be done for example by torus construction (see e.g. Binney and McMillan 2011) or by using the adiabatic approximation (Binney 2010), though the latter only holds for stars that stay close to the mid-plane of the Galaxy. A nowadays popular method is the Stäckel fudge for axisymmetric potentials, in which we approximate the region of the potential explored by the orbit locally by a Stäckel potential, which allows us to calculate the actions and angles numerically (Binney 2012). As this is an approximation, the actions are not exactly conserved along the orbit and uncertainties on the percentage level are expected (Binney 2012; Sanders 2012).

[36] A large part of this section is adapted from Section 3.5 of Binney and Tremaine 2008

[37] However, an action J_i that has a fundamental frequency $\Omega_i = 0$ is not an adiabatic invariant.

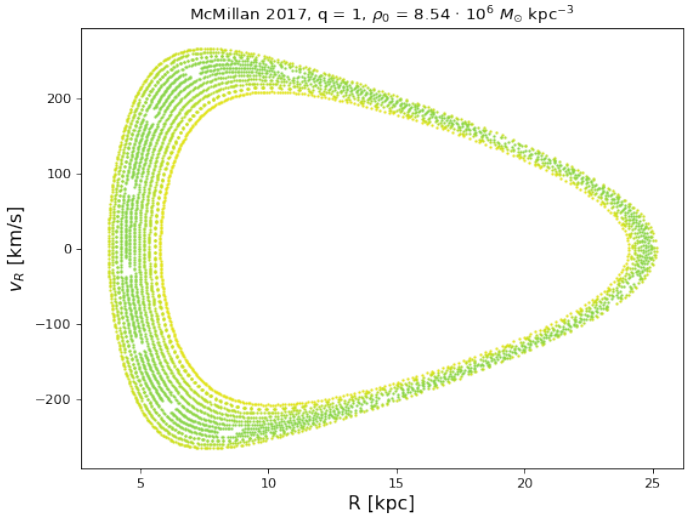

(a)

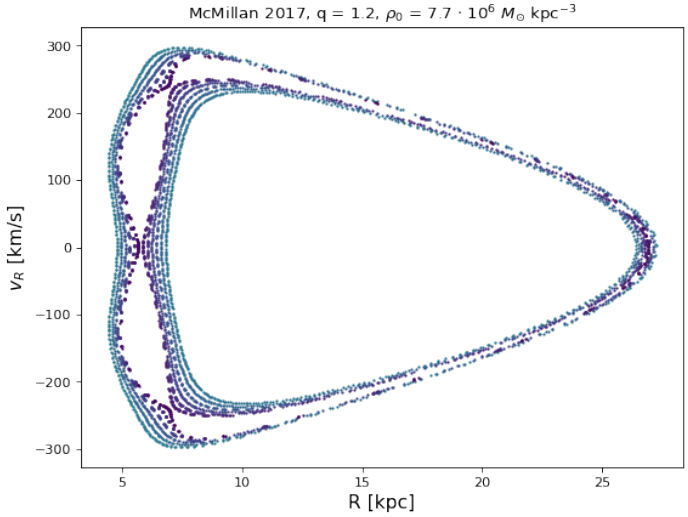

(b)

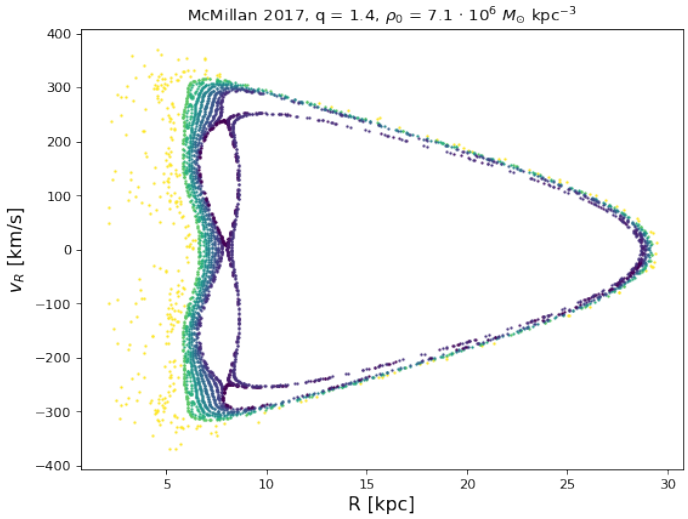

(c)

Figure 62: SoS of 12 stars located close to each other in phase space ($L_z = 1000\,\mathrm{kpc\,km\,s^{-1}}$, $E = -122500\,\mathrm{km^2\,s^{-2}}$, $z = 1$ kpc, $v_z = 250\,\mathrm{km\,s^{-1}}$, $\phi = \pi$, and R ranges from 6.8 till 9.3 kpc. $v_\phi = L_z/R$ and v_R follows from conservation of energy) in three potentials with different values for the flattening in the density and density parameter ρ_0, *Panel (a):* $q = 1$, $\rho_0 = 8.54 \cdot \mathrm{M_\odot\,kpc^{-3}}$ (McMillan 2017) *Panel (b):* $q = 1.2$, $\rho_0 = 7.7 \cdot \mathrm{M_\odot\,kpc^{-3}}$ (default) and *Panel (c)* $q = 1.4$, $\rho_0 = 7.1 \cdot \mathrm{M_\odot\,kpc^{-3}}$. The colours indicate how far away from the $\Omega_z : \Omega_R$ is 2 : 3 resonance the stars are, the darker the closer, where the darkest colour indicates that the distance from 2 : 3 is less than 0.002, and where the lightest colour indicates that the distance from 2 : 3 is more than 0.025 in frequency space.

References

Ahumada, Romina et al. (July 2020). "The 16th Data Release of the Sloan Digital Sky Surveys: First Release from the APOGEE-2 Southern Survey and Full Release of eBOSS Spectra". In: *ApJS* 249.1, 3, p. 3. DOI: 10.3847/1538-4365/ab929e. arXiv: 1912.02905 [astro-ph.GA].

Amarante, João A. S., Victor P. Debattista, Leandro Beraldo e Silva, Chervin F. P. Laporte, and Nathan Deg (Apr. 2022). "GASTRO library I: the simulated chemodynamical properties of several GSE-like stellar halos". In: *arXiv e-prints*, arXiv:2204.12187, arXiv:2204.12187. arXiv: 2204.12187 [astro-ph.GA].

Amorisco, Nicola C., Facundo A. Gómez, Simona Vegetti, and Simon D. M. White (July 2016). "Gaps in globular cluster streams: giant molecular clouds can cause them too". In: *Monthly Notices of the Royal Astronomical Society: Letters* 463.1, pp. L17–L21. ISSN: 1745-3925. DOI: 10.1093/mnrasl/slw148. eprint: https://academic.oup.com/mnrasl/article-pdf/463/1/L17/8010309/slw148.pdf. URL: https://doi.org/10.1093/mnrasl/slw148.

Anderhalden, Donnino, Aurel Schneider, Andrea V. Macciò, Juerg Diemand, and Gianfranco Bertone (Mar. 2013). "Hints on the nature of dark matter from the properties of Milky Way satellites". In: *J. Cosmology Astropart. Phys.* 2013.3, 014, p. 014. DOI: 10.1088/1475-7516/2013/03/014. arXiv: 1212.2967 [astro-ph.CO].

Antoja, T. et al. (Sept. 2018). "A dynamically young and perturbed Milky Way disk". In: *Nature* 561.7723, pp. 360–362. DOI: 10.1038/s41586-018-0510-7. arXiv: 1804.10196 [astro-ph.GA].

Astropy Collaboration et al. (Oct. 2013). "Astropy: A community Python package for astronomy". In: *A&A* 558, A33, A33. DOI: 10.1051/0004-6361/201322068. arXiv: 1307.6212 [astro-ph.IM].

Baade, W. (Aug. 1946). "A Search For the Nucleus of Our Galaxy". In: *PASP* 58.343, pp. 249–252. DOI: 10.1086/125835.

Babusiaux, C. et al. (June 2022). "Gaia Data Release 3: Catalogue Validation". In: *arXiv e-prints*, arXiv:2206.05989, arXiv:2206.05989. arXiv: 2206.05989 [astro-ph.SR].

Balbinot, E. et al. (Mar. 2016). "The Phoenix Stream: A Cold Stream in the Southern Hemisphere". In: *ApJ* 820.1, 58, p. 58. DOI: 10.3847/0004-637X/820/1/58. arXiv: 1509.04283 [astro-ph.GA].

Banik, Nilanjan and Jo Bovy (Apr. 2019). "Effects of baryonic and dark matter substructure on the Pal 5 stream". In: *MNRAS* 484.2, pp. 2009–2020. DOI: 10.1093/mnras/stz142. arXiv: 1809.09640 [astro-ph.GA].

Barber, Christopher, Else Starkenburg, Julio F. Navarro, Alan W. McConnachie, and Azadeh Fattahi (Jan. 2014). "The orbital ellipticity of satellite galaxies and the mass of the Milky Way". In: *MNRAS* 437.1, pp. 959–967. DOI: 10.1093/mnras/stt1959. arXiv: 1310.0466 [astro-ph.GA].

Barbuy, Beatriz, Cristina Chiappini, and Ortwin Gerhard (Sept. 2018). "Chemodynamical History of the Galactic Bulge". In: *ARA&A* 56, pp. 223–276. DOI: 10.1146/annurev-astro-081817-051826. arXiv: 1805.01142 [astro-ph.GA].

Bastian, Nate and Carmela Lardo (Sept. 2018). "Multiple Stellar Populations in Globular Clusters". In: *ARA&A* 56, pp. 83–136. DOI: 10.1146/annurev-astro-081817-051839. arXiv: 1712.01286 [astro-ph.SR].

Behroozi, Peter, Risa H. Wechsler, Andrew P. Hearin, and Charlie Conroy (Sept. 2019). "UNIVERSEMACHINE: The correlation between galaxy growth and dark matter halo assembly from z = 0-10". In: *MNRAS* 488.3, pp. 3143–3194. DOI: 10.1093/mnras/stz1182. arXiv: 1806.07893 [astro-ph.GA].

Belokurov, V. et al. (Mar. 2007). "An Orphan in the "Field of Streams"". In: *ApJ* 658.1, pp. 337–344. DOI: 10.1086/511302. arXiv: astro-ph/0605705 [astro-ph].

Belokurov, Vasily, Denis Erkal, N. W. Evans, S. E. Koposov, and A. J. Deason (July 2018). "Co-formation of the disc and the stellar halo". In: *MNRAS* 478.1, pp. 611–619. DOI: 10.1093/mnras/sty982. arXiv: 1802.03414 [astro-ph.GA].

Bennett, Morgan and Jo Bovy (Jan. 2019). "Vertical waves in the solar neighbourhood in Gaia DR2". In: *MNRAS* 482.1, pp. 1417–1425. DOI: 10.1093/mnras/sty2813. arXiv: 1809.03507 [astro-ph.GA].

Bensby, T., A. Alves-Brito, M. S. Oey, D. Yong, and J. Meléndez (July 2011). "A First Constraint on the Thick Disk Scale Length: Differential Radial Abundances in K Giants at Galactocentric Radii 4, 8, and 12 kpc". In: *ApJ* 735.2, L46, p. L46. DOI: 10.1088/2041-8205/735/2/L46. arXiv: 1106.1914 [astro-ph.GA].

Bensby, T. et al. (Sept. 2017). "Chemical evolution of the Galactic bulge as traced by microlensed dwarf and subgiant stars. VI. Age and abundance structure of the stellar populations in the central sub-kpc of the Milky Way". In: *A&A* 605, A89, A89. DOI: 10.1051/0004-6361/201730560. arXiv: 1702.02971 [astro-ph.GA].

Besla, Gurtina et al. (Oct. 2007). "Are the Magellanic Clouds on Their First Passage about the Milky Way?" In: *ApJ* 668.2, pp. 949–967. DOI: 10.1086/521385. arXiv: astro-ph/0703196 [astro-ph].

Bienaymé, O. et al. (Nov. 2014). "Weighing the local dark matter with RAVE red clump stars". In: *A&A* 571, A92, A92. DOI: 10.1051/0004-6361/201424478. arXiv: 1406.6896 [astro-ph.GA].

Binney, James (Feb. 2010). "Distribution functions for the Milky Way". In: *MNRAS* 401.4, pp. 2318–2330. DOI: 10.1111/j.1365-2966.2009.15845.x. arXiv: 0910.1512 [astro-ph.GA].

– (Oct. 2012). "Actions for axisymmetric potentials". In: *MNRAS* 426.2, pp. 1324–1327. DOI: 10.1111/j.1365-2966.2012.21757.x. arXiv: 1207.4910 [astro-ph.GA].

Binney, James, Ortwin Gerhard, and David Spergel (June 1997). "The photometric structure of the inner Galaxy". In: *MNRAS* 288.2, pp. 365–374. DOI: 10.1093/mnras/288.2.365. arXiv: astro-ph/9609066 [astro-ph].

Binney, James and Paul J. McMillan (May 2011). "Models of our Galaxy - II". In: *MNRAS* 413.3, pp. 1889–1898. DOI: 10.1111/j.1365-2966.2011.18268.x. arXiv: 1101.0747 [astro-ph.GA].

Binney, James and Scott Tremaine (2008). *Galactic Dynamics: Second Edition*.

Bland-Hawthorn, Joss and Ortwin Gerhard (Sept. 2016). "The Galaxy in Context: Structural, Kinematic, and Integrated Properties". In: *ARA&A* 54, pp. 529–596. DOI: 10.1146/annurev-astro-081915-023441. arXiv: 1602.07702 [astro-ph.GA].

Bobylev, V. V. and A. T. Bajkova (Aug. 2021). "Estimation of the Radial Scale Length and Vertical Scale Height of the Galactic Thin Disk from Cepheids". In: *Astronomy Letters* 47.8, pp. 534–543. DOI: 10.1134/S1063773721070033. arXiv: 2110.11203 [astro-ph.GA].

Bonaca, Ana and David W. Hogg (Nov. 2018). "The Information Content in Cold Stellar Streams". In: *ApJ* 867.2, 101, p. 101. DOI: 10.3847/1538-4357/aae4da. arXiv: 1804.06854 [astro-ph.GA].

Bonaca, Ana, David W. Hogg, Adrian M. Price-Whelan, and Charlie Conroy (July 2019). "The Spur and the Gap in GD-1: Dynamical Evidence for a Dark Substructure in the Milky Way Halo". In: *ApJ* 880.1, 38, p. 38. DOI: 10.3847/1538-4357/ab2873. arXiv: 1811.03631 [astro-ph.GA].

Bonaca, Ana et al. (Mar. 2021). "Orbital Clustering Identifies the Origins of Galactic Stellar Streams". In: *ApJ* 909.2, L26, p. L26. DOI: 10.3847/2041-8213/abeaa9. arXiv: 2012.09171 [astro-ph.GA].

Bovy, Jo (Feb. 2015). "galpy: A python LIBRARY FOR GALACTIC DYNAMICS". In: *The Astrophysical Journal Supplement Series* 216.2, p. 29. ISSN: 1538-4365. DOI: 10.1088/0067-0049/216/2/29. URL: http://dx.doi.org/10.1088/0067-0049/216/2/29.

Bovy, Jo, Anita Bahmanyar, Tobias K. Fritz, and Nitya Kallivayalil (Dec. 2016a). "The Shape of the Inner Milky Way Halo from Observations of the Pal 5 and GD–1 Stellar Streams". In: *ApJ* 833.1, 31, p. 31. DOI: 10.3847/1538-4357/833/1/31. arXiv: 1609.01298 [astro-ph.GA].

Bovy, Jo et al. (May 2016b). "The Stellar Population Structure of the Galactic Disk". In: *ApJ* 823.1, 30, p. 30. DOI: 10.3847/0004-637X/823/1/30. arXiv: 1509.05796 [astro-ph.GA].

Bowden, A., V. Belokurov, and N. W. Evans (May 2015). "Dipping our toes in the water: first models of GD-1 as a stream". In: *MNRAS* 449.2, pp. 1391–1400. DOI: 10.1093/mnras/stv285. arXiv: 1502.00484 [astro-ph.GA].

Bower, Richard G. et al. (Feb. 2017). "The dark nemesis of galaxy formation: why hot haloes trigger black hole growth and bring star formation to an end". In: *MNRAS* 465.1, pp. 32–44. DOI: 10.1093/mnras/stw2735. arXiv: 1607.07445 [astro-ph.GA].

Boylan-Kolchin, Michael, James S. Bullock, and Manoj Kaplinghat (July 2011). "Too big to fail? The puzzling darkness of massive Milky Way subhaloes". In: *MNRAS* 415.1, pp. L40–L44. DOI: 10.1111/j.1745-3933.2011.01074.x. arXiv: 1103.0007 [astro-ph.CO].

– (May 2012). "The Milky Way's bright satellites as an apparent failure of ΛCDM". In: *MNRAS* 422.2, pp. 1203–1218. DOI: 10.1111/j.1365-2966.2012.20695.x. arXiv: 1111.2048 [astro-ph.CO].

Breddels, Maarten A. and Jovan Veljanoski (Oct. 2018). "Vaex: big data exploration in the era of Gaia". In: *A&A* 618, A13, A13. DOI: 10.1051/0004-6361/201732493. arXiv: 1801.02638 [astro-ph.IM].

Buder, Sven et al. (Sept. 2021). "The GALAH+ survey: Third data release". In: *MNRAS* 506.1, pp. 150–201. DOI: 10.1093/mnras/stab1242. arXiv: 2011.02505 [astro-ph.GA].

Bullock, James S. and Michael Boylan-Kolchin (Aug. 2017). "Small-Scale Challenges to the ΛCDM Paradigm". In: *ARA&A* 55.1, pp. 343–387. DOI: 10.1146/annurev-astro-091916-055313. arXiv: 1707.04256 [astro-ph.CO].

Callingham, Thomas M. et al. (Apr. 2019). "The mass of the Milky Way from satellite dynamics". In: *MNRAS* 484.4, pp. 5453–5467. DOI: 10.1093/mnras/stz365. arXiv: 1808.10456 [astro-ph.GA].

Callingham, Thomas M. et al. (Feb. 2022). "The Chemo-Dynamical Groups of Galactic Globular Clusters". In: *arXiv e-prints*, arXiv:2202.00591, arXiv:2202.00591. arXiv: 2202.00591 [astro-ph.GA].

Caranicolas, N.D. and E.E. Zotos (Mar. 2010). "The evolution of chaos in active galaxy models with an oblate or a prolate dark halo component". In: *Astronomische Nachrichten* 331.3, pp. 330–337. DOI: 10.1002/asna.200911302. URL: https://doi.org/10.1002%5C%2Fasna.200911302.

Cardelli, Jason A., Geoffrey C. Clayton, and John S. Mathis (Oct. 1989). "The Relationship between Infrared, Optical, and Ultraviolet Extinction". In: *ApJ* 345, p. 245. DOI: 10.1086/167900.

Carlberg, Raymond G. (July 2018). "Globular Clusters in a Cosmological N-body Simulation". In: *ApJ* 861.1, 69, p. 69. DOI: 10.3847/1538-4357/aac88a. arXiv: 1706.01938 [astro-ph.GA].

Cautun, Marius, Carlos S. Frenk, Rien van de Weygaert, Wojciech A. Hellwing, and Bernard J. T. Jones (Dec. 2014). "Milky Way mass constraints from the Galactic satellite gap". In: *MNRAS* 445.2, pp. 2049–2060. DOI: 10.1093/mnras/stu1849. arXiv: 1405.7697 [astro-ph.CO].

Cautun, Marius et al. (May 2020). "The milky way total mass profile as inferred from Gaia DR2". In: *MNRAS* 494.3, pp. 4291–4313. DOI: 10.1093/mnras/staa1017. arXiv: 1911.04557 [astro-ph.GA].

Cheng, Judy Y. et al. (June 2012). "A Short Scale Length for the α-enhanced Thick Disk of the Milky Way: Evidence from Low-latitude SEGUE Data". In: *ApJ* 752.1, 51, p. 51. DOI: 10.1088/0004-637X/752/1/51. arXiv: 1204.5179 [astro-ph.GA].

Chiba, Masashi and Timothy C. Beers (June 2000). "Kinematics of Metal-poor Stars in the Galaxy. III. Formation of the Stellar Halo and Thick Disk as Revealed from a Large Sample of Nonkinematically Selected Stars". In: *The Astronomical Journal* 119.6, pp. 2843–2865. DOI: 10.1086/301409. URL: https://doi.org/10.1086%5C%2F301409.

Contopoulos, G. and M. Harsoula (June 2010). "Stickiness effects in chaos". In: *Celestial Mechanics and Dynamical Astronomy* 107.1-2, pp. 77–92. DOI: 10.1007/s10569-010-9282-6.

Cordero, M. J. et al. (Mar. 2017). "Differences in the rotational properties of multiple stellar populations in M13: a faster rotation for the 'extreme' chemical subpopulation". In: *MNRAS* 465.3, pp. 3515–3535. DOI: 10.1093/mnras/stw2812. arXiv: 1610.09374 [astro-ph.GA].

Correa Magnus, Lilia and Eugene Vasiliev (Apr. 2022). "Measuring the Milky Way mass distribution in the presence of the LMC". In: *MNRAS* 511.2, pp. 2610–2630. DOI: 10.1093/mnras/stab3726. arXiv: 2110.00018 [astro-ph.GA].

Cui, Xiang-Qun et al. (Sept. 2012). "The Large Sky Area Multi-Object Fiber Spectroscopic Telescope (LAMOST)". In: *Research in Astronomy and Astrophysics* 12.9, pp. 1197–1242. DOI: 10.1088/1674-4527/12/9/003.

Cunningham, Emily C. et al. (July 2020). "Quantifying the Stellar Halo's Response to the LMC's Infall with Spherical Harmonics". In: *ApJ* 898.1, 4, p. 4. DOI: 10.3847/1538-4357/ab9b88. arXiv: 2006.08621 [astro-ph.GA].

Dalessandro, Emanuele et al. (Oct. 2019). "A Family Picture: Tracing the Dynamical Path of the Structural Properties of Multiple Populations in Globular Clusters". In: *ApJ* 884.1, L24, p. L24. DOI: 10.3847/2041-8213/ab45f7. arXiv: 1910.00613 [astro-ph.SR].

Dalton, Gavin et al. (July 2014). "Project overview and update on WEAVE: the next generation wide-field spectroscopy facility for the William Herschel Telescope". In: *Ground-based and Airborne Instrumentation for Astronomy V*. Ed. by Suzanne K. Ramsay, Ian S. McLean, and Hideki Takami. Vol. 9147. Society of Photo-Optical Instrumentation Engineers (SPIE) Conference Series, 91470L, p. 91470L. DOI: 10.1117/12.2055132. arXiv: 1412.0843 [astro-ph.IM].

de Boer, T. J. L., Denis Erkal, and M. Gieles (June 2020). "A closer look at the spur, blob, wiggle, and gaps in GD-1". In: *MNRAS* 494.4, pp. 5315–5332. DOI: 10.1093/mnras/staa917. arXiv: 1911.05745 [astro-ph.GA].

de Boer, T. J. L. et al. (June 2019). "Globular cluster number density profiles using Gaia DR2". In: *MNRAS* 485.4, pp. 4906–4935. DOI: 10.1093/mnras/stz651. arXiv: 1901.08072 [astro-ph.GA].

de Jong, R. S. et al. (Mar. 2019). "4MOST: Project overview and information for the First Call for Proposals". In: *The Messenger* 175, pp. 3–11. DOI: 10.18727/0722-6691/5117. arXiv: 1903.02464 [astro-ph.IM].

de Salas, P. F., K. Malhan, K. Freese, K. Hattori, and M. Valluri (Oct. 2019). "On the estimation of the local dark matter density using the rotation curve of the Milky Way". In: *J. Cosmology Astropart. Phys.* 2019.10, 037, p. 037. DOI: 10.1088/1475-7516/2019/10/037. arXiv: 1906.06133 [astro-ph.GA].

de Zeeuw, P. T. (Sept. 1985). "Elliptical galaxies with separable potentials". In: *MNRAS* 216, pp. 273–334. DOI: 10.1093/mnras/216.2.273.

Deason, Alis J., Vasily Belokurov, and Jason L. Sanders (Dec. 2019). "The total stellar halo mass of the Milky Way". In: *MNRAS* 490.3, pp. 3426–3439. DOI: 10.1093/mnras/stz2793. arXiv: 1908.02763 [astro-ph.GA].

Denissenkov, P. A. and F. D. A. Hartwick (Jan. 2014). "Supermassive stars as a source of abundance anomalies of proton-capture elements in globular clusters". In: *MNRAS* 437.1, pp. L21–L25. DOI: 10.1093/mnrasl/slt133. arXiv: 1305.5975 [astro-ph.SR].

Di Matteo, P. et al. (Dec. 2019). "The Milky Way has no in-situ halo other than the heated thick disc. Composition of the stellar halo and age-dating the last significant merger with Gaia DR2 and APOGEE". In: *A&A* 632, A4, A4. DOI: 10.1051/0004-6361/201834929. arXiv: 1812.08232 [astro-ph.GA].

Dierickx, Marion I. P. and Abraham Loeb (Feb. 2017). "Predicted Extension of the Sagittarius Stream to the Milky Way Virial Radius". In: *ApJ* 836.1, 92, p. 92. DOI: 10.3847/1538-4357/836/1/92. arXiv: 1611.00089 [astro-ph.GA].

Dodd, Emma, Amina Helmi, and Helmer H. Koppelman (May 2021). "Substructures, Resonances and debris streams". In: *arXiv e-prints*, arXiv:2105.09957, arXiv:2105.09957. arXiv: 2105.09957 [astro-ph.GA].

Dodd, Emma et al. (June 2022). "The Gaia DR3 view of dynamical substructure in the stellar halo near the Sun". In: *arXiv e-prints*, arXiv:2206.11248, arXiv:2206.11248. arXiv: 2206.11248 [astro-ph.GA].

Eilers, Anna-Christina, David W. Hogg, Hans-Walter Rix, and Melissa K. Ness (Jan. 2019). "The Circular Velocity Curve of the Milky Way from 5 to 25 kpc". In: *ApJ* 871.1, 120, p. 120. DOI: 10.3847/1538-4357/aaf648. arXiv: 1810.09466 [astro-ph.GA].

Erkal, Denis, Vasily Belokurov, Jo Bovy, and Jason L. Sanders (Nov. 2016). "The number and size of subhalo-induced gaps in stellar streams". In: *MNRAS* 463.1, pp. 102–119. DOI: 10.1093/mnras/stw1957. arXiv: 1606.04946 [astro-ph.GA].

Erkal, Denis et al. (Aug. 2019). "The total mass of the Large Magellanic Cloud from its perturbation on the Orphan stream". In: *MNRAS* 487.2, pp. 2685–2700. DOI: 10.1093/mnras/stz1371. arXiv: 1812.08192 [astro-ph.GA].

Errani, Raphaël et al. (Mar. 2022). "The Pristine survey XVIII: C-19: Tidal debris of a dark matter-dominated globular cluster?" In: *arXiv e-prints*, arXiv:2203.02513, arXiv:2203.02513. arXiv: 2203.02513 [astro-ph.GA].

Eyre, Andy and James Binney (Oct. 2009). "Fitting orbits to tidal streams with proper motions". In: *MNRAS* 399.1, pp. L160–L163. DOI: 10.1111/j.1745-3933.2009.00744.x. arXiv: 0908.2081 [astro-ph.GA].

Fardal, Mark A. et al. (Mar. 2019). "Connecting the Milky Way potential profile to the orbital time-scales and spatial structure of the Sagittarius Stream". In: *MNRAS* 483.4, pp. 4724–4741. DOI: 10.1093/mnras/sty3428. arXiv: 1804.04995 [astro-ph.GA].

Fattahi, Azadeh et al. (Oct. 2020). "A tale of two populations: surviving and destroyed dwarf galaxies and the build-up of the Milky Way's stellar halo". In: *MNRAS* 497.4, pp. 4459–4471. DOI: 10.1093/mnras/staa2221. arXiv: 2002.12043 [astro-ph.GA].

Forbes, Duncan A. (Mar. 2020). "Reverse engineering the Milky Way". In: *MNRAS* 493.1, pp. 847–854. DOI: 10.1093/mnras/staa245. arXiv: 2002.01512 [astro-ph.GA].

Foreman-Mackey, Daniel (June 2016). "corner.py: Scatterplot matrices in Python". In: *The Journal of Open Source Software* 1.2, p. 24. DOI: 10.21105/joss.00024. URL: https://doi.org/10.21105/joss.00024.

Foreman-Mackey, Daniel, David W. Hogg, Dustin Lang, and Jonathan Goodman (Mar. 2013). "emcee: The MCMC Hammer". In: *PASP* 125.925, p. 306. DOI: 10.1086/670067. arXiv: 1202.3665 [astro-ph.IM].

Frenk, Carlos S., Simon D. M. White, Marc Davis, and George Efstathiou (Apr. 1988). "The Formation of Dark Halos in a Universe Dominated by Cold Dark Matter". In: *ApJ* 327, p. 507. DOI: 10.1086/166213.

Fritz, T. K. et al. (Nov. 2018). "Gaia DR2 proper motions of dwarf galaxies within 420 kpc. Orbits, Milky Way mass, tidal influences, planar alignments, and group infall". In: *A&A* 619, A103, A103. DOI: 10.1051/0004-6361/201833343. arXiv: 1805.00908 [astro-ph.GA].

Gaia Collaboration, A. G. A. Brown, A. Vallenari, T. Prusti, et al. (May 2021a). "Gaia Early Data Release 3. Summary of the contents and survey properties". In: *A&A* 649, A1, A1. DOI: 10.1051/0004-6361/202039657. arXiv: 2012.01533 [astro-ph.GA].

Gaia Collaboration, A. Vallenari, A.G.A. Brown, T. Prusti, et al. (2022). "Gaia Data Release 3. Summary of the content and survey properties". In: *A&A*. DOI: 10.1051/0004-6361/202243940.

Gaia Collaboration et al. (Nov. 2016). "The Gaia mission". In: *A&A* 595, A1, A1. DOI: 10.1051/0004-6361/201629272. arXiv: 1609.04153 [astro-ph.IM].

Gaia Collaboration et al. (Aug. 2018). "Gaia Data Release 2. Summary of the contents and survey properties". In: *A&A* 616, A1, A1. DOI: 10.1051/0004-6361/201833051. arXiv: 1804.09365 [astro-ph.GA].

Gaia Collaboration et al. (May 2021b). "Gaia Early Data Release 3. The Galactic anticentre". In: *A&A* 649, A8, A8. DOI: 10.1051/0004-6361/202039714. arXiv: 2101.05811 [astro-ph.GA].

Gallart, Carme et al. (July 2019). "Uncovering the birth of the Milky Way through accurate stellar ages with Gaia". In: *Nature Astronomy* 3, pp. 932–939. DOI: 10.1038/s41550-019-0829-5. arXiv: 1901.02900 [astro-ph.GA].

Garavito-Camargo, Nicolás et al. (Oct. 2019). "Hunting for the Dark Matter Wake Induced by the Large Magellanic Cloud". In: *ApJ* 884.1, 51, p. 51. DOI: 10.3847/1538-4357/ab32eb. arXiv: 1902.05089 [astro-ph.GA].

Garavito-Camargo, Nicolás et al. (Oct. 2021). "Quantifying the Impact of the Large Magellanic Cloud on the Structure of the Milky Way's Dark Matter Halo Using Basis Function Expansions". In: *ApJ* 919.2, 109, p. 109. DOI: 10.3847/1538-4357/ac0b44. arXiv: 2010.00816 [astro-ph.GA].

Gómez, Facundo A. and Amina Helmi (Feb. 2010). "On the identification of substructure in phase space using orbital frequencies". In: *MNRAS* 401.4, pp. 2285–2298. DOI: 10.1111/j.1365-2966.2009.15841.x. arXiv: 0904.1377 [astro-ph.GA].

Gómez, Facundo A., Amina Helmi, Anthony G. A. Brown, and Yang-Shyang Li (Oct. 2010). "On the identification of merger debris in the Gaia era". In: *MNRAS* 408.2, pp. 935–946. DOI: 10.1111/j.1365-2966.2010.17225.x. arXiv: 1004.4974 [astro-ph.GA].

Gómez, Facundo A. et al. (Apr. 2015). "And Yet it Moves: The Dangers of Artificially Fixing the Milky Way Center of Mass in the Presence of a Massive Large Magellanic Cloud". In: *ApJ* 802.2, 128, p. 128. DOI: 10.1088/0004-637X/802/2/128. arXiv: 1408.4128 [astro-ph.GA].

Grand, Robert J. J. et al. (May 2017). "The Auriga Project: the properties and formation mechanisms of disc galaxies across cosmic time". In: *MNRAS* 467.1, pp. 179–207. DOI: 10.1093/mnras/stx071. arXiv: 1610.01159 [astro-ph.GA].

Grand, Robert J. J. et al. (July 2019). "The effects of dynamical substructure on Milky Way mass estimates from the high-velocity tail of the local stellar halo". In: *MNRAS* 487.1, pp. L72–L76. DOI: 10.1093/mnrasl/slz092. arXiv: 1905.09834 [astro-ph.GA].

Gravity Collaboration et al. (July 2018). "Detection of the gravitational redshift in the orbit of the star S2 near the Galactic centre massive black hole". In: *A&A* 615, L15, p. L15. DOI: 10.1051/0004-6361/201833718. arXiv: 1807.09409 [astro-ph.GA].

Grillmair, C. J. (July 2006). "Detection of a 60°-long Dwarf Galaxy Debris Stream". In: *ApJ* 645.1, pp. L37–L40. DOI: 10.1086/505863. arXiv: astro-ph/0605396 [astro-ph].

Grillmair, C. J. and O. Dionatos (May 2006). "Detection of a 63° Cold Stellar Stream in the Sloan Digital Sky Survey". In: *ApJ* 643.1, pp. L17–L20. DOI: 10.1086/505111. arXiv: astro-ph/0604332 [astro-ph].

Haines, Tim, Elena D'Onghia, Benoit Famaey, Chervin Laporte, and Lars Hernquist (July 2019). "Implications of a Time-varying Galactic Potential for Determinations of the Dynamical Surface Density". In: *ApJ* 879.1, L15, p. L15. DOI: 10.3847/2041-8213/ab25f3. arXiv: 1903.00607 [astro-ph.GA].

Harris, William E. (Dec. 2010). "A New Catalog of Globular Clusters in the Milky Way". In: *arXiv e-prints*, arXiv:1012.3224, arXiv:1012.3224. arXiv: 1012.3224 [astro-ph.GA].

Hayes, Christian R., David R. Law, and Steven R. Majewski (Nov. 2018). "Constraining the Solar Galactic Reflex Velocity using Gaia Observations of the Sagittarius Stream". In: *ApJ* 867.2, L20, p. L20. DOI: 10.3847/2041-8213/aae9dd. arXiv: 1809.07654 [astro-ph.GA].

Helmi, Amina (Aug. 2020). "Streams, Substructures, and the Early History of the Milky Way". In: *ARA&A* 58, pp. 205–256. DOI: 10.1146/annurev-astro-032620-021917. arXiv: 2002.04340 [astro-ph.GA].

Helmi, Amina and P. T. de Zeeuw (Dec. 2000). "Mapping the substructure in the Galactic halo with the next generation of astrometric satellites". In: *MNRAS* 319.3, pp. 657–665. DOI: 10.1046/j.1365-8711.2000.03895.x. arXiv: astro-ph/0007166 [astro-ph].

– (Apr. 2002). "Mapping the substructure in the Galactic halo with the next generation of astrometric satellites". In: *Monthly Notices of the Royal Astronomical Society* 319.3, pp. 657–665. DOI: 10.1046/j.1365-8711.2000.03895.x. URL: https://doi.org/10.1046%5C%2Fj.1365-8711.2000.03895.x.

Helmi, Amina and Simon D. M. White (Aug. 1999). "Building up the stellar halo of the Galaxy". In: *MNRAS* 307.3, pp. 495–517. DOI: 10.1046/j.1365-8711.1999.02616.x. arXiv: astro-ph/9901102 [astro-ph].

Helmi, Amina, Simon D. M. White, P. T. de Zeeuw, and Hongsheng Zhao (Nov. 1999). "Debris streams in the solar neighbourhood as relics from the formation of the Milky Way". In: *Nature* 402.6757, pp. 53–55. DOI: 10.1038/46980. arXiv: astro-ph/9911041 [astro-ph].

Helmi, Amina et al. (Oct. 2018). "The merger that led to the formation of the Milky Way's inner stellar halo and thick disk". In: *Nature* 563.7729, pp. 85–88. DOI: 10.1038/s41586-018-0625-x. arXiv: 1806.06038 [astro-ph.GA].

Hernquist, Lars (June 1990). "An Analytical Model for Spherical Galaxies and Bulges". In: *ApJ* 356, p. 359. DOI: 10.1086/168845.

Hernquist, Lars and Jeremiah P. Ostriker (Feb. 1992). "A Self-consistent Field Method for Galactic Dynamics". In: *ApJ* 386, p. 375. DOI: 10.1086/171025.

Hidalgo, S. L. (Oct. 2017). "Mass-metallicity relation of dwarf galaxies and its dependency on time: clues from resolved systems and comparison with massive galaxies". In: *A&A* 606, A115, A115. DOI: 10.1051/0004-6361/201630264. arXiv: 1707.01840 [astro-ph.GA].

Hogg, David W., Anna-Christina Eilers, and Hans-Walter Rix (Oct. 2019). "Spectrophotometric Parallaxes with Linear Models: Accurate Distances for Luminous Red-giant Stars". In: *AJ* 158.4, 147, p. 147. DOI: 10.3847/1538-3881/ab398c. arXiv: 1810.09468 [astro-ph.GA].

Horta, Danny et al. (Apr. 2020). "The chemical compositions of accreted and in situ galactic globular clusters according to SDSS/APOGEE". In: *MNRAS* 493.3, pp. 3363–3378. DOI: 10.1093/mnras/staa478. arXiv: 2001.03177 [astro-ph.GA].

Horta, Danny et al. (Jan. 2021). "Evidence from APOGEE for the presence of a major building block of the halo buried in the inner Galaxy". In: *MNRAS* 500.1, pp. 1385–1403. DOI: 10.1093/mnras/staa2987. arXiv: 2007.10374 [astro-ph.GA].

Huang, Y. et al. (Dec. 2016). "The Milky Way's rotation curve out to 100 kpc and its constraint on the Galactic mass distribution". In: *MNRAS* 463.3, pp. 2623–2639. DOI: 10.1093/mnras/stw2096. arXiv: 1604.01216 [astro-ph.GA].

Hunt, Jason A. S., Adrian M. Price-Whelan, Kathryn V. Johnston, and Elise Darragh-Ford (June 2022). "Multiple phase-spirals suggest multiple origins in Gaia DR3". In: *arXiv e-prints*, arXiv:2206.06125, arXiv:2206.06125. arXiv: 2206.06125 [astro-ph.GA].

Hunter, J. D. (2007). "Matplotlib: A 2D graphics environment". In: *Computing in Science & Engineering* 9.3, pp. 90–95. DOI: 10.1109/MCSE.2007.55.

Ibata, R., G. F. Lewis, N. F. Martin, M. Bellazzini, and M. Correnti (Mar. 2013). "Does the Sagittarius Stream Constrain the Milky Way Halo to be Triaxial?" In: *ApJ* 765.1, L15, p. L15. DOI: 10.1088/2041-8205/765/1/L15. arXiv: 1212.4958 [astro-ph.GA].

Ibata, Rodrigo A., G. Gilmore, and M. J. Irwin (July 1994). "A dwarf satellite galaxy in Sagittarius". In: *Nature* 370.6486, pp. 194–196. DOI: 10.1038/370194a0.

Ibata, Rodrigo A., Khyati Malhan, and Nicolas F. Martin (Feb. 2019). "The Streams of the Gaping Abyss: A Population of Entangled Stellar Streams Surrounding the Inner Galaxy". In: *ApJ* 872.2, 152, p. 152. DOI: 10.3847/1538-4357/ab0080. arXiv: 1901.07566 [astro-ph.GA].

Iocco, Fabio, Miguel Pato, and Gianfranco Bertone (Mar. 2015). "Evidence for dark matter in the inner Milky Way". In: *Nature Physics* 11.3, pp. 245–248. DOI: 10.1038/nphys3237. arXiv: 1502.03821 [astro-ph.GA].

Johnston, Kathryn V., HongSheng Zhao, David N. Spergel, and Lars Hernquist (Feb. 1999). "Tidal Streams as Probes of the Galactic Potential". In: *ApJ* 512.2, pp. L109–L112. DOI: 10.1086/311876. arXiv: astro-ph/9807243 [astro-ph].

Jurić, Mario et al. (Feb. 2008). "The Milky Way Tomography with SDSS. I. Stellar Number Density Distribution". In: *ApJ* 673.2, pp. 864–914. DOI: 10.1086/523619. arXiv: astro-ph/0510520 [astro-ph].

Kallivayalil, Nitya, Roeland P. van der Marel, Gurtina Besla, Jay Anderson, and Charles Alcock (Feb. 2013). "Third-epoch Magellanic Cloud Proper Motions. I. Hubble Space Telescope/WFC3 Data and Orbit Implications". In: *ApJ* 764.2, 161, p. 161. DOI: 10.1088/0004-637X/764/2/161. arXiv: 1301.0832 [astro-ph.CO].

Karukes, E. V., M. Benito, F. Iocco, R. Trotta, and A. Geringer-Sameth (Sept. 2019). "Bayesian reconstruction of the Milky Way dark matter distribution". In: *J. Cosmology Astropart. Phys.* 2019.9, 046, p. 046. DOI: 10.1088/1475-7516/2019/09/046. arXiv: 1901.02463 [astro-ph.GA].

– (May 2020). "A robust estimate of the Milky Way mass from rotation curve data". In: *J. Cosmology Astropart. Phys.* 2020.5, 033, p. 033. DOI: 10.1088/1475-7516/2020/05/033. arXiv: 1912.04296 [astro-ph.GA].

Katz, D. et al. (June 2022). "Gaia Data Release 3 Properties and validation of the radial velocities". In: *arXiv e-prints*, arXiv:2206.05902, arXiv:2206.05902. arXiv: 2206.05902 [astro-ph.GA].

Kepley, Amanda A. et al. (Oct. 2007). "Halo Star Streams in the Solar Neighborhood". In: *AJ* 134.4, pp. 1579–1595. DOI: 10.1086/521429. arXiv: 0707.4477 [astro-ph].

Kirby, Evan N. et al. (Dec. 2013). "The Universal Stellar Mass-Stellar Metallicity Relation for Dwarf Galaxies". In: *ApJ* 779.2, 102, p. 102. DOI: 10.1088/0004-637X/779/2/102. arXiv: 1310.0814 [astro-ph.GA].

Kluyver, Thomas et al. (2016). "Jupyter Notebooks a publishing format for reproducible computational workflows". In: *Positioning and Power in Academic Publishing: Players, Agents and Agendas*. Ed. by Fernando Loizides and Birgit Scmidt. IOS Press, pp. 87–90. URL: https://eprints.soton.ac.uk/403913/.

Klypin, Anatoly, Andrey V. Kravtsov, Octavio Valenzuela, and Francisco Prada (Sept. 1999). "Where Are the Missing Galactic Satellites?" In: *ApJ* 522.1, pp. 82–92. DOI: 10.1086/307643. arXiv: astro-ph/9901240 [astro-ph].

Koposov, Sergey E., Hans-Walter Rix, and David W. Hogg (Mar. 2010). "Constraining the Milky Way Potential with a Six-Dimensional Phase-Space Map of the GD-1 Stellar Stream". In: *ApJ* 712.1, pp. 260–273. DOI: 10.1088/0004-637X/712/1/260. arXiv: 0907.1085 [astro-ph.GA].

Koppelman, Helmer H., Jorrit H. J. Hagen, and Amina Helmi (Mar. 2021). "Frequencies, chaos, and resonances: A study of orbital parameters of nearby thick-disc and halo stars". In: *A&A* 647, A37, A37. DOI: 10.1051/0004-6361/202039390. arXiv: 2009.04849 [astro-ph.GA].

Koppelman, Helmer H. and Amina Helmi (May 2021). "Time evolution of gaps in stellar streams in axisymmetric Stäckel potentials". In: *A&A* 649, A55, A55. DOI: 10.1051/0004-6361/202039968.

Koppelman, Helmer H., Amina Helmi, Davide Massari, Adrian M. Price-Whelan, and Tjitske K. Starkenburg (Nov. 2019a). "Multiple retrograde substructures in the Galactic halo: A shattered view of Galactic history". In: *A&A* 631, L9, p. L9. DOI: 10.1051/0004-6361/201936738. arXiv: 1909.08924 [astro-ph.GA].

Koppelman, Helmer H., Amina Helmi, Davide Massari, Sebastian Roelenga, and Ulrich Bastian (May 2019b). "Characterization and history of the Helmi streams with Gaia DR2". In: *A&A* 625, A5, A5. DOI: 10.1051/0004-6361/201834769. arXiv: 1812.00846 [astro-ph.GA].

Kruijssen, J. M. Diederik, Joel L. Pfeffer, Marta Reina-Campos, Robert A. Crain, and Nate Bastian (July 2019). "The formation and assembly history of the Milky Way revealed by its globular cluster population". In: *MNRAS* 486.3, pp. 3180–3202. DOI: 10.1093/mnras/sty1609. arXiv: 1806.05680 [astro-ph.GA].

Kruijssen, J. M. Diederik et al. (Oct. 2020). "Kraken reveals itself - the merger history of the Milky Way reconstructed with the E-MOSAICS simulations". In: *MNRAS* 498.2, pp. 2472–2491. DOI: 10.1093/mnras/staa2452. arXiv: 2003.01119 [astro-ph.GA].

Kuijken, Konrad and Gerard Gilmore (Jan. 1991). "The Galactic Disk Surface Mass Density and the Galactic Force K Z at Z = 1.1 Kiloparsecs". In: *ApJ* 367, p. L9. DOI: 10.1086/185920.

Küpper, Andreas H. W. et al. (Apr. 2015). "Globular Cluster Streams as Galactic High-Precision Scales—the Poster Child Palomar 5". In: *ApJ* 803.2, 80, p. 80. DOI: 10.1088/0004-637X/803/2/80. arXiv: 1502.02658 [astro-ph.GA].

Laskar, Jacques (May 1993). "Frequency Analysis of a Dynamical System". In: *Celestial Mechanics and Dynamical Astronomy* 56.1-2, pp. 191–196. DOI: 10.1007/BF00699731.

Li, Yang-Shyang and Amina Helmi (Mar. 2009). "Group infall of substructures on to a Milky Way-like dark halo". In: *The Galaxy Disk in Cosmological Context*. Ed. by Johannes Andersen, Nordströara, Birgitta m, and Joss Bland-Hawthorn. Vol. 254, pp. 263–268. DOI: 10.1017/S1743921308027683. arXiv: 0807.2780 [astro-ph].

Libeskind, Noam I. et al. (Oct. 2020). "The HESTIA project: simulations of the Local Group". In: *MNRAS* 498.2, pp. 2968–2983. DOI: 10.1093/mnras/staa2541. arXiv: 2008.04926 [astro-ph.GA].

Lilleengen, Sophia et al. (May 2022). "The effect of the deforming dark matter haloes of the Milky Way and the Large Magellanic Cloud on the Orphan-Chenab stream". In: *arXiv e-prints*, arXiv:2205.01688, arXiv:2205.01688. arXiv: 2205.01688 [astro-ph.GA].

Lilley, Edward J., Jason L. Sanders, and N. Wyn Evans (July 2018). "A two-parameter family of double-power-law biorthonormal potential-density expansions". In: *MNRAS* 478.1, pp. 1281–1291. DOI: 10.1093/mnras/sty1038. arXiv: 1804.11190 [astro-ph.GA].

Lindegren, L. et al. (May 2021). "Gaia Early Data Release 3. Parallax bias versus magnitude, colour, and position". In: *A&A* 649, A4, A4. DOI: 10.1051/0004-6361/202039653. arXiv: 2012.01742 [astro-ph.IM].

Lövdal, Sofie S. et al. (Jan. 2022). "Substructure in the stellar halo near the Sun. I. Data-driven clustering in Integrals of Motion space". In: *arXiv e-prints*, arXiv:2201.02404, arXiv:2201.02404. arXiv: 2201.02404 [astro-ph.GA].

Lowing, Ben, Adrian Jenkins, Vincent Eke, and Carlos Frenk (Oct. 2011). "A Halo Expansion (HEX) Technique for Approximating Simulated Dark Matter Haloes". In: *Monthly Notices of The Royal Astronomical Society - MON NOTIC ROY ASTRON SOC* 416, pp. 2697–2711. DOI: 10.1111/j.1365-2966.2011.19222.x.

Maffione, N. P. et al. (Nov. 2015). "On the relevance of chaos for halo stars in the solar neighbourhood". In: *MNRAS* 453.3, pp. 2830–2847. DOI: 10.1093/mnras/stv1778. arXiv: 1508.00579 [astro-ph.GA].

Malhan, Khyati (May 2022). "A New Member of the Milky Way's Family Tree: Characterizing the Pontus Merger of Our Galaxy". In: *ApJ* 930.1, L9, p. L9. DOI: 10.3847/2041-8213/ac67da. arXiv: 2204.09058 [astro-ph.GA].

Malhan, Khyati and Rodrigo A. Ibata (July 2018). "STREAMFINDER - I. A new algorithm for detecting stellar streams". In: *MNRAS* 477.3, pp. 4063–4076. DOI: 10.1093/mnras/sty912. arXiv: 1804.11338 [astro-ph.GA].

– (July 2019). "Constraining the Milky Way halo potential with the GD-1 stellar stream". In: *MNRAS* 486.3, pp. 2995–3005. DOI: 10.1093/mnras/stz1035. arXiv: 1807.05994 [astro-ph.GA].

Malhan, Khyati, Rodrigo A. Ibata, and Nicolas F. Martin (Dec. 2018). "Ghostly tributaries to the Milky Way: charting the halo's stellar streams with the Gaia DR2 catalogue". In: *MNRAS* 481.3, pp. 3442–3455. DOI: 10.1093/mnras/sty2474. arXiv: 1804.11339 [astro-ph.GA].

Malhan, Khyati et al. (Feb. 2022). "The Global Dynamical Atlas of the Milky Way mergers: Constraints from Gaia EDR3 based orbits of globular clusters, stellar streams and satellite galaxies". In: *arXiv e-prints*, arXiv:2202.07660, arXiv:2202.07660. arXiv: 2202.07660 [astro-ph.GA].

Manos, T. and E. Athanassoula (July 2011). "Regular and chaotic orbits in barred galaxies - I. Applying the SALI/GALI method to explore their distribution in several models". In: *MNRAS* 415.1, pp. 629–642. DOI: 10.1111/j.1365-2966.2011.18734.x. arXiv: 1102.1157 [astro-ph.GA].

Martin, Nicolas F. et al. (Jan. 2022a). "A stellar stream remnant of a globular cluster below the metallicity floor". In: *Nature* 601.7891, pp. 45–48. DOI: 10.1038/s41586-021-04162-2. arXiv: 2201.01309 [astro-ph.GA].

Martin, Nicolas F. et al. (Jan. 2022b). "The Pristine survey – XVI. The metallicity of 26 stellar streams around the Milky Way detected with the STREAMFINDER in Gaia EDR3". In: *arXiv e-prints*, arXiv:2201.01310, arXiv:2201.01310. arXiv: 2201.01310 [astro-ph.GA].

Massari, D., H. H. Koppelman, and A. Helmi (Oct. 2019). "Origin of the system of globular clusters in the Milky Way". In: *A&A* 630, L4, p. L4. DOI: 10.1051/0004-6361/201936135. arXiv: 1906.08271 [astro-ph.GA].

Mateu, Cecilia (Apr. 2022). "galstreams: A Library of Milky Way Stellar Stream Footprints and Tracks". In: *arXiv e-prints*, arXiv:2204.10326, arXiv:2204.10326. arXiv: 2204.10326 [astro-ph.GA].

Matsuno, Tadafumi et al. (Mar. 2022). "High-precision chemical abundances of Galactic building blocks. II. Revisiting the chemical distinctness of the Helmi streams". In: *arXiv e-prints*, arXiv:2203.11808, arXiv:2203.11808. arXiv: 2203.11808 [astro-ph.GA].

McConnachie, Alan W. and Kim A. Venn (Dec. 2020). "Updated Proper Motions for Local Group Dwarf Galaxies Using Gaia Early Data Release 3". In: *Research Notes of the American Astronomical Society* 4.12, 229, p. 229. DOI: 10.3847/2515-5172/abd18b. arXiv: 2012.03904 [astro-ph.GA].

McMillan, Paul J. (Feb. 2017). "The mass distribution and gravitational potential of the Milky Way". In: *MNRAS* 465.1, pp. 76–94. DOI: 10.1093/mnras/stw2759. arXiv: 1608.00971 [astro-ph.GA].

McMillan, Paul J. and James J. Binney (Oct. 2008). "Disassembling the Galaxy with angle-action coordinates". In: *MNRAS* 390.1, pp. 429–437. DOI: 10.1111/j.1365-2966.2008.13767.x. arXiv: 0806.0319 [astro-ph].

Merritt, David and Monica Valluri (Nov. 1996). "Chaos and Mixing in Triaxial Stellar Systems". In: *ApJ* 471, p. 82. DOI: 10.1086/177955. arXiv: astro-ph/9602079 [astro-ph].

Mestre, Martın, Claudio Llinares, and Daniel D. Carpintero (Mar. 2020). "Effects of chaos on the detectability of stellar streams". In: *MNRAS* 492.3, pp. 4398–4408. DOI: 10.1093/mnras/stz3505. arXiv: 1912.05592 [astro-ph.GA].

Milone, A. P., A. F. Marino, A. Mastrobuono-Battisti, and E. P. Lagioia (Oct. 2018). "Gaia unveils the kinematics of multiple stellar populations in 47 Tucanae". In: *MNRAS* 479.4, pp. 5005–5011. DOI: 10.1093/mnras/sty1873. arXiv: 1807.03511 [astro-ph.SR].

Miyamoto, M. and R. Nagai (1975). "Three-dimensional models for the distribution of mass in galaxies". In: *PASJ* 27, pp. 533–543.

Monari, G. et al. (Aug. 2018). "The escape speed curve of the Galaxy obtained from Gaia DR2 implies a heavy Milky Way". In: *A&A* 616, L9, p. L9. DOI: 10.1051/0004-6361/201833748. arXiv: 1807.04565 [astro-ph.GA].

Moore, Ben et al. (Oct. 1999). "Dark Matter Substructure within Galactic Halos". In: *ApJ* 524.1, pp. L19–L22. DOI: 10.1086/312287. arXiv: astro-ph/9907411 [astro-ph].

Mróz, Przemek et al. (Jan. 2019). "Rotation Curve of the Milky Way from Classical Cepheids". In: *ApJ* 870.1, L10, p. L10. DOI: 10.3847/2041-8213/aaf73f. arXiv: 1810.02131 [astro-ph.GA].

Myeong, G. C., N. W. Evans, Vasily Belokurov, N. C. Amorisco, and S. E. Koposov (Apr. 2018). "Halo substructure in the SDSS-Gaia catalogue: streams and clumps". In: *MNRAS* 475.2, pp. 1537–1548. DOI: 10.1093/mnras/stx3262. arXiv: 1712.04071 [astro-ph.GA].

Myeong, G. C., E. Vasiliev, G. Iorio, N. W. Evans, and Vasily Belokurov (Sept. 2019). "Evidence for two early accretion events that built the Milky Way stellar halo". In: *MNRAS* 488.1, pp. 1235–1247. DOI: 10.1093/mnras/stz1770. arXiv: 1904.03185 [astro-ph.GA].

Myeong, G. C. et al. (June 2022). "Milky Way's eccentric constituents with *Gaia*, APOGEE *amp*; GALAH". In: *arXiv e-prints*, arXiv:2206.07744, arXiv:2206.07744. arXiv: 2206.07744 [astro-ph.GA].

Naidu, Rohan P. et al. (Sept. 2020). "Evidence from the H3 Survey That the Stellar Halo Is Entirely Comprised of Substructure". In: *ApJ* 901.1, 48, p. 48. DOI: 10.3847/1538-4357/abaef4. arXiv: 2006.08625 [astro-ph.GA].

Navarro, Julio F., Carlos S. Frenk, and Simon D. M. White (May 1996). "The Structure of Cold Dark Matter Halos". In: *ApJ* 462, p. 563. DOI: 10.1086/177173. arXiv: astro-ph/9508025 [astro-ph].

Ness, M. et al. (Apr. 2013). "ARGOS - III. Stellar populations in the Galactic bulge of the Milky Way". In: *MNRAS* 430.2, pp. 836–857. DOI: 10.1093/mnras/sts629. arXiv: 1212.1540 [astro-ph.GA].

Newberg, Heidi Jo (Jan. 2016). "Introduction to Tidal Streams". In: *Tidal Streams in the Local Group and Beyond*. Ed. by Heidi Jo Newberg and Jeffrey L. Carlin. Vol. 420. Astrophysics and Space Science Library, p. 1. DOI: 10.1007/978-3-319-19336-6_1. arXiv: 2103.04440 [astro-ph.GA].

Ngan, Wayne et al. (Apr. 2015). "Simulating Tidal Streams in a High-resolution Dark Matter Halo". In: *ApJ* 803.2, 75, p. 75. DOI: 10.1088/0004-637X/803/2/75. arXiv: 1411.3760 [astro-ph.GA].

Nitschai, Maria Selina, Anna-Christina Eilers, Nadine Neumayer, Michele Cappellari, and Hans-Walter Rix (Aug. 2021). "Dynamical Model of the Milky Way Using APOGEE and Gaia Data". In: *ApJ* 916.2, 112, p. 112. DOI: 10.3847/1538-4357/ac04b5. arXiv: 2106.05286 [astro-ph.GA].

O'Donnell, James E. (Feb. 1994). "R v-dependent Optical and Near-Ultraviolet Extinction". In: *ApJ* 422, p. 158. DOI: 10.1086/173713.

Odenkirchen, Michael et al. (Feb. 2001). "Detection of Massive Tidal Tails around the Globular Cluster Palomar 5 with Sloan Digital Sky Survey Commissioning Data". In: *ApJ* 548.2, pp. L165–L169. DOI: 10.1086/319095. arXiv: astro-ph/0012311 [astro-ph].

Pascale, Raffaele, Carlo Nipoti, and Luca Ciotti (Jan. 2022). "Regular and chaotic orbits in axisymmetric stellar systems". In: *MNRAS* 509.1, pp. 1465–1477. DOI: 10.1093/mnras/stab2693. arXiv: 2109.07501 [astro-ph.GA].

Pato, Miguel and Fabio Iocco (Jan. 2017). "galkin: A new compilation of Milky Way rotation curve data". In: *SoftwareX* 6, pp. 54–62. DOI: 10.1016/j.softx.2016.12.006. arXiv: 1703.00020 [astro-ph.GA].

Pearson, Sarah, Adrian M. Price-Whelan, and Kathryn V. Johnston (Aug. 2017). "Gaps and length asymmetry in the stellar stream Palomar 5 as effects of Galactic bar rotation". In: *Nature Astronomy* 1, pp. 633–639. DOI: 10.1038/s41550-017-0220-3. arXiv: 1703.04627 [astro-ph.GA].

Petersen, Michael S. and Jorge Peñarrubia (May 2020). "Reflex motion in the Milky Way stellar halo resulting from the Large Magellanic Cloud infall". In: *MNRAS* 494.1, pp. L11–L16. DOI: 10.1093/mnrasl/slaa029. arXiv: 2001.09142 [astro-ph.GA].

Piffl, T. et al. (Feb. 2014). "The RAVE survey: the Galactic escape speed and the mass of the Milky Way". In: *A&A* 562, A91, A91. DOI: 10.1051/0004-6361/201322531. arXiv: 1309.4293 [astro-ph.GA].

Posti, Lorenzo and Amina Helmi (Jan. 2019). "Mass and shape of the Milky Way's dark matter halo with globular clusters from Gaia and Hubble". In: *A&A* 621, A56, A56. DOI: 10.1051/0004-6361/201833355. arXiv: 1805.01408 [astro-ph.GA].

Price-Whelan, Adrian M. (June 2015). *SuperFreq*. DOI: 10.5281/zenodo.18787.

– (Oct. 2017). "Gala: A Python package for galactic dynamics". In: *The Journal of Open Source Software* 2. DOI: 10.21105/joss.00388.

Price-Whelan, Adrian M. and Ana Bonaca (Aug. 2018). "Off the Beaten Path: Gaia Reveals GD-1 Stars outside of the Main Stream". In: *ApJ* 863.2, L20, p. L20. DOI: 10.3847/2041-8213/aad7b5. arXiv: 1805.00425 [astro-ph.GA].

Price-Whelan, Adrian M., Branimir Sesar, Kathryn V. Johnston, and Hans-Walter Rix (June 2016a). "Spending Too Much Time at the Galactic Bar: Chaotic Fanning of the Ophiuchus Stream". In: *ApJ* 824.2, 104, p. 104. DOI: 10.3847/0004-637X/824/2/104. arXiv: 1601.06790 [astro-ph.GA].

Price-Whelan, Adrian M. et al. (Jan. 2016b). "Chaotic dispersal of tidal debris". In: *MNRAS* 455.1, pp. 1079–1098. DOI: 10.1093/mnras/stv2383. arXiv: 1507.08662 [astro-ph.GA].

Price-Whelan, Adrian M. et al. (Oct. 2020). *adrn/gala: v1.3*. Version v1.3. DOI: 10.5281/zenodo.4159870. URL: https://doi.org/10.5281/zenodo.4159870.

Reid, M. J. et al. (Mar. 2014). "Trigonometric Parallaxes of High Mass Star Forming Regions: The Structure and Kinematics of the Milky Way". In: *ApJ* 783.2, 130, p. 130. DOI: 10.1088/0004-637X/783/2/130. arXiv: 1401.5377 [astro-ph.GA].

Renzini, Alvio, Anna F. Marino, and Antonino P. Milone (Apr. 2022). "The formation of globular clusters as a case of overcooling". In: *MNRAS*. DOI: 10.1093/mnras/stac973. arXiv: 2203.03002 [astro-ph.GA].

Rodriguez Wimberly, M. K. et al. (July 2022). "Sizing from the smallest scales: the mass of the Milky Way". In: *MNRAS* 513.4, pp. 4968–4982. DOI: 10.1093/mnras/stac1265. arXiv: 2109.00633 [astro-ph.GA].

Ruiz-Lara, Tomás, A Helmi, C Gallart, F Surot, and S Cassisi (2022a). "The star formation history of a Galactic halo building block: The Helmi streams". In: *arXiv preprint arXiv:2205.13810*.

Ruiz-Lara, Tomás et al. (Jan. 2022b). "Substructure in the stellar halo near the Sun. II. Characterisation of independent structures". In: *arXiv e-prints*, arXiv:2201.02405, arXiv:2201.02405. arXiv: 2201.02405 [astro-ph.GA].

Sanders, Jason L. (Oct. 2012). "Angle-action estimation in a general axisymmetric potential". In: *MNRAS* 426.1, pp. 128–139. DOI: 10.1111/j.1365-2966.2012.21698.x. arXiv: 1208.2813 [astro-ph.GA].

Sanders, Jason L. and James Binney (Aug. 2013). "Stream-orbit misalignment - I. The dangers of orbit-fitting". In: *MNRAS* 433.3, pp. 1813–1825. DOI: 10.1093/mnras/stt806. arXiv: 1305.1935 [astro-ph.GA].

– (Feb. 2016). "A review of action estimation methods for galactic dynamics". In: *Monthly Notices of the Royal Astronomical Society* 457.2, pp. 2107–2121. ISSN: 0035-8711. DOI: 10.1093/mnras/stw106. eprint: https://academic.oup.com/mnras/article-pdf/457/2/2107/2922842/stw106.pdf. URL: https://doi.org/10.1093/mnras/stw106.

Sanders, Jason L., Edward J. Lilley, Eugene Vasiliev, N. Wyn Evans, and Denis Erkal (Dec. 2020). "Models of distorted and evolving dark matter haloes". In: *MNRAS* 499.4, pp. 4793–4813. DOI: 10.1093/mnras/staa3079. arXiv: 2009.00645 [astro-ph.GA].

Santistevan, Isaiah B. et al. (Sept. 2020). "The formation times and building blocks of Milky Way-mass galaxies in the FIRE simulations". In: *MNRAS* 497.1, pp. 747–764. DOI: 10.1093/mnras/staa1923. arXiv: 2001.03178 [astro-ph.GA].

Schlegel, David J., Douglas P. Finkbeiner, and Marc Davis (June 1998). "Maps of Dust Infrared Emission for Use in Estimation of Reddening and Cosmic Microwave Background Radiation Foregrounds". In: *ApJ* 500.2, pp. 525–553. DOI: 10.1086/305772. arXiv: astro-ph/9710327 [astro-ph].

Schmidt, M. (June 1956). "A model of the distribution of mass in the Galactic System". In: *Bull. Astron. Inst. Netherlands* 13, p. 15.

Schönrich, Ralph, James Binney, and Walter Dehnen (Apr. 2010). "Local kinematics and the local standard of rest". In: *MNRAS* 403.4, pp. 1829–1833. DOI: 10.1111/j.1365-2966.2010.16253.x. arXiv: 0912.3693 [astro-ph.GA].

Shao, Shi, Marius Cautun, Alis Deason, and Carlos S. Frenk (July 2021). "The twisted dark matter halo of the Milky Way". In: *MNRAS* 504.4, pp. 6033–6048. DOI: 10.1093/mnras/staa3883. arXiv: 2005.03025 [astro-ph.GA].

Shen, Jeff et al. (Nov. 2021). "The Mass of the Milky Way from the H3 Survey". In: *arXiv e-prints*, arXiv:2111.09327, arXiv:2111.09327. arXiv: 2111.09327 [astro-ph.GA].

Shipp, Nora et al. (Dec. 2021). "Measuring the Mass of the Large Magellanic Cloud with Stellar Streams Observed by S ^{5}". In: *ApJ* 923.2, 149, p. 149. DOI: 10.3847/1538-4357/ac2e93. arXiv: 2107.13004 [astro-ph.GA].

Simon, Joshua D. et al. (May 2011). "A Complete Spectroscopic Survey of the Milky Way Satellite Segue 1: The Darkest Galaxy". In: *ApJ* 733.1, 46, p. 46. DOI: 10.1088/0004-637X/733/1/46. arXiv: 1007.4198 [astro-ph.GA].

Skowron, Dorota M. et al. (Aug. 2019). "A three-dimensional map of the Milky Way using classical Cepheid variable stars". In: *Science* 365.6452, pp. 478–482. DOI: 10.1126/science.aau3181. arXiv: 1806.10653 [astro-ph.GA].

Sofue, Yoshiaki (Apr. 2020). "Rotation Curve of the Milky Way and the Dark Matter Density". In: *Galaxies* 8.2, p. 37. DOI: 10.3390/galaxies8020037. arXiv: 2004.11688 [astro-ph.GA].

Stebbins, Joel and A. E. Whitford (Sept. 1947). "Six-Color Photometry of Stars. V. Infrared Radiation from the Region of the Galactic Center." In: *ApJ* 106, p. 235. DOI: 10.1086/144954.

Steinmetz, Matthias et al. (Aug. 2020). "The Sixth Data Release of the Radial Velocity Experiment (RAVE). II. Stellar Atmospheric Parameters, Chemical Abundances, and Distances". In: *AJ* 160.2, 83, p. 83. DOI: 10.3847/1538-3881/ab9ab8. arXiv: 2002.04512 [astro-ph.SR].

Strigari, Louis E. et al. (May 2008). "The Most Dark-Matter-dominated Galaxies: Predicted Gamma-Ray Signals from the Faintest Milky Way Dwarfs". In: *ApJ* 678.2, pp. 614–620. DOI: 10.1086/529488. arXiv: 0709.1510 [astro-ph].

Tenachi, Wassim et al. (June 2022). "Typhon: a polar stream from the outer halo raining through the Solar neighborhood". In: *arXiv e-prints*, arXiv:2206.10405, arXiv:2206.10405. arXiv: 2206.10405 [astro-ph.GA].

Tolstoy, Eline, Vanessa Hill, and Monica Tosi (Sept. 2009). "Star-Formation Histories, Abundances, and Kinematics of Dwarf Galaxies in the Local Group". In: *ARA&A* 47.1, pp. 371–425. DOI: 10.1146/annurev-astro-082708-101650. arXiv: 0904.4505 [astro-ph.CO].

Valluri, Monica, Victor P. Debattista, Thomas Quinn, and Ben Moore (Mar. 2010). "The orbital evolution induced by baryonic condensation in triaxial haloes". In: *MNRAS* 403.1, pp. 525–544. DOI: 10.1111/j.1365-2966.2009.16192.x. arXiv: 0906.4784 [astro-ph.CO].

Valluri, Monica, Victor P. Debattista, Thomas R. Quinn, Rok Roškar, and James Wadsley (Jan. 2012). "Probing the shape and history of the Milky Way halo with orbital spectral analysis". In: *MNRAS* 419.3, pp. 1951–1969. DOI: 10.1111/j.1365-2966.2011.19853.x. arXiv: 1109.3193 [astro-ph.GA].

Valluri, Monica and David Merritt (Oct. 1998). "Regular and Chaotic Dynamics of Triaxial Stellar Systems". In: *ApJ* 506.2, pp. 686–711. DOI: 10.1086/306269. arXiv: astro-ph/9801041 [astro-ph].

van der Marel, Roeland P., Gurtina Besla, T. J. Cox, Sangmo Tony Sohn, and Jay Anderson (July 2012). "The M31 Velocity Vector. III. Future Milky Way M31-M33 Orbital Evolution, Merging, and Fate of the Sun". In: *ApJ* 753.1, 9, p. 9. DOI: 10.1088/0004-637X/753/1/9. arXiv: 1205.6865 [astro-ph.GA].

van der Walt, Stéfan, S. Chris Colbert, and Gaël Varoquaux (Mar. 2011). "The NumPy Array: A Structure for Efficient Numerical Computation". In: *Computing in Science and Engineering* 13.2, pp. 22–30. DOI: 10.1109/MCSE.2011.37. arXiv: 1102.1523 [cs.MS].

VandenBerg, Don A., K. Brogaard, R. Leaman, and L. Casagrande (Oct. 2013). "The Ages of 55 Globular Clusters as Determined Using an Improved ΔV_{TO}^{HB} Method along with Color-Magnitude Diagram Constraints, and Their Implications for Broader Issues". In: *ApJ* 775.2, 134, p. 134. DOI: 10.1088/0004-637X/775/2/134. arXiv: 1308.2257 [astro-ph.GA].

Vasiliev, Eugene (Oct. 2013). "A new code for orbit analysis and Schwarzschild modelling of triaxial stellar systems". In: *MNRAS* 434.4, pp. 3174–3195. DOI: 10.1093/mnras/stt1235. arXiv: 1307.8116 [astro-ph.GA].
– (Feb. 2018). "Agama reference documentation". In: *arXiv e-prints*, arXiv:1802.08255, arXiv:1802.08255. arXiv: 1802.08255 [astro-ph.IM].
– (Jan. 2019). "AGAMA: action-based galaxy modelling architecture". In: *MNRAS* 482.2, pp. 1525–1544. DOI: 10.1093/mnras/sty2672. arXiv: 1802.08239 [astro-ph.GA].
Vasiliev, Eugene and Vasily Belokurov (Oct. 2020). "The last breath of the Sagittarius dSph". In: *MNRAS* 497.4, pp. 4162–4182. DOI: 10.1093/mnras/staa2114. arXiv: 2006.02929 [astro-ph.GA].
Vasiliev, Eugene, Vasily Belokurov, and Denis Erkal (Feb. 2021). "Tango for three: Sagittarius, LMC, and the Milky Way". In: *MNRAS* 501.2, pp. 2279–2304. DOI: 10.1093/mnras/staa3673. arXiv: 2009.10726 [astro-ph.GA].
Vera-Ciro, Carlos and Amina Helmi (Aug. 2013). "Constraints on the Shape of the Milky Way Dark Matter Halo from the Sagittarius Stream". In: *ApJ* 773.1, L4, p. L4. DOI: 10.1088/2041-8205/773/1/L4. arXiv: 1304.4646 [astro-ph.GA].
Virtanen, Pauli et al. (2020). "SciPy 1.0: Fundamental Algorithms for Scientific Computing in Python". In: *Nature Methods*. DOI: https://doi.org/10.1038/s41592-019-0686-2.
Vogelsberger, Mark, Simon D. M. White, Amina Helmi, and Volker Springel (Mar. 2008). "The fine-grained phase-space structure of cold dark matter haloes". In: *MNRAS* 385.1, pp. 236–254. DOI: 10.1111/j.1365-2966.2007.12746.x. arXiv: 0711.1105 [astro-ph].
Wang, F. et al. (June 2022). "Probing the Galactic halo with RR Lyrae stars - II. The substructures of the Milky Way". In: *MNRAS* 513.2, pp. 1958–1971. DOI: 10.1093/mnras/stac874. arXiv: 2203.17032 [astro-ph.GA].
Wang, Shu, Xiaodian Chen, Richard de Grijs, and Licai Deng (Jan. 2018). "The Near-infrared Optimal Distances Method Applied to Galactic Classical Cepheids Tightly Constrains Mid-infrared Period-Luminosity Relations". In: *ApJ* 852.2, 78, p. 78. DOI: 10.3847/1538-4357/aa9d99. arXiv: 1711.06966 [astro-ph.SR].
Wang, WenTing, JiaXin Han, Marius Cautun, ZhaoZhou Li, and Miho N. Ishigaki (May 2020). "The mass of our Milky Way". In: *Science China Physics, Mechanics, and Astronomy* 63.10, 109801, p. 109801. DOI: 10.1007/s11433-019-1541-6. arXiv: 1912.02599 [astro-ph.GA].
Waskom, Michael L. (2021). "seaborn: statistical data visualization". In: *Journal of Open Source Software* 6.60, p. 3021. DOI: 10.21105/joss.03021. URL: https://doi.org/10.21105/joss.03021.
Watkins, Laura L., Roeland P. van der Marel, Sangmo Tony Sohn, and N. Wyn Evans (Mar. 2019). "Evidence for an Intermediate-mass Milky Way from Gaia DR2 Halo Globular Cluster Motions". In: *ApJ* 873.2, 118, p. 118. DOI: 10.3847/1538-4357/ab089f. arXiv: 1804.11348 [astro-ph.GA].
Wetzel, Andrew R. et al. (Aug. 2016). "Reconciling Dwarf Galaxies with ΛCDM Cosmology: Simulating a Realistic Population of Satellites around a Milky Way-mass Galaxy". In: *ApJ* 827.2, L23, p. L23. DOI: 10.3847/2041-8205/827/2/L23. arXiv: 1602.05957 [astro-ph.GA].
White, Simon D. M. and M. J. Rees (May 1978). "Core condensation in heavy halos: a two-stage theory for galaxy formation and clustering." In: *MNRAS* 183, pp. 341–358. DOI: 10.1093/mnras/183.3.341.
Willman, B. and J. Strader (Sept. 2012). ""Galaxy," Defined". In: *AJ* 144.3, 76, p. 76. DOI: 10.1088/0004-6256/144/3/76. arXiv: 1203.2608 [astro-ph.CO].
Wolf, Joe et al. (Aug. 2010). "Accurate masses for dispersion-supported galaxies". In: *MNRAS* 406.2, pp. 1220–1237. DOI: 10.1111/j.1365-2966.2010.16753.x. arXiv: 0908.2995 [astro-ph.CO].
Woudenberg, Hanneke C. (July 2019). *Stellar Streams Investigated: Constraining the Milky Way halo potential with GD-1 and Palomar 5 and unraveling the secrets of Jhelum using Gaia DR2 and SDSS DR9 data.*
Woudenberg, Hanneke C., Orlin Koop, Eduardo Balbinot, and Amina Helmi (Feb. 2022). "Characterization and dynamics of the peculiar stream Jhelum, A tentative role for the Sagittarius dwarf galaxy". In: *arXiv e-prints*, arXiv:2202.02132, arXiv:2202.02132. arXiv: 2202.02132 [astro-ph.GA].
Wu, Youjia et al. (Feb. 2022). "Using action space clustering to constrain the recent accretion history of Milky Way-like galaxies". In: *MNRAS* 509.4, pp. 5882–5901. DOI: 10.1093/mnras/stab3306. arXiv: 2104.08185 [astro-ph.GA].
Xiang, Maosheng and Hans-Walter Rix (Mar. 2022). "A time-resolved picture of our Milky Way's early formation history". In: *arXiv e-prints*, arXiv:2203.12110, arXiv:2203.12110. arXiv: 2203.12110 [astro-ph.GA].
Yavetz, Tomer D., Kathryn V. Johnston, Sarah Pearson, Adrian M. Price-Whelan, and Martin D. Weinberg (Feb. 2021). "Separatrix divergence of stellar streams in galactic potentials". In: *MNRAS* 501.2, pp. 1791–1802. DOI: 10.1093/mnras/staa3687. arXiv: 2011.11919 [astro-ph.GA].
Yong, David et al. (Oct. 2013). "High precision differential abundance measurements in globular clusters: chemical inhomogeneities in NGC 6752". In: *MNRAS* 434.4, pp. 3542–3565. DOI: 10.1093/mnras/stt1276. arXiv: 1307.4486 [astro-ph.GA].

Yoon, Joo Heon, Kathryn V. Johnston, and David W. Hogg (Apr. 2011). "Clumpy Streams from Clumpy Halos: Detecting Missing Satellites with Cold Stellar Structures". In: *ApJ* 731.1, 58, p. 58. DOI: 10.1088/0004-637X/731/1/58. arXiv: 1012.2884 [astro-ph.GA].

Yuan, Zhen, Jiang Chang, Timothy C. Beers, and Yang Huang (Aug. 2020). "A Low-mass Stellar-debris Stream Associated with a Globular Cluster Pair in the Halo". In: *ApJ* 898.2, L37, p. L37. DOI: 10.3847/2041-8213/aba49f. arXiv: 2007.05132 [astro-ph.GA].

Yuan, Zhen et al. (Mar. 2022). "The Pristine survey – XVII. The C-19 stream is dynamically hot and more extended than previously thought". In: *arXiv e-prints*, arXiv:2203.02512, arXiv:2203.02512. arXiv: 2203.02512 [astro-ph.GA].

Zaritsky, Dennis et al. (Jan. 2020). "A Lower Limit on the Mass of Our Galaxy from the H3 Survey". In: *ApJ* 888.2, 114, p. 114. DOI: 10.3847/1538-4357/ab5b93. arXiv: 1909.02025 [astro-ph.GA].

Zavala, Jesús and Carlos S. Frenk (Sept. 2019). "Dark Matter Haloes and Subhaloes". In: *Galaxies* 7.4, p. 81. DOI: 10.3390/galaxies7040081. arXiv: 1907.11775 [astro-ph.CO].

Zhao, Gang, Yong-Heng Zhao, Yao-Quan Chu, Yi-Peng Jing, and Li-Cai Deng (2012). "LAMOST spectral survey—An overview". In: *Research in Astronomy and Astrophysics* 12.7, p. 723.

Zotos, Euaggelos E. (Feb. 2014). "Classifying orbits in galaxy models with a prolate or an oblate dark matter halo component". In: *Astronomy &amp Astrophysics* 563, A19. DOI: 10.1051/0004-6361/201322867. URL: https://doi.org/10.1051%5C%2F0004-6361%5C%2F201322867.